

UNIVERSITY OF ŽILINA



TRANSCOM 2011

9-th EUROPEAN CONFERENCE
OF YOUNG RESEARCH AND SCIENTIFIC WORKERS

PROCEEDINGS

SECTION 5

MATERIAL ENGINEERING
MECHANICAL ENGINEERING TECHNOLOGIES

ŽILINA June 27 - 29, 2011
SLOVAK REPUBLIC

UNIVERSITY OF ŽILINA



TRANSCOM 2011

9-th EUROPEAN CONFERENCE
OF YOUNG RESEARCH AND SCIENTIFIC WORKERS

under the auspices of

Ing. Eugen Jurzyca

Minister of Education, Science, Research and Sport of the Slovak Republic

&

Prof. Ing. Tatiana Čorejová, PhD.

Rector of the University of Žilina

SECTION 5

**MATERIAL ENGINEERING
MECHANICAL ENGINEERING TECHNOLOGIES**

ŽILINA June 27 - 29, 2011
SLOVAK REPUBLIC

Edited by Alan Vaško, Peter Brída
Copyright©by University of Žilina, 2011
ISBN: 978-80-554-0374-8

TRANSCOM 2011

9-th European conference of young research and scientific workers

TRANSCOM 2011, the 9-th international conference of young European researchers, scientists and educators, aims to establish and expand international contacts and co-operation. The main purpose of the conference is to provide young scientists with an encouraging and stimulating environment in which they present results of their research to the scientific community. TRANSCOM has been organised regularly every other year since 1995. Between 160 and 400 young researchers and scientists participate regularly in the event. The conference is organised for postgraduate students and young research workers up to the age of 35 and their tutors. Young workers are expected to present the results they had achieved.

The conference is organised by the University of Žilina. It is the university with about 13 000 graduate and postgraduate students. The university offers Bachelor, Master and PhD programmes in the fields of transport, telecommunications, forensic engineering, management operations, information systems, in mechanical, civil, electrical, special engineering and in social sciences.

SECTIONS AND SCIENTIFIC COMMITTEE

1. TRANSPORT AND COMMUNICATIONS TECHNOLOGY.

Scientific committee: Černý J. (CZ), Drozdziel P. (PL), Dydkowski G. (PL), Gašparík J. (SK), Havel K. (SK), Janáček J. (SK), Jánošíková L. (SK), Kampf R. (CZ), Kavička A. (CZ), Kazda A. (SK), Novák A. (SK), Palúch S. (SK), Peško Š. (SK), Rievaj V. (SK), Šulgan M. (SK), Volek J. (CZ), Žarnay M. (SK), Žarnay P. (SK)

2. ECONOMICS AND MANAGEMENT.

Scientific committee: Bartošová V. (SK), Blašková M. (SK), Borkowski S. (PL), Březinová O. (CZ), Ďurišová M. (SK), Glebocki K. (PL), Gražulis V. (LT), Hittmár Š. (SK), Hrnčiar M. (SK), Kucharčíková A. (SK), Lyakin A. (RUS), Rostášová M. (SK), Rybakov F. (RUS), Seemann P. (SK), Strenitzerová M. (SK), Tomová A. (SK), Veretennikova B.O (RUS)

3. INFORMATION AND COMMUNICATION TECHNOLOGIES.

Scientific committee: Dado M. (SK), Diviš Z. (CZ), Drozdová M. (SK), Hudec R. (SK), Huotari J. (FIN), Keil R. (DE), Klimo M. (SK), Kolev P. (BG), Kotsopoulos S. (GR), Koudelka O. (A), Kováčiková T. (SK), Madleňák R. (SK), Matiaško K. (SK), Ranc D. (FR), Spalek J. (SK), Vaculík J. (SK), Vaculík M. (SK), Vrček N. (CR), Wieser V. (SK), Zábovský M. (SK)

4. ELECTRIC POWER SYSTEMS. ELECTRICAL AND ELECTRONIC ENGINEERING.

Scientific committee: Altus J. (SK), Blažek V. (DE), Brandstetter P. (ČR), Capolino G. A. (FR), Consoli A. (IT), Čápová K. (SK), Dobrucký B. (SK), Janoušek L. (SK), Luft M. (PL), Rusek S. (ČR), Szkutnik, J. (PL), Špánik P. (SK), Vittek J. (SK)

5. MATERIAL ENGINEERING. MECHANICAL ENGINEERING TECHNOLOGIES.

Scientific committee: Adamczak S. (PL), Bokůvka O. (SK), Dzimko M. (SK), Guagliano M. (I), Kunz L. (CZ), Meško J. (SK), Neslušán M. (SK), Nicoletto G. (I), Palček P. (SK), Skočovský P. (SK), Takács J. (H)

6. MACHINES AND EQUIPMENTS. APPLIED MECHANICS.

Scientific committee: Dekýš V. (SK), Gerlici J. (SK), Chudzikiewicz A. (PL), Jandačka J. (SK), Kalinčák D. (SK), Malenovský E. (CZ), Medvecký Š. (SK), Nemček M. (CZ), Sága M. (SK), Sitarz M. (PL), Szava I. (RO), Zapoměl J. (CZ), Žmindák M. (SK)

7. CIVIL ENGINEERING.

Scientific committee: Bujňák J. (SK), Ferrero A. M. (IT), Garbuz A. (UA), Horváth F. (HU), Ižvolt L. (SK), Melcer J. (SK), Petkova R. (BG), Plášek O. (CZ), Malachova A. (RU), Ungureanu V. (RO)

8. SOCIAL SCIENCES.

Scientific committee: Banáry B. (SK), Cabanová V. (SK), Grecmanová H. (CZ), Hádková M. (CZ), Kráľová Z. (SK), Larry Fast (USA), Lengyelfalusy T. (SK)

9. SECURITY ENGINEERING. FORENSIC ENGINEERING.

Scientific committee: Artamonov S. V. (RU), Burg H. (DE), Dudáček A. (CZ), Horák R. (CZ), Kasanický G. (SK), Klučka J. (SK), Leitner B. (SK), Navrátil L. (CZ), Podbregar I. (SLO), Poledňák P. (SK), Šimák L. (SK), Štofko S. (SK)

ORGANIZING COMMITTEE

CHAIRPERSONS Čelko Ján, Bokůvka Otakar

EXECUTIVE SECRETARY Vráblová Helena

MEMBERS Bača Tomáš, Bačová Katarína, Baďurová Silvia, Belan Juraj, Bomba Lukáš, Brída Peter, Brumerčík František, Gavláková Eva, Hampl Marek, Harušinec Jozef, Horváth Peter, Hrbček Jozef, Jošt Jozef, Kittel Ladislav, Kolla Eduard, Koniar Dušan, Kopas Peter, Land'ák Milan, Lieskovský Anton, Mendrošová Katarína, Mišiaková Kvetoslava, Mokryš Michal, Mrvová Miroslava, Mužíková Karolína, Pácha Matěj, Peterková Andrea, Pilát Peter, Pitor Ján, Raždík Ján, Smetana Milan, Spuchľáková Erika, Šípek Michal, Šramová Veronika, Tengler Jiří, Tkáčová Gabriela, Vaško Alan, Vaško Milan, Vlček Jozef, Vrábel Ján, Vráblová Lucia, Závodská Anna, Zvaríková Katarína, Žiačková Vladimíra



SECTION 5 MATERIAL ENGINEERING MECHANICAL ENGINEERING TECHNOLOGIES

REVIEWERS:

Barta Dalibor
Belan Juraj
Bokúvka Otakar
Czán Andrej
Fabian Peter
Fintová Stanislava
Hadzima Branislav
Jandačka Jozef
Konečná Radomila
Kuric Ivan
Liptáková Tatiana
Meško Jozef
Mičian Miloš
Mičietová Anna
Mintách Rastislav
Moravec Ján
Neslušán Miroslav
Nový František
Palček Peter
Pilc Jozef
Poppeová Viera
Sládek Augustín
Škublová Lenka
Tillová Eva
Vaško Alan
Zatkalíková Viera

Note:

Authors are responsible for language contents of their papers

CONTENTS

BAŇÁKOVÁ, ALENA – MEŠKO, JOZEF, Žilina, Slovak Republic: Material for Roller Bearings and Heat Treatment of Components	11
BEREŠÍK, TOMÁŠ – MIČIETOVÁ, ANNA – MÔCIK, STANISLAV, Žilina, Slovak Republic: New Options of the Utilization of the Technical Information System Monaco	15
BOHUŠOVÁ, ZDENA – MORAVEC, JÁN, Žilina, Slovak Republic: Analysis of Mechanical Values of Coated Sheets Aluminerit	19
BREZÁNI, JAROSLAV – MIČIETOVÁ, ANNA, Kysucké Nové Mesto, Slovak Republic: Optimalization of Parameters in Model for Selection of Unconventional Method of Material Dividing	23
BREZNIČAN, MARTIN – FABIAN, PETER, Žilina, Slovak Republic: The Volume Changes of Components of Special Steels after Vacuum Quenching	27
BUBENKO, LUKÁŠ – KONEČNÁ, RADOMILA – NICOLETTO, GIANNI, Žilina, Slovak Republic: Fatigue Crack Propagation Properties of ADI 1050 and IDI	31
BUKOVINA, MICHAL – HADZIMA, BRANISLAV – ŠKUBLOVÁ, LENKA, Žilina, Slovak Republic: Effect of Phosphate Conversion Coating on Electrochemical Properties of AE21 Magnesium Alloy	35
CĂPĂȚÎNĂ, CAMELIA – GĂMĂNECI, GHEORGHE, Gorj, Romania: Composite Materials Achievement in order to Develop Insulations for Furnaces in Machinery Building Industry	39
CZÁNOVÁ, TATIANA – PILC, JOZEF – NOSÁK, TOMÁŠ, Žilina, Slovak Republic: Analysis of Milling Tools Wears Intensity in the Primary Interaction	43
ČERNIAUSKAS, EGIDIJUS – KERŠYS, ARTŪRAS – KERŠIENĖ, NERINGA, Kaunas, Lithuania: Research of the Vehicle Side Impact against an Immovable Obstacle	47
DEKAN, JÁN – KOŠINÁR, MATÚŠ – PILC, JOZEF, Žilina, Slovak Republic: Verify the Accuracy of Positioning the Lathe's School EMCO ConceptTurn 55	53
DERBAS, MICHAL – CZÁN, ANDREJ – SPORKA, MICHAL, Žilina, Slovak Republic: Renovating Intensification of Machining Nitrided Layers of Tools for Volume Forming	57
DOMAGAŁA, AGNIESZKA – TOFIL, SZYMON, Kielce, Poland: The Comparison between Different Types of Cutting – Selection of the Best Method	61
ĎURINÍKOVÁ, EMÍLIA – TILLOVÁ, EVA – CHALUPOVÁ, MÁRIA, Žilina, Slovak Republic: Influence of Annealing on Hardness of the Recycled AlZn10Si8Mg Cast Alloy	65
FAJNOR, PAVOL – LIPTÁKOVÁ, TATIANA – ZATKALÍKOVÁ, VIERA, Žilina, Slovak Republic: Electrochemical Properties of the AISI 316Ti Stainless Steel in Different Redox Potential Environment	69
GARBALA, MARTA, Kielce, Poland: The Influence Tantalum Placed Foil between Two Steel Plates on the Weld Penetration Shape Formed during Welding Laser	73
GHELICHI, RAMIN – GUAGLIANO, MARIO, Milan, Italy: Determination of Critical Velocity in Cold Spray Coating by Finite Element Analysis	77
HOPKO, ANTON – MEŠKO, JOZEF – KOŇAR, RADOSLAV, Žilina, Slovak Republic: Influence Shielding Gases on Weld Penetration	81

HURTALOVÁ, LENKA – TILLOVÁ, EVA, Žilina, Slovak Republic: Evolution of the Mechanical Properties in Recycled AlSi9Cu3 Cast Alloy during Age-Hardening	85
KOKAVEC, MARIÁN – KONEČNÁ, RADOMILA – NICOLETTO, GIANNI, Žilina, Slovak Republic: Role of Surface Condition on Fatigue Behavior of Nodular Cast Iron	89
KOŇÁR, RADOSLAV – MIČIAN, MILOŠ – HOPKO, ANTON, Žilina, Slovak Republic: Analysis of Boundary Conditions for the Simulation of Welding in the Repair of Gas Pipelines with Steel Sleeve	93
KOWALCZYK, JAKUB – JOSKO, MARIAN, Poznan, Poland: Ultrasonic Testing of Adhesive Joints with a Low Defectosopic Susceptibility	97
MASLÁKOVÁ, KRISTÍNA – FRANKOVSKÝ, PETER, Košice, Slovak Republic: The Determination of the Material Composition of the Pressure Vessel by Using EDX Analysis	101
MAZUR, MAGDALENA – SZATANIAK, PAWEŁ – ULEWICZ, ROBERT, Czestochowa, Poland: Analysis of Causes of Blistering in Welded Joints	105
MEDLEN, DUŠAN – BOLIBRUCHOVÁ, DANA, Žilina, Slovak Republic: Heat Treatment Effect on the Mechanical Properties of Aluminum Alloy AlSi6Cu4 Modified by Antimony	109
MELO, BORISLAV – MORAVEC, JÁN, Martin, Slovak Republic: Analysis of W.Nr. 1.2311 and W.Nr. 1.2311 Toolsteels Used for Less Stressed Components of Cold-Molding Tools	113
MÔCIK, STANISLAV – MIČIETOVÁ, ANNA – BEREŠÍK, TOMÁŠ, Žilina, Slovak Republic: The Surface State of Materials after Thermal Cutting	117
MRÁZIKOVÁ, RASTISLAVA – HADZIMA, BRANISLAV – ŠKUBLOVÁ, LENKA, Žilina, Slovak Republic: Corrosion Resistance of Ti6Al4V Titanium Alloy with Electroerosive Modified Surface	121
MRÁZOVÁ, MICHAELA – PILC, JOZEF – STANČEKOVÁ, DANA, Žilina, Slovak Republic: Comparison of Machinability of Biocompatible Materials Use for Dental Implants	125
NAVRÁTILOVÁ, LUCIE – KUNZ, LUDVÍK – NOVÝ, FRANTIŠEK – MINTÁCH, RASTISLAV, Brno, Czech Republic: Influence of Gigacycle Fatigue on Development of Surface Relief in UFG Copper	129
ORZECOWSKI, TADEUSZ – STOKOWIEC, KATARZYNA, Kielce, Poland: Solar Energy Storage on the Example of a Paraffin Tank	133
ORZECOWSKI, TADEUSZ – ZWIERZCHOWSKA, SYLWIA, Kielce, Poland: Heat Transfer Coefficient Components of the Large Droplets of Water in the Range of Film Boiling	137
OTŘÍŠAL, PAVEL – FLORUS, STANISLAV, Vyškov, Czech Republic: Chosen Methods and Ways for Barrier Materials Protective Properties Evaluation towards Toxic Compounds Permeation	141
PALLO, PETER – MIČIAN, MILOŠ – STRAŠKO, JÁN, Žilina, Slovak Republic: Experimental Measurement of Thermal Cycles and Drilling Strength at Welding of Fitting	147
PASTIRČÁK, RICHARD – URGELA, DUŠAN, Žilina, Slovak Republic: Construction of Milling Machine for Production Moulds Made by Patternless Process	151
PORUBČAN, JAKUB – BLAŽEK, DALIBOR – PALČEK, PETER, Žilina, Slovak Republic: Amplitude Dependence of Internal Damping in Extruded Aluminium Alloy AW-2007	155
ROSIPAL, MARTIN – NESLUŠAN, MIROSLAV – FAKTOR, MIROSLAV, Žilina, Slovak Republic: Multiparametric Evaluation of Barkhausen Noise Envelopes	159
SEEWALD, RÓBERT – PALČEK, PETER – BRANDT, MARTIN – NEČAS, LIBOR, Žilina,	

Slovak Republic: Measurement of Surface Temperature of Polymerization Reaction of Bone Cement with Thermovision Camera	163
SEK, PIOTR, Kielce, Poland: Experimental Comparising Evaluation of Tribological Properties of Surface with Geometrical Texture	167
SELEJDAK, JACEK – SLÁDEK, AUGUSTÍN, Czestochowa, Poland: Efficiency Assessment of Sheet Pile Rolling Technology	171
SPADŁO, SŁAWOMIR – DUDEK, DOMINIK – MŁYNARCZYK, PIOTR, Kielce, Poland: Analyzing the Shape Deviation Cylindrical Holes Machined by EDM (Electro Discharge Machining) Process	175
ŠÍPEK, MICHAL – NESLUŠAN, MIROSLAV, Žilina, Slovak Republic: Tool Wear Monitoring by Hard Turning of Hardened Steel 100Cr6	179
ŠKORÍK, VIKTOR – ŠKUBLOVÁ, LENKA – HADZIMA, BRANISLAV – FAKTOROVÁ, DAGMAR, Žilina, Slovak Republic: Electrochemical Properties of Heat Influenced Structures Made of Austenitic Stainless Steel	185
TRŠKO, LIBOR – MIKOVÁ, KATARÍNA – BOKŮVKA, OTAKAR, Žilina, Slovak Republic: Ultra – High Cycle Fatigue of High Grade Carbon Steel	189
ULEWICZ, ROBERT – NOVÝ, FRANTIŠEK – MAZUR, MAGDALENA, Czestochowa, Poland: Fatigue Properties of S235J2 Steel in the Ultra-High-Cycle Area	193
VARGA, MILOŠ – MIČIAN, MILOŠ, Žilina, Slovak Republic: Analysis of Simulation Technology Faults in Dip and Pulse Transfer of GMAW Welding	197
VELAS, STANISLAV – CZÁN, ANDREJ – STANČEKOVÁ, DANA, Žilina, Slovak Republic: ISF Method – Isotropic Superfinishing	201
VOJSOVIČOVÁ, MICHAELA – LIPTÁKOVÁ, TATIANA – GAŇA, DUŠAN, Žilina, Slovak Republic: Evaluation of Rheological Properties of Thermoplastic Polymers after Degradation	05
ŽÁK, JOSEF – VAVŘIČKA, JIŘÍ, Prague, Czech Republic: Load Distribution in Hamburg Wheel Tracking Test	209
MUCHA, ZYGMUNT - KURP, PIOTR, Kielce, Poland: Modeling of Non Contact Laser Forming and Microstructure Investigations of Flat Plates.....	215



Material for Roller Bearings and Heat Treatment of Components

* Alena Baňáková, * Jozef Meško

* University of Žilina, Faculty of Mechanical Engineering, Department of Technological Engineering,
Univerzitná 1, 01026 Žilina, Slovakia, alena@banakova.sk, jozef.mesko@fstroj.uniza.sk

Abstract. The article discusses possibilities of use roller bearing materials in industry. It describes roller bearing steel mostly used for its components. Also discusses isothermal beneficiation of roller bearing steel.

Keywords: roller bearing, heat treatment, beneficiation.

1. Introduction

According to the type of use, roller bearing steel belongs into the group of construction steel, where it is also standardized. According to the carbon content and the content of the other main compounds is its chemistry almost the same world-wide. Very high demand is put on the quality of this sort of steel (stability of dimensions according to the temperature change, mechanical stress, ductility etc).

2. Roller Bearings Material

Both metal and non metal materials are used to produce roller bearing components. Rings and corpuscles of the roller bearings are mostly made of roller bearing steel “Fig. 1.”, but manufacture and operation conditions of roller bearing often demand use of other materials, such as: cementation steel, surface hardened steel, thermal stabilized steel and stainless steel. Also construction ceramic is used during the production of the components lately. Demands on roller bearing material [1] are mentioned in the Fig. 2.

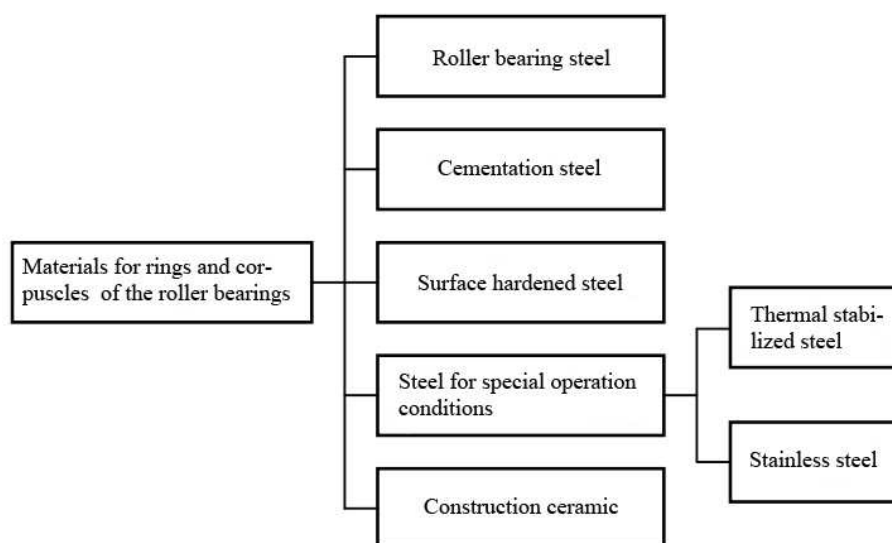


Fig. 1. Distribution of materials used for rings and corpuscles of the roller bearing [1]

Aspect of assessment	Demands on material
Hertzian pressure Rolling Sliding	high hardness, generating pressure resistance, purity grade, wear-out resistance
Impact stress resistance	ductility adequate to hardness
Dimensional stability	no structural changes
Operational conditions	high temperature and corrosion resistance
Distribution of rolling components	elasticity and firmness, gliding features, weight
Economic aspect	price of material, tooling expenses

Fig. 2. Demands on roller bearing material according to demands on roller bearings [1]

2.1. Roller Bearing Steel

Rings and corpuscles of the roller bearings are mostly made of the roller bearing steel, while the through-hardening roller bearing steel has the dominant position in this group. According to STN EN ISO 683-17, is this through-hardening steel used for roller bearings, commonly called “roller bearing steel” [3] in wide range of literature and also in practical use.

During the last 30 years, the range of roller bearing steel settled on those with the carbon content of 1% with various content of alloy components, like chromium and manganese. Basically it is possible to divide recently used roller bearing steel into four groups according to content of basic compounds:

- 1% carbon, and 0.5 % chromium steel for corpuscles up to 10-13 mm;
- 1% carbon, and 1 % chromium steel for corpuscles up to 17-22.5 mm;
- 1% carbon, and 1.5 % chromium steel for corpuscles up to 25-30 mm;
- 1% carbon, and 1 % manganese and 1-1.5 % chromium steel for corpuscles above 25 mm and rings more than 16 mm [2] thick.

Two types of doped hypereutectoid hardenable chrome steel, brand 100Cr6 a 100CrMnSi6-4 of chemistry according to the Tab. 1 and Tab. 2 [3] is commonly used in domestic production.

Norm	Steel brand	Chemistry (weight %)								
		C	Si	Mn	Cr	Mo	P _{max}	S _{max}	Ni _{max}	Cu _{max}
STN	14109 ¹⁾	0,90 1,10	0,15 0,35	0,30 0,50	1,30 1,65		0,027	0,030	0,30	0,25
STN EN ISO 683 - 17	100Cr6 ²⁾	0,93 1,05	0,15 0,35	0,25 0,45	1,35 1,60	max. 0,10	0,025	0,015		0,30
ASTM	52 100	0,98 1,10	0,15 0,35	0,25 0,45	1,30 1,60	≤ 0,10	0,025	0,025	0,25	0,35
DIN	100Cr6	0,90 1,05	0,15 0,35	0,25 0,40	1,40 1,65		0,025	0,025	0,30	0,30
JIS	SUJ 2	0,95 1,10	0,15 0,35	≤ 0,5 0	1,30 1,60	≤ 0,08	0,025	0,025	0,25	0,25
GOST	Šch 15	0,95 1,05	0,17 0,37	0,20 0,40	1,30 1,65		0,027	0,020	0,30	0,25

Tab. 1. Chrome steel for standard roller bearings [3]

Norm	Steel brand	Chemistry (weight %)								
		C	Si	Mn	Cr	Mo	P _{max}	S _{max}	Ni _{max}	Cu _{max}
STN	14209 ¹⁾	0,90 1,10	0,35 0,65	0,90 1,20	1,30 1,65		0,027	0,030	0,30	0,25
STN EN ISO 683 - 17	100CrMnSi6- 4 ²⁾	0,93 1,05	0,45 0,75	1,00 1,20	1,40 1,65	max. 0,010	0,025	0,015		0,30
ASTM	52 100 E	0,85 1,00	0,50 0,80	1,40 1,70	1,40 1,80	≤ 0,06	0,025	0,025	0,25	0,35
DIN	100CrMnSi6-4	0,90 1,05	0,50 0,70	1,00 1,20	1,40 1,65		0,030	0,025	0,30	0,30
JIS	SUJ 3	0,95 1,10	0,40 0,70	0,90 1,15	0,90 1,20	≤ 0,08	0,025	0,025	0,25	0,25
GOST	Šch 15SG	0,95 1,05	0,40 0,65	0,90 1,20	1,30 1,65		0,027	0,020	0,30	0,25

Tab. 2. CrMn(Mo), CrMnSi steel for standard roller bearings [3]

3. Heat Treatment of Roller Bearing Components

According to the best functionality of the roller bearings, their components must have certain mechanical features. These features are commonly achieved by hardening to martensite and then backing up under lower temperatures. The process of hardening provides the steel with high hardness while backing up lowers the inner tension level and fragility of the steel. Hardening into cold environment causes high thermal and structural tensions, which often result in various deformations, especially cracking of complicated product shapes. After hardening to the martensite, there still remains some austenite in the structure. It is an unwanted component because when exceeding certain amount, it has an adverse influence on the hardness and structural stability of the roller bearings [1].

Perspective technology for thermal treatment of roller bearings components (especially rings), is isothermal benefication. After austenite treatment of the roller bearing steel and it's cooling by over critical speed into isothermal change of austenite in the bainite zone, isothermal hold-off in this temperature follows. The result of this precisely controlled proceeding of the thermal treatment is roller bearing steel with bainite or bainite-martensite structure. Comparing to martensite hardening, slightly lower hardness is achieved after isothermal benefication of the roller bearing steel, however its ductility is several times higher. Also its inner tension levels are lower comparing to martensite hardening [1].

3.1. Isothermal Transformation of the Austenite in the Bainite Structure

Under "isothermal treatment" we understand transformation of the austenite in the bainite zone during the isothermal hold-off in the temperature of the bainite change. The cooling speed of the steel from the austenite temperature into the bainite zone has to be high enough to avoid transformation of the austenite in the pearlitic zone. The main structural compound of the steel after the isothermal treatment is upper or lower bainite. Another compound is residual austenite, or also martensite. Isothermal transformation temperature of the austenite to the bainite is usually above Ms. The time of the hold-off has to be long enough to allow the complete bainite transformation under given thermal conditions. Prolonging of this hold-off time might be adverse according to the resulting mechanical features, because it may cause reverse back up fragility in the steels predisposed to this effect [1]. Theoretical and real curves of the pearlite and bainite transformation [1] in IRA diagram on Fig. 3.

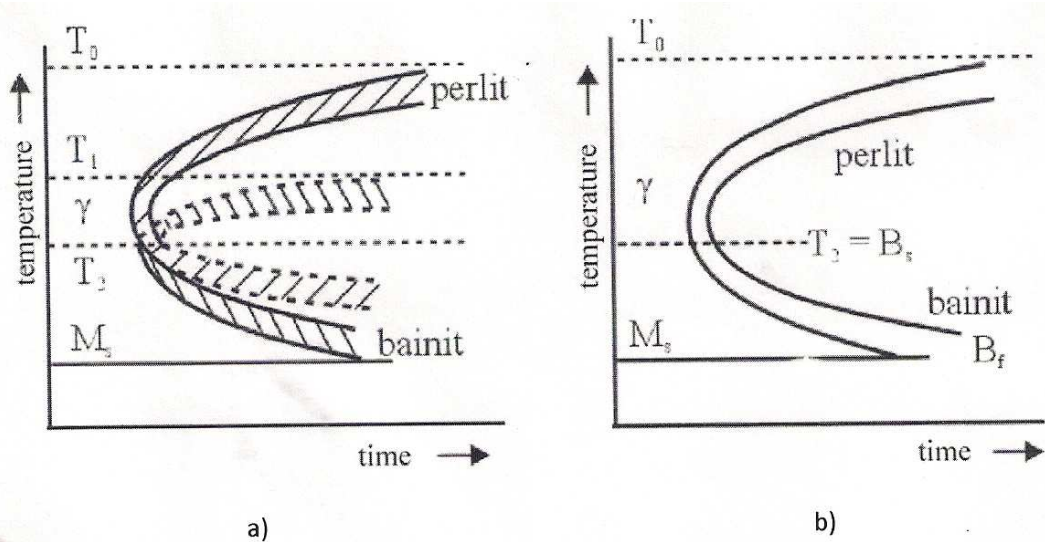


Fig. 3. IRA Diagram of the carbon steel [1]

a) theoretical curves of the beginning and the end of pearlite and bainite transformation of the carbon steel with eutectoid composition, b) real curves for the same conditions and composition

4. Conclusion

Components of the roller bearings are exposed to extreme mechanical stress. Choice of the suitable material for these components as well as thermal treatment method is very important according to stability of dimensions and durability of components. Also economic aspects and quality rate of the finished roller bearing should be considered.

References

- [1] HOZÁK, M. *Vplyv izotermického zušľachtovania na vlastnosti ložiskovej ocele 100CrMnSi6-4*: dizertačná práca. Žilina: Žilinská univerzita v Žiline, 2005.
- [2] JECH, J. *Oceli na valivá ložiska a jejich tepelné zpracování*. 1. vyd. Praha: SNTL – Nakladatelství technické literatury, 1968
- [3] KRUPKA, J. *Optimalizácia kaliaceho procesu ložiskovej ocele 100Cr6*: diplomová práca. Žilina: Žilinská univerzita v Žiline, 2010.



New Options of the Utilization of the Technical Information System Monaco

*Tomáš Berešík, *Anna Mičietová, *Stanislav Môcik

* University of Žilina, Faculty of Mechanical Engineering, Department of Machining and Manufacturing Engineering, Univerzitná 1, 010 26 Žilina, Slovakia, {Tomas.Beresik, Anna_Micietova, Stanislav.Mocik}@fstroj.uniza.sk.

Abstract. This article displays the options of using of the SYSKLASS system in support of the production preparation in section of non-conventional methods of machining. Described topic is discussed these days in connection with increasing tendency towards practical use of methods in engineering company during machining of hard-to-machine materials and design complicated components.

Keywords: Non-conventional methods of machining, technical information system MONACO.

1. Introduction

System MONACO is software for managing TPV in different departments using web services. The system is a solution for various sized companies, starting from the smallest, where the office consists of one person, to the large companies, where the technical department having statute of division consists of several people. The system offers unified process of documentation evidence and its accessibility. Nowadays, when non-conventional methods of machining are discussed more often, it is necessary to search for new view of the manufacturing and consider the possibilities but also constraints of implementation of the non-conventional methods in computer aided systems.

2. New Conception of the Technical Information System Monaco

For successful integration of non-conventional methods of machining into the technical information system MONACO it is necessary to modify and supplement the existing databases and create new ones. This includes mainly the following databases: Materials, Workplaces, Tools. Once the databases are completed by the necessary parameters the system MONACO is ready for use also in the field of non-conventional methods of machining.

2.1. Materials

This database should contain all hardmachining materials used in the factory. All materials should be sorted out in detail and each of them should include all important parameters and properties, which influence the choice of additional data from databases in the process of creation of the technological process. This includes mainly the following parameters:

- Primary parameters : Rm, Re, %C, Mn, Si, S, P.
- Secondary parameters : weight, technical standard.
- Selection criteria: sets the range from-to and the order of parameters.
- Workability : accuracy, hardness, fragility, workability, concept.
- Physical parameters : electrical conductivity, melting point, heat conductivity, chemical reactivity, mass density.

Materials will not be classified into the previously created databases. This solution is nowadays inconvenient. Materials will be classified through technical documents directly into the system MONACO. This system of classification of the materials through documents seems to be the best solution “Fig. 1”.

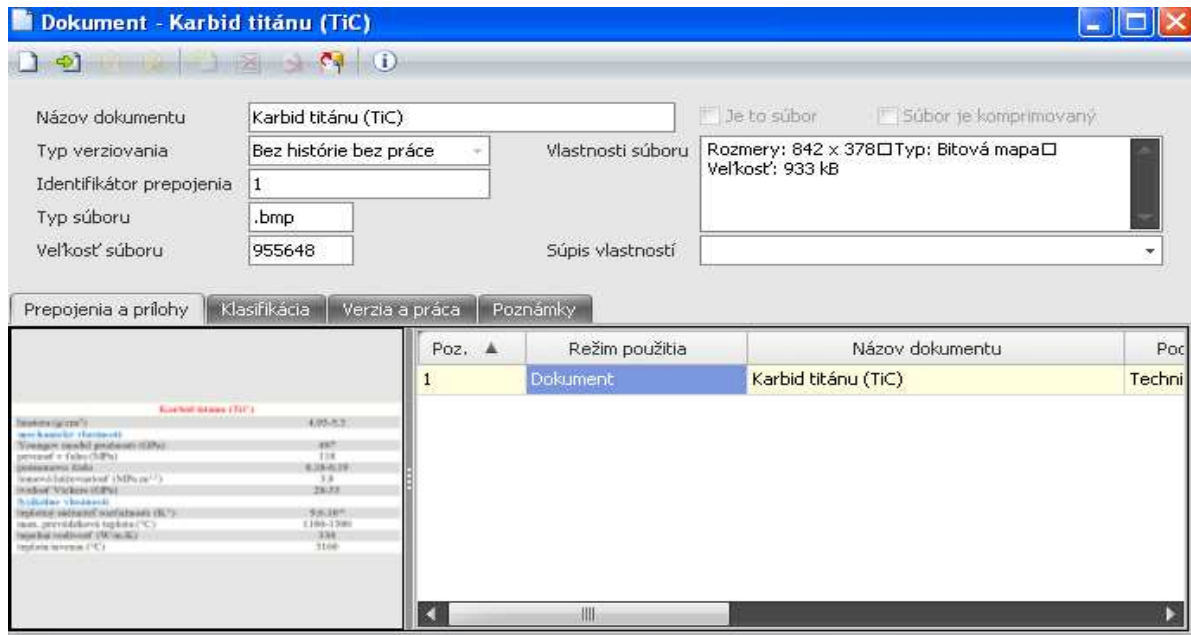


Fig.1. System for classification of the materials

Each document will contain only one material and will be named by this material. Each document will contain an attachment, which will contain all necessary properties of the material. Through the material documents there are created imaginary databases in the system MONACO.

The biggest advantage of the material documents is the possibility to link them easily to the real semi – workpiece.

2.2. Workstations

This database contains information about the mechanical and manual workstations used in the factory as well as machines for non - conventional machining methods “Fig. 2“. All machines are sorted out in detail according to the method and type of machining, and by each machine there are mentioned important parameters and properties, which influence the choice of additional data from databases in the process of creation of the technological process.

The basic database named Workstations will contain the following sub-databases: Ultrasonic machining, Water jet machining, Electro – chemical machining, Electro discharge machining, Laser beam machining, and Plasma beam machining “Fig. 3”.

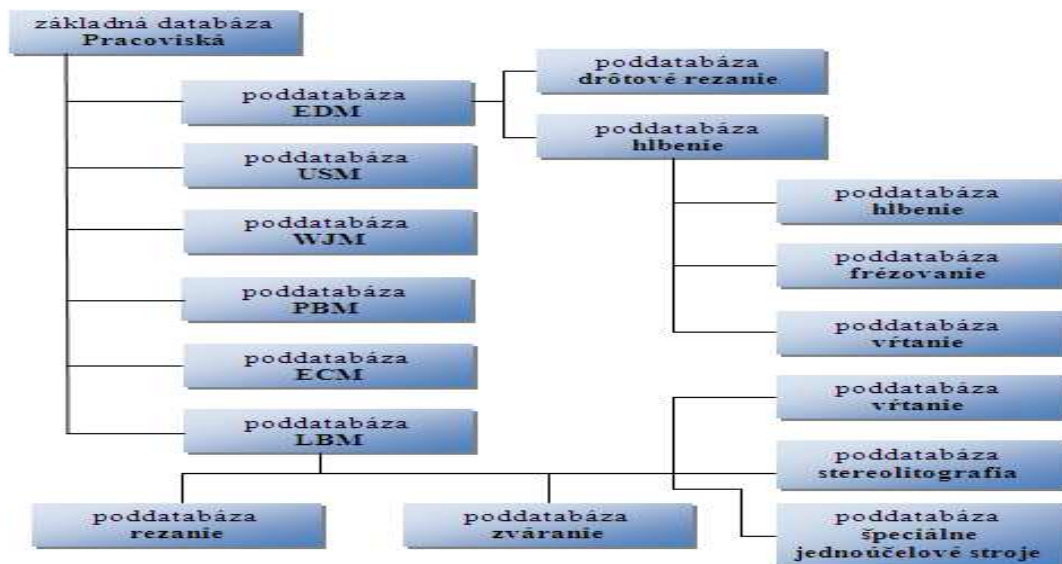


Fig. 2. Structure of database Workstations



Fig. 3. Database Workstations in the system MONACO

2.3. Tools

This database contains information about the most-frequently used equipment standards, fixtures, gauges, working media, support equipments and etc. Single elements in the sub-databases are sorted out by the type of method and contain important parameters and properties which influence the choice of additional data from databases in the process of creation of the technological process. Suggested structure of the database Tools is in the Figure 4. Figure 5 presents the newly created database Tools in the system MONACO “Fig. 5”.

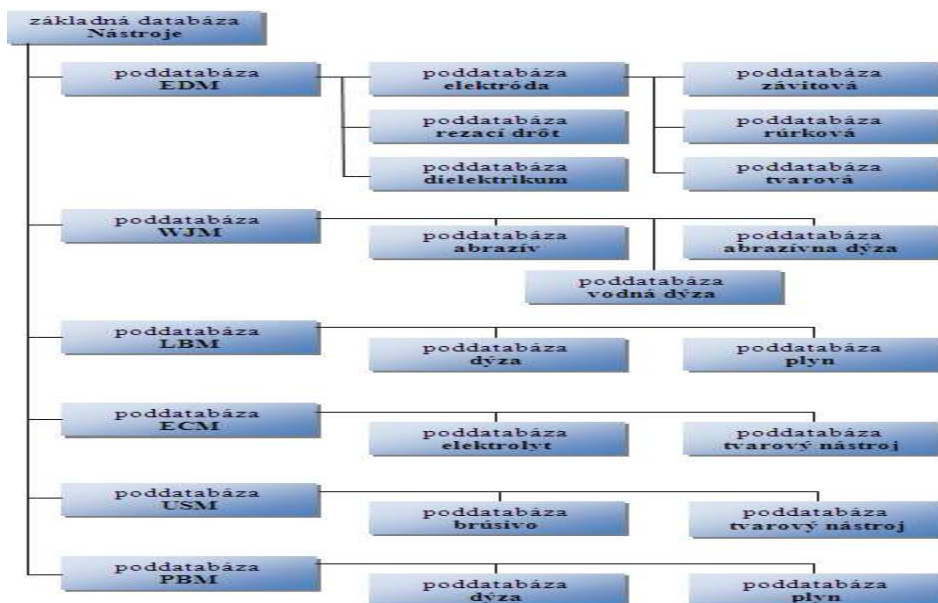


Fig. 4. Structure of the database Tools



Fig. 5. Database Tools in the system MONACO

3. Conclusion

Incorporation of the automation contributes to the modernization of the technological production preparation process in a short time. At the same time it enables faster reaction to the market swings and moves in demand and innovations of the competition.

Introduction of the system MONACO for the non-conventional methods of machining is very important in term of increasing tendency towards using these methods in engineering firms.

References

- [1] KASAJOVÁ, M., RAKYTA, M. *Nové trendy v technickej príprave výroby*, Zborník referátov, InvEnt 2009, Žilina, 2009, pp. 102 – 107
- [2] KURIC, I., KOŠTURIK, J., JANÁČ, A., PETERKA, J., MARCINČIN, J. *Počítačom podporované systémy v strojárstve*. EDIS – Vydavateľstvo Žilinskej univerzity, Žilina, 2002.
- [3] KURIC, I., MATUSZEK, J., DEBNÁR, R. *Computer Aided Process Planning in Machinery Industry*. Politechnika Lodzka, Bielsko Biala, 1999, p. 139
- [4] KURIC, I., VAREŠINSKÝ, E., ČUBOŇOVÁ, N. *Computer aided process planning based on Group Technology*. Textbooks, 2.Edition, Sjf-KMA, Žilina, 1999, p. 39
- [5] MIČIETOVÁ, A. *Nekonvenčné metódy obrábania*, EDIS – vydavateľstvo Žilinskej univerzity, Žilina, 2001



Analysis of Mechanical Values of Coated Sheets Aluminerit

*Zdena Bohušová, *Ján Moravec,

*University of Žilina, Faculty of Mechanical Engineering, Department of Technological Engineering,
Univerzitna 2, 01026 Žilina, Slovakia, {zdenka.bohusova, jan.moravec}@fstroj.uniza.sk

Abstract. The paper evaluated the base mechanical values of material Aluminerit, which is a new material used in industry. It is sheet from deep drawn steel with aluminium coating. There were also evaluated the real 3D deformations measured by an optical system ARAMIS. Experiments were carried out in cooperation with the Technical University of Liberec.

Keywords: coating, deformation, tensile test

1. Introduction

Coated steel sheets now extend to the most of the industries and on its importance decided the quality and operational reliability of the future products. Protective coatings on metal surfaces played an irreplaceable role in a very wide range of using construction materials.

Aluminerit is deep-drawing steel DX56D EN 10346 coated with aluminium (90% Al and 10% Si) melt by continuous electroplating. The depth concentration profile of aluminium layer was detected by GD-OES method “Fig. 1.”. The thickness of the aluminium layer ranges from 10 to 30 μm “Fig. 2.”.

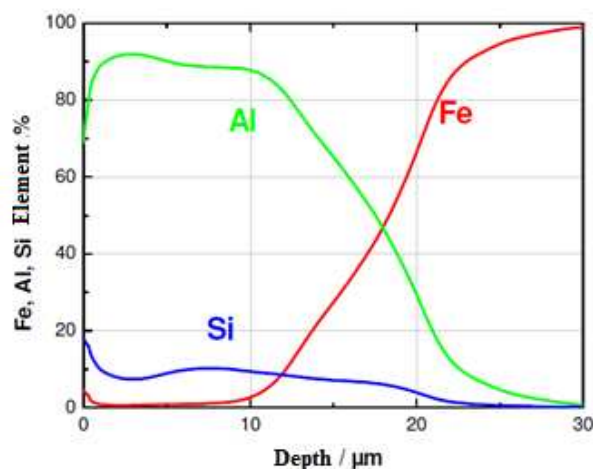


Fig. 1. GD-OES analysis of Aluminerit

Passive layer of aluminium oxide formed immediately after contact with oxygen in the air. Since the passive layer is naturally restores after the damage, the coating by aluminium is excellent protection against corrosion and chemical attack.

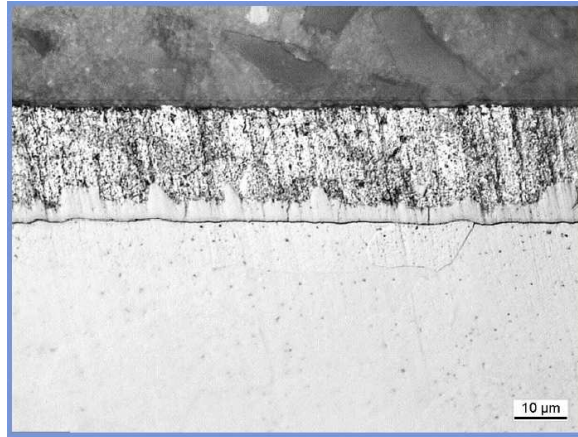


Fig. 2. Longitudinal section through Aluminerit, 150 x, non-etched

2. Tensile Test

Suitability of steel sheets for forming is generally assessed by the results of tensile test. It is the most widespread test for getting the basic mechanical characteristics of the sheet metal. Measured values will be used for qualitative evaluation of sheet and its assessment in terms of further processing.



Fig. 3. Workplace of the tensile testing

The aim of the test, which conditions and shape of the test sample indicates the standard STN EN 10002-1, is to get the value of basic mechanical characteristics:

$R_{p\ 0.2}$ - yield strength, R_m - ultimate strength, A_{50} – ductility, r - coefficient of the normal anisotropy, n - strain hardening exponent.

These values give a complete picture of the properties of the sheet, but do not give clear information about its behaviour when formed. Fig. 3 shows a workplace for static tensile testing.

For tensile testing were use flat bars with their heads, exactly according to the standards “Fig. 4”.

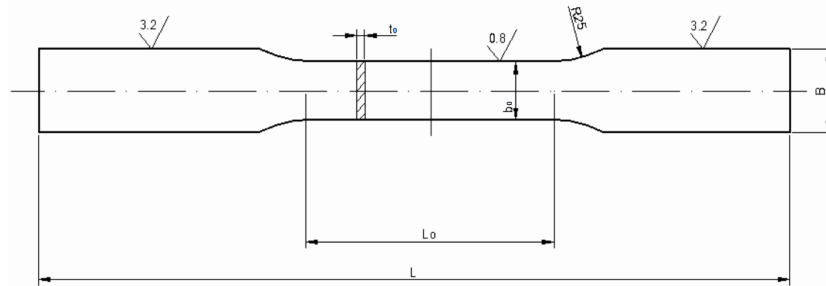


Fig. 4. Dimensions of the test sample for tensile test

3. Experiment

To assess the anisotropic properties of the material there were for tensile test collect 3 samples in directions 0 °, 45 ° and 90 ° toward the rolling direction. The measured values of yield strength, ductility and ultimate strength are shown in Tab. 1.:

b_0 is the initial width of test bar, b_1 is a finite width of test bar, L_0 is the initial gauge length of the test bar, L_1 is the final measured length of the test bar, r is the coefficient of normal anisotropy, which is determined according to “(1)”, t_0 is thickness.

$$r = \frac{\ln(b_0/b_1)}{\ln((L_1, b_1)/(b_0, L_0))} \quad (1)$$

	Sample	b_0 (mm)	t_0 (mm)	b_1 (mm)	L_0 (mm)	L_1 (mm)	r (-)	$R_{p0,2}$ (MPa)	R_m (MPa)	A_{50} (%)
0°	1	20,118	0,801	17,846	80	97,1	1,724	135,9	291,2	44,81
	2	20,120		17,727				138,3	290,6	43,25
	3	20,125		17,824				136,1	292,0	45,34
Average value:								136,8	291,3	44,47
45°	1	20,123	0,801	17,942	80	97,11	1,363	145,3	300,2	39,66
	2	20,122		17,909				146,4	299,0	39,98
	3	20,128		18,135				145,3	299,0	40,94
Average value:								145,7	299,4	40,20
90°	1	20,112	0,801	17,690	80	97,22	1,989	140,4	289,9	39,33
	2	20,108		17,60				138,2	289,4	39,31
	3	20,109		17,698				139,1	289,2	39,70
Average value:								139,2	289,5	39,45

Tab. 1. Measured values obtained by tensile test of the material ALUMINERIT

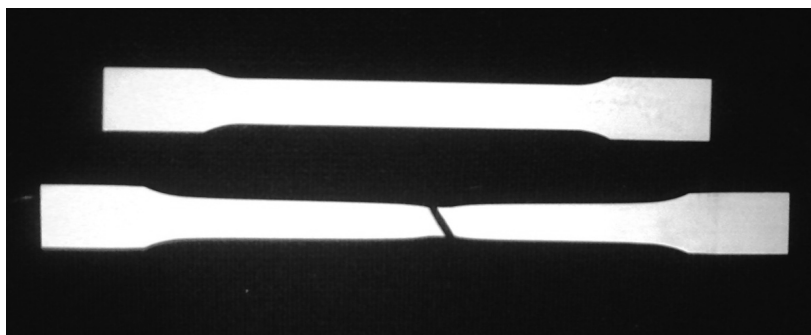


Fig. 5. Test samples before and after tensile test

3.1. Determination of Limit Values

ARAMIS is a non-contact measuring system from GOM for real 3D measurement of deformations. The result is a colourful map of the distribution of deformations on the object strain either statically or dynamically. It uses still perfecting recording technology in the form of two CCD cameras.

The principle of detection, whether displacements or deformations, is in contrast of the model applied on the surface of the object under examination. Contrast pattern when the object is loaded deforms with the object at the same. This deformation is recorded by a pair of cameras and then evaluated on the principle of correlation. For the analysis of forming processes is used forming flow limit curve (FLC). Combinations of these curves in the diagram give a comprehensive overview of the material cut-off characteristics due to its forming capabilities.

Values thus obtained are the basis for drawing a diagram FLD (Forming Limit Diagram), which is then use for comparison as the results of the simulation, or for example real measurement results of forming.

As we can seen on Fig. 6, by optical measurement of strain field at surface of the tested samples was found that the deformation is unevenly distributed and the largest strain is in the place where the neck is formed.

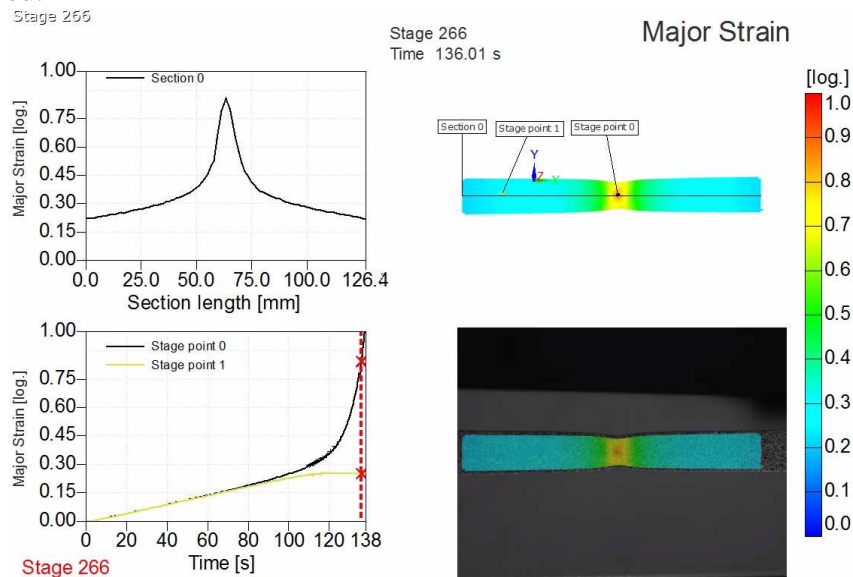


Fig. 6. Final evaluation of the main supply system ARAMIS

4. Conclusion

In the paper was observed results of mechanical values of the material ALUMINERIT provided by tensile test. The largest yield strength, 145,7 MPa, tensile strength, 299,4 MPa and ductility, 40,20% was measured in the direction of 45 ° toward the rolling direction. There were also measured real deformations by an optical system ARAMIS.

Acknowledgement

This article was created with the help of Ministry of Education of the Slovak republic, grant KEGA 216-007ŽU-4/2010.

References

- [1] SOBOTKA, J. *Formability of TWIP Materials and its Evaluation by Optical Systems*. Liberec, 2010.
- [2] <http://www.mcae.cz/aramis>



Optimalization of Parameters in Model for Selection of Unconventional Method of Material Dividing

*Jaroslav Brezáni,**Anna Mičietová

* Ing. Jaroslav Brezáni, INA Schaeffler Gruppe, Dr. G. Schaefflera 1, 024 01 Kysucké Nové Mesto, Slovak Republic, e-mail.: jaroslav.brezani@schaeffler.com

**prof.Ing.Anna Mičietová, PhD., University of Žilina, Faculty of Mechanical Engineering, Department of Machining and Manufacturing Engineering, Univerzitná 1, 010 26 Žilina, Slovak Republic, e-mail:anna.micietova@fstroj.uniza.sk.

Abstract. This paper deals with the selection of electric discharge cutting method based on assessed target function and optimization of factors acquired experimental equations. Optimization of parameters for electric discharge cutting is part of proposed integrated model for the selection of unconventional methods of material dividing by means of thermal effect, e.g. electro-erosive cutting, laser and plasma beam cutting.

Keywords: Optimization of parameters, unconventional methods of machining, electric discharge cutting, target function, gradient of factors.

1. Introduction

The choice of machining method from a set of suitable methods using which it can be achieved the required product quality in an integrated model for selection of unconventional dividing method is determined by accomplishing prescribed target or cost function of given method. For the selection of method is necessary to determine optimal values of factors from the acquired experimental equations to reach prescribed target function.

2. Target Function and Optimization of Parameters for Electric Discharge Cutting

Effect of machining various materials on the quality of finished surface by electric discharge cutting method is determined by comparing the obtained experimental equations for materials with different machinability. In Tab. 1 are shown representative materials of the model.

Material being cut	Marking	
Hardened tool steel	X155CrVMo12-1	1.2379
Electrolytic copper	Cu99	
Hardmetal	HM Feinkorn	K10-K40

Tab. 1. Representative materials of the model.

Experimental equation (hardened tool steel) for limiting condition of the surface roughness optimization Ra_{dov} :

$$Ra_{dov} = 13,74611 \times h^{0,071378} \times t_i^{-0,07453} \times I_e^{0,368575} \times t_d^{-0,12747} \times F_w^{-0,74604} \quad (1)$$

Experimental equation for feed rate v_f :

$$v_f = 194,0642 \times h^{-1,700621} \times t_i^{0,368444} \times I_e^{-0,021982} \times t_d^{-0,163948} \times F_w^{0,468931} \quad (2)$$

where:

- I_e - electrical discharge current,
- t_i - temporal pulse duration,
- F_w - wire tension,
- t_d - empty running,
- h - material thickness.

Target – criterial function:

$$v_f = 194,0642 \times h^{-1,700621} \times t_i^{0,368444} \times I_e^{-0,021982} \times t_d^{-0,163948} \times F_w^{0,468931} = v_f \max \quad (3)$$

Logarithming and rewriting “(3)” results in linear dependency:

$$v_f = 2,2879 - 1,700621 \cdot h + 0,368444 \cdot t_i - 0,021982 \cdot I_e - 0,163948 \cdot t_d + 0,468931 \cdot F_w = v_f \max \quad (4)$$

Experimental equations R_a , v_f for representative materials Cu99 and hardmetal are determined similarly.

2.1. Determination of Optimization Parameters Values

Values of optimization parameters for $R_{a_{dov}}$ results from magnitude of effect optimized parameters F_w , t_i , I_e , t_d in target function $v_f = \max$ “(3)”. In Tab.2 modul $s \times n$ determines magnitude gradient of individual parameters according to the target function “(4)” based on the possibilities AGIECUT 100D+F cutting machine (range of cutting parameters). To assess the magnitude of gradient their absolute value should be taken into account.

Cutting parameter	t_i	I_e	t_d	F_w
Parameter s range	1÷8	1÷15	10÷47,5	1÷20
Coefficient n	0,368444	-0,021982	-0,163948	0,468931
Modul $s \times n$	2,947552	-0,32973	-7,78753	9,37862

Tab. 2. Magnitude gradient of individual parameters according to the target function.

Sequence of the optimized parameters for $R_{a_{dov}}$ according to the “(1)” is given by relation:

$$F_w > t_d > t_i > I_e \quad (5)$$

The Fig.1 and Fig.2 is a graphical representation in logarithmic scale of the impact of the magnitude and direction of the factors gradients F_w , t_i , I_e , t_d on the feed rate v_f according to the “(2)”.

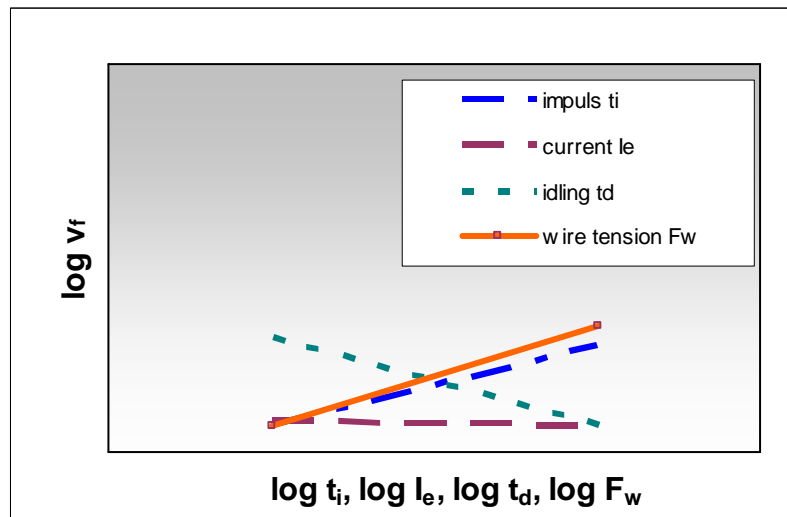


Fig. 1. Impact of the magnitude and direction of the factors gradients F_w , t_i , I_e , t_d on the feed rate v_f .

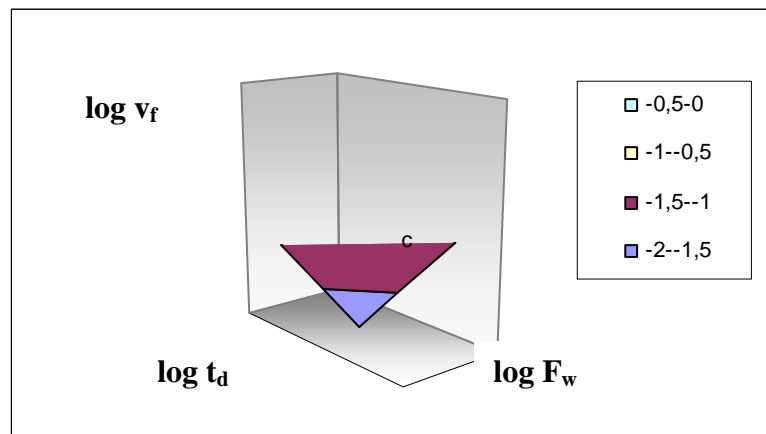


Fig. 2. Impact of the factors F_w , t_d on the feed rate v_f according to the (2).

Optimal factor values in the “(1)” for given Ra_{dov} value are determined by numerical algorithms. Approximating of an optimized factor toward Ra_{dov} is doing step by step in the sequence given by relation $F_w > t_d > t_i > I_e$. Factor approximation is finished when the best value of Ra_{dov} is reached. Direction of approximation each factor determines the sign +/- of the coefficient n . If some parameter has the direction of approximation toward Ra_{dov} opposite of direction of given factor according to the “(1)”, see for example wire tension F_w and impulse duration t_i , then aspect of the target function is preferred. Then in the case of the factors F_w and t_i optimization will be based on their maximum values $F_{w,max}$, $t_{i,max}$. Impact of the parameter I_e considering the target function is negligible. Basis for approximating of the next factor is an optimized factor value achieved from the previous step. Fig. 3 depicts impact of the factors F_w and t_d on the surface roughness Ra according to the “(1)”.

The same procedure is used to determine optimal parameters values for other quality indicators of finished surface appointed by experimental equations, e.g. surface straightness Pt , waviness Wz , load ratio parameters Rk , heat affected zone, residual tension, etc.

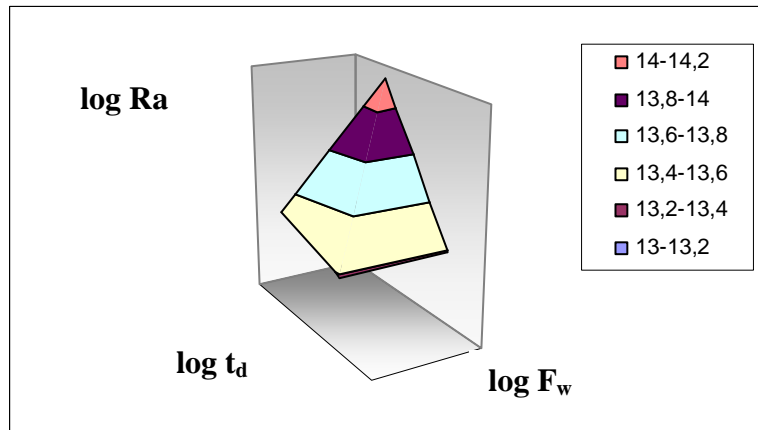


Fig. 3. Impact of the factors F_w and t_d on the surface roughness Ra according to the (1).

3. Conclusion

By optimizing the values of machining parameters for achieving the required quality parameter value based on meeting the criteria of target function, respectively cost function can be determined comparison for selection from suitable methods convenient to achieve the desired values, e.g. surface roughness Ra , surface straightness Pt , surface waviness Wz , heat affected zone, residual tensions, etc. Optimization of parameters for electric discharge cutting is part of proposed integrated model for the selection of unconventional methods of material dividing by means of thermal effect, e.g. electro-erosive cutting, laser and plasma beam cutting.

References

- [1] BÉKÉŠ, J., ANDONOV, I. *Analýza a syntéza strojárskych objektov a procesov*. Alfa Bratislava, 1986.
- [2] BÉKÉŠ, J., KOVÁČ, J., VASKÝ, J. *Automatizácia inžinierskych prác*. Edičné stredisko SVŠT, Bratislava, 1990.
- [3] HARANT, M. *Matematické metódy v experimentálnej praxi*. Žilina, 1970.
- [4] MÁDL, J. *Experimentální metody v teorii obrábění*. ČVUT, Praha, 1986.
- [5] NESLUŠAN, M. A KOL. *Experimentálne metódy v trieskovom obrábaní*. Žilina: EDIS - vydavateľstvo ŽU, 2007, 343 s., ISBN 978-80-8070-711-8.



The Volume Changes of Components of Special Steels after Vacuum Quenching

*Martin Brezničan, *Peter Fabian

*University of Žilina, Faculty of Mechanical Engineering, Department of Technological Engineering,
Univerzitná 1, 01026 Žilina, Slovakia, {martin.breznican, peter.fabian}@fstroj.uniza.sk

Abstract. This article contains of the problem solution with volume change of selected special steels. The first experimental measurements were realized to stainless steel X12Cr13 and tool steel 90MnCrV8. The quenching was realized in a bicameral vacuum quenching furnace. We checked the dimensions change, geometry change and full volume change. The results show the influence of chemical composition of martensite on intensity and character of volume change of components after quenching.

Keywords: Special steel, vacuum quenching, volume change.

1. Introduction

Requirements for tools and for components in energy industry are very high at present. The most required properties of quenched components are lifetime, dimensional precision and stability. That is the reason why is the vacuum heat treatment focused on achieving homogeneous martensitic microstructure with minimum content of residual austenite.

Vacuum quenching or quenching in special furnace atmosphere is the only way to quench steels without scalings production on the surface of quenched components. At components with pure surface we may relevantly compare dimensions and geometry before and after quenching.

Vacuum quenching is especially significant in order to quench stainless and tool steels which often need high austenitizing temperature before quenching. The higher austenitizing temperature is, the higher increase of decarburization layer is. The vacuum does not allow production and increase of decarburization layer on the surface.

2. Materials and Experimental Methods

As experimental materials there were selected stainless steel with low carbon content and tool steel with higher carbon content "Tab. 1 and Tab. 2". Both are special steels, but X12Cr13 is steel which contains chromium low-carbon martensite after quenching.

(Wt. %)		C	Cr	Mn	Si	Ni
X12Cr13	Min.	0.08	11.50	–	–	–
	Max.	0.15	13.50	1.50	1.00	0.75

Tab. 1. Chemical composition of X12Cr13 steel

(Wt. %)		C	Mn	Cr	V	Si
90MnCrV8	Min.	0.85	1.80	0.20	0.05	0.10
	Max.	0.95	2.20	0.50	0.20	0.40

Tab. 2. Chemical composition of 90MnCrV8 steel

As a measure content there was selected a shaft. Drawing is on Fig. 1. Experimental heat treatment was realized in a bicameral vacuum furnace with use of standard heat treatment

parameters for following steels. Steel X12Cr13 was heated by 3 steps with austenitizing temperature 1030°C and quenching medium was a high pressure gas (argon). Steel 90MnCrV8 was heated by 2 steps with austenitizing temperature 800°C and quenching medium was special oil for vacuum quenching. Both steels were low-temperature tempered after quenching. In the case of microstructure samples heat treatment regime was corrected for dimensions of these samples.

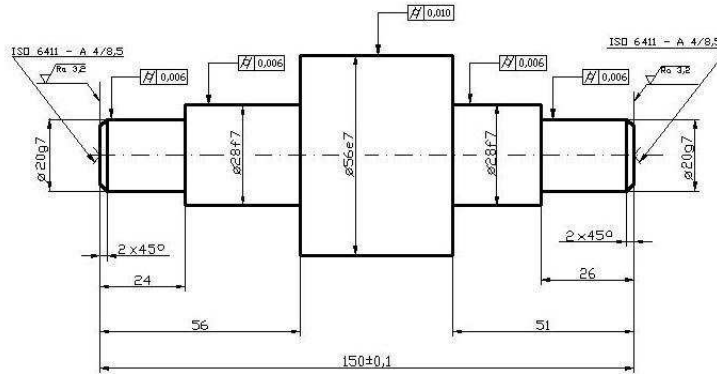


Fig. 1. Drawing of quenched sample

3. Results and Discussion

The Microstructure and hardness correspond with used temperature regime. The microstructure consists of δ -ferrite with chromium martensite “Fig. 2” in the case of X12Cr13 steel and tempered martensite with carbides “Fig. 3” in the case of 90MnCrV8 steel (correspond with CCT diagrams for these steels).



Fig. 2. The microstructure after quenching of X12Cr13 steel (500x)

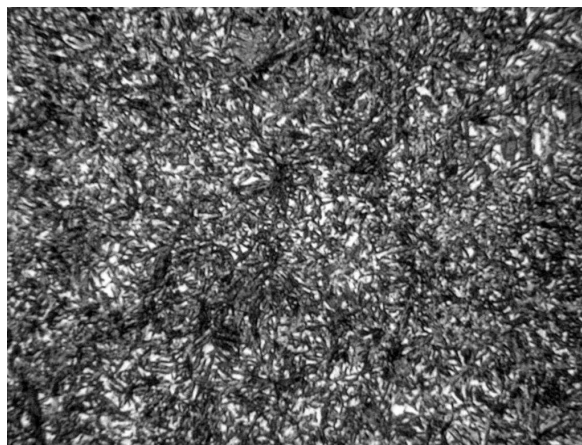


Fig. 3. The microstructure after quenching of 90MnCrV8 steel (500x)

Big clearly bounded grains on Fig. 2 are δ -ferrite. Needles inside the grains are martensite. Dark field on Fig. 3 represents tempered martensite. White field represents carbides.

Average hardness of quenched X12Cr13 steel is 54 HRC and of quenched 90MnCrV8 steel is 60 HRC “Tab. 3”. Both are normally achieved hardness in these steels after quenching.

X12Cr13		90MnCrV8	
54,55	54,75	59,15	59,50
54,30	54,12	59,45	60,01
54,15	54,04	59,95	59,88
Average: 54		Average: 60	

Tab. 3. Hardness of quenched components (HRC)

Change of dimension was measured by 3D measuring device. Volume change dependency on the dimensions is on Fig. 4. Geometry change dependency on the dimension is on Fig. 5.

The results show that low-carbon (chromium) martensite reduces volume of content after quenching by 0.1%. Standard high-carbon martensite increases volume of content after quenching by 0.2%. It is clear, that type of martensite affects not only on the mechanical properties of steels, but on the character of deformations too. In the case of 90MnCrV8 steel change of dimension is double higher than in the case of X12Cr13 steel “Fig. 4”.

Geometry change depends not only on the type of martensite, but on the full chemical composition of steel too. Higher geometric stability as X12Cr13 steel has 90MnCrV8 steel “Fig. 5”. It is known, steel 90MnCrV8 is very geometrically stable steel.

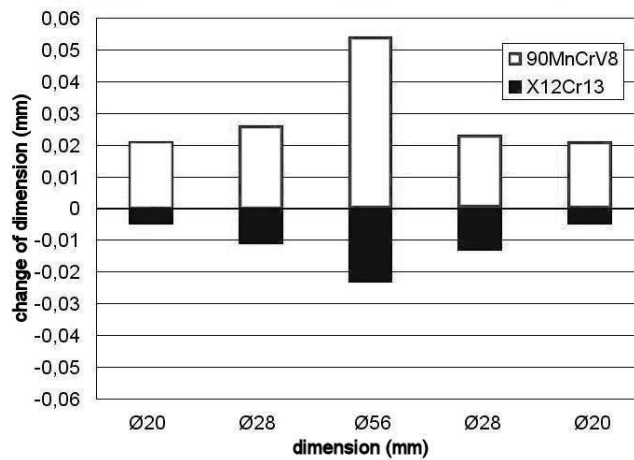


Fig. 4. Change of dimensions

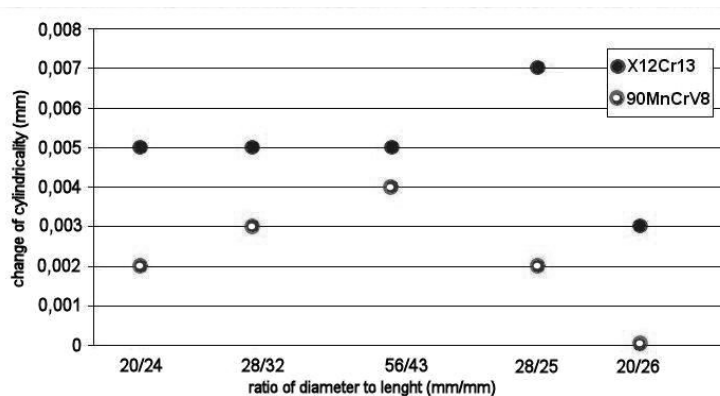


Fig. 5. Change of cylindricality dependency on the dimensions of component

4. Conclusion

Vacuum quenching is energy intensive technology, but the best results in quenching of stainless and tool steels are achieved with this. This is also the deformations that are the lowest with use of vacuum quenching. The results in this document are initial only. The results showed that the character of volume change depend mainly on chemical composition of martensite. Quantity of volume change is not exact parameter and depends on the temperature regime, type of quenching medium and other technological parametres, but especially on the chemical composition of material.

Acknowledgement

This article was created with the help of Ministry of Education of the Slovak republic, grant KEGA 135-054ŽU/2010.

References

- [1] DURAND-CHARRE, M. *Microstructure of Steels and Cast Irons*. Berlín: Springer-Verlag Berlin Heidelberg New York, 2004. 399 p. ISBN 978-3-540-20963-8.
- [2] KOUTSKÝ, J. *Slitinové oceli pro energetické strojírenství*. Praha: SNTL, 1981. 340 s.
- [3] MARTIENSSEN, W, WARLIMONT, H. *Springer Handbook of Condensed Matter and Materials Data*. Berlín: Springer-Verlag Berlin Heidelberg, New York, 2005. 1120 p. ISBN 978-3-540-44376-6.
- [4] MORÁVEK, O., BABOROVSKÝ, V. *Nástrojové materiály a tepelné zpracování nástrojů*. Praha: SNTL, 1972. 508 s.



Fatigue Crack Propagation Properties of ADI 1050 and IDI

*Lukáš Bubenko, *Radomila Konečná, **Gianni Nicoletto

*University of Žilina, Faculty of Mechanical Engineering, Department of Materials Engineering,
Univerzitná 1, 01026 Žilina, Slovakia, {lukas.bubenko, radomila.konecna}@fstroj.uniza.sk

**University of Parma, Department of Industrial Engineering,
Viale G.P. Usberti 181/A, 43100 Parma, Italy, {gianni.nicoletto}@unipr.it

Abstract. Fatigue crack propagation properties of Austempered Ductile Iron (ADI) and Perferritic Isothermed Ductile Iron (IDI[®]) are evaluated in this article. ADI represents the top strength material of the ductile iron (DI) family. IDI[®] is defined as an intermediate grade between the low hardness grades of ADI and pearlitic DI. Generally, both DI's are intended to be used for castings subjected to variable dynamic loading during their service, where familiarity with fatigue properties has the great importance. Fatigue crack propagation curves da/dN vs. K_a and the threshold amplitude of stress intensity factors K_{ath} for ADI 1050 and IDI[®] are presented here.

Keywords: Austempered Ductile Iron, Perferritic Isothermed Ductile Iron, fatigue crack propagation, threshold amplitude of stress intensity factor.

1. Introduction

Ductile iron is still an important material produced throughout the world and used for a wide range of technical applications. Mechanical properties of DI can be significantly improved by the austempering heat treatment performed under carefully controlled conditions [1, 2].

ADI with its combination of properties presents an engineering material that may be substitute for steel (cast, forged and/or heat treated) or aluminum in applications where high strength/weight ratio is important. Exemplary applications are given in [1, 3, 4]. The production of ADI component starts with the production of high quality DI castings of an appropriate composition, followed by heat treatment [1]. The conventional process consists of austenitizing the casting for sufficient time to get a fully austenitic matrix, and consequent quenching to the austempering temperature [1-3]. Chemical composition of ADI is related to hardenability and austemperability of DI. The alloying elements typically added include Cu, Ni and Mo [2, 5]. The microstructure of ADI consists of acicular ferrite, present in fine (lower bainite) or coarse form (upper bainite), high carbon austenite and graphite nodules [2]. Mechanical properties of ADI vary depending on austenitizing and austempering temperatures and times, as-cast structure, chemical composition and section size, with the austempering temperature as the most important [1]. High austempering temperatures result in high ductility, high fatigue and impact strengths and relatively low yield and tensile strengths. At low austempering temperatures ADI displays high yield and tensile strengths, high wear resistance and lower ductility and impact strength [3, 6].

In recent years, the increase in cost of the alloying elements of the low hardness ADI grades has led to a reduced growth rate of new applications and created the opportunity for the development of Perferritic IDI by Zanardi Fonderie [7]. IDI is an intermediate grade between the low hardness ADI grades and pearlitic DI. Compared with pearlitic DI grades, IDI combines similar strength with higher toughness properties as a result of the isothermal heat treatment. IDI is produced by heat treating of DI, cast after a special preconditioning of the metal bath. The isothermal heat treatment consists in heating the casting above the critical temperature, followed by cooling at a rate able to promote the formation of pearlite [7]. Microstructure of IDI consists of ferrite and pearlite with different distribution compared to the as cast DI (forming thus a new

“Perferritic” matrix), and graphite nodules. IDI has no alloy addition hence benefiting in terms of cost, as well as in the technical performance, while the absence of alloying elements (Mo in particular) implies less segregation and as a consequence lower sensitivity to thickness [7].

In general, ADI and IDI castings are proposed for service under dynamic variable loading. Hence it is necessary to understand their properties, especially in case of fatigue design. The fatigue crack propagation curves, (i.e. da/dN vs. K_a) and fatigue crack propagation threshold K_{ath} , are presented in this contribution.

2. Material and Experimental Methods

2.1. Material and Mechanical Properties

The experimental materials investigated here were i) austempered ductile iron ADI 1050 for production of high fatigue resistance castings [7], and ii) a perferritic IDI. Materials were supplied in the form of cast blocks by Zanardi Fonderie. The typical microstructure of ADI 1050 and perferritic IDI is given in Fig. 1a and Fig. 1b respectively.

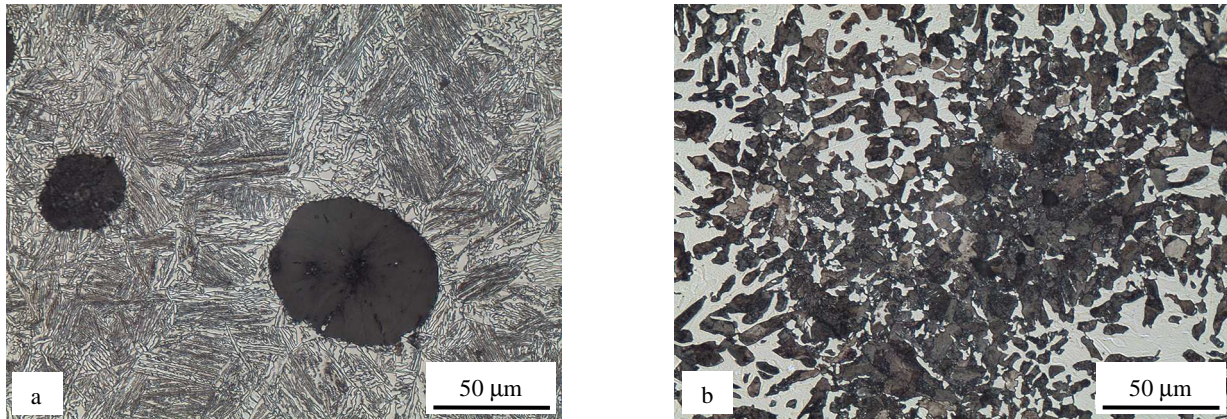


Fig. 1. Typical microstructure of experimental material, etched with 3% Nital, a) ADI 1050, b) IDI.

The microstructure of ADI 1050 is formed by spheroidal graphite particles uniformly distributed in matrix that consisted of thick acicular ferrite laths, usually aligned in clusters with the same direction (Fig. 2a), and retained high carbon austenite, the structure characteristic for upper bainite (Fig. 1a). The microstructure of IDI consisted of ferrite and pearlite with uniform distribution of graphite nodules (Fig. 1b), with increased volume of pearlite at the borders of eutectic cells (Fig. 2b).

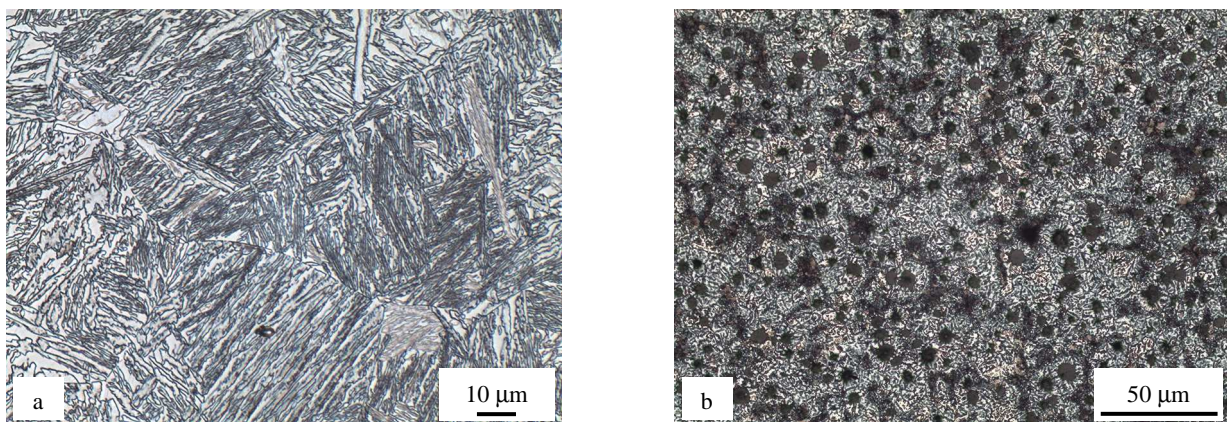


Fig. 2. a) ADI 1050, clusters of ferrite laths, b) IDI, pearlite at the borders of eutectic cells, both etched with 3% Nital

Mechanical properties of experimental material were measured on flat tensile testing specimens, extracted from halves of compact tension (CT) specimens broken after fatigue crack propagation (FCP) experiments.

2.2. Fatigue Crack Growth Rate and Near Threshold Fatigue Testing

FCP experiments were performed according to the ASTM standard E 647-08 [8]. Chevron notched CT specimens of thickness $B = 10 \text{ mm}$ and width $W = 50 \text{ mm}$ were machined. To provide a sufficient visibility of propagating fatigue crack, relevant observed surfaces were polished by 1 micron grain size diamond paste. CCD cameras were applied to monitor propagating cracks, while the increase of crack length (a) was measured by digital micrometers and recorded simultaneously with number of cycles (N). All tests were performed in electromagnetic resonant testing machine Roell Amsler HFP 5100 at constant load ratio $R = 0.1$, and at the room temperature in ambient air.

Six identical CT specimens (three of ADI 1050, three of IDI) were tested and the fatigue crack propagation curves da/dN vs. K_a were determined according to the ASTM standard E 647-08 [8]. The stress intensity factor amplitude K_a is given by:

$$K_a = \frac{P_a}{B\sqrt{W}} \frac{(2+\alpha)}{(1-\alpha)^{3/2}} (0.886 + 4.64\alpha - 13.32\alpha^2 + 14.72\alpha^3 - 5.6\alpha^4), \quad \alpha = a/W \quad (1)$$

where P_a [MPa] - the load amplitude; B [mm] - the specimen thickness; W [mm] - the specimen width; a [mm] - the crack size.

Load shedding technique was applied, following the ASTM standard E 647-08 [8], to determine the threshold amplitude of stress intensity factor K_{ath} . This procedure involves slowly reducing the applied load, by reducing the stress intensity amplitude stepwise after the crack had grown by at least 1 mm in length at the previous K_a level, and recording the crack growth rate da/dN . The threshold values K_{ath} were then identified as the values of K_a at which the crack growth rate was of the order of 10^{-10} m/cycle .

3. Results and Discussion

Fatigue crack propagation data da/dN vs. K_a , plotted in logarithmic scale are given in Fig. 3. It is evident that ferritic IDI has higher values of threshold K_a , comparing to the ADI 1050, however the gradient of crack growth rate, given by the slope m , is higher too. Threshold amplitude of stress intensity factor K_{ath} and slope m of FCP curves in region of stable crack growth rate controlled by the Paris law are defined in Tab. 1.

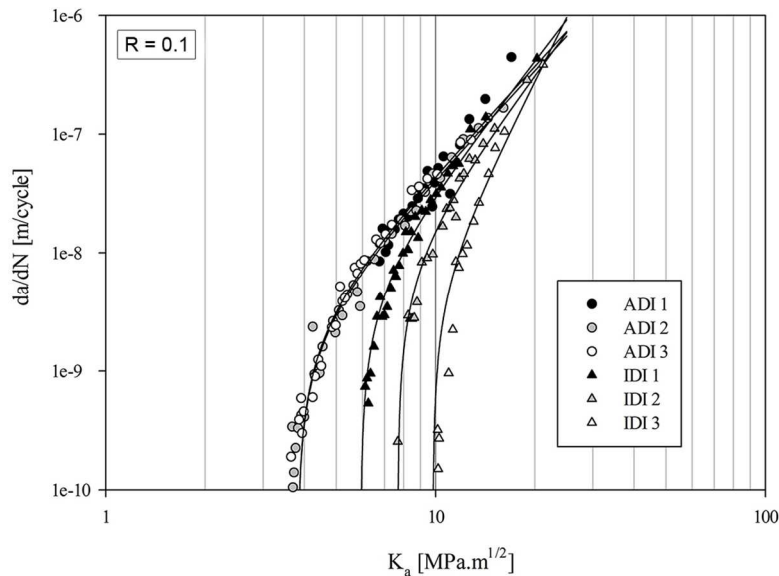


Fig. 3. Fatigue crack growth rate data of ADI 1050 and IDI, $R = 0.1$.

The FCP curves measured using three identical CT specimens of ADI 1050 (Fig. 3) are in excellent correlation. However, FCP curves determined with the three IDI CT specimens show

large differences, especially in near threshold region. These data scatter may be caused by the different microstructure in different parts of the casting block. Thus, further microstructural analysis of IDI specimens is needed.

	R _m [MPa]	R _{p0.2} [MPa]	E [GPa]	A [%]	HBW	K _{ath} [MPa.m ^{1/2}]	m
ADI 1	901	708	152.4	4.3	270	-	-
ADI 2	918	714	141.2	2.6	270	3.82	3.01
ADI 3	912	730	144.3	3.8	268	3.82	3.03
IDI 1	818	500	164.0	6.9	223	5.93	3.59
IDI 2	809	472	149.3	9.1	210	7.68	3.73
IDI 3	732	425	140.3	7.5	205	9.81	5.54

Tab. 1. Mechanical properties, threshold amplitudes of stress intensity factor K_{ath} and slopes of ADI 1050 and IDI.

Tab. 1 reports the mechanical properties measured on particular specimens of ADI 1050 and ferritic IDI. A correlation of the yield stress and K_{ath} is observed. The crack growth rate and K_{ath} and yield strength of ADI 1050 do not vary significantly. On the other hand, in the ferritic IDI the yield stress increases from specimen to specimen while, correspondingly, K_{ath} decreases.

4. Conclusion

The aim of presented experiments was to determine long fatigue crack propagation properties of ADI 1050 and ferritic IDI. The following conclusions were reached:

- The average threshold stress intensity factor amplitude K_{ath} of ADI 1050 is 3.82 MPa.m^{1/2};
- Threshold stress intensity factor amplitude K_{ath} of ferritic IDI vary between 5.93 - 9.81 MPa.m^{1/2},
- The yield stress, the FCG and K_{ath} of ADI 1050 are constant within the examined material block,
- The yield stress of ferritic IDI vary with specimen location within the block while the K_{ath} decreases.

Acknowledgement

Authors thank the support of experimental research by national project VEGA 1/0242/10.

References

- [1] HARDING, R. A. The production, properties and automotive applications of austempered ductile iron. *Kovove Materialy*. Vol. 45, 2007, No. 1, p. 1-16.
- [2] HAYRYNEN, K. L. The production of austempered ductile iron (ADI). *2002 World Conference on ADI*. Louisville (KY), Ductile Iron Society and the American Foundry Society 2002.
- [3] YANG, J., PUTATUNDA, S. K. Near threshold crack growth behavior of austempered ductile cast iron (ADI) processed by a novel two-step austempering process. *Materials Science and Engineering: A*. Vol. 393, 2005, No. 1-2, p. 254-268.
- [4] ZIMBA, J., SIMBI, D. J., NAVARA, E., Austempered ductile iron: an alternative material for earth moving components. *Cement and Concrete Composites*. Vol. 25, 2003, No. 6, p. 643-649.
- [5] ERIC, O., SIDJANIN, L., MISKOVIC, Z., ZEC, S., JOVANOVIC, M. T. Microstructure and toughness of CuNiMo austempered ductile iron. *Materials Letters*. Vol. 58, 2004, No. 22-23, p. 2707-2711.
- [6] KIM, Y. J., SHIN, H., PARK, H., LIM, J. D. Investigation into mechanical properties of austempered ductile cast iron (ADI) in accordance with austempering temperature. *Materials Letters*. Vol. 62, 2008, No. 3, p. 357-360.
- [7] MASSAGIA, S. The development of ADI and IDI in Italy. *Procedia Engineering*. Vol. 2, 2010, No. 1, p. 1459-1476.
- [8] ASTM Standard E 647-08, Standard Test Method for Measurement of Fatigue Crack Growth Rates, ASTM International, West Conshohocken (PA), 2009.



Effect of Phosphate Conversion Coating on Electrochemical Properties of AE21 Magnesium Alloy

*Michal Bukovina, *Branislav Hadzima, *Lenka Škublová

*University of Žilina, Faculty of Mechanical Engineering, Department of Materials Engineering,
Univerzitna 2, 01026 Žilina, {michal.bukovina, branislav.hadzima, lenka.skublova}@fstroj.uniza.sk

Abstract. Contribution deals with evaluation of corrosion resistance of AE21 magnesium alloy. The surface of tested alloy was treated by the phosphating process. We compared the electrochemical characteristics of specimens without and with phosphated layer by electrochemical impedance spectroscopy in 0.1 M NaCl solution. Results of the electrochemical measurements are complemented by metallographic evaluation of the tested alloy.

Keywords: EIS, corrosion resistance, AE21 magnesium alloy, phosphate coating.

1. Introduction

Improvements in fuel efficiency and reductions in environmentally damaging emissions are primary concerns for automotive and aerospace structures. One of the effective ways to mitigate the concerns is to reduce the weight of vehicles. Moreover, such weight reduction could provide a significant contribution to reducing the CO₂ emission. The density of magnesium is about two-third that of aluminum and is only slightly higher than that of fiber-reinforced plastics with excellent mechanical and physical properties as well as processability and recyclability. Some of the advantages of the magnesium alloys for industrial and structural applications are their lightweight, high specific strength and stiffness, high electromagnetic interference shielding and damping capabilities, dimensional stability, impact and dent resistance, anti-galling, and good electrical and thermal conductivity [1,2].

However, the application of magnesium alloys has been limited due to their undesirable properties including poor corrosion and low wear resistance. A more effective way to prevent corrosion of magnesium alloys is to coat the substrate materials. Surface treatments, such as the formation of conversion coatings, are commonly applied to magnesium alloys in order to increase the corrosion resistance. Phosphate technique has been used to steel, aluminum alloy and titanium alloy as protective coating or pretreatment to underneath the paint. In fact, phosphating may be a promising method for magnesium alloys anticorrosion and pretreatment process before paint [3].

2. Experimental materials

The AE21 magnesium alloy after extrusion from as cast state was used as an experimental material. The extrusion of the material was prepared at 370°C with extrusion ratio of 22 at University of Technology in Clausthal, Germany. The normalized chemical composition of AE21 alloy is in Tab. 1.

Element	Al	Re	Mn	Mg
Content [wt.%]	2	1	0.3	balance

Tab. 1. The chemical composition of AE21 magnesium alloy.

The surface treatment of the specimens was realized by phosphate process. Phosphate coating is a conversion coating of an insoluble crystalline metal-phosphate salt formed in a chemical reaction between the substrate metal and a phosphoric acid solution containing ions of metals.

2.1. Microstructure analysis

Microstructure of AE21 alloy (Fig. 1) is created by polyedric grains of the solid solution of aluminium, rare earth metals, manganese and other additions of elements in magnesium. The microstructure contains the areas of Al₄MM (Al₄RE) phase [4,5]. The detail of this phase is in Fig. 2.

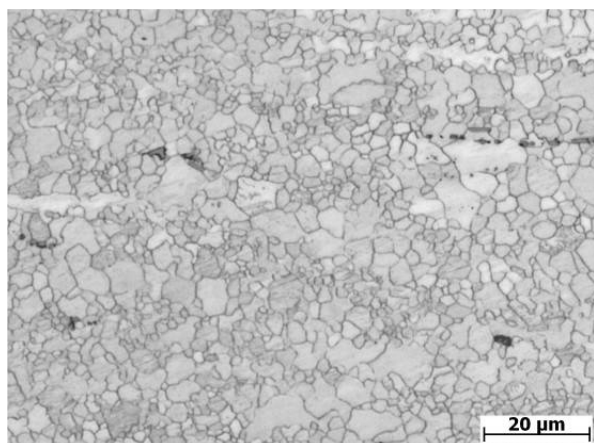


Fig. 1. Microstructure of tested AE21 magnesium alloy initial state, longitudinal section; etch. acetic and picric acid + ethanol + water.

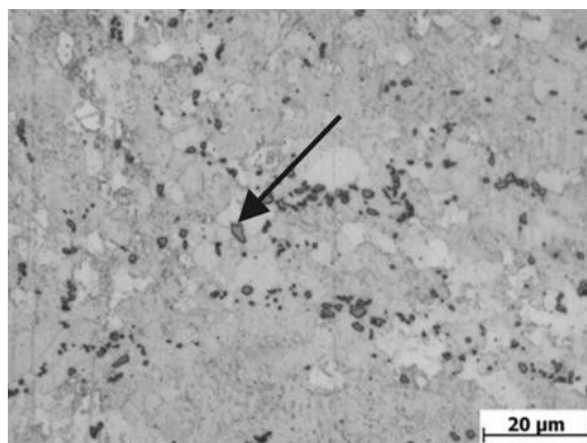


Fig. 2. Detail of Al₄MM (Al₄RE) phase, cross section; etch. acetic and picric acid + ethanol + water.

3. Results and discussion

The measurements of electrochemical impedance spectroscopy were realized on grinded surfaces (AE21 G) and on surfaces with phosphate coating layer (AE21 P) in 0.1 M NaCl solution at laboratory temperature of 22±1°C. The method of EIS provide values of polarization resistances (R_p), directly proportional to corrosion resistance of material surface in the environment. The exposure times before EIS measurements were 5 minutes, 1, 4, 8, 16, 24, 48, 96 and 168 hours, respectively. Frequency range was from 100 kHz to 20 mHz with frequency changing of 20 times per decade. Amplitude of AC voltage was 20 mV. The connection and principle of measurement is described elsewhere [6,7].

The specimens before phosphating were grinded, rinsed with demineralized water, dried and then followed by pickling in 75 % phosphoric acid for 30 seconds and rinsed with water. The phosphating was carried out in the phosphate solution (Tab. 2) for 10 minutes at temperature of 45±2°C [8,9]. The rate of specimen during phosphate process was 350 rpm.

pH	Chemical composition of the phosphate solution
3 ± 0.2	Na ₂ HPO ₄ (20g.l ⁻¹) + H ₃ PO ₄ (7.4 ml) + NaNO ₂ (3 g.l ⁻¹) + NaNO ₃ (1.84 g.l ⁻¹) + Zn(NO ₃) ₂ (5 g.l ⁻¹) + NaF(1 g.l ⁻¹)

Tab. 2. pH and chemical composition of phosphate solution.

Results of EIS measurements in the form of Nyquist diagrams are in Fig. 3 for grinded surfaces of AE21 alloy and in Fig. 4 for surfaces with phosphate coating. It is possible to find out values of polarizing resistances (R_p) by Nyquist diagram analyzing. Outcomes of analyses are to be found in Tab. 3 referring to alloy AE21 in grinded state and phosphated surface of the alloy. These values were determined by employing software analysis using VoltaMaster 4 software based on circular

regression. Equivalent circuits used in analysis performance help us to model conditions on the electrolyte-specimen interface [9,10].

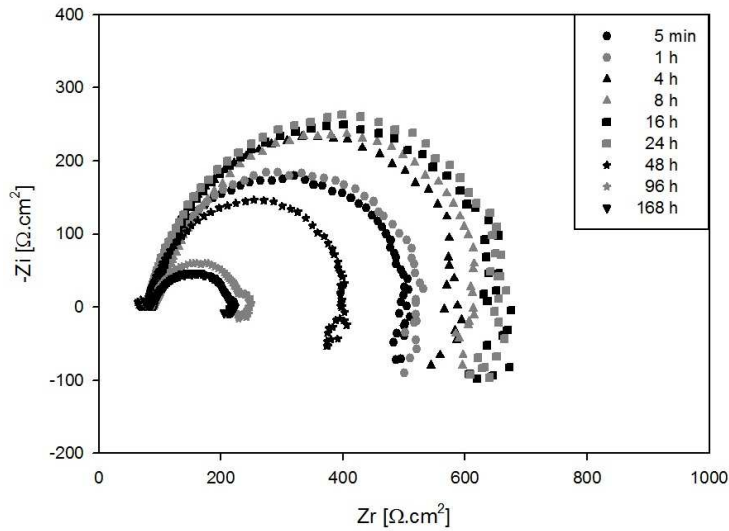


Fig. 3. Nyquist diagrams of AE21 G in 0.1 M NaCl

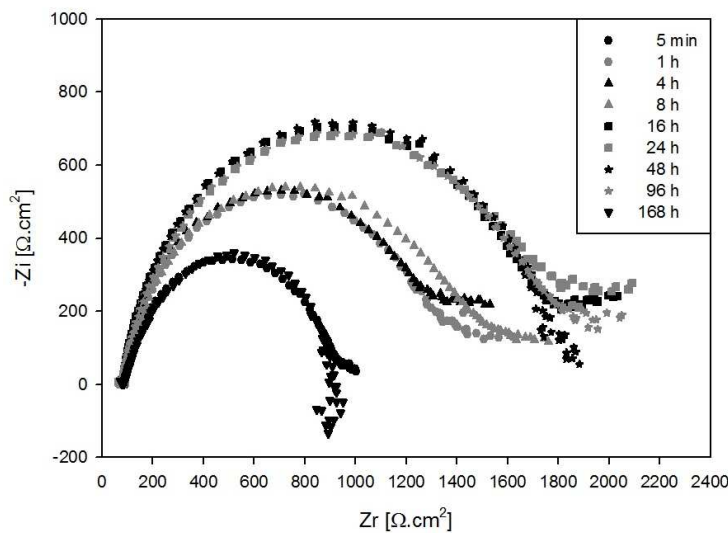


Fig. 4. Nyquist diagrams of AE21 P in 0.1 M NaCl

Exposure time	grinded surface	phosphated surface	Exposure time	grinded surface	phosphated surface
	R_p [$\Omega.cm^2$]	R_p [$\Omega.cm^2$]		R_p [$\Omega.cm^2$]	R_p [$\Omega.cm^2$]
5 min	430 ± 18	832 ± 13	24 h	612 ± 17	1719 ± 41
1 h	448 ± 4	1259 ± 17	48 h	340 ± 35	1707 ± 13
4 h	515 ± 2	1270 ± 10	96 h	152 ± 2	1728 ± 22
8 h	571 ± 21	1372 ± 14	168 h	112 ± 18	866 ± 26
16 h	578 ± 52	1691 ± 49			

Tab. 3. Electrochemical characteristics of AE21 G and P specimens in 0.1 M NaCl solution

Analysis of the Nyquist plots shows that polarisation resistance values of grinded surface of AE21 alloy increase with increasing of exposure time up to 24 hours ($612 \Omega.cm^2$). Polarization resistance of the surface after 24 hours of exposition ($430 \Omega.cm^2$) is 1.5 time higher than polarization resistance after 5 minutes of grinded surface exposition. The resistance increasing on the material-electrolyte interface is caused by increasing of corrosion products probably based on magnesium hydroxide. The total polarization resistance is decreasing ranging between 24 to 168 hours of

exposition. It is caused by dropping out of corrosion products which have protective nature. Dropping out of corrosion products causes contact of corrosion environment with metal surface and further active development of active corrosion process. In the case of EIS curves measured on phosphated surface, the polarisation resistance immediately (within 5 min) after immersion of materials into the 0.1 M sodium chloride solution was 2 times higher than the R_p value of grinded surface. The maximum value of R_p was observed in the case of phosphated surfaces after 96 hours ($1728 \Omega \cdot \text{cm}^2$). It is four times more than on grinded surfaces. The local damage of phosphated coating layer on the AE21 alloy occurs after 168 hours in a corrosive environment and the R_p values decrease.

4. Conclusions

The metallographic and electrochemical investigations of various exposure times on the corrosion resistance of extruded AE21 magnesium alloy with grinded and phosphated surface have been carried out in 0.1 M solution of sodium chloride. The following conclusions can be drawn from this study:

- Microstructure of AE21 alloy is created by polyedric grains of the solid solution of Al, RE, Mn in magnesium and the areas of Al_4MM (Al_4RE) phase,
- Polarisation resistance values of grinded surface of AE21 alloy in 0.1 M NaCl solution increase up to 24 hours of exposure time. Polarization resistance after 24 hours of exposition is 1.5 time higher than polarization resistance after 5 minutes of grinded surface exposition. Dropping out of corrosion products occurs after 48-168 hours, R_p values decrease and grinded alloy loses the ability to resist corrosion in 0.1 M NaCl.
- Maximum value of R_p was observed on phosphated surface after 96 hours of exposition in corrosive environment. When we compare the maximum values of R_p for phosphated and grinded surfaces, we investigate that R_p values of phosphated surface are 3 times higher than on grinded surface of AE21 magnesium alloy. The R_p of specimen with phosphated layer after 168 hours ($866 \Omega \cdot \text{cm}^2$) is 7.5 times higher than the R_p of grinded surface ($112 \Omega \cdot \text{cm}^2$)

Acknowledgement

The research is supported by European regional development fund and Slovak state budget by the project ITMS 26220220048 (call OPVaV-2008/2.2/01-SORO).

References

- [1] PATEL, H.A., CHEN, D.L., BHOLE, S.D., SADAYAPPAN, K. *Cyclic deformation and twinning in a semi-solid processed AZ91D magnesium alloy*. Materials Science and Engineering A 528 (2010) 208–219.
- [2] MEHTA, D.S., MASOOD, S.H., SONG, W.Q. *Investigation of wear properties of magnesium and aluminum alloys for automotive applications*. Journal of Materials Processing Technology 155–156 (2004) 1526–1531.
- [3] LI, G.Y., LIAN, J.S., NIU, L.Y., JIANG, Z.H., JIANG, Q. *Growth of zinc phosphate coatings on AZ91D magnesium alloy*. Surface & Coatings Technology 201 (2006) 1814–1820.
- [4] WEI, L.Y., DUNLOP, G.L. *The solidification behavior of Mg – Al – rare earth alloys*. Journal of Alloys and compounds 232 (1996) 264 – 268.
- [5] WU, G., GAO, Y.F.H., ZHAI, CH., ZHU, Y.P. *The effect of Ca and rare earth elements on the microstructure, mechanical properties and corrosion behavior of AZ91D*. Mat. Sci and Engineering A 408 (2005) 255 – 263.
- [6] Electrochemical software Voltmaster 4. Radiometer Analytical-Electrochemistry. 2002.
- [7] HADZIMA, B. Corrosion of alloys Mg-Al-Zn. [Dissertation thesis]. ŽU in Žilina. Žilina
- [8] KOUISNI, L. *Phosphate coatings on magnesium alloy AM60 part 1: study of the formation and the growth of zinc phosphate films*. Surface & Coatings Technology 185 (2004) 58– 67.
- [9] KOUISNI L. *Phosphate coatings on magnesium alloy AM60 Part 2: Electrochemical behaviour in borate buffer solution*. Surface & Coatings Technology 192 (2005) 239– 246.
- [10] SONG, G.L. „Electroless” deposition of a pre-film of electrophoresis coating and its corrosion resistance on a Mg alloy. Electrochimica Acta 55 (2010) 2258–2268.



Composite Materials Achievement In Order To Develop Insulations for Furnaces in Machinery Building Industry

Camelia Căpăţînă^{*}, Gheorghe Gămănesci^{**}

^{*,**} „Constantin Brâncuşi” University of Târgu-Jiu, Faculty of Engineering, Street Geneva No 3, Târgu-Jiu, 210152, Gorj, Romania, cam@utgjiu.ro

Abstract. The main composites on hydraulic binding material and ceramic fibres are materials consisting in a hydraulic binding material matrix (aluminous cement) reinforced with short or long ceramic fibres which distinguish themselves through their special physical-mechanical properties and good behaviour during operation. This paper presents the achievement of some composites meant for achieving furnaces insulations in the machinery building industry.

Keywords: composite, materials.

1. Introduction

Composite materials are one of the categories of new, modern materials rapidly developing and assimilating, artificially created through the international combination of parts, materials for future technologies.

Composite materials are a mixture of two main categories of components: the matrix in which the fittings are also distributed, physically and chemically distinct, physically and chemically compatible, being in a state of thermodynamic balance, without resulting an interaction with unwanted chemical reactions, net separation surfaces exist between the components [1-4]. Composite materials may include different additives, colorants and pigments. Composite materials have final properties superior to their components (synergism) and sometimes unique in comparison to them.

2. Experimental part

The reinforcing agent is represented by ceramic fibre resistant to the temperature of 1260⁰C. In order to reduce the length of fibres from P150 mm to 3 – 5 mm they are moist chopped in a malaxating machine. In order to achieve a hydraulic socket at the temperature of the room with the role of matrix for the monolith mass with fibres, we use aluminous cement.

Sodium silicate is the non-hydraulic mineral binder that plays an important role in achieving the socket in the field of low and average temperatures and in granting the material certain machinability.

Kaolin or refractory clay has the role of providing a good machinability of the mixture. Fine burnt fire clay and siliceous sand are added in order to influence some of the physical properties of ceramic fibres and hydraulic binders composites.

Tab. 1 presents the oxide composition of raw materials used.

No.	Raw materials	P.C.	SiO ₂	Al ₂ O ₃	Fe ₂ O ₃	CaO + MgO	Na ₂ O + K ₂ O	Other oxides
1	Ceramic fibre 1260 ^o C	0,5	49,3	48	0,4	0,9	0,9	-
2	Aluminous cement	-	5	68	0,4	26,2	-	0,4
3	Refractory clay	-	-	-	-	-	-	-
4	Sodium silicate	-	-	32	-	-	11	-
5	Burnt fire clay	0,5	67,46	17,82	3,89	4,61	4,92	0,8

Tab. 1. Oxide composition of raw materials

No.	Raw materials (percentage composition %)								
	Composite material	Ceramic fibre	Aluminous cement	Refractory clay	Burnt fire clay	Siliceous sand	Sodium silicate	Mono-phosphate	Water
1	M ₁	7	22	18	18	-	4,8	0,5	29,7
2	M ₂	7	20	18	-	18	7,9	0,6	28,5

Tab. 2. Percentage composition of raw materials used for achieving composite materials

3. Results and discussions

For physical-chemical and mechanical characterization test tubes with the sizes 160x40x30 mm were made in metallic matrices.

For every composition (M₁ and M₂) on the test tubes made in the laboratory, physical-chemical and structural determinations on raw masses thermally treated at e 410^oC, 780^oC and 1180^oC were made; apparent density, linear contraction, bending resistance through 3-point loading.

Results are presented in Tab. 3.

No.	Determination	Recipe	
		M ₁	M ₂
1	Apparent density g/cm ³		
	- raw	1,36	1,78
	- burnt 410 ^o C	1,09	1,18
	- burnt 780 ^o C	1,08	1,15
	- burnt 1180 ^o C	1,20	1,13
2	Linear contraction %		
	- raw	0,55	1,65
	- burnt 410 ^o C	1,12	3,05
	- burnt 780 ^o C	1,19	1,46
	- burnt 1180 ^o C	3,63	3,02
3	Bending resistance daN/cm ² - raw	6,51	10,87
	- burnt 410 ^o C	18,53	14,21
	- burnt 780 ^o C	15,87	20,59
	- burnt 1180 ^o C	40	32,34

Tab. 3. Physical – mechanic determinations of test tubes

The composition M₁ – raw sample: a crystalline mass of particles is revealed with a general polyhedral form with sizes between 1,4 and 6 µm. In some places, we notice ceramic fibres with smooth surfaces, without any unevenness, recrystallizations, cracks or other faults. The average size of the fibre is 2 µm. On the sample burnt at 4100C we do not find any significant differences from the raw sample. We notice a crystalline mass with a mixture of plaquette like and polyhedral particles with different sizes: 2,5-20 µm. Fibres have variable sizes, the average diameter being between 2-10 µm. At 780^oC the crystalline mass is compacted forming large sized agglomerates reaching 80 µm, revealing areas of glossy mass. The sample burnt at 1180^oC generally has a compact mass similar to a “agglomeration” process. Just like in the case of “agglomeration”, we

notice intense intragranular porosity. Pores are round, well defined, both in the glassy mass and in the area where particles can still be seen. They have values between 8-20 μm and are polyhedral.

M_2 composition – raw sample: the fibre is clearer than in the case of M_1 composition, both in raw state and in temperature variations. Several distinct phases can be revealed: a phase consisting of plaquette like and polyhedral particles similar to those in the M_1 recipe with sizes of 3-18 μm , the fibre having average diameters of 2 μm and a range of values between 1,5-16 μm , as well as the third phase of acicular particles that clamp it in distinct areas or cover the fibre. They have thicknesses between 2-5,6 μm . On the sample burnt at 410⁰C, as well as on the one burnt at 780⁰C we clearly notice the fibre covered in various acicular and polyhedral particles. The acicular particles that form the main phase at 410⁰C can be noticed clearly, especially in the area of the fibre, and at 780⁰C the crystalline phase occurs, consisting of polyhedral and plaquette like particles with sizes between 4-10 μm . Just like in the case of M_1 composition, the sample burnt at 1180⁰C has a general compact aspect similar to an “agglomeration”, with both intragranular and intergranular porosity.

4. Conclusion

We experimentally noticed that by adding burnt fire clay we get the advantage of a decrease of the linear contraction after burning between 1,12 – 3,63% depending on the burning temperature.

Experimental results confirm an optimal structure of the composite material and an improvement of the mechanic resistance while bending by adding sand up to 39%, depending on the burning temperature.

References

- [1] Mc CAULEY, J.W.: *Ceramic Bulletin*, Vol. 67, nr. 12, 1998, p. 1903 – 1910.
- [2] KAPURI, R.J.colab.: *Interceram*, vol.45, nr. 6, 1996, p.427 – 430.
- [3] ALIPRANDI, G.: *Materiaux refractaries et ceramiques techniques*, Ed. Septima, Paris, 1989.
- [4] CIOHODARU, L.: *General chemistry for engineers*, Matrix ROM Press, Bucharest, 2000, ISBN 973-685-188-5, p. 384 – 390.

Analysis of Milling Tools Wears Intensity in the Primary Interaction

*Tatiana Czánová, *Jozef Pilc, *Tomáš Nosák

*University of Zilina, Faculty of Mechanical Engineering, Department of Machining and Manufacturing technology, Univerzitna 1, 01026 Žilina, Slovakia, {tatiana.czanova jozef.pilc tomas.nosak}@fstroj.uniza.sk

Abstract. The article analyzes the intensity of milling tool wear in the primary interaction of cutting edges and machined material. Based on the observation of wear, we follow a different character and intensity of wear of the cutting edge, which is dependent on the position of the milling tool to the machined material frame. Given this problem it is necessary to analyze the situation, which is necessary to propose an optimal solution start-up and movement of milling tool to increase tool life.

Keywords: Intensity, wear, milling, primary interaction.

1. Introduction

It is now necessary to address the issue of primary interaction tool cutting wedge with working materials. It is necessary to establish a mathematical model and experimentally verify the effects of selected geometric profile milling tool for milling application of modern cutting materials in the machining process conditions, such as working without applying the process media, working high-hard materials with hardness greater than 65 HRC, high-speed machining. Gained knowledge will be beneficial for designers and manufacturers of tools as a basis for appropriate design of tool for a given technological conditions.

2. Wear Mechanisms of Cutting Edge Tool

All tips of cutting wedges of tool are exposed to effects, which result gradually wears. This wear is exposed to the point of achieving the end of the period of their durability. Durability is the period during which the tool works by clamping the tip to wear and be counted in minutes. It is a feature of the tool when it is able to work within the established parameters of quality to give the desired workpiece shape. Wear of cutting edge tool can be determined by weight or volume indicators of wear. In these pictures is an example of tool tip wear and there are dimensioned wear size in different locations.

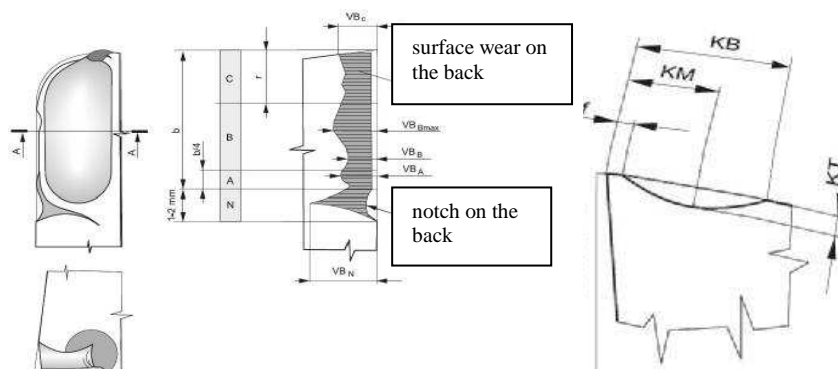


Fig. 1. Scheme of wear of cutting wedge with orientation and description of each area.



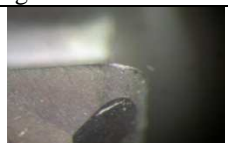
a) Total view of the character of wear b) Dimensional insight into the wear face of the [15]
















VB_i wear on the main dorsal surface of the cutting edge tool in different places divided by the cutting edge. Kf is a distance between the trace of cutting edge and the closer edge of the groove wear. KB is a distance between the trace of cutting edge and the remoted edge groove wear. KM is a distance between the trace of cutting edge and the center groove wear on the face of the cutting edge. KT is a depth from the original face surface to the bottom wear groove. By observed the right conditions of cultivation can be achieved an increased productivity by taking account the geometry of the cutting edge and cutting conditions. Durability and mechanical time (to produce a single component) may be very different in the choice of different tools. On the course and intensity of wear in dependence of time can identify three basic characteristic areas. Primary wear area, which is influenced by aligning the peaks and inequality of the back of the tool eventually the defective surface layer of the dorsal surfaces. Following areas is secondary wear, where the peaks are aligned and the course is almost linear course with a slight tendency to increase depending on the workpiece and the supporting factors. The final area is the tertiary wear, which reflected the intensity of accelerated wear, which causing fracture and destruction of the cutting edge tool. Cause of wear is the interaction between the tool, working material and cutting conditions. The most important types of wear generated at surfaces of the cutting edge are in most cases, mechanical, heat, chemical, abrasive. [15]

Mechanical load we mean as static as dynamic power load. These arise during machining. They are emerging as the burden of cutting force components and the strength creating splinters, or different dynamic loads due to uneven cutting layer or intermittent cutting. In machining of metal creates large quantity of heat, which develops on front face surface and back cutting plate. This heat load very strains material of tool. During the cutting splinter arises on metal tool cutting edge clean surface, which tends to chemically react with working material. Some cultivated materials containing hard particles, which sometimes resemble the characteristics of their instruments. These may affect abrasive on tool. Allocation of mechanisms wear can we divided on the basis of the action of the above burdensome factors on the instrument, which is manifested as one or a combination of several basic forms of wear. They are divided into these basic methods of adhesive wear, abrasive wear, static and dynamic fracture, fatigue violation, diffusion wear and oxidation wear. The first four of these methods are caused by wear on the mechanical effects, the other two are caused on the principle of the chemical. On the total wear does not participate under certain conditions aside all going the same rate. For a pair of workpiece cemented carbide - can (under conditions aside) dominate one or the other action. The decisive factor in determining which type of action in the machining process dominates is the temperature of the interaction tool with the workpiece.



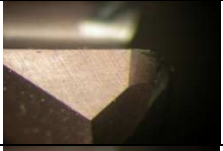


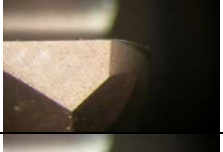





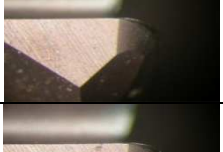
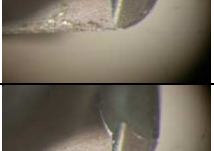

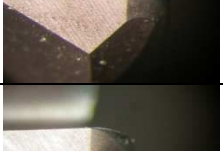
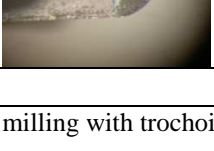
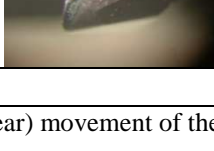
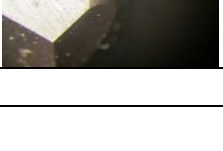
3. Experimental Measurement of Wear

The objective of measurement was necessary to determine wear on the head back and side back of tool for machining workpieces, cutting down all the conditions, for direct and trochoidal movement of tool. On the milling was used monolith milling cutter F6AV1200AWL45 KC637M with six cutting edges. The main geometry of tool diameter D_c 12mm diameter of the clamping 12mm, active part of the tool a_{p1max} 45 mm and 93 mm length of the tool. Cutting conditions of the experiment, cutting speed v_c = 132m.min⁻¹, feed rate v_f = 430 mm.min⁻¹ and depth of cut a_p = 3 mm. Measured values of wear “Table 1 and Table 2”.

Tooth cutting tool	Wear on the front face of Aγ		Wear on the head back of Aα		Wear on the side back of Aα'	
	KB	Figure	VB	Figure	VB'	Figure
1	0,17		0,23		0,12	

2	0,14		0,28		0,07	
3	0,17		0,20		0,17	
4	0,18		0,26		0,08	
5	0,19		0,21		0,07	
6	0,21		0,19		0,06	
average	0,176		0,23		0,095	

Tab. 1. Values wear when milling straight movement of the tool

	Wear on the front face		Wear on the head back		Wear on the side back	
	KB	Picture	VB	Picture	VB'	Picture
1	0,11		0,15		0,1	
2	0,12		0,10		0,07	
3	0,08		0,11		0,08	
4	0,048		0,09		0,07	
5	0,105		0,08		0,04	
6	0,11		0,10		0,06	
average	0,096		0,105		0,07	

Tab. 2. Values wear when milling with trochoidal (non-linear) movement of the tool

	KB	VB	VB'
direct movement of the tool	0,176	0,23	0,95
trochoidal movement of the tool	0,096	0,105	0,07

Tab. 3. A comprehensive comparison of the wear from measured values

4. Conclusion

The main purpose of the experiment was to compare trochoid (non-linear) movement with a direct (linear) movement by the milling and find the effect of technology movement milling tool with given to interactions cutting wedge and workpiece to the total wear after milling in both ways. The results obtained, it was found that the method of movement of the tool in milling is an important factor affecting the strength and wear of the cutting edge of tool. When using trochoid (non-linear) movement we reached a reduction of wear intensity more than 100% to each parameter observed. This finding leads to new possibilities of using non-linear movements milling tools in order to reduce the main dynamic of the cutting edge of tool and hence to more efficient use of machining tools in achieving a comparable tool wear when using the direct movement of the tool. Another advantage of the trochoid movement is the possibility of milling a wider area compared to average cutting higher tool parameters, as compared with straight motion leads to a reduction in the number of needed transitions.

References

- [1] MRKVICA, M. *Přípravky a obráběcí nástroje I. Díl – Řezné nástroje*. 3. vydání. Ostrava: VŠB – TU Ostrava, 2001, 192s. ISBN 80-7078-941-7
- [2] MRKVICA, M. *Přípravky a obráběcí nástroje II. Díl – Přípravky*. 2. vydání: VŠB – TU Ostrava, 1991, 184s.
- [3] BEŇO, J. *Teória rezania kovou*. Košice: Strojnícka fakulta TU Košice, 1999, 255 s. ISBN 80-7099-429
- [4] BUDA, J., SOUČEK, J., VASILKO, K. *Teória obrábania*, ALFA Bratislava, 1983.
- [5] [http://www.kvt.sjf.stuba.sk/WEB/3%20Frezy%20\(nastroje\).pdf](http://www.kvt.sjf.stuba.sk/WEB/3%20Frezy%20(nastroje).pdf) [cit.2010-25-04]
- [6] <http://www.matnet.sav.sk/index.php?ID=159> [cit.2010-16-03]
- [7] Sandvik Coromant. *Technical guide and product catalogues*, AB Sandvik Coromant 2010.01, SE-811 81 Sandviken, Sweden, C-2948:123
- [8] <http://www.pramet.com/download/katalog/pdf/Solid%20End%20Mills%202009%20screen.pdf> [cit.2010-25-04]
- [9] http://www.schiertechnik.sk/CAD/index.php?option=com_content&task=view&id=29&Itemid=75 [cit.2010-25-04]
- [10] <http://www.strojarskatechnologia.info> [cit.2010-25-04]
- [11] http://www.tribotechnika.sk/application_data/tribo/uploads/Image/orelikon4.JPG [cit.2010-28-04]
- [12] MAŇKOVÁ, I. *Vybrané aspekty monitorovania stavu nástroja v procese rezania*, Košice, 2004, ISBN 80-8073-1837
- [13] NESLUŠAN, M., ČILÍKOVÁ, M. *Teória obrábania*, EDIS Žilina, 2007, 167 s.
- [14] NESLUŠAN, M., TUREK, S., BRYCHTA, J., ČEP, R., TABAČEK, M. *Experimentálne metódy v trieskovom obrábaní*, EDIS Žilina, 2007, ISBN 978-80-8070-811-8
- [15] JARKOVSKÝ, I. *Obrábanie izotermicky zušľachtených bainitických liatin* : doktorandská práca: ŽU, 2008.
- [16] STANČEKOVÁ, D., ČILLÍKOVÁ, M., CZÁN, A., MORAVEC, J., ENGLÁRT, A. *Úvod do inžinierskeho štúdia*, EDIS Žilina, 2002.



Research of The Vehicle Side Impact Against An Immovable Obstacle

*Egidijus Černiauskas, * Artūras Keršys, ** Neringa Keršienė

*Kaunas University of Technology, Faculty of Mechanical Engineering and Mechatronics,
Department of Transport Engineering, Kęstučio 27, LT-44312 Kaunas, Lithuania,
{egidijus.cerniauskas, arturas.kersys}@ktu.lt

*Kaunas University of Technology, Faculty of Mechanical Engineering and Mechatronics,
Department of Solid Mechanics, Kęstučio 27, LT-44312 Kaunas, Lithuania, {neringa.kersiene}@ktu.lt

Abstract. The paper analyses one of measures of the interior passive safety - efficiency of anti-intrusion side door beam in the case of vehicle side impact on the immovable obstacle. The impact testing and analysis of the applicable regulations used in the world practice and examination of characteristics of side impact test are carried out in this work. With numerical models of the anti-intrusion side-door beams of a unique cross-sectional geometry being created, shock-absorption tests were conducted using computer-aided design system Solid Works and the finite element method (software package LS DYNA). Based on dependences of the beam energy absorbed and the simulated pole deceleration on time obtained, the most effective profile of a anti-intrusion beam in a passive safety aspect was then defined. The survey results allow a preliminary assessment of structural stiffness during a vehicle impact against an immovable side barrier.

Keywords: internal passive safety, side impact, anti-intrusion beam, numerical model, absorbed energy, deceleration.

1. Introduction

Over the past ten years about 40 thousands of people are killed and injured more than 3 million people are injured during vehicle crashes on European roads every year [1, 2]. These facts testify the numerous economic loss, therefore the target set by the European Commission meeting the strategy of sustainable development is natural - over the next ten years, at least halving the number of road casualties [4st]. One of the preconditions for the realization of this goal is the development of advanced vehicle reducing amount of deaths and injuries in so-called survival collisions along with implementation of effective internal and external passive safety measures. Progress of fast production methods and technologies in the automotive industry caused increasingly popular application of welded and molded constructions of light aluminum and composite materials [3]. By raising higher and higher requirements to accidents assessment and passenger safety theoretical, numerical modeling and dynamic testing of ground vehicle safety elements and energy-absorbing structures conducted by the researchers are of major importance [1-3].

Vehicle accident statistics shows that the article dealt with the case of passenger side-impact, one of the most dangerous cases in respect of death-rate – side-impacts make up one third of all impacts in which 35% are fatal cases [3-4]. The researchers in their works carried out side impact tests of two types: a vehicle on a vehicle and a vehicle on a pole.

The second case – an impact of vehicle moving on its side on a permanently fixed pole simulating a tree, light pole or other obstacle was investigated in this work. Standards and regulations used in practice and describing vehicle side impact against an obstacle analyze dynamics behavior of the complete vehicle and occupant without taking into account the general requirements to buildings of isolated structures [4]. This article presents research of behavior of the most important structural vehicle element in safety aspect – the front side-door anti-intrusion beam impacting against a pole.

2. Analysis of a vehicle side impact test

Vehicle crash test is a complex process - the collision mechanism can be highly variable, depending on factors - movement regime before the impact (braking, movement at angle, sliding sideways, etc.), the speed before the impact, movement after the impact (rotation, skidding, turning, etc.), and the vehicle construction. One of the most widely used and accurate methodologies of evaluation of vehicle passive safety is full-scale impact testing. Regulated vehicles crash tests are focused on the behavior of the body structure and strength with short-term impact loading. Despite the fact that currently in the world there are about ten independent organizations investigating and assessing vehicles safety by their own rules and standards, no uniform test procedures exist. Existing standards and regulations are fundamentally different due to severity of assessment of results of the tests.

Towards a more effective passive safety measures in case of side impact, in the National Highway Traffic Safety Authority (NHTSA) there was developed the side impact test - Federal Motor Vehicles Safety Standard No. 214 (FMVSS 214), added by dynamic test with shifting obstacle [5]. Side-impact tests according to FMVSS Directive No. 214 were conducted for two cases: quasi-static and dynamic. Quasi-static test reveals a rigid body reaction when it is intruding into the vehicle cabin area. The test is carried out by pushing the rigid cylinder of 450 mm length, 300 mm in diameter into a vehicle door at a steady speed of 0.03 m/s.

During impact test against a pole (Fig. 1) the vehicle is fixed on special trolley and pushed to a permanently fixed pole at speed 29 km/h. The vehicle is directed to a pole so that it would be in one plane with the driver's head. The pole itself is 254 mm in diameter, so during an impact it is intruding inside the vehicle rather deep. A dummy constructed specially for side-impact tests was seated in the driver's seat, in order to assess the human head and legs injuries (Fig.2). Vehicles without side airbags for a driver's head may hit posts or pillars as a result he may die.

Although anti-intrusion beams are probably the only structural response of the side door to protect passengers during an impact against the side obstacle, but there are no regulations or standards for testing separate beams. During a side impact of experimental or numerical-experimental studies interaction of side airbags, an occupant's head and the central pillar, and dynamics of the passenger movement across are analyzed, but strength or stiffness of the components of the side door are not separately analyzed in a standardized way.

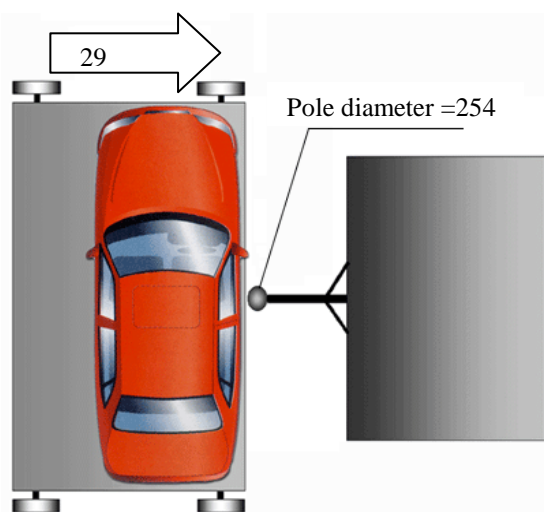


Fig. 1. Test of side impact on a pole according to Euro-NCAP.

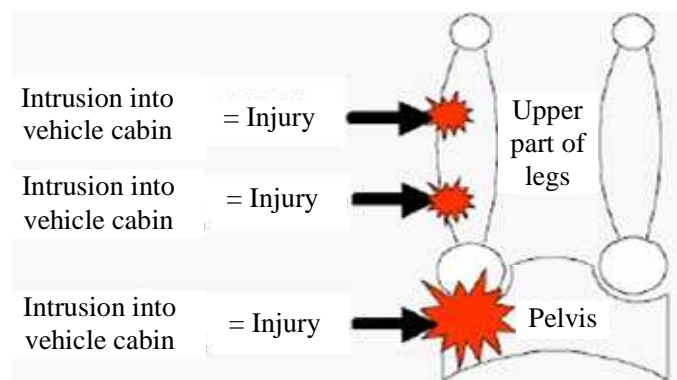


Fig. 2. Cases of sustained legs injuries.

3. Numerical research of vehicle side door anti-intrusion beam during an impact on immovable obstacle

Anti-intrusion beams designed to protect passengers during side impact when a foreign object from outside intrudes into interior space are mounted inside the vehicle door cavity at exterior plane and are attached to the front and rear door pillars (Fig. 3). These beams are slightly curved outwards – thus impact strain energy absorbed is primarily directed to the door sides which rest on the body pillars. Strength, stiffness or energy absorbance of vehicle retaining structures is determined in two ways: using approximate methods and the high safety factors and exact numerical methods and minimum ratios. The first method in this case is unacceptable, since it is used for various low speed machines and structures, for which their own weight is irrelevant. The second method allows a significant reduction in structural weight with assuring the required operational safety, but requires an accurate assessment of all possible structural features.

Simplified calculation schemes were used in initial stages of the study, with evaluation of characteristic working conditions of the vehicle side structure. By finite element modeling of complex structures such as the vehicle door some model simplifications can often be realized, isolating the specific elements and maintaining the boundary conditions, while speeding up decision time and without affecting the accuracy of the solution. In this case, a number of schemes are used in calculation for the same structure, depending on what operational conditions simulates the structure. At this stage the experimental and numerical results of research of insulated protective side door beams are compared. Although the overall stiffness of protective beams defined fully reflects the structural reliability of a side impact event, at this research stage the structure optimality is associated with regulated calculation results of power parameters.

Six anti-intrusion side door beam models chosen from the door-mounted forms mostly used by vehicle manufacturers were investigated in the work. With the numerical models of the side-door anti-intrusion beams of a unique cross-sectional geometry created (Fig. 3), side impact research has been conducted, using computer-aided design system Solid Works and the finite element method (software package LS DYNA). While modeling the vehicle side door anti-intrusion beam behavior in the case of a collision in the work, relevant contact target formulation and solution is important. For this purpose very efficient single-sided impact contact *CONTACT_FORMING_ONE_WAY_NODES_TO_SURFACE has been specially selected to similar challenges [6]. An explicit task solution was used for calculations, the impactor's speed 2mm/ms is recommended to quasi-static molding pressing tasks.

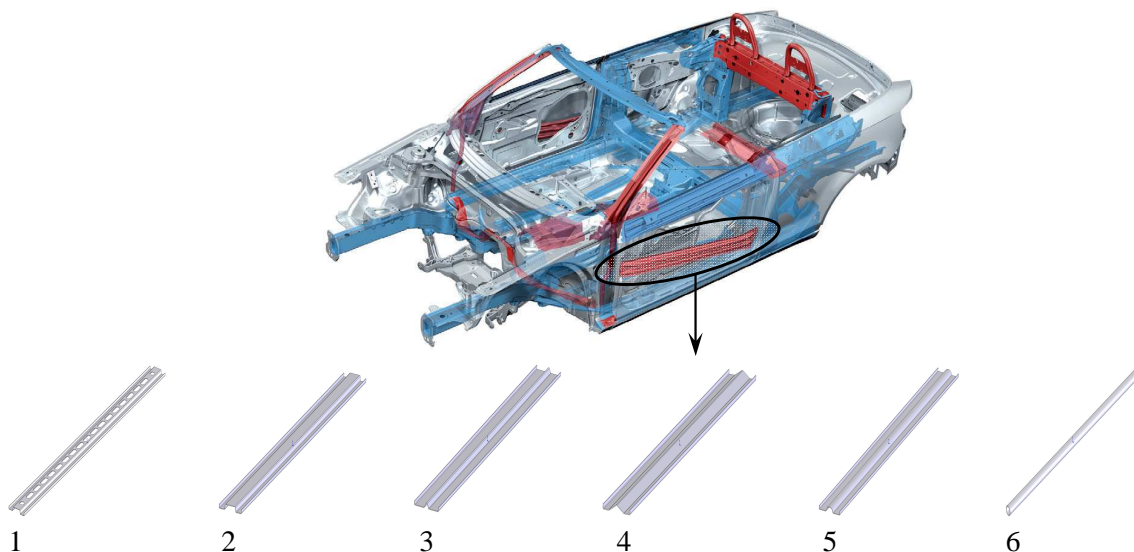


Fig. 3. Vehicle body protective shell and anti-intrusion side door beams examined.

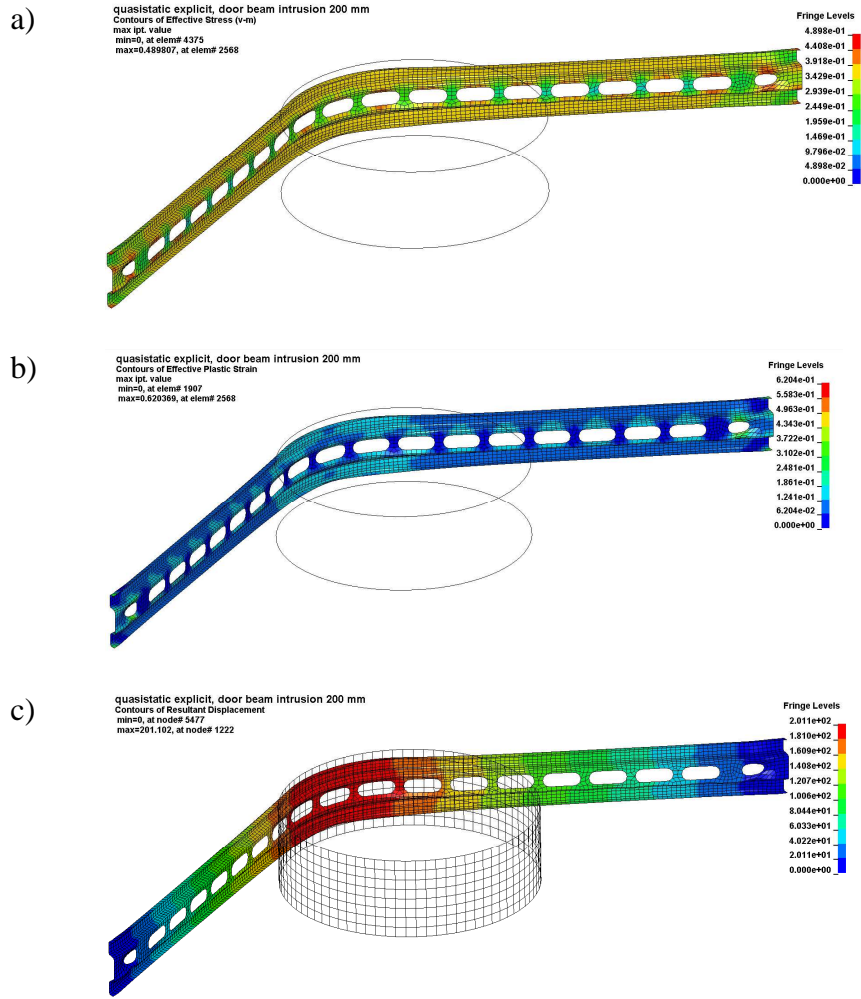


Fig. 4. Variation of stress (a), plastic deformations (b), and displacements (c) with beam deformation of 200 mm.

When modeling thin structural elements of vehicle beams shell finite elements are commonly used. About 20 different types of shell finite elements are introduced in the program LS-DYNA. Nonlinear shell finite elements of four nodes were selected in this work, and they were calculated by Mindlin-Reissner theory of thick boards, evaluating variation of element thickness during deformation, having five integration points in the plane of the element and two integration points in the element width. Increasing the strain rate in the model may lead to non-physical deformation (Hourglassing) effect, to avoid which the additional control factors are selected for elements. The finite element mesh fineness has significant effects on accuracy of results of the numerical model. In order to evaluate grid density effects the element edge length $L_e=5 \text{ mm}$ is chosen in these numerical models discussed in this work.

Constructing the finite element numerical model of the anti-intrusion beams (FEM), the material (DIN EN 10025 – 91: St 52–3 N, (AISI 1040)) in the software package LS DYNA is described by the law, where the model describing behavior of the material in an elastic-plastic area is based on strengthening law. In the linear strengthening model link between stress - strain is expressed as [6]:

$$\sigma = E \cdot \varepsilon, \text{ when } \sigma \leq \sigma_y \text{ and } \sigma = E \cdot \varepsilon + E_t (\varepsilon - \varepsilon_y), \text{ when } \sigma \geq \sigma_y, \quad (1)$$

where E_t – factor describing the tilt of the strengthening line called the tangential modulus, which can be determined in two ways, i.e. by values of the strength or the breaking threshold.

$$E_{t,U} = \frac{\sigma_{U,tikr} - \sigma_Y}{\varepsilon_{U,tikr} - \varepsilon_Y}. \quad (2)$$

The calculations are based on two conditions. As already mentioned, the explicit calculation quasi-static approach was used: a beam is strained at very low speed (2 mm/ms) by a pole, until 200 mm displacement is reached. Results demonstrate (Fig. 4) the amount of force required for each profile in order to achieve this displacement. Using the explicit method of calculation, when a concrete speed equal to 29 km/h acting on the beam is known, a certain pole weight - 50 kg is chosen. In this case, a test for testing new vehicles corresponding to the standards was simulated: the vehicle placed on a platform is side moving at speed 29 km/h and hits at right angle to a rigid pole of 254 mm in diameter.

During a quasi-static numerical test the reaction force was determined (Fig. 5.). According to requirements of FMVSS-214 (Federal Motor Vehicle Safety Standards, Side intrusion/Roof Crush test) [5], when the pole 254 mm in diameter intrudes by 150 mm into the vehicle door anti-intrusion beam, the reaction force must not be less than 5 kN. From Fig. 5 we can see, that the maximum force is needed to deform the beam of 2nd profile and it is equal to 23.13 kN. The minimum force needed to deform the beam of 1st profile is equal to 19.26 kN. It should be noted that the mass of the second beam is the largest of the six beams investigated, resulting in increased resources needed for reaching the target displacement.

Dependences of energy absorbed by beams on time are given in Fig. 6. Beam deformation takes place 30 ms with the impactor acting at 29 km/h. The maximum energy is absorbed by the beam of the 2nd profile as well as – it is equal to almost 1.6 kJ. By contrast the lowest energy is absorbed by the beam of the 1st profile.

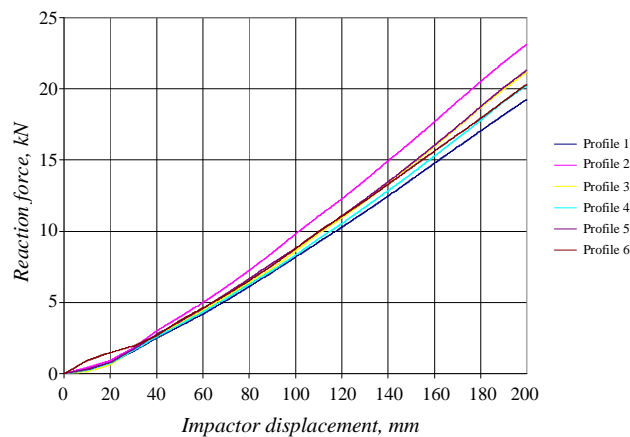


Fig. 5. Displacement curve of the force and the impactor acting on the beam.

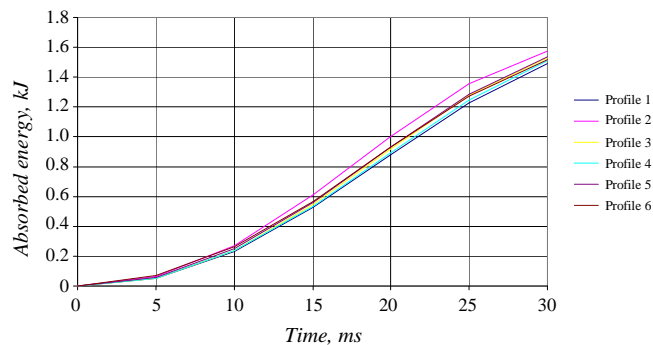


Fig. 6. Dependence of energy absorbed by the beam on time.

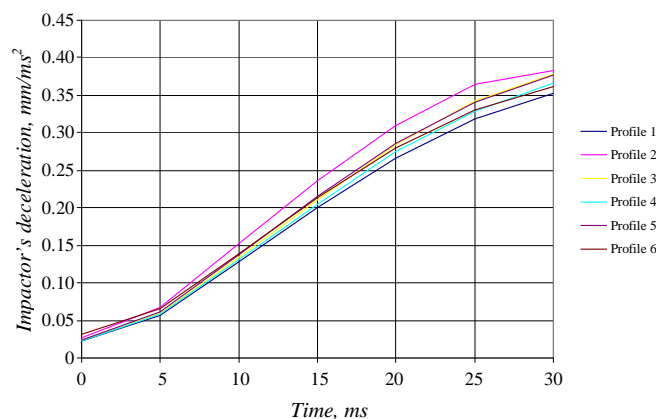


Fig. 7. Dependence of deceleration of the pole simulated on time.

Dependence of deceleration of the pole simulated (impactor) on time is shown in Fig. 7. The maximum value is again reached by beam of the 2nd profile - it makes 0.38 mm/ms². The greater the deceleration, the sooner the beam deformation stops. And under real conditions the sooner intrusion of outside obstacle (e.g., in the case of collision of another vehicle, tree, pole) into the vehicle interior is stopped. In summary, from the results of Fig. 5-7, it follows that the beam of the 2nd profile is the most optimal.

4. Conclusion

In the absence of separate regulations and standards for testing of structural response of side door element – anti-intrusion beam, protecting passengers during an impact on the side barrier, during practical side impact experiments or a numerical-experimental studies, interaction of the side airbags, a passenger’s head and the central strut, and dynamics of passenger’s side moving are analyzed, but strength or stiffness of the side door components are not analyzed separately.

Based on obtained dependencies of the beam energy absorbed and deceleration of the pole simulated on time, the most effective profile of protective beam in passive safety terms was determined – the maximum value (0.38 mm/ms²) of dependence of deceleration of pole (impactor) simulated on time was defined in case of the beam of the 2nd profile – under the real road accident conditions an intrusion of a foreign obstacle into the vehicle cabin is stopped the most quickly.

Results of the research done allow preliminary assessment of structural stiffness when a vehicle impacts against a immovable side obstacle. In assessing the true functioning of side impact beams and dealing with their effectiveness, it is important for simulation to adjust the computational model adding to it certainty of mounting of the anti-intrusion beams in the side door.

References

- [1] PRENTKOVSKIS, O., SOKOLOVSKIJ, E., BARTULIS, V. *Investigating traffic accidents: a collision of two motor vehicles*. Transport 25(2), 2010, pp. 105-115.
- [2] RUKUIŽA, E., EIDUKYNAS, V. Investigation of drivers poses influence to the intervertebral forces in the junction of thoracic and lumbar spinal curves. *Mechanika* 76(2), 2009, pp. 61-64.
- [3] TENG, T. L., WU, C. H., WANG, S. W. *The injury analysis of occupant in side impact collisions*. Journal of Science and Engineering Technology, vol. 3(1), 2006, pp. 33-41.
- [4] TENG, T. L., CHANG, K. C., NGUEYN, T. H. *Crashworthiness evaluation of side-door beam of vehicle*. Technische Mechanik, Band 28, Heft 3-4, 2008, pp. 268-278.
- [5] Evaluation of FMVSS 214 – Side Impact Impact Protection: Dynamic Performance Requirement. NHTSA Technical Report, U.S. Department of Transportation, National Highway Traffic Safety Administration, 1999.-238p.
- [6] WEIMER, K. LS-DYNA User’s Guide CAD-FEM GmbH. 2001, 200 p.



Verify the Accuracy of Positioning the Lathe's School EMCO ConceptTurn 55

*Ján Dekan, **Matúš Košinár, * Jozef Pilc

*University of Žilina, Faculty of Mechanical Engineering, Department of Machining and Manufacturing Technology, Univerzitná 1, 01026 Žilina, Slovakia, jan.dekan(jozef.pilc)@fstroj.uniza.sk

** University of Žilina, Faculty of Mechanical Engineering, Department of Automation and Production Systems, Univerzitná 1, 01026 Žilina, Slovakia, matus.kosinar@fstroj.uniza.sk

Abstract. This article addresses the need to measure the geometric accuracy of CNC machine tools and introduction of modern diagnostic system working on the principle of light interferometry. The experimental section describes how the measurement of positional deviation Reviews Support school lathe when measured with the scroll at different speeds.

Keywords: geometric precision, laser interferometer, position deviation, systematic positional deviation, numbness, positioning accuracy

1. Introduction

Progress of the country's economy shows a high level of mechanical engineering, which is in most represented by machining. Its improvement is closely linked with improving the construction and maintenance of the degree of precision machine tools. Machine tool positional accuracy and repeatability are core descriptors of a machine tool and indicate the machine's expected level of performance. Precision of machine tool is determined by accuracy of labor movements and their relative positions at work. Machine tool users are faced to proven verifying and documenting their accuracy, which allows exclusion of unforeseen downtime due to failure to comply with the required tolerances of the product. Diagnosis of machine tool brings the trend of precision machine tool and it is detected early date machine repairs and therefore subsequent saving of the finances, which is the basis for sustainable production.

2. Precision Machine Tools

Precision of machine tool is a feature, that characterizes the ability of machine tool produces components in the required quality. Precision of machine tool is conditional to the requirements for the degree of quality component. This sustained precision machine work is intended primarily in accuracy of its individual parts and their mutual imposition. Effect of compliance with precision manufacturing and assembly of parts and nodes of machine tools evaluates static, also called **geometric precision** of machine tool. This is the entry subject to the accuracy production of finished component.

The first conditions for the control of geometric accuracy machine tools compiled in 1927 dr. Georg Schlesinger. These conditions were taken and modified for current conditions. They are part of the ISO, DIN, STN standard, ... These tests include the detection of deviations of shape and position of individual parts onto fully assembled machine. They reveal hidden defects caused by an inaccurate production and assembly of machine part [1]. To maintain the quality of production is the main assumption control and prediction of the state machine tools. From the archive of the measurements is obtained a continuous overview about the evolution of precision machine tools.

This allows the allocation of production of component on machine tool to ensure the required quality and reduce production rejects. This allow several diagnostic systems. In the experiment is used a laser interferometer diagnostic system XL-80 from British Renishaw.

2.1. Presentation of the Laser System Renishaw XL-80

It is a modern laser diagnostic system with a modular concept that uses the phenomenon of light interferometry. It allows linear measurement of length, angle measurement, the angular rotational axis cutting, flatness, straightness and squareness of movement axis of the machine working .

On the Fig.1 is set to measure the linear distance. The beam 4 enters to ray splitter, which divides its into rays 2 and 3. The referenced beam 2 is reflected from a linear mirror fixed on a linear beam splitter back to the splitter. The measured beam 3 passes to beam splitter to the movable linear mirror, from which is reflected back into the laser head. From beam splitter enters to the laser head combined volume of two beams with different polarization. The referenced beam is vertically polarized and the measured beam is horizontally polarized. Transition through the optic in laser head, beams interfere. Measurement is evaluated on the basis of rotation of light and dark stripes, which is recorded as a pulse by sensor.

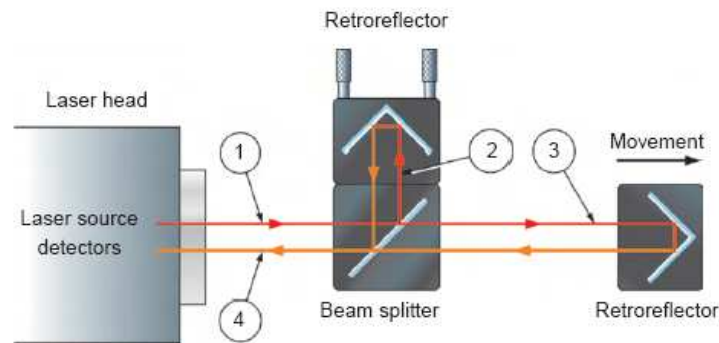


Fig. 1. Configuration for linear measurement.

Laser head produces a stable volume of laser radiation. Accuracy of laser measurements is $\pm 0.5 \mu\text{m.m}^{-1}$ in the full range of measurements at $0^\circ \text{C} - 40^\circ \text{C}$ and pressure of 65 kPa - 115 kPa. On the size of the wave-length of the laser beam has a significant effect of temperature, pressure, humidity of enviroment, expansion of material (motion mechanizmus). The measuring system is equipped by the compensatory unit for guarantee the accuracy. It provides compensation for wave-length of laser beam by the measured values of pressure, humidity, ambient temperature and material temperature machine [2].

Part of the diagnostic system is the software XL Laser, allowing processing of measured data by various international standards. It also includes possibility of creating a table of compensation values which is entered directly to the machine controller. It is intended for fast and easy analyze the characteristic of the motion mechanism of the machine tool.

3. Measure the Positioning Accuracy

In the experimental measurement was a measurement precision of positioning Reviews Support on school lathe EMCO Concept Turn 55 using a laser interferometer system, XL-80. While a number of standards and guidelines exist outlining how to evaluate machine tool positional accuracy and repeatability, they differ in their analysis procedures and in key parameter definition. As a result the values reported for positional accuracy and repeatability for any one machine can vary depending on which standard was used. Measurements for evaluating is in standard ISO 230-2: 2006. Scope of the standard: To specify the methods of testing and evaluating the accuracy and

repeatability of positioning of NC machine tools and components by direct measurement of independent axes on the machine. Used for type testing, acceptance testing, comparison testing, periodic verification, machine compensation. In Tab.1 are some characteristics of the measured machine.

Distance between centers	335 mm
Swing diameter over bed	130 mm
Traveling in the x- axis	48 mm
Traveling in the z- axis	236 mm
Minimum step feed	0,0005 mm

Tab. 1. Data on the machine.

Before the start of measurement was necessary to create a program to test a lathe, which has control system SINUMERIK 840D from Siemens. Subsequently, it was necessary to cleanse dirt from the line and install the measuring optics, where was used model with fixed interferometer splitter and movable reflector. Also was connected compensation unit to minimize the effect of environment on the measured values. After establishing laser head and optics followed Reviews Support "in operation empty" (about 30min). Measurement of deviations of position were realized at length 170 mm with interval of split 10 mm at different feed speeds. The most common feed speed was half the maximum speed. Were used 20, 50, 80 and 110% maximum feed speed, while 100% represents 33.3 mm.s^{-1} . In Tab. 2 are showing the values used at the other feed and in Tab.3. average values for which the measurements were realized. Support ranged with an interval of 5s because leveling position. As Fig. 2 shows the measurement took place in both directions raid to measured positions in five cycles (five courses bidirectional cycle).

Air temperature	23,81°C	20 % speed	$6,66 \text{ m.s}^{-1}$
The temperature motion mechanism	25,93°C	50%	$16,65 \text{ m.s}^{-1}$
Air pressure	981,28 mbar	80%	$26,64 \text{ m.s}^{-1}$
Air relative humidity	39,62 %	110%	$36,63 \text{ m.s}^{-1}$

Tab. 2. Measurement conditions.

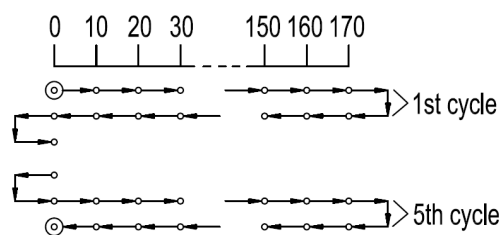


Fig. 2. Measurement scheme.

We compared the evaluation results given by the manufacturer in the documents of the machine EmcoConcept Turn55 where was permitted the accuracy of positioning in the Z axis 0,08mm, and measured to 0,05 mm. The machine is relatively new and the number of hours worked on it is minimal, it should not depart from the values provided by the manufacturer

Example of the evaluation results by to ISO 230-2 is on the Fig. 3, where we used measurements at 50% speed. As it is shown in the graph, our values were in the range from 0,061 mm to 0,062 mm. Because the manufacturer states that the machine has only allowed values in the range of one hundredth of a millimeter, is therefore irrelevant to measure more decimal places. Our results on the results of the producer are different, but on the other hand, are within the limits set by the manufacturer.

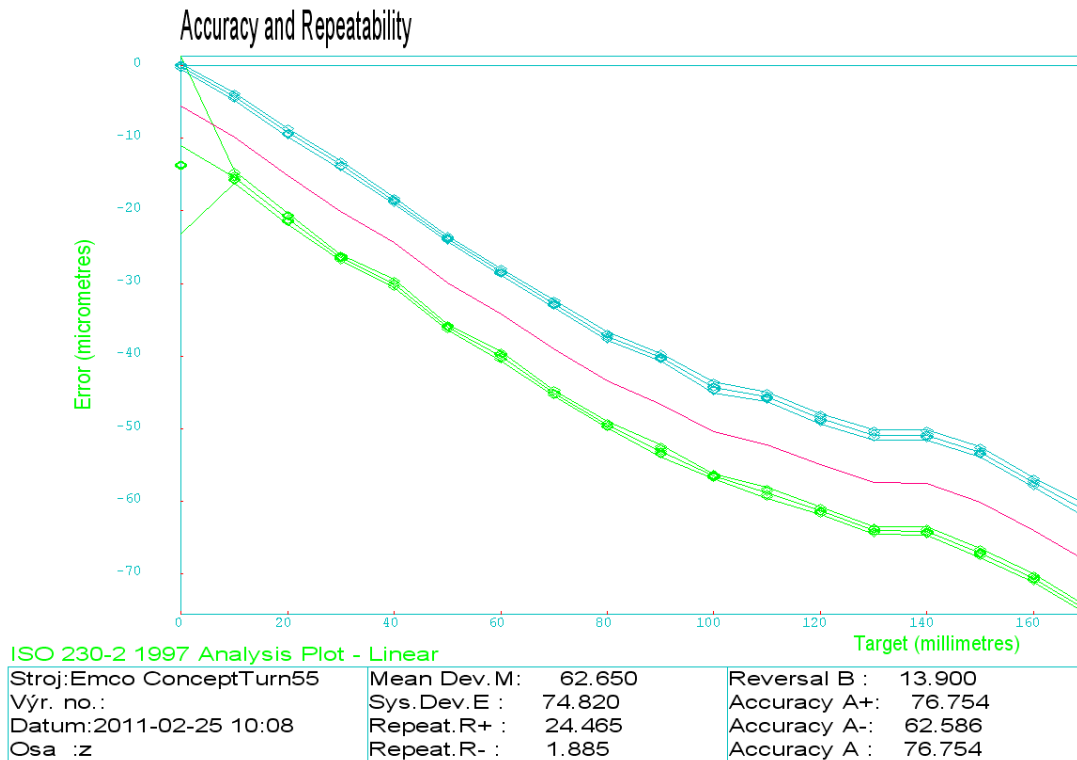


Fig. 3. XL-80 output at 50% speed feed

Various statistical characteristics of location accuracy, which shows that the change of feed speed causes little change in their view of the declared accuracy of the machine are shown in Tab. 4.

	20% velocity [mm]	50% velocity [mm]	80% velocity [mm]	110% velocity [mm]
Mean Deviation	0,061	0,063	0,063	0,062
Systematic Deviation	0,072	0,074	0,075	0,075
Reversal	0,012	0,014	0,014	0,015
Accuracy	0,074	0,077	0,076	0,076

Tab. 4. Values of statistical characteristics of accuracy

4. Conclusion

Measurement we are convinced that the positional accuracy of the school lathe is such as it is specified by the manufacturer. Also at different feed speeds is the accuracy in using of machine the same. In the future it would be appropriate to measure another axis machine too. XL software created for the measurement also correction values, which is necessary to enter to the the control system. This could be improve the accuracy of positioning the axis Z.

References

- [1] DEMEČ, P. *Presnosť obrábacích strojov a jej matematické modelovanie*. Viena. Košice, 2001.
- [2] [http://resources.renishaw.com/download/\(d45dd6569592477a8c634cf5b4deb032\)?lang=cs&inline=true](http://resources.renishaw.com/download/(d45dd6569592477a8c634cf5b4deb032)?lang=cs&inline=true)



Renovating Intensification of Machining Nitride Layers of Tools for Volume Forming

*Michal Derbas, *Andrej Czán, *Michal Sporka

*University of Zilina, Faculty of Mechanical Engineering, Department of Machining and Manufacturing technology, Univerzitna 1, 01026 Žilina, Slovakia, {michal.derbas, andrej.czán, michal.sporka}@fstroj.uniza.sk

Abstract. The work deals with the machining of nitrided layers in renovation tools for forming volume.

Keywords: turning, nitride, machining, tool, renovating, forging, non – destructive testing, ultrasound

1. Introduction

Tools made of special hardened materials processed are highly cost-intensive, and therefore already in the design consider the possibility of its manufacture, renovation or repair. The biggest problem is to choose the right technology, which returns tool as soon as possible mechanical and physical properties, of course, a profitable price. In most cases, the repaired tools represents the forging block, which is heat treated to a hardness about 50 HRC with a thickness of nitride layer from 800 to 900 drawings, it is further processed powdered steel into hardness about 64 HRC used as shaping tool and materials in excess of the hardness over 65 HRC from sintered materials as carbides non-ferrous metals and the like. The mentioned tools are difficult tested elements in the process exposed to temperatures around 1300 °C and more. This, together with mechanical stress causes on the surface microcracks, that by the time growing into uncontrollable fractures or occur to brittle fracture. Tools to be worn by the mechanical load lose its function and therefore must be replaced.

2. Current status of solved issue

Renovating is a special case of repair, where the repaired object is machine component. It is a work in renewing when damaged machine parts are to their functional properties. Renovation is a set of activities carried out in order to restore operational status of components and their life. It is reparation in which we return of wear parts its geometric shape, the original size, functional and mechanical properties in accordance with drawings and technical specifications. Renovation may be seen as a repair sub-sector, which contributes to reducing the cost of restoration and operation of machinery, but it will be seen as a special case of recycling materials, which, moreover, reduces the demand for raw materials and energy sources [1].

Management of the renovation process usually develops spontaneously, where lacks a systemically approach in terms of an objective decision about the effectiveness of organization's renovation. These problems remain in the literature and in practice need to solve and increases proportionally with the possibilities of current computer and communication technology [2].

3. Block forging

It is a shaping process, in which a forging is formed from the initial forging blank, either in a single cavity swage, or to more cavities, while the flow of metal is regulated or restricted in the cavities. A block is a tool used for forging applications. It is essentially a steel block, which has a section adapted to fit in the ram, the second part is mounted on the table. In the block, a forging is formed on the active surface of the block cavity, it has a shape, which will have block forging divided into two parts. Block forging has many advantages to free forging. Labour productivity is several times higher than in free forging. Precision of forgings is much greater than in free forging. With block forging we can produce the products already done. This favorably affects not only the total consumption of material required to manufacture parts, but it also reduces the labor intensity required for production parts.

Some negative aspect of block forging is the complexity of the tool. Block forging, it can be used for complicated forgings, which should not be done by free forging. Block forging is used in the production of a large quantity of equal forgings. The nature of nitriding is two-staged, where in the first period of time - in the first instance is surface intensively nurtured by nitrogen at high partial pressure of NH_3 . In the second stage occurs the diffusion layer growth at zero partial pressure of NH_3 , where is absorbed nitrogen from the atmosphere into the metal and nitrogen diffusion takes place from the ϵ -phase to α -phase. This is achieved by block a high resistance to sudden temperature changes, increase resistance to abrasion and cavitations wear of block [3]. Nitrided blocks show a significant increase in lifetime compared with unnitrided cavities. It was found that the lifetime of a re-nitrided block is comparable to the results of the life of a block made by basically technology. Re-nitrided block was actually used twice, while primary nitriding was carried out on newly manufactured block, which after completing its life in production was enhanced mechanically for base metal and after obtaining drawing was again nitrided [3].

4. Experimental test of fitness using VRP for repair block forging

Forging tools wear in the production process due to the large temperature and pressure's stress. This wear is relatively rapid, and therefore the tool must be changed frequently to achieve the desired geometric properties of forging (e.g. parallelism areas and nominal size), but also because, in order to prevent irreparable cracks across all block. Most susceptible part to cracking is one in which is broken the integrity of the surface, for example in Fig. 1 of the exhaust vents on the right.



Fig. 1. Visualization of wear forging tool

The main points of the technological process renovation forging block are:

- remove surface nitride layer, cracks and other defects by cutting methods - roughing - working a new shape,
- machining the desired shape according to drawings - fine turning and milling,
- nitriding - process technology to achieve hard surface layer.

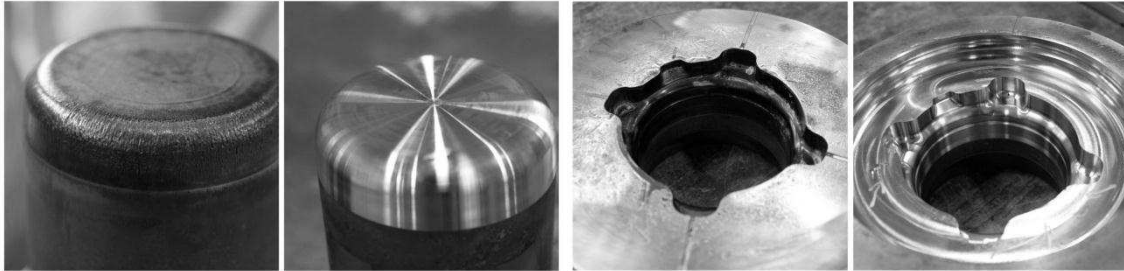


Fig. 2. Visualization of forging tool before and after renovation of cutting operation

On Fig. 3 we can see, how to fix forging block. After wear of functional area, forging block is repaired by deepening its original shape by drawings. In our case for better visualization is about 10 mm. Deepen the new shape has the same inner diameters and distances from the front office as the original part. However, the total amount is reduced by the dimension of the cavity which has been deepened. To achieve the required level of separation plane when mounted on a forging press, we have to be placed under the block, whose width is equal to the value of which is a diminished amount of repair block.

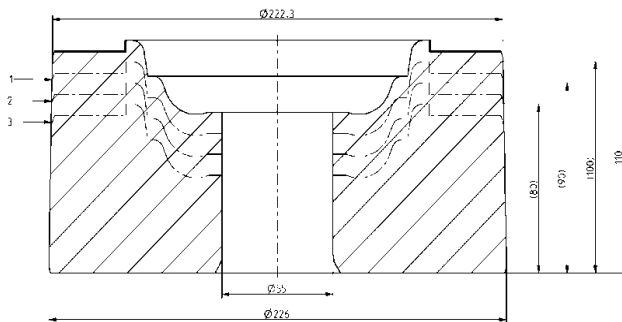


Fig. 3. Schematic representation of the process of repair (1 - the first reparation, 2 - the second reparation, 3 - third reparation)



Fig. 4. Sample of materials

Another issue that must be overcome during the machining of the block is surfaced nitride layer, how affecting the life of the individual instruments, also find comparative test. This means that each type of tool will machine the sample, which will not be rid of nitride layer on the forehead. Although this layer has a thickness of only about 0.2 mm, but the hardness is up to 56 to 57 HRC.

5. Non – destructive testing

Ultrasonically testing arose from the need to identify hidden internal defects in components that cannot be well outshined and those defects which could lead to accidents of finished products. This method uses non-destructive testing methods of materials and has considerable importance for improving the quality and reliability in the industry, especially in engineering. Belongs to one of the most important methods of non-destructive testing of materials in which it is possible to detect material discontinuities resulting in the production respectively in operation as a result of mechanical stress [4].

Effect of defects on the strength of the material depends on its nature, size and shape. Distinguish the nature of spatial defects. Planar nature of the defects are cracks, cold joints, unattaching and duality, while the spatial character defects, they are usually less dangerous for the strength of the material, the bubbles, cavities and pores. Outside of these defects, whose nature is to be determined, there are also forming a transition between major groups. These are such as rows of pores, hair pores. Option to specify the nature of the defect depends on the shape of the object and the presence of surface to which it is possible to attach the appropriate type of ultrasound probe. Detection of the nature or orientation of the defect is based on the directivity of ultrasonic transmission. On the nature and size of the defect depends on the reflective property of these components, and thus the shape of the echo [5].

6. Summary of current status

The work contains a summary of current knowledge concerning the renovations to restore operational status of components, their life and thus contributes to reducing the cost of restoration and operation of machinery. For the purposes of renovation is using ultrasound defectoscopy, which is one of the most important methods of non-destructive testing of materials in which it is possible to detect material discontinuities resulting in the production respectively in operation as a result of mechanical stress. Using ultrasonic non – destructive testing in renovation tools for bulk-forming intensifies machining of nitride layers. Detection of internal defects by non-destructive testing improves the quality and reliability of the renovation. Using this method and the right technology we can achieve a reduction costs for the rehabilitation and operation of machinery.

Managing of restoration processes in most cases carried out spontaneously, which lacks regular access in terms of an objective decision about appropriateness, quantity and promotion process itself. Before the renovation is necessary to extent of damage of wear components, which are machined for adjusting the dimensions and then decide the intensity of the renovation.

During the renovation we think about tools that achieve high productivity. Exchangeable cutting plates must be able to trim high-hard layers and exhibit the most satisfaction wear while ensuring optimum dimensional accuracy and surface roughness.

Acknowledgement

This article was written within the project of OPVaV: Intelligent system for non-destructive technology to evaluate the functional properties of components of X-ray diffractometry, code ITMS 26220220101.

References

- [1] PARKER, D. Remanufacturing in the UK; A Significant Contributor to Sustainable Development; Aylesbury, UK Oakdene Hollins, 2003.
- [2] SPROW, E. *The Mechanics of Remanufacturin*. Manufacturing Engineering, 1992.
- [3] HÍREŠ, O., PERNIS, R., KASALA, J. *Zvyšovanie životnosti pečovacej zápusťky*, Zborník z konferencie Funkčné povrchy, 2001, Trenčín, FŠT TnU, 2001.
- [4] KOPEC, B. *Nedestruktivní zkoušení materiálů a konstrukcí*. Akademické nakladatelství CERM s.r.o, 2008.
- [5] OBRAZ, J. *Zkoušení materiálu ultrazvukom*, SNTL Nakladatelství technické literatury Praha, 1989.
- [6] BLAŠČÍK, F. *Technológia objemového tvárnenia: Návody na cvičenia (skriptá)*, Alfa, Bratislava, 1988.



The Comparison Between Different Types of Cutting – Selection of the Best Method

*Agnieszka Domagała, *Szymon Tofil

*University of Technology, Centre of Laser Technology, Aleja Tysiąclecia Państwa Polskiego 7, 25-314
Kielce, Poland, a_domagała@onet.eu, tofil@tu.kielce.pl

Abstract. The comparison between four different types of cutting is presented, which are: oxy – fuel, plasma, laser and water cutting. The main purpose is to present all of those methods and then summarise the most crucial features of it. Nowadays, users do not have any problem with finding information about modern punches but at the same time it can be problematic which method of cutting should be chosen. Information below might help potential users choose the most appropriate method.

Keywords: Cutting, laser, punch.

1. Introduction

In every centuries, mankind has mastered a new form of energy. From 1960 – when the laser was discovered, to this days, there are a large amount of expectations that laser gives to the everyday life. They have become ubiquitous, finding utility in thousands of applications in every section of society, including, information technology, science, law enforcement, entertainment, medicine, industry and the military. The newest and more improved lasers optimized for different performance goals, such as: maximum peak pulse power and energy, maximum average output power, minimum output pulse duration and minimum cost.

A plasma and an oxy – fuel cutting are the most common method, which can be an alternative to each other. An important benefit of the water cutting is the ability to cut material without interfering with the material structure.

2. Description of the Experiment

On the market, there is many different types of punches. Their technical parameters differ one from another. It gives operators chances to choose the most suitable machine for them and the way they want to cut. Large diversity between them gives opportunity to fulfill one's needs. Below features like thickness of cutting material, possibility of drilling vents, cutting, investment costs are included. Those results present the best features of punches which are on the market. The table that depicts conditions of experiment is based on the information from producers websites. All of those relevant information have been gathered in Tab. 1 [1].

Compered Feature	Oxy – fuel cutting	Plasma cutting	Laser cutting	Water cutting
Type of material	Non – alloy steel	All metals, seldom some nonmetals	All metals and nonmetals, beside combustible and fragile	All metals and nonmetals, beside extra hard
Thickness of the material	200 - 300 mm; till 2000 mm	50 – 150 mm	< 300 mm	Till 250 mm
Possibility of drilling vents	As a additional task, vents have small quality	As a additional task, vents have small quality	As a main task; vent has got good quality and its minimal diameter = 0,3 mm	As a main task; vent has got good quality and its minimal diameter = 1,5 mm
Width and shape of gap after cutting	From 2 – 6 mm, depends on material's thickness; parallel gap	From 3 – 8 mm, depends on material's thickness; non – parallel gap	From 0,3 – 2 mm, depends on material's thickness; parallel gap	From 0,4 – 3 mm, depends on material's thickness
Precision in cutting	It depends on gap's width and shape			
Surface smoothness	Low	Low	Very high	High
Surface oxidation	High	During oxygen and air using	During oxygen using	Do not exist
Investments costs	The smallest	Small	The largest	Large
Cost cutting	Small during cutting thick steel	Lower then during oxy – fuel cutting	Law during cutting thin steel, much more higer during cutting thick steel	Higer then in laser cutting

Tab. 1. Comparison between different types of cutting

3. Results Analysis

In comparison with those four methods of cutting an oxy – fuel cutting is the most economically profitable method. Steel can be cut even till 2000 mm by a special gas burner and from 200 to 300 mm by normal gas burner in every conditions. The biggest disadvantages of it is wide gap from 2 – 6 mm. “Fig.1”.

Plasma cutting seems to be the most effective method. It is possible to cut almost every kind of materials of width till 150 mm. Costs of this method is not really high as in another. “Fig.2”.

Laser cutting for metals has the advantages over plasma cutting of being more precise and using less energy when cutting sheet metal, however, most industrial lasers cannot cut through the greater metal thickness that plasma can.

In water cutting “Fig. 3”, minimizing the effects of heat allows metal to be cut without harming or changing intrinsic properties. Unfortunately, cutting costs in this method are high, sometimes even more than during laser cutting “Fig. 4”.



Fig. 1. Oxy – fuel cutting

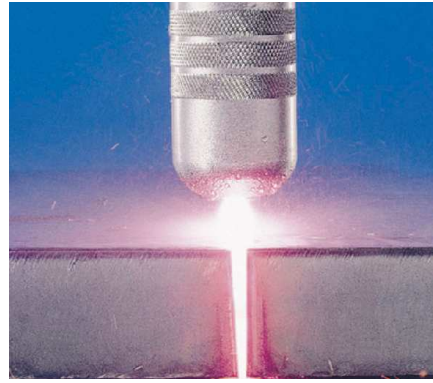


Fig. 2. Plasma cutting



Fig. 3. Water cutting



Fig. 4. Laser cutting

4. Conclusion

It is hardly difficult to find only one opinion which method of cutting is the most appropriate. There is a big range of specific purposes in companies. The analysis of pros and cons can allow avoid unnecessary cost in companies and factories.

Certainly, the most prospective method is laser cutting. The new technology gives opportunity to use it with better results. It means that laser cutting properties will improve. The newest lasers are designed not only for industry but also for everyone who has got such a need. Thanks to the many advantages, laser cutting become an increasingly popular method. The main advantages are: high speed and very good quality of cutting material. During laser cutting with oxygen as the gas associated, even a small change on the cut line in chemical composition of cutting material has influence on the optimum cutting speed.

Many entrepreneurs have already realised that cutting with using lasers can avoid many unneeded costs and give them new chance.

References

- [1] DOMAGAŁA, A. *Comperative analysis of modern shearing machines for cutting metal* [in Polish], master thesis (prof. B. Radziszewski), Kielce University of Technology, Kielce 2009.
- [2] KLIMPEL, A. *Welding and cutting of metals* [in Polish], WNT, Warszawa 1999.



Influence of Annealing On Hardness of The Recycled AlZn10Si8Mg Cast Alloy

*Emília Ďuriníková, *Eva Tillová, *Mária Chalupová

*University of Žilina, Faculty of Mechanical Engineering, Department of Material Engineering,
Univerzitná 1, 010 26 Žilina, Slovakia, {emilia.durinikova, eva.tilova, maria.chalupova}@fstroj.uniza.sk

Abstract. The contribution describes influence of the annealing (by different temperatures 20 - 400°C) on Brinell hardness of the recycled AlZn10Si8Mg cast alloy. Secondary AlZn10Si8Mg cast alloys are used for engine and vehicle constructions, hydraulic unit and mouldmaking without heat treatment. Properties include good castability, very good mechanical strength and elongation, light weight, good wear resistance and very good machining. Their mechanical properties are strongly dependent upon the morphologies, type and distribution of the second phases, which are in turn a function of alloy composition and cooling rate. With reference using this alloy for high-temperature castings it is necessary to study their structure and mechanical properties in dependence on the temperature. The experiment was realized out using Brinell hardness tester and interpretation of structural change was studied on optical microscope and SEM.

Keywords: aluminium alloys, microstructure, intermetallic phases, hardness

1. Introduction

Aluminium has been recognized as one of the best candidate materials for various applications by different sectors such as automotive, construction, aerospace, etc. The increasing demand for aluminium-based products and further globalization of the aluminium industry have contributed significantly to the higher consumption of aluminium scrap for re-production of aluminium alloys [1]. It is to the aluminium industry's advantage to maximize the amount of recycled metal, for both the energy-savings and the reduction of dependence upon overseas sources.

The remelting of recycled metal saves almost 95 % of the energy needed to produce prime aluminium from ore, and, thus, triggers associated reductions in pollution and greenhouse emissions from mining, ore refining, and melting. Increasing the use of recycled metal is also quite important from an ecological standpoint, since producing aluminium by recycling creates only about 5 % as much CO₂ as by primary production [2, 3]. Recycled Al-Si-Zn casting alloys can often be used directly in new cast products for mechanical engineering, in hydraulic castings, textile machinery parts, cable car components, mould construction or big parts without heat treatment [4].

One major hurdle in the direct use of recycled aluminium for new applications is the level of impurities present in the recycled (secondary) alloy; which is considered to impair the overall properties of Al-Zn-Si based casting alloys. By implementing adaptable alloying and process technology, the mechanical properties will therefore be radically enhanced, leading to larger application fields of complex cast aluminium components such as safety details. The presence of additional elements in the Al-Zn-Si alloys allows many complex intermetallic phases to form, such as binary phases (e.g. Mg₂Si or Mg₂Zn), ternary phases (e.g. Al₂CuMg, AlFeMn and AlFeNi) and quaternary phases (e.g. cubic α -Al₁₅(FeMn)₃Si₂ and Al₅Cu₂Mg₈Si₆) [5, 6], all of which may have some solubility for additional elements.

The present study is a part of larger research project, which was conducted to investigate and to provide better understanding mechanical properties (e.g. after annealing at higher temperatures) of the secondary (recycled) AlZn10Si8Mg cast alloy.

2. Experimental procedure

As an experimental material was used secondary (scrap-based - recycled) AlZn10Si8Mg cast alloy (UNIFONT® - 90) with very good casting properties, good wear resistance, low thermal expansion and very good machining [4]. Alloy contains relatively high Si, and their impurity limits tend to be relatively loose. Test bars (\varnothing 20 mm with length 300 mm) were produced by process sand casting in foundry Zátor, Ltd. Czech Republic. The melt was not modified or refined. Chemical composition of the alloy is given in Tab. 1.

Zn	Si	Cu	Fe	Mn	Mg	Ti	Ni
9.6	8.64	0.005	0.1143	0.181	0.452	0.0622	0.0022
Cr	Hg	Ca	Cd	Bi	P	Sb	Al
0.0014	0.0006	0.0002	0.0001	0.0003	0.0001	0.0007	rest

Tab. 1. Chemical composition of AlZn10Si8Mg alloy.

AlZn10Si8Mg cast alloy is a self-hardening alloy that is particularly used when good strength values are required without the need for heat treatment. Self-hardening starts when the castings are removed from the mould and the final mechanical properties are achieved after storage of approximately 7 to 10 days at room temperature ($R_m = 220 - 250$ MPa, $R_p0.2 = 190 - 230$ MPa, $A = 1 - 2$ %, $HB = 90 - 100$ [4 - 6]).

Temperature- and time-dependent processes determine how aluminium alloy castings behave at high temperatures. Depending on their initial state, annealing, dissolution and precipitation processes, ageing or overageing all have a role to play. One single form of measurement cannot record the various influences with any accuracy. Brief measurements of mechanical properties (e.g. hardness) at elevated temperatures do not include time-dependent processes and therefore only have limited use.

Experimental cast samples were heat treated by annealing at different temperature (20, 50, 100, 150, 200, 250, 300, 350 and 400 °C) with holding time 20 minutes, cooling at room temperature. After heat treatment were samples subjected for mechanical test (impact test and Brinell hardness). Cast samples for metallographic observation were sectioned from the test bars, standard prepared and etched by 0.5 % HF [7, 8]. The various intermetallic phases were identified using scanning electron microscope VEGA LMU II linked to the energy dispersive X-ray spectroscopy (EDX analyser Brucker Quantax). The hardness was measured using a Brinell hardness tester CV - 3000 LDB under a 250 kp load, a 5 mm diameter ball for 10 s (HBW 5/250/10). Three measurements were taken per sample and the median hardness was determined.

3. Results

Typical microstructures of the as-cast alloy are shown in “Fig. 1”. The microstructure of recycled AlZn10Si8Mg cast alloy consists of a primary phase (α -solid solution), a eutectic (mixture of α -matrix and fine spherical Si-particles) and variously type's intermetallic phases (Chinese script - Mg_2Si , oval round-like particles Al_2CuMg , Fe-needles - $AlFeMnSi$, sharp-edged particles - $AlFeMnSiNi$ and ternary eutectic $Al-MgZn_2-Al_2Cu$) [5 - 6]. The α -matrix precipitates from the liquid as the primary phase in the form of dendrites and is nominally comprised of Al and Zn - Fig. 1a.

Identified types of intermetallic phases are documented in Fig. 1b. Phase in the form of needles with a thickness of a few tenths of a micrometre and other dimensions of the order of 10 μm were identified as $AlFeMnSi$ -phase. It is these plate-shaped phases that are considered most deleterious to mechanical properties (particularly ductility), Fe-needles also reported to reduce the castability, the corrosion resistance, and the machinability of Al-casting alloys. Platelets act as potential nucleation sites for porosity [7, 8] and sites for crack initiation that, consequently, results in

decohesion failure. Besides the Fe-needles were observed Fe-rich phases with Ni (AlFeMnSiNi or AlFeNi) in the form sharp-edged coarse particles.

Addition of Mg to Al-Zn-Si alloys leads to formation strengthening Mg-rich intermetallic compounds. Mg-phases can in Al-Zn-Si alloy solidify in two different forms: Mg_2Si and Al_2CuMg . The Mg_2Si phase was identified by EDX analysis as individual skeleton-like or script-like so called “Chinese script” morphology. Oval round-like particles was detected as S-phase (Al_2CuMg phase). Observed was the appearance of Zn-eutectic, respectively Al-MgZn₂-Cu phase too. The 20 minutes annealing at the temperatures (20-400 °C) induced any changes in the microstructures of experimental alloy.

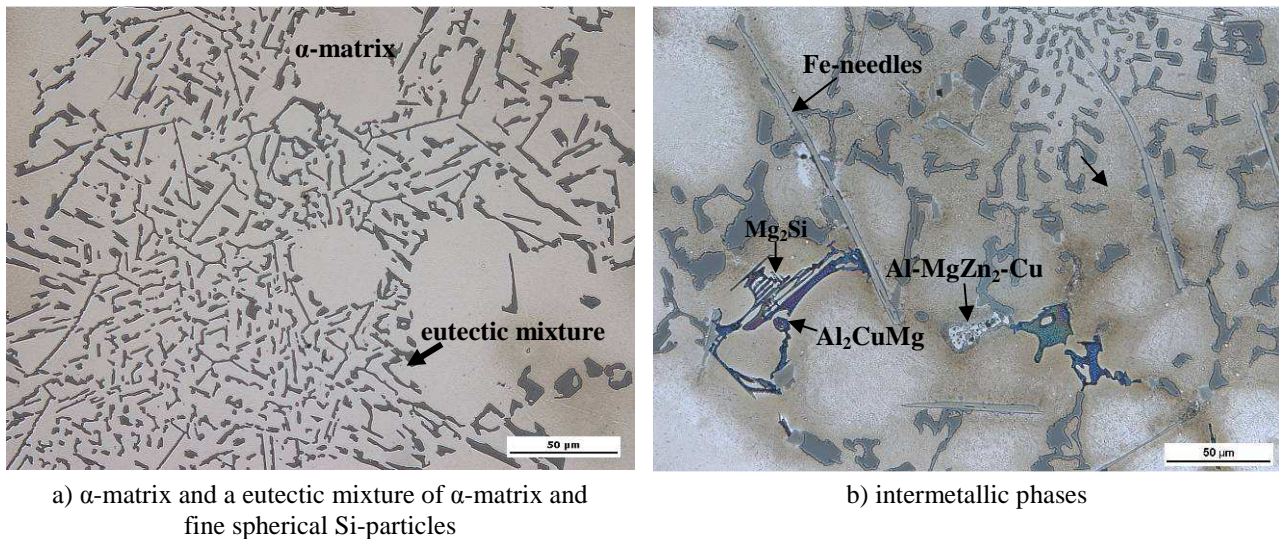


Fig. 1 Microstructure of AlZn10Si8Mg cast alloy, etch. 0.5 % HF

Hardness measurement was performed by a Brinell hardness tester (HB) with a 5 mm diameter ball, load of 250 Kp, and a dwell time of 10 s. The Brinell hardness value at each state was obtained by an average of at least three measurements in samples which were 20 minutes annealed at different temperatures: 20 (ambient temperature at the time of trial), 50, 100, 150, 200, 250, 300, 350 and 400 °C and followed by cooling at room temperature.

The diagram in Fig. 2 shows the results of the hardness measurements after annealing at the temperatures. Aluminium alloys are annealed to soften them and increase ductility. It can be seen that the measured Brinell hardness decreases with increasing annealing temperature. The lowest hardness was measured at 200 °C (64.9 HBW) and the maximum hardness value, compared with baseline (21 °C - HBW 93), was measured at 50 °C (97.6 HBW).

Some materials (metals with a cubic space-centred lattice) in changing the loading conditions (especially temperature, stress state and loading rate) suddenly changing from ductile to brittle state. However, aluminium and its alloys that have a transition with increasing annealing temperature was increased toughness material responds well what course material hardness, which has a decreasing character.

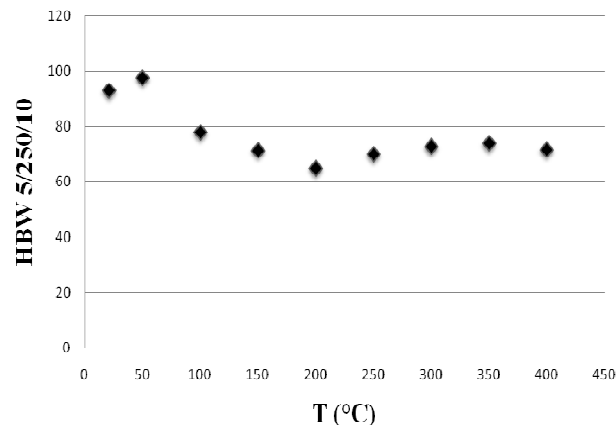


Fig. 2. The effect of annealing on the hardness

4. Conclusion

Understanding of metal quality is of superior importance for control and prediction of casting characteristics. With reference using recycled AlZn10Si8Mg cast alloy for high-temperature castings the experimental results are summarized as follows:

- Structural analysis of secondary alloy AlZn10Si8Mg identified as basic structural elements: α -phase (solid solution of Zn in Al), Si particles in the form of rounded grains and intermetallic phases (Fe-based phases in the form of needles - AlFeMn or sharp-edged coarse particles AlFeNi; Mg₂Si phase in the form of script-like so called “Chinese script”, rounded grains Al₂CuMg and Zn eutectics Al-MgZn₂-Cu). Chemical composition of these phases was confirmed by EDX analysis.
- The 20 minutes annealing at the temperatures (20-400 °C) induced any changes in the microstructures of experimental alloy.
- Annealing heating at higher temperatures result a process that reduces hardness of the alloy while increasing plasticity (ductility). The temperature of the annealing process play the meaningful role and also have got the biggest influence on the plastically properties on AlZn10Si8Mg castings.

Acknowledgement

This work has been supported by Scientific Grant Agency of Ministry of Education of Slovak republic No1/0249/09, No1/0841/11 and SK-CZ-0086-09.

References

- [1] DAS, K. S.: Designing Aluminum Alloys for a Recycle-Friendly World. Materials Science Forum, Vols. 519-521, pp. 1239-1244, (2006).
- [2] SENČÁKOVÁ, L., VIRČÍKOVÁ, E.: Life cycle assessment of primary aluminium production. Acta Metallurgica Slovaca, 13, 3, pp. 412-419, (2007).
- [3] DAS, K. S., GREN, J. A. S.: Aluminum Industry and Climate Change-Assessment and Responses. JOM, 62, 2, pp. 27-31, (2010).
- [4] Casting material - www.sag.at
- [5] ĎURINÍKOVÁ, E., TILLOVÁ, E., CHALUPOVÁ, M.: Letná škola únavy materiálov, s. 174-177, (2010).
- [6] TILLOVÁ, E., ĎURINÍKOVÁ, E., CHALUPOVÁ, M.: Quo vadis foundry III. - Ekologické aspekty zlievarenstva a hutníctva I., Tatranská Lomnica, s. 191-197, (2010).
- [7] TILLOVÁ, E., CHALUPOVÁ, M.: Štruktúrna analýza zliatin Al-Si. EDIS Žilina, (2009), in Slovak.
- [8] BOLIBRUCHOVÁ, D., TILLOVÁ, E.: Zliatiny Al-Si na odliatky. EDIS Žilina, (2005), in Slovak.



Electrochemical Properties of The AISI 316Ti Stainless Steel In Different Redox Potential Environment

*Pavol Fajnor, *Tatiana Liptáková, *Viera Zatkalíková,

*University of Žilina, Faculty of Mechanical Engineering, Department of Materials Engineering,
Univerzitná 1, 01026 Žilina, Slovakia, {pavol.fajnor, tatiana.liptakova, viera.zatkalikova}@fstroj.uniza.sk

Abstract. The subject of this work is to study the surface treatment effect on the resistance of AISI 316Ti stainless steel to pitting corrosion. The tested specimens had ground surfaces and blasted surfaces with and without chemical treatment. The corrosion tests are carried out by electrochemical impedance spectroscopy. According to the results the surface treatment has a significant influence on the resistance of the tested material to pitting.

Keywords: AISI 316Ti stainless steel, ground surface, blasted surface, electrochemical impedance spectroscopy, redox potential

1. Introduction

The aim of this work is to study the effect of surface treatment of AISI 316Ti stainless steel on pitting corrosion resistance in solutions with different value of redox potential. Statistical data classify pitting corrosion in terms of frequency caused emergencies in different industries to the third place in the overall corrosion and corrosion cracking. The attack of pitting corrosion affects only a small fraction of the surface but it penetrates into the depth of the material and significantly reduces the effective cross-section components or changes properties of equipment. In practice this kind of corrosion often causes collapses and large economic and environmental damages [1]. In practice, blasting by metallic and non-metallic particles, grinding or cutting operations are used for surface treatment of stainless steel. It is necessary to realize all mechanical treatments to avoid unacceptable oxidation, excessive roughness of surface, contamination, especially by metallic materials with different potential. In many cases, it is acceptable to combine mechanical treatment with chemical treatment (grinding, blasting, pickling) [2]. The experimental solutions were 5% NaCl and 4.6% FeCl₃. Testing solution contain the same amount of chlorides per dm⁻³ (3.032 Cl⁻ mol. dm⁻³). In this aspect, these solutions have the same concentration of the aggressive ions, but the redox potentials of the solutions is different.

2. Experimental material

The AISI 316Ti austenitic Cr-Ni-Mo stainless steel stabilized by Ti was used as an experimental material (STN 41 7348). The chemical composition is shown in Table 1.

Due to molybdenum additives, AISI 316Ti stainless steel has good plasticity and high resistance against acids and deep local corrosion. It is a non-ferromagnetic steel, with higher yield stress and strength. After welding of thin plate heat treatment is not necessary, because the steel is stabilized by Ti. All methods of arc-welding are possible to be used for this steel except gas-welding [3].

Content element [wt %]	Cr	Ni	Mo	Mn	N	Fe
	16.5	10.6	2.12	1.69	0.012	R E S T
	Ti	C	Si	P	S	
	0.41	0.04	0.43	0.026	0.002	

Tab.1. Chemical composition of AISI 316Ti stainless steel.

2.1 Metallography of experimental material

The specimens obtained from the middle of the plate (transverse and longitudinal section) are used for microstructural analysis of the experimental material (Fig. 1.). Preparation of metallographic specimens includes sample preparation, grinding, polishing and etching [3].

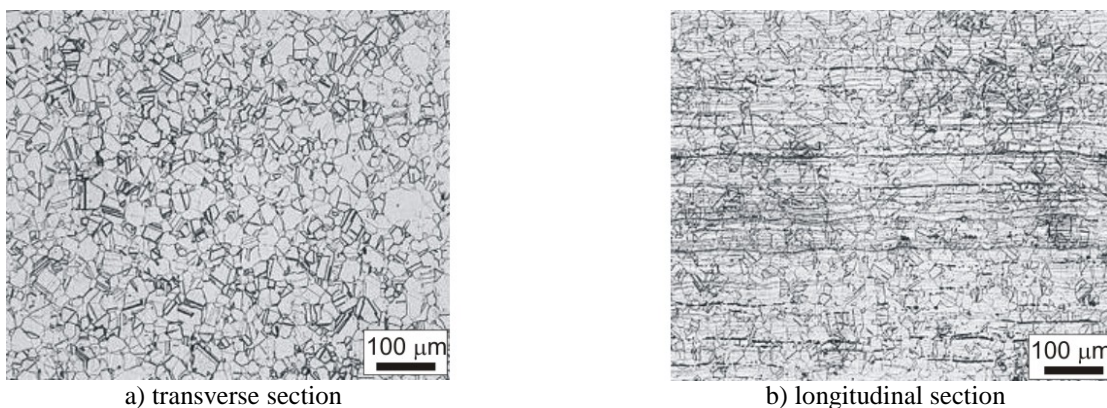


Fig. 1. AISI 316Ti stainless steel microstructure, etch. 10 ml HNO₃ + 30 ml HCl + 30 ml glycerine

The microstructure of the steel is created by polyedric grains of austenite with deformation and annealing twins formed during rolling and annealing. The significant lining is caused by rolling. Sharp coarse particles of a cuboid shape can be observed in the microstructure too. AISI 316Ti stainless steel is stabilized by Ti (0.41 %) and also some content of Mo (2.12 %) tends to enter into carbides of Ti. There are the carbides of the type (Ti, Mo)C [4].

2.2 Surface treatment of specimens

The experimentally tested surfaces were mechanically and chemically modified. First set of specimens was mechanical treatment consisted of grinding by SiC paper with granularity of 320 in transverse section and by SiC paper with granularity of 500 in longitudinal section (Fig. 2). The second set of specimens was blasted with nonmetallic sharpness particles - Almandine (almandine is sharpness natural garnet). The chemical treatment consists of pickling in both of sets.

Pickling parameters: composition of solution - 220 ml of 65% HNO₃ + 22 ml of 40% HF + 758 ml of distilled H₂O, time of 30 min, temperature of 21 ± 1 °C.

Blasting parameters: pressure - 0.4 MPa, jet distance from surface - 220 mm, mean grain size of almandine - 0.15 mm,

The sets of specimen were divided into four groups:

G - ground specimen, GP - ground and pickling specimen, BA - almandine blasted, BAP - almandine blasted and pickling specimen.

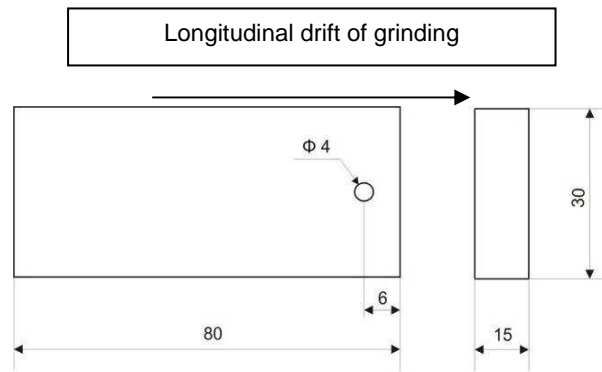


Fig. 2. Specimen shape for experiment

3. Electrochemical impedance spectroscopy

The electrochemical tests are performed by using the electrochemical impedance spectroscopy (EIS) in solutions of 5% NaCl (redox potential by DIN 38404 is 247 mV_H, pH - 7.27) and 4.6% FeCl₃ (redox potential by DIN 38404 is 526 mV_H, pH - 1.20) at laboratory temperatures (21 ± 1 °C). This method allows establishing the value of polarization resistance of less conductive corrosion systems, for example when a passive layer with good adhesion is created on the metal surface. The electrochemical experiments were performed in a conventional three-electrode cell system with a calomel reference electrode (SCE) and a platinum auxiliary electrode (Pt) using Voltalab corrosion measuring system with PGZ 100 measuring unit. The scheme of circuit connection and measuring principle are described in detail in [5] and measurement conditions are in [6].

Results of the electrochemical impedance spectroscopy are Nyquist diagrams in the coordinates of the imaginary and real components of impedance (Figs. 3, 4). The resistance of electrical components and phase shift versus voltage passing alternating electric current of the frequency we call impedance. Nyquist diagrams analysis characterizes the material resistance to influence of surrounding environment. Diameter of determined semicircle represents the value of material resistance.

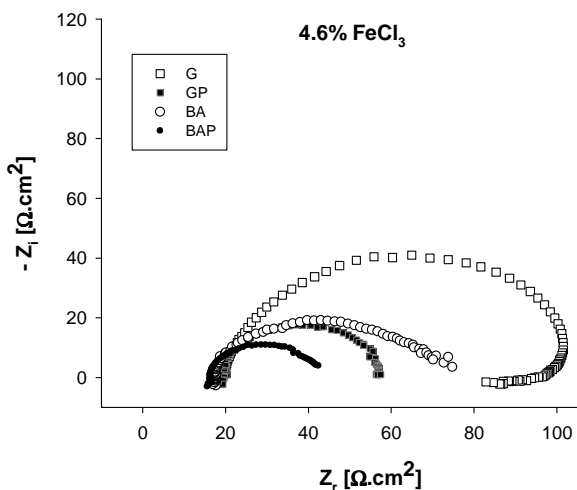


Fig. 3. Nyquist diagram of AISI 316 Ti in 4.6% FeCl₃ solution

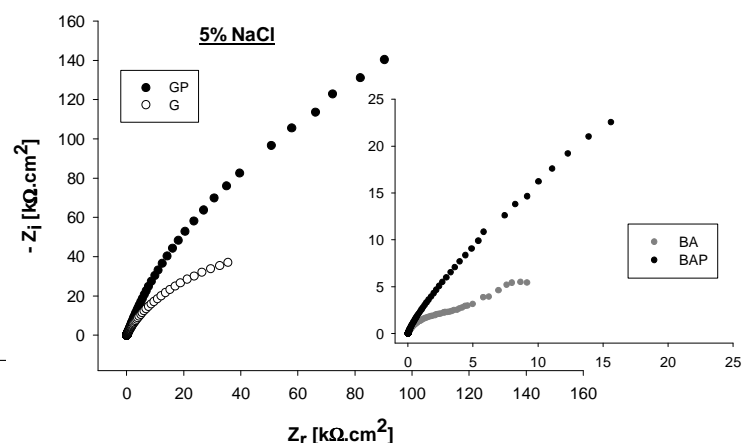


Fig. 4. Nyquist diagram of AISI 316 Ti in 5% NaCl solution

The polarization resistance (R_p) is an electrochemical property characterizing the material resistance to polarization in the experimental environment. The higher value of polarization resistance R_p represents better corrosion resistance of the material in corrosion environment.

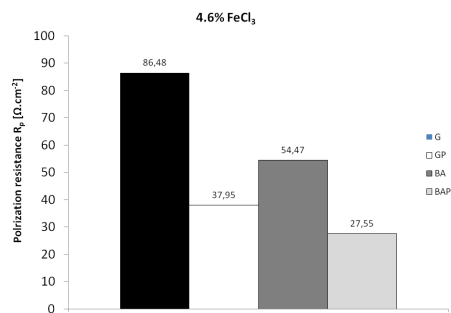


Fig. 5. Polarization resistance of AISI 316 Ti in 4.6% FeCl₃ solution

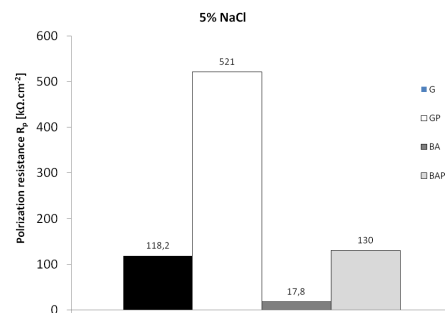


Fig. 6. Polarization resistance of AISI 316 Ti in 5% NaCl solution

4. Conclusion

- The mechanical treated specimens are more corrosion resistant (higher value of polarization resistance R_p) in solution with a *higher redox potential* (4.6% FeCl₃). Ground specimens - 86.48 $\Omega \cdot \text{cm}^2$ and blasted specimens - 54.47 $\Omega \cdot \text{cm}^2$.
- In the opposite the chemical treated specimen are more resistant in solution with a *lower redox potential* (5% NaCl). Ground + pickled specimens - 521 $\text{k}\Omega \cdot \text{cm}^2$ and blasted + pickled - 130 $\text{k}\Omega \cdot \text{cm}^2$.
- Values of polarization resistance of the specimens tested in the chosen solutions are different actually in the order (Fig. 5 and 6). It means that the different surface treatment reacts very sensitive on the solution properties (differences in the redox potential value).
- According to our results the surface treatment of the material with the same chemical composition significantly affects corrosion resistance.
- The resistance to pitting corrosion of AISI 316Ti stainless steel with diverse surface treatment in solutions with different redox potential is various, although in both solutions was the same concentration of chloride ions. This fact confirms that the mechanism of corrosion process of the same material with various treated surface is different in the same chemical composition environment too.
- The choice of the surface treatment follows the character of environment in which the article should be applied.

Acknowledgement

This research was supported partially by the grant VEGA grant No. 1/0603/08 and RAILLCOT, ITMS Code 26220220011 V. Authors gratefully acknowledge this support.

References

- [1] LIPTÁKOVÁ, T.: *Bodová korózia nehrdzavejúcich ocelí*. – EDIS ŽU, 2009, ISBN 978-80-554-0083-9.
- [2] PRAŽÁK, M.: *Koroze a ochrana kovů*. – In.: Medzinárodná konferencia RVHP, Varna, 1985.
- [3] LIPTÁKOVÁ, T., ZATKALÍKOVÁ, V.: *The variability of chemical composition of the AISI 316Ti and pitting*, Transactions of FAMENA, XXXIII - 1, Croatia, Zagreb, 2009.
- [4] PARDO, A., MERINO, M.C., COY, A.E., VIEJO, F., CARBONERAS, M., ARRABAL, R.: *Influence of Ti, C and N concentration on the intergranular corrosion behaviour of AISI 316Ti and 321 stainless steels*, Acta Materialia, Vol. 55, 2007, ISSN: 1359-6454.
- [5] ŠKUBLOVÁ, L., HADZIMA, B., BORBÁS, L., VITOSOVÁ, M.: *The influence of temperature on corrosion properties of titanium and stainless steel biomaterials*, Materials engineering, Vol. 15, Issue 4, 2008, ISSN: 1335-0803
- [6] FAJNOR, P. - LIPTÁKOVÁ, T. - KONSTANTOVÁ, V.: *Influence of AISI 316Ti stainless steel surface treatment on pitting corrosion in various solution*, Materials Engineering, Vol. 17., No. 3/2010, 2010, ISSN 1335-0803
- [7] DIN 38404: 1. April 1995. German standard methods for the examination of water, waste water and sludge - Physical and physicochemical parameters (group C) - Determination of calcite saturation of water (C 10).



The Influence Tantalum Placed Foil between Two Steel Plates on the Weld Penetration Shape Formed during Welding Laser

*Marta Garbala

*University of Technology, Centre of Laser Technology, Aleja Tysiąclecia Państwa Polskiego 7,
25-314 Kielce, Poland, martaaa7@o2.pl

Abstract. The experimental analysis of the influence tantalum foil placed between two steel plates on the weld penetration shape formed during welding laser for stainless steel X5CrNi1810 is presented. The aim of the research was to determine the influence foil onto the process and to elaborate analytical models. The experiment was carried out on TRUMPF TLF 6000 Turbo laser at Centre of Laser Technology of Metals (joint Kielce University of Technology and Polish Academy of Sciences unit) in Kielce (Poland). They were done two experiments, on variable of the rate of laser beam feed. In the first experiment specimen was melt with tantalum foil of 0.7 [mm] thickness, while in the second experiment without her. It has been found that tantalum foil has a significant influence on the course of the process, weld penetration shape changes slightly.

Keywords: Laser welding; stainless steel; tantalum foil, weld penetration

1. Introduction

There is a lot of information about laser welding and generally about laser material processing in scientific literature. Much information may be found in works and publications such authors as: Steen, Beyer, Myśliwiec, Szymański or Hoffman. Beyer was first who in his paper: “Schweißen mit Laser” described the method of determination of keyhole shape by means of so called trace experiment [1]. This method consists in analysis of melted areas of trace material, placed in the base material. In these experiments thin tantalum foil was placed between two steel plates which was welded then [2]. Because the melting point of tantalum (3269 K) is close to temperature of boiling of stainless steel (3133 K) [2] we can accept, that the tantalum foil undergoes melting only in the area where the steel meets the temperature of boiling.

The aim of this work was examining whether tantalum foil between two steel plates has influence on weld penetration shape formed during laser welding.

2. Description of the Experiment

The experiments were carried out by laser TRUMPF TLF 6000 Turbo at Centre of Laser Technology of Metals (joint Kielce University of Technology and Polish Academy of Sciences unit) in Kielce (Poland). In this type of laser, the active medium is carbon dioxide (CO₂). The laser can work in a continuous mode or in a pulse mode. Its maximal power is 6 kW and the wavelength 10,6 μm. The material used in the experimental researches was stainless steel X5CrNi1810. It is commonly used stainless steel containing 18 % of chromium and 9 % of nickel [3].

In the first experiment tantalum foil was placed between two steel plates and welded. Steel plates were prepared from flat steel sheet, 10 mm thick “Fig. 1.”. That plates were milled on wedge shape, and then tantalum foil about 0.7 mm thick was placed obliquely “Fig. 2.”.

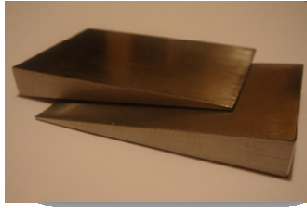


Fig. 1. Steel plates on wedge shape.



Fig. 2. Tantalum foil placed between two steel plates.

After specimen's arrangement, five melted of different rate of laser beam feed was done. They were: 1500, 1200, 1000, 900, 700 mm/min. Average power carried out 6250 [W]. The working gas was helium and his expense carried out 10 l/min. Focal position was on surface of the metal plate. After this specimen was cut in the way which gave the greatest quantity of measurements.

After cutting received 11 specimens on which measurements could be done and obtained information about weld penetration shape section on different depths. Then the specimens were subjected to milled and etched in 50% saline acid.

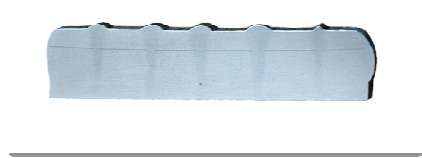


Fig. 4. The example of measured specimen.

In the second experiment were done series weld penetration on flat steel sheet 10 [mm] thick without using tantalum foil. Parameters have not changed. Average laser power carried out 6250 [W], the working gas was helium (expense 10 l/min), focal position was on surface of the metal plate and the rate of laser beam feed 1500,1200,1000,900 as well as 700 mm/min.

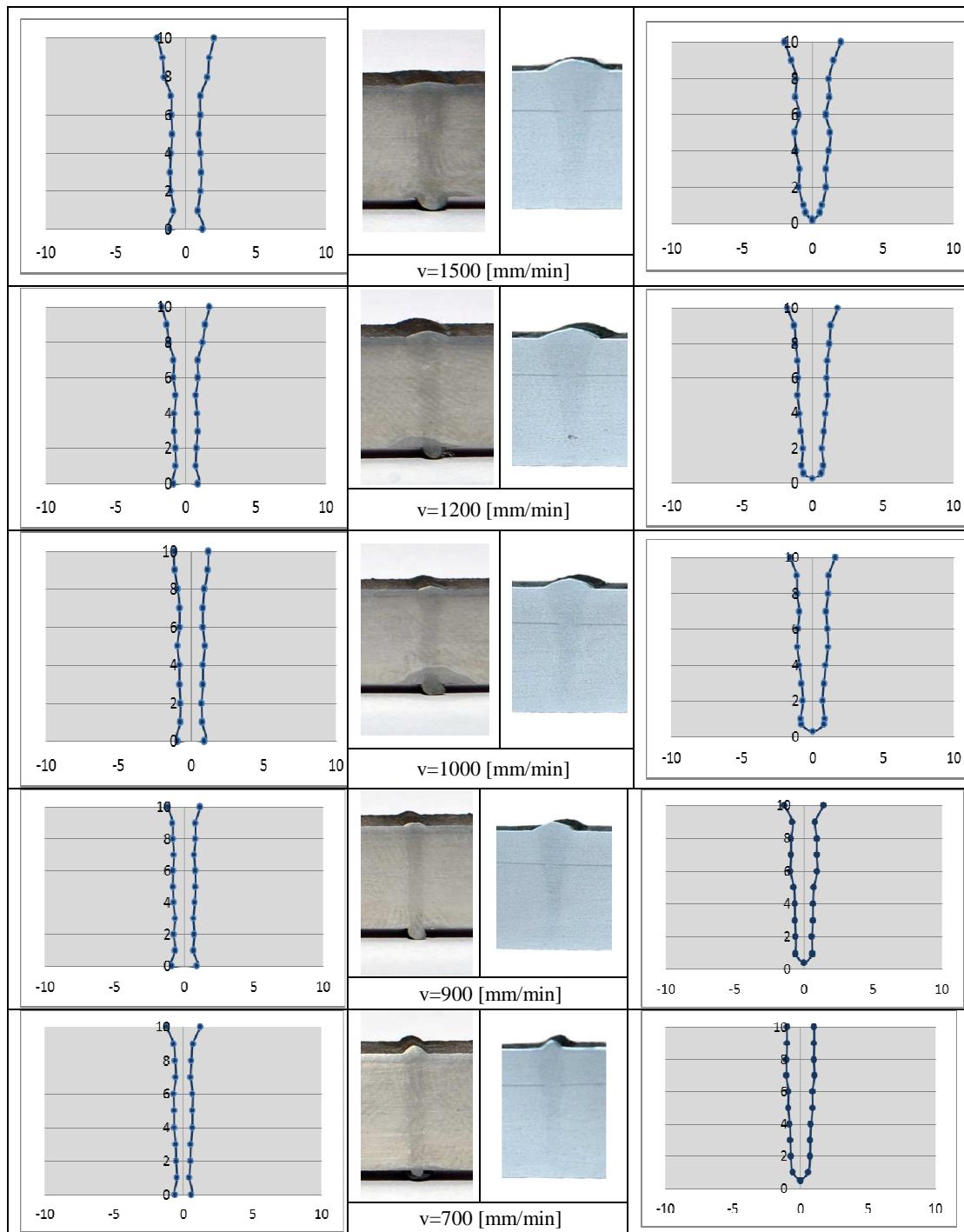
Specimen submits the following processings. She was milled on wedge shape, polished and etched in saline acid in order to obtain visible melt shape.



Fig. 5. Specimen with visible weld penetration shapes.

2. Results Analysis

The next step was carrying out measurements under optical microscope, realization of graphs, as well as the comparison in results. Measurements did for specimen, in which tantalum foil was placed on depth 2.8 mm. It below presents graphs of the weld penetration for the next rate of laser beam feed "Tab. 1."



Tab. 1. Graphs and photos present the weld penetration shape which was obtained during two experiments (on the left with tantalum foil, on the right without it).

3. Conclusion

How to be visible on place above graphs and photos width weld penetration does not submit larger changes. They have hesitated from hundredth to thousandth millimeter. If however it concerns about weld penetration depth to be visible, that to specimen without tantalum foil follow penetrate laser beam throughout, however to specimen with tantalum can observe, that together with growth rate of laser beam feed the weld penetration depth grows up. This is the most probably bring about with this, that tantalum foil temporarily blocks laser beam welding causing, that the laser power was accumulated in grounds of placed foil before her melting will follow.

To sum up, putting tantalum foil between two steel plates in order to research the shape keyhole, do not have real influence on changes in weld penetration shapes. The differences noticed in the measurements are so small that are still in the limits of error.

This paper was treated with support of European Union, project name: Program rozwoju potencjału dydaktycznego Politechniki Świętokrzyskiej: Kształcenie w Nowoczesnych Obszarach Techniki, Project agreement: UDA-POKL.04.01.01-00-395/09-00.

References

- [1] BEYER E. *Schweißen mit Laser*, Springer – Verlag, Berlin.
- [2] STEEN W. M. *Laser Material Processing*, Springer – Verlag, Berlin 1991.
- [3] SZYMAŃSKI, Z., HOFFMAN J. *Fizyka spawania laserowego*, Instytut Podstawowych Problemów Techniki PAN, Warszawa 2004.



Determination of Critical Velocity in Cold Spray Coating by Finite Element Analysis

*Ramin Ghelichi, *Mario Guagliano,

*Politecnico di Milano, Department of Mechanical Engineering, via G la Masa,1, Milan, Italy,
{ramin.ghelichi, mario.guagliano}@mail.polimi.it

Abstract. In cold spray coating, bonding happens when the velocity of the particles exceeds a certain so called 'critical velocity'(CV). The challenging problem of detecting the CV using the discrete output of numerical simulation has been solved applying Fourier transformation and the second derivative of the physical parameters in Sobolev space. The results are compared with the other numerical models and the experimental results available in the literature.

Keywords: Cold spray coating, critical velocity, FEM, Fourier transform

1. Introduction

Cold spraying is an emerging coating process in which in contrast to the well-known thermal spray processes such as flame, arc, and plasma spraying, the powders does not melt before impacting the substrate [1]. Bonding of particles in cold gas spraying is presumed to be the result of extensive plastic deformation and related phenomena at the interface [2]. It is well recognized that particle velocity prior to impact is a key parameter in cold spray process [3]. It determines what phenomenon occurs upon the impact of spray particles, whether it would be the deposition of the particle or the erosion of the substrate. In this regard for a given material; the critical velocity (CV) is the velocity at which the transition from erosion of the substrate to deposition of the particle takes place. Experimental investigations also reveal that successful bonding is achieved only above this certain amount of particle velocity, the value of which is associated with temperature and thermo-mechanical properties of the sprayed material [4, 5]. Adiabatic shear instability and the resultant plastic flow localization are the phenomena that are believed to play the major role in the particle/substrate bonding during cold spray process [4, 6]. Commonly the shear instability appears as a singularity in the parameters such as equivalent plastic strain while defined as a function of time. Finding the minimum velocity at which the shear instability occurs using these discrete data is much tricky and challenging due to the discontinuity of the results. In the present study the shear instability is acknowledged using a far more precise criterion based on a very sensitive method for shear instability detection.

2. Numerical Approach

A 3D full model of particle impact on substrate has been simulated using ABAQUS/Explicit with Lagrangian formulation. Different partitions shown in Fig. 1 are created to obtain an optimized mesh distribution in order to reduce the number of elements in non-impact zones. One of the demanding aspects of high velocity impact simulations is the wave speed spread through the elements and the fluctuations of this wave which remains in the model preventing the possibility of having stable results. The half infinite bottom-up elements have been used in the boundaries of the model in order to damp the wave fluctuations. Different analyses have been performed by varying the velocity of the particles in the range of 200-1000 m/s. The particle temperature is set to 150 °C

and the temperature of the substrate is the ambient temperature both chosen according to the experimental setup in [10].

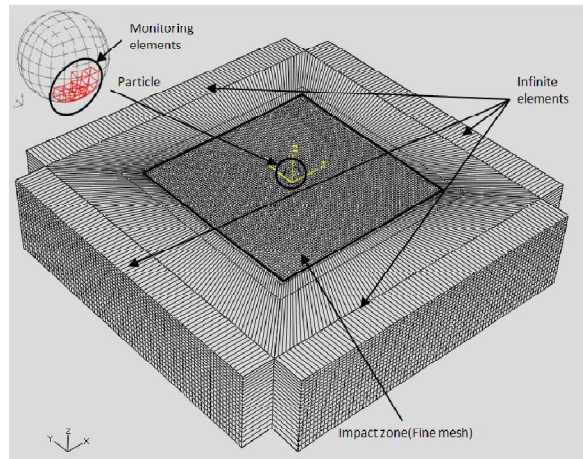


Fig. 1: 3D model of FEM analysis in Abaqus

3. Critical Velocity Detection Procedure

The algorithm developed for finding CV requires performing a series of numerical tests in Abaqus and evaluating the second derivative of different physical parameters which are practically affected by shear instability in the Johnson-Cook material model. In this regard, Python [7] is used to develop a subroutine to be implemented in Abaqus for performing the numerical tests automatically. The developed algorithm is described as following:

1. Based on the experimental results, no material bounding occurs in cold spray coating with velocities less than 200 m/s and almost all the tested materials bound with a velocity lower than 1000 m/s. Thus, the first step has been set to perform 8 sets of analysis with different velocities in the practical range of 200-1000 m/s, in order to obtain an approximation of the CV for the considered material types.
2. Then for each parameter, the maximum jump in second derivative in the Sobolev space based on Fourier transform has been located. Having performed this step, the CV for the considered shot and substrate material type is achieved in the range of 100 (due to the step of velocity change set to 100 m/s). In order to reach a better judgment of the material behavior, the evaluation is performed for different parameters such as equivalent plastic strain (PEEQ), equivalent Von-Mises stress, temperature of the particle and equivalent plastic strain rate. These properties all appear in the Johnson-Cook [8] material model.
3. In the view of the results obtained in previous step, another series of analysis are performed using a smaller pace in order to obtain a narrower range of the CV approximation. For example, if in the second step the CV is found to be between 500m/s and 600 m/s, in this level, the analysis is performed changing the particle velocities from 500m/s to 600m/s with the pace of 10m/s.
4. The 3rd step is repeated over to obtain an accurate enough evaluation of the CV.
5. After having detected the CV, the whole process should be reproduced with three different sizes of the mesh in order to assess the linear variation trend and then apply the zero element size extrapolating method and eventually obtain the mesh size independent CV.

Fig. 2 shows the flowchart of the CV detection algorithm based on the second derivative of the physical parameters. It is worthy to note that due to many numerical limitations such as the minimum number of increments in Abaqus and analysis time and also the numerical sensitivity of the chosen procedure, it is hardly practical to obtain an absolute value for the CV. Thus the results will be stated in a delicate range of CV.

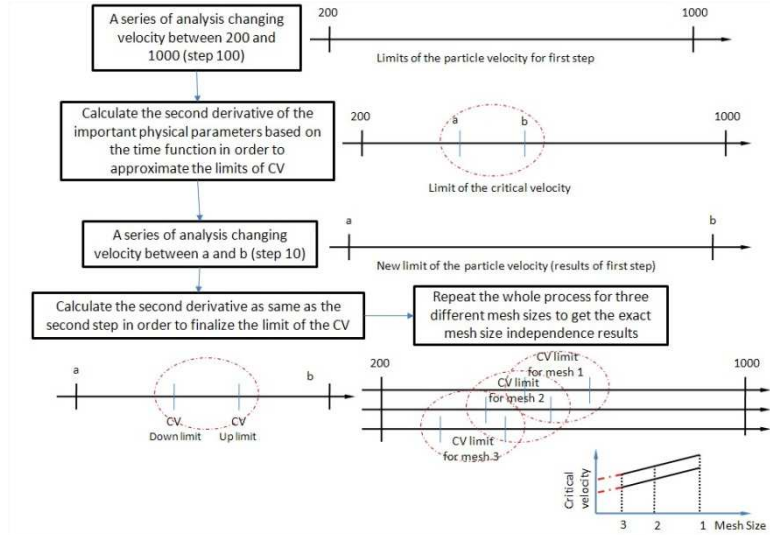


Fig. 2: Flowchart of CV calculation algorithm

4. Results and Discussion

Compression ratio is defined as a parameter related to the particle geometry to keep track of the particle deformation during the impact process. It is calculated based on Eq. 1:

$$R_p = \frac{D-h_p}{D} \times 100 \quad (1)$$

In which R_p is the compression ratio, h_p is the smallest diameter after deformation and D is the original particle diameter. Fig. 3 shows the compression ratio of the modeled particle in different velocities for two Cu-Cu. The element sizes are kept equal to 0.4 mm in all presented graphs. In Fig 7 which represents the deformation evolution of the particle for Cu-Cu with different velocities at 0.5ns time intervals of the process. Fig 4 represents the effect of velocity on the deformation of particle after impact on substrate

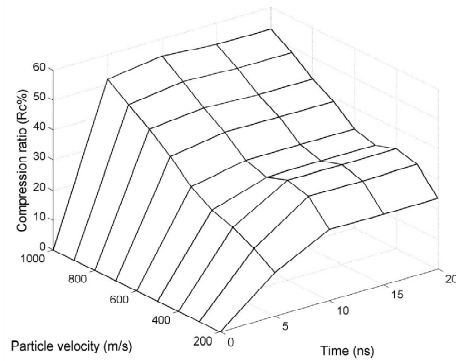


Fig. 3: Rc as a function of time and particle velocity after impact for different materials

As discussed in previous sections and also confirmed by the literature [4, 9], the results of the finite element model does not converge by decreasing the element size. Thus in order to find the final value independent from element size, the “Zero Element” method has been used.



Fig. 4: Deformation of the particle after 0.5 and 1 ns considering different particle velocities

5. Comparison with Experimental and Numerical Simulations

The obtained numerical results are compared with the experimental data available in the literature and also with other references which have used numerical finite element approach for CV calculation. In the present study, the CV has been calculated considering the same process condition used in the experimental study of Raletz et al. [10]. In order to validate the comparison of the obtained results with the experimental results of Raletz et al. [10]; in this work, the Kinetic 3000M system from CGT GmbH has been used in order to perform the cold spray process for three different materials for the particle and substrate. Table 1 shows the final calculated results for Copper on Copper. This table shows also the results obtained from other numerical approaches developed in other references. The final obtained results by the proposed method in this article show a very good correspondence with the experimental results in [10].

			Experimental	Numerical results in literature		
Powder	Substrate	Calculated	Raletz[10] CV (m/s)	Grujicic[6] CV (m/s)	Wen-Ya Li[9] CV (m/s)	SL[6] CV (m/s)
Cu	Cu	400-450	422 ±45	575-585	298-356	571

Tab 1: Final calculated results for CV

6. Conclusion

A 3D finite element model is developed in order to calculate the CV in the cold spray coating process. Abaqus 6.9-1 Explicit has been used in order to perform the numerical analysis, and Python 2.4-1 is used for elaborating Abaqus discrete outputs and performing a series of numerical tests. Regarding the mesh convergence, "Zero Element" method has been used to find the element size independent results. The obtained results from the software are converted to Fourier parameters in order to calculate the second derivative of the physical parameters in Sobolev space. A difference of 12 to 20% is observed between previous numerical simulations and Raletz experimental work [10], whereas the presented results in this article fall in the experimental measures range and show a good correspondence with them.

References

- [1] CHAMPAGNE, V.: The cold spray materials deposition process, Fundamentals and application, Woodhead Publishing (2007)
- [2] McCUNE, R., DONLON, W., CARTWRIGHT, E., PAPYRIN, A., RYBICKI, E., SHADLEY, J.: Characterization of copper and steel coatings made by the cold-gas-dynamic spray method, ASM International, p. 397-403,(1996)
- [3] PAPYRIN, A.: The development of the cold spray process, Cold Spray Technology(CST), USA
- [4] ASSADI, H., GAURTNER, F., STOLTENHO, T., KREYE, H.: Bonding mechanism in cold gas spraying, Acta Materialia 51,,p.4379-4394(2003)
- [5] ALKIMOV, A., KOSAREV, V., PAPYRIN, A.: A Method of Cold Gas Dynamic Deposition, Dokl. Akad. Nauk SSSR, 318(5), p.1062- 1065,(1990)
- [6] GRUJICIC, M., ZHAO, C., DEROSSET, W., HELFRITCH, D.: Adiabatic shear instability based mechanism for particles/substrate bonding in the cold-gas dynamic-spray process, Materials and Design 25, 681_688, (2004)
- [7] Python documentation, <http://docs.python.org/>
- [8] JOHNSON, G., COOK, W.: Fracture Characteristics of three metals subjected to various strains, strain rates, temperatures and pressures", Eng. Frac. Mech., Vol. 21, 1, P. 31-48, (1985)
- [9] LI, C., LI, W., LIAO, H.: Examination of the Critical Velocity for Deposition of Particles in Cold Spraying, Journal of Thermal Spray Technology Volume 15(2), p.212-222,(2006)
- [10] RALETZ, F., VARDELLE, M., EZO'O, G.: Critical particle velocity under cold spray conditions, surface & coating Technology 201, 1942-1947, (2006)



Influence Shielding Gases on Weld Penetration

*Anton Hopko, *Jozef Meško, *Radoslav Koňar

*University of Žilina, Faculty of Mechanical Engineering, Department of Technological Engineering,
Univerzitná 1, 01026 Žilina, Slovakia, {anton.hopko, jozef.mesko, radoslav.konar}@fstroj.uniza.sk

Abstract. This article discusses the influence of shielding gases on penetration in welded joints. The primary gases used for electric welding and cutting are argon, helium, hydrogen, nitrogen, oxygen and carbon dioxide. The composition of the gas can and should be tailored to meet the process, material, and application requirements. Shielding gases are used in either a pure form or in blends of varying components. Therefore, the selection of a gas or gas mixture can become quite complex due to the many combinations available. Argon, helium, and their mixtures are used for nonferrous metals as well as stainless and alloy steels. In addition to its shielding function, each gas or gas blend has unique physical properties that can have a major effect on welding speed, penetration, mechanical properties, weld appearance and shape, fume generation, weld color, and arc stability.

Keywords: welding, shielding gas, GMAW

1. Introduction

The gas metal arc welding (GMAW) process has been dominating the welding construction world for several years now. This fact is related to its high flexibility, which allows the welding of a great variety of materials and thickness, and to its considerable potential for automation and robotization. During any welding process, oxygen and other atmospheric gas can react with the molten metal, causing defects that weaken the weld. The primary function of a shielding gas is to protect the molten weld metal from atmospheric contamination [1, 3].

2. Shielding Gases

2.1. Argon

Argon is an inert gas which is used both singularly and in combination with other gases to achieve desired arc characteristics for the welding of both ferrous and non-ferrous metals. Almost all welding processes can use argon or mixtures of argon to achieve good weldability, mechanical properties, arc characteristics and productivity. Argon is used singularly on non-ferrous materials such as aluminum, nickel based alloys, copper alloys, and reactive metals which include zirconium, titanium, and tantalum. Argon provides excellent spray arc welding stability, penetration and bead shape on these materials. Some short circuiting arc welding of thin materials is also practiced [4]. When using ferrous materials, argon is usually mixed with other gases such as oxygen, helium, hydrogen, carbon dioxide and/or nitrogen. The low ionization potential of argon creates an excellent current path and superior arc stability. Argon produces a constricted arc column at a high current density which causes the arc energy to be concentrated in a small area. The result is a deep penetration profile having a distinct "finger like" shape [4].

2.2. Carbon Dioxide

Pure carbon dioxide is not an inert gas, because the heat of the arc breaks down the CO₂ into carbon monoxide and free oxygen. This oxygen will combine with elements transferring across the

arc to form oxides which are released from the weld puddle in the form of slag and scale. Although CO₂ is an active gas and produces an oxidizing effect, sound welds can be consistently and easily achieved which are free of porosity and defects. Carbon dioxide is widely used for the welding of steel. Its popularity is due to the common availability and quality weld performance as well as its low cost and simple installation. It should be mentioned that low cost per unit of gas does not automatically translate to lower cost per foot of weld and is greatly dependent on the welding application. Factors such as lower deposition efficiency for CO₂ caused by spatter loss, influence the final weld cost [4].

Carbon dioxide will not spray transfer; therefore, the arc performance is restricted to short circuiting and globular transfer. The advantage of CO₂ is fast welding speeds and deep penetration. The major drawbacks of CO₂ are a harsh globular transfer and high weld spatter levels. The weld surface resulting from pure CO₂ shielding is usually heavily oxidized. A welding wire having higher amounts of deoxidizing elements is sometimes needed to compensate for the reactive nature of the gas. Overall, good mechanical properties can be achieved with CO₂. Argon is often mixed with CO₂ to off-set pure CO₂ performance characteristics. If impact properties have to be maximized, a CO₂ + argon mixture is recommended [4].

2.3. Argon - Carbon Dioxide Mixtures

The argon-carbon dioxide mixtures are mainly used on carbon and low alloy steels and limited application on stainless steels. The argon additions to CO₂ decrease the spatter levels usually experienced with pure CO₂ mixtures. Small CO₂ additions to argon produce the same spray arc characteristics as small additions. The difference lies mostly in the higher spray arc transition currents of argon - CO₂ mixtures. In GMAW welding with CO₂ additions, a slightly higher current level must be reached in order to establish and maintain stable spray transfer of metal across the arc. Oxygen additions reduce the spray transfer transition current. Above approximately 20% CO₂ spray transfer becomes unstable and random short circuiting and globular transfer occurs.

This mixture range has been used for various narrow gap, out-of-position sheet metal and high speed GMAW applications. Most applications are on carbon and low alloy steels. By mixing the CO₂ within this range, maximum productivity on thin gauge materials can be achieved. This is done by minimizing burn through potential while at the same time maximizing deposition rates and travel speeds. The lower CO₂ percentages also improve deposition efficiency by lowering spatter loss [4].

3. Influence of Shielding Gases on Weld Process

The arc energy is less uniformly dispersed in an Ar arc than in a He arc because of the lower thermal conductivity of Ar. Consequently, the Ar arc plasma has a very high energy core and an outer mantle of lesser thermal energy. This helps produce a stable, axial transfer of metal droplets through an Ar arc plasma. The resultant weld transverse cross section is often characterized by a papillary- (nipple-) type penetration pattern. With pure He shielding, on the other hand, a broad, parabolic-type penetration is often observed [2].

With ferrous metals, however, He shielding may produce spatter and Ar shielding may cause undercutting at the fusion lines. Adding O₂ (about 3%) or CO₂ (about 9%) to Ar reduces the problems. Carbon and low-alloy steels are often welded with CO₂ as the shielding gas, the advantages being higher welding speed, greater penetration, and lower cost. Since CO₂ shielding produces a high level of spatter, a relatively low voltage is used to maintain a short buried arc to minimize spatter; that is, the electrode tip is actually below the workpiece surface. Selections of a shielding gas or blend must be based on a knowledge of the gases available, their applications, and the overall effect they have on the welding process [2].

4. Influence Shielding Gases on Welding Steel

For the experiment we used as a base material steel plate S355J2G3 with a thickness of 15 mm. Macrostructure of welded joints are shown in Fig. 1, Fig. 2 and Fig. 3. Average welding parameters and types of shielding gases are listed in Tab. 1. Dimensions of the welds are listed in Tab. 2. For made weld joints, we used short-circuit mode and pulse mode.

For the experiment we used three types of shielding gases:

- Carbon dioxide,
- Argon – Carbon dioxide mixture,
- Argon.

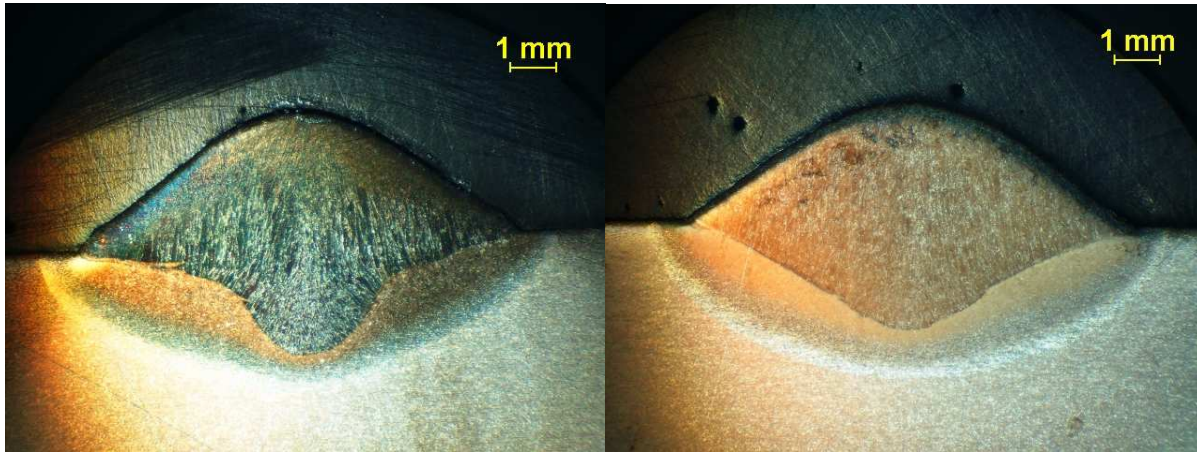


Fig. 1. Macrostructure of weld using gas 18% CO₂ + 82% Argon; left Pulsed transfer, right Dip transfer.

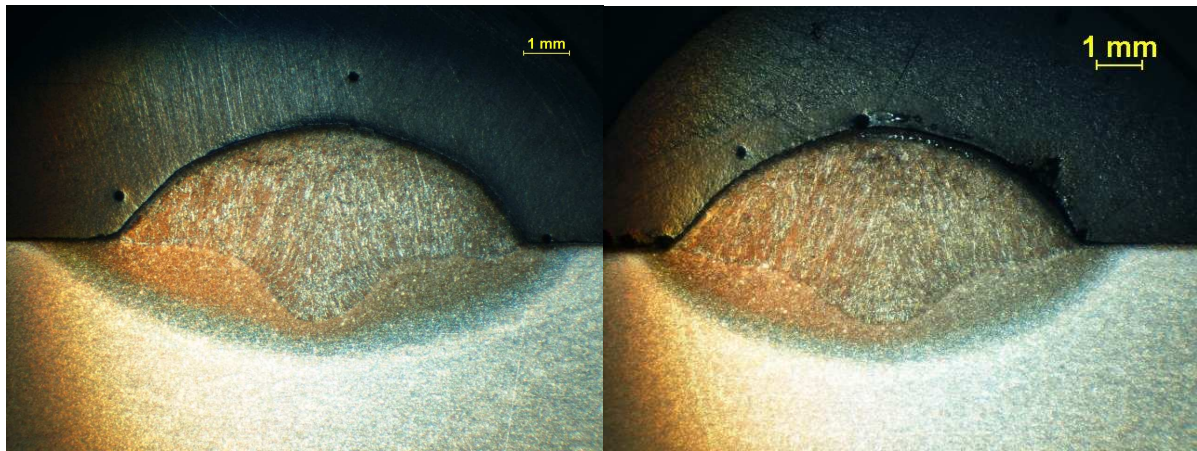


Fig. 2. Macrostructure of weld using gas 99,996% Argon; left Pulsed transfer, right Dip transfer.

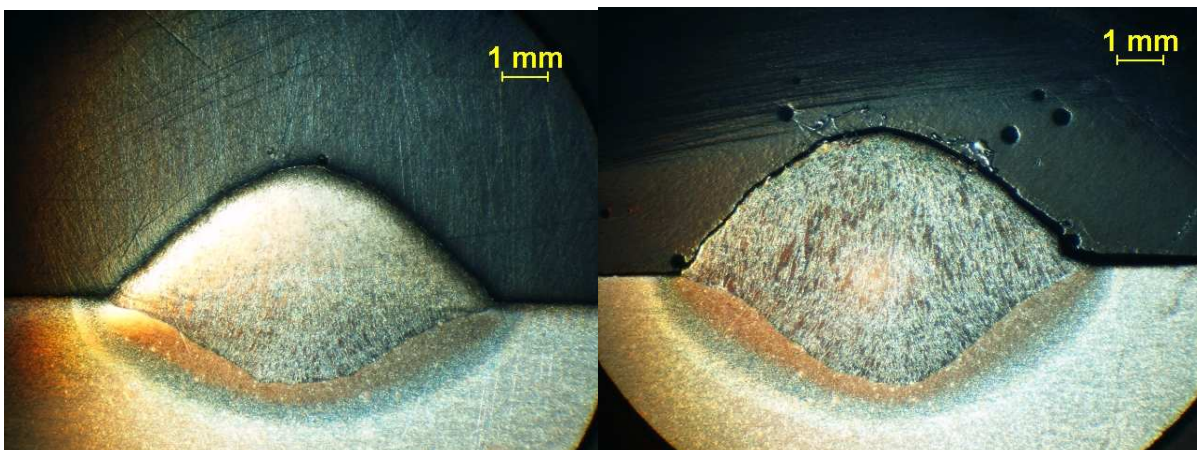


Fig. 3. Macrostructure of weld using gas CO₂; left Pulsed transfer, right Dip transfer.

	Welding parameters					
	Pulsed transfer			Dip transfer		
Shielding gas	I [A]	U [V]	v [m/min]	I [A]	U [V]	v [m/min]
CO ₂	152	22,7	0,8	184	23,2	0,8
18% CO ₂ +82% Argon	161	24,1	0,8	196	22,8	0,8
99,996% Argon	161	24,2	0,8	189	22,8	0,8

Tab. 1. Welding parameters using different types of shielding gases.

Dimension	Dimensions of welds [mm]					
	Fig.1. left	Fig.1. right	Fig.2. left	Fig.2. right	Fig.3. left	Fig.3. right
Height of weld	2,86	2.72	2.55	2.69	2.95	3.05
Width of weld	9,61	9.86	9.04	9.18	8.51	8.89
depth of penetration	2,43	2.25	1.79	1.69	1.87	2.41

Tab. 2. Weld dimensions as shown in Fig.1, Fig.2, Fig.3.

5. Conclusion

We can observed that shielding gas significantly affected the penetration of the weld. Tab. 2 shows the dimensions of weld joints made out during the experiment. When using different types of shielding gases for weld the dimensions vary significantly. For the experiment we used three types of gases. The most appropriate dimensions of the weld was achieve by using shielding gas 18% carbon dioxide + 82% argon.

Acknowledgement

This contribution was created within the project KEGA No. 3/3668/08 and VEGA project No. 1/0186/09. The principal investigator is prof. Ing. Jozef Meško, PhD.

References

- [1] PIRES, I. *Analysis of the influence os shielding gas mixtures on features of MIG/MAG*. MSc thesis, Lisbon Technical University, 1996.
- [2] KOU, S. *Welding metallurgy*. Wiley-interscience, Second edition, USA, ISBN 0-471-43491-4, 2003.
- [3] LARSON, E. N. *Influence of shielding gases on the quality of welds*. 2nd International Symposium on "Orbital welding in High Purity Industries". La Baule France.1998
- [4] Esab handbook. 2011[cit. 2011.3.7] Internet source: http://www.esabna.com/EUWeb/MIG_handbook/592mig4_1.htm



Evolution of the Mechanical Properties in Recycled AlSi9Cu3 Cast Alloy During Age-Hardening

*Lenka Hurtalová, *Eva Tillová

*University of Žilina, Faculty of Mechanical Engineering, Department of Material Engineering, Univerzitná 1, 010 26 Žilina, Slovakia, E-mail: lenka.hurtalova{eva.tilova}@fstroj.uniza.sk

Abstract. The influence of the age-hardening on mechanical properties (strength tensile, impact test and Brinell hardness) was studied. Age-hardening consisted of solution treatment by 515°C with holding time 4 hours, water quenching at 40°C and artificial aging by different temperature 130°C, 150°C, 170°C, 190°C and 210°C with different holding time 2, 4, 8, 16 and 32 hours. Mechanical properties were measured in line with STN EN ISO. Age-hardening leads to changes in microstructure include the spheroidization and coarsening of eutectic silicon, gradual disintegration, shortening and thinning of Fe-rich intermetallic phases, the dissolution of precipitates and the precipitation of finer hardening phase (Al₂Cu) further increase in the hardness and tensile strength in the alloy. Recycled (secondary) AlSi9Cu3 cast alloy uses especially in automotive and aerospace industry.

Keywords: recycled aluminium alloys, age-hardening, mechanical properties

1. Introduction

The alloys of the Al-Si-Cu system have become increasingly important in recent years, mainly in the automotive industry that uses recycled (secondary) aluminium in the form of various motor mounts, engine parts, cylinder heads, pistons and so on [1, 2].

The recycled Al-Si-Cu alloys are extensively used to reduce materials cost compared to the pure alloys. The increase in recycled metal becoming available is a positive trend, as secondary aluminium produced from recycled metal requires only about 2.8 kWh/kg of metal produced while primary aluminium production requires about 45 kWh/kg produced. It is to the aluminium industry's advantage to maximize the amount of recycled metal, for both the energy-savings and the reduction of dependence upon overseas sources. The remelting of recycled metal saves almost 95 % of the energy needed to produce prime aluminium from ore, and, thus, triggers associated reductions in pollution and greenhouse emissions from mining, ore refining, and melting. Increasing the use of recycled metal is also quite important from an ecological standpoint, since producing aluminium by recycling creates only about 5 % as much CO₂ as by primary production [3, 4, 5].

The present study is a part of larger research project, which was conducted to investigate and to provide a better understanding of mechanical properties and microstructure (Si morphology, Fe- and Cu-rich phases) in secondary (recycled) AlSi9Cu3, details of which have already been published [6, 7]. Work is focused on study of the effect of age-hardening on changes of mechanical properties.

2. Experimental work

Mechanical properties of Al-Si alloys are largely dependent upon an appropriate heat treatment technology, prior to use T6 condition. T6 involves solution and aging heat treatment, during which a series of changes in microstructure occur, which then leads to the improvement of strength. These

changes in microstructure include the dissolution of precipitates, the homogenization of the cast structure, such as the minimization of alloying element segregation, the spheroidization and coarsening of eutectic silicon and the precipitation of finer Al_2Cu or Mg_2Si hardening phase. Although the morphology, the amount and the distribution of the precipitates during aging process significantly influence the mechanical properties. From this point of view, the age-hardening is critical in determining the final microstructure and mechanical properties of the alloys. Thus, it is very important to investigate the effects of age-hardening on the alloys [8].

Heat treatment is used to obtain the optimal combination of strength and ductility in casting. It involves: a) solutionizing to thermally prepare the material; b) quenching to retain the maximum concentration of age-hardening constituent (Al_2Cu) in solid solution and c) a combination of artificial and over-ageing to obtain the desired mechanical properties in the casting. Solution treatment performs three roles: homogenization of as-cast structure; dissolution of certain intermetallic phases such as Al_2Cu ; changes the morphology of eutectic Si phase by fragmentation, spheroidization and coarsening, thereby improving mechanical properties, particularly ductility. Most of the recommended heat treatment of alloys that contain copper restricts the solution temperature below the final solidification point in order to avoid the melting of copper-rich phases [9].

Age-hardening heat treatment is most commonly heat treatment process used to obtain the optimal combination of strength and ductility in Al-Si-Cu casting. The precipitation sequence for AlSi9Cu3 alloy is based upon the formation of Al_2Cu based precipitates. The sequence is described as $\alpha_{\text{ss}} \rightarrow \text{GP zones} \rightarrow \theta' \rightarrow \theta$ (Al_2Cu). The sequence begins upon aging when the supersaturated solid solution (α_{ss}) gives way first to small coherent precipitates called GP zones. These particles are invisible in the optical microscope but macroscopically, this change is observed as an increase in the hardness and tensile strength of the alloy. As the process proceeds, the GP zones start to dissolve, and θ' begins to form, which results in a further increase in the hardness and tensile strength in the alloy. Continued aging causes the θ' phase to coarsen and the θ (Al_2Cu) precipitate to appear. The θ phase is completely incoherent with the matrix, has a relatively large size, and has a coarse distribution within the aluminium matrix. Macroscopically, this change is observed as an increase in the ductility and a decrease in the hardness and tensile strength of the alloy [10].

2.1. Experimental material

As an experimental material was used secondary hypoeutectic AlSi9Cu3 alloy, that contains 10.7 % Si, 2.4 % Cu, 0.9 % Fe, 0.27 % Mg and so on. The melt was not modified or refined. AlSi9Cu3 cast alloy has lower corrosion resistance and is suitable for high temperature applications (dynamic exposed casts, where are not so big requirements on mechanical properties) - it means to max. 250 °C. The AlSi9Cu3 alloy has these technological properties: tensile strength ($R_m = 240 - 310$ MPa), offset 0.2 % yield stress ($R_{p0.2} = 140 - 240$ MPa), however the low ductility limits ($A_5 = 0,5 - 3$ %) and hardness HB 80 - 120.

Structure hypoeutectic AlSi9Cu3 cast alloy consists of dendrites α -phase, eutectic and intermetallic Fe- and Cu-rich phases [7, 11, 12]. Experimental cast samples were heat treated by age-hardening. Age hardening consist of solution treatment by 515°C with holding time 4 hours, water quenching at 40°C and artificial aging by different temperature 130°C, 150°C, 170°C, 190°C and 210 °C with different holding time 2, 4, 8, 16 and 32 hours. After age-hardening were samples subjected for mechanical test (strength tensile, impact test and Brinell hardness).

2.2. Experiment

Hardness measurement was performed by a Brinell hardness tester with a load of 62.5 Kp, 2.5 mm diameter ball and a dwell time of 15s. The Brinell hardness value at each state was obtained by an average of at least six measurements. Fig. 1 shows the variation in hardness with aging time 2, 4, 8, 16 and 32 hours at different temperatures. It can be seen that there is an obvious age-hardening

phenomenon for each curve. At the early stage of aging for temperature 130 and 150 °C the hardness increases with aging time until reaches the first peak (after 4 h). At intermediate stage of aging, after a little decrease the hardness increases again and reaches the potential second peak for temperature 130 and 150 °C after 32 h. The final stage of aging, when the hardness decreases as a result of over-aging, was not observed.

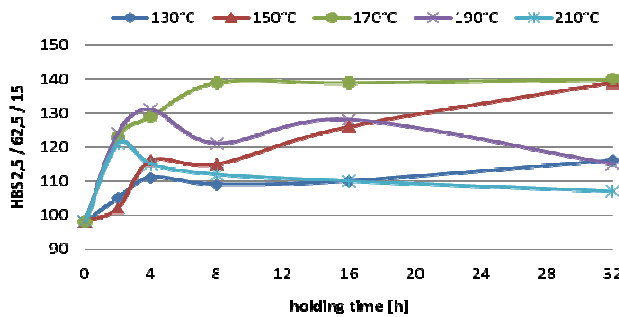


Fig. 1. Influence of age-hardening on Brinell hardness

For samples aged at temperature 170 °C a single aging peak after 8 hours and next a hardness high plateau from 8 to 32 hours was measured. The early stage of aging for temperature 190 °C by 4 hours and 210 °C by 2 hours was measured. The second aging peak for temperature 190 °C by 16 hours was observed. For temperature 210 °C the final stage of aging, when the hardness decreases as a result of over-aging, was not observed. The age-hardening peaks are correlated to their precipitation sequence. The first hardness peak of age-hardening curve is attained depending on the high density GP zones (especially GP II zones), while the second one is acquired in terms of metastable particles. The aging plateau is corresponding to the continuous transition from GP zones to metastable phases. Highest Brinell hardness was 140 HBS for 515 °C / 4 hours and artificial aging 170 °C / from 8 to 32 hours.

In order to investigate the double-peak phenomenon of the AlSi9Cu3 alloy, tensile properties of the alloy aged at 130, 150, 170, 190 and 210°C for different times have been measured. The results are shown in Fig. 2. It can be found that the double aging peaks were for temperature 130, 150 and 170 °C measured, but for temperature 190 and 210 °C was only one aging peak measured. For temperature 130, 150 and 170 °C we observed the first aging peak after holding time 4 hours. The second aging peak we observed after holding time 16 hours. For temperature 190 °C we observed the first aging peak after 16 hours and for temperature 210 °C after 8 hours. Highest strength tensile was 211 MPa for 515 °C / 4 hours and artificial aging 170 °C / from 16 hours.

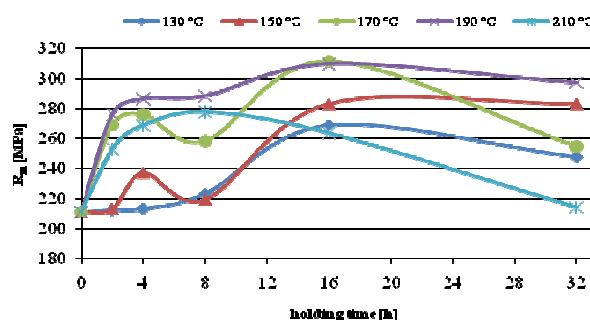


Fig. 2. Influence of age-hardening on strength tensile

Fig. 3 shows the change of impact strength during age - hardening. It can be found that the highest impact strength was by temperature 130 °C and the minimum by temperature 170 °C.

The mechanical properties of cast component are determined largely by the shape and distribution of Si particles in α -matrix. Optimum tensile, impact and fatigue properties are obtained with small, spherical and evenly distributed particles. Silicon also imparts heat treating ability to the casting through the formation of compounds with Mg, Fe and Cu.

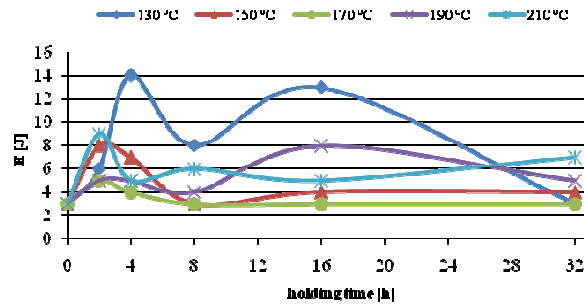


Fig. 3. Influence of age-hardening on impact strength

3. Conclusion

The mechanical properties (Brinell hardness, tensile strength and impact strength) increase after age-hardening for all artificial temperatures. In the hardness age-hardening curve single aging peak (at 4 h) and hardness plateau (at 16 h) are present. In the tensile strength age-hardening curve the double-peak phenomenon (at 4h and at 16h) are observed.

The „optimum“ schedule for mechanical properties is as follows: solution treatment: 4 h at 515°C; water quenching at 40°C; artificial aging: 16 h at 170°C. This will produce the following properties: HB was in compare with untreated state of 29 % higher and strength tensile was of 32 % higher.

Acknowledgement

This work has been supported by Scientific Grant Agency of Ministry of Education of Slovak republic N°1/0249/09, N°1/0841/11 and SK-CZ-0086-09.

References

- [1] RIOS, C. T., CARAM, R. *Intermetallic compounds in the Al-Si-Cu system*. - Acta Microscopica, Vol.12, N°1, pp. 77-81, 2003.
- [2] LI R. X., LI R. D., ZHAO Y. H., HE L. Z., LI C. X., GUAN H. R. AND HU Z. Q. (2004): *Age-hardening behaviour of cast Al-Si base alloy*. - Materials Letters, 58, pp. 2096-2101.
- [3] DAS, S. K. *Designing Aluminum Alloys for a Recycling Friendly World*. - Materials Science Forum, Vol. 519-521, pp. 1239-1244, 2006.
- [4] SENČÁKOVÁ, L., VIRČÍKOVÁ, E. *Life cycle assessment of primary aluminium production*. "Acta Metallurgica Slovaca", 13, 3, pp. 412-419, 2007.
- [5] DAS K, S., GREN, J. A. S. *Aluminum Industry and Climate Change-Assessment and Responses*. "Jom", 62, 2, pp.27-31, 2010.
- [6] PANUŠKOVÁ, M., TILLOVÁ, E., CHALUPOVÁ, M. *Relation between mechanical properties and microstructure of cast aluminum alloy AlSi9Cu3*. - Strength of Materials, 1, pp. 109-112, 2008.
- [7] HURTALOVÁ, L., TILLOVÁ, E. *Evolution of the structure in recycled AlSi9Cu3 cast alloy during solution treatment*. - Journal of Machine Manufacturing, XLIX, E3-E5, pp. 6-13, 2009.
- [8] LI, R. *Solution heat treatment of 354 and 355 cast alloys*. AFS Transaction, 26, 777-783, 1996.
- [9] PARAY F., GRUZLESKI J. E. *Cast Metals*, Vol.7, pp. 29-40, 1994.
- [10] ABDULWAHAB, M. *Australian Journal of Basic and Applied Sciences*, 2 (4), pp. 839-843, 2008.
- [11] TILLOVÁ, E., PANUŠKOVÁ, M. *Effect of solution treatment on intermetallic phase's morphology in AlSi9Cu3 cast alloy*. - Materials Engineering, 14, pp. 73-76, 2007.
- [12] TILLOVÁ, E., PANUŠKOVÁ M. *Effect of solution treatment on intermetallic phases morphology in AlSi9Cu3 cast alloy*. - Metallurgija / METABK 47, pp. 133-137, pp. 1-4, 2008.



Role of Surface Condition on Fatigue Behavior of Nodular Cast Iron

*Marián Kokavec, *Radomila Konečná, **Gianni Nicoletto

*University of Žilina, Faculty of Mechanical Engineering, Department of Materials Engineering, Univerzitná 1, 01026 Žilina, Slovakia, {marian.kokavec, radomila.konecna}@fstroj.uniza.sk

**University of Parma, Department of Industrial Engineering, Viale G. P. Usberti 181/A, 431 00 Parma, Italy, {gianni.nicoletto}@unipr.it

Abstract. The fatigue strength evaluation of nodular cast iron with as-cast surfaces involves several complicated factors such as surface roughness, transition of microstructures from surface to interior, several types of defects and residual stresses. Fatigue testing in cyclic plane bending was performed to investigate the response of a nodular cast iron with different surface conditions, namely as-cast, sand blast and fine ground. The results show fatigue data that can be interpreted considering the surface features at the origin of the formation of the main fatigue crack.

Keywords: nodular cast iron, fatigue properties, surface conditions.

1. Introduction

Nodular cast iron (NCI) is a structural material for many industrial applications and its resistance to fracture in static and cyclic loading has been subject of extensive investigation. The mechanical properties of NCI are comparable with those of cast steels but with improved castability. Therefore NCI is often used for the automobile and engineering components [1, 2].

The fatigue properties of NCI are influenced by the matrix structure, the percentage of spheroidal graphite, and the presence of mechanical notches. Slightly higher percentages of spheroidal graphite increase the fatigue strength as well as the endurance limit. The presence of a larger amount of pearlite in the matrix structure also increased the fatigue strength. The effect of matrix structure on the fatigue strength is less pronounced and the fatigue strength is significantly lower in the presence of notches [3].

Fatigue properties of NCI with as-cast surfaces are influenced by various factors such as: i) surface roughness, ii) changes in the mechanical properties of the metal surface, and iii) changes in the residual stress condition near the surface. As these factors work together and influence fatigue strength in a complex manner, the quantitative evaluation of the fatigue strength of NCI having casting surfaces is very complex, resulting in a different fatigue strength from that observed for smooth specimens. Specimens with as-cast surfaces are expected to show a reduced fatigue strength compared to machined and polished specimens [4].

This paper presents a study of the fatigue behavior of pearlite/ferrite NCI specimens having different surface conditions, namely as-cast, sand blast and fine ground. The dependence of the fatigue behavior on specific surface condition is highlighted using prismatic specimens tested under cyclic plane bending ($R = 0$) with maximum stress reached at the surface of interest. The characteristics of the surface layers in the different test specimens are examined by metallographically.

2. Material and experiments

The experimental metal charge was prepared from a 2000 kg of pig iron, 300 kg of steel scrap, 1500 kg of cast iron scrap. Melting was performed in electric arch furnace. The experimental

material was treated during heating with addition of 35 kg FeSi [5]. Chemical composition of the pearlite/ferrite NCI is given in Tab. 1.

The cast material was delivered in the form of 130 x 90 x 20 mm plates. No annealing treatment was performed before machining the specimens used for tensile and fatigue testing. The structural analysis was performed on polished and etched specimens taken from the cast plates. Structure details were analyzed in the light metallographic microscope according to the EN STN 42 0461 standard and by the methods of quantitative metallography [6].

C	Si	Mn	S	P	Mg	Cr	Cu	Ni
3.68	2.62	0.51	0.005	0.05	0.034	0.2	0.02	0.01

Tab. 1. Chemical composition of pearlite/ferrite NCI, [wt. %].

The graphite nodules were observed in fully and only partly not fully globular shape and they were located in ferrite. Size of graphite particles was predominately ranging from 30 to 60 μm (VI 6) and with a small number of nodules ranging in the size from 15 to 30 μm (VI 7). Graphite nodule count N was 260 mm^{-2} in average. The NCI matrix was not homogeneous with different content of ferrite and pearlite, Fig. 1. The microstructure of specimens according to the standard EN STN 42 0461 was indicated as Fe 55 (it means 40 to 70 % of ferrite in the matrix). The effective ferrite (EF) content (% of ferrite in the volume of specimen) was 34 % for specimen with as-cast and sand blast surface and 48 % for specimen with fine ground surface. The average mechanical properties of the present NCI were tensile strength $R_m = 576 \text{ MPa}$ and elongation to rupture $A = 6 \%$.

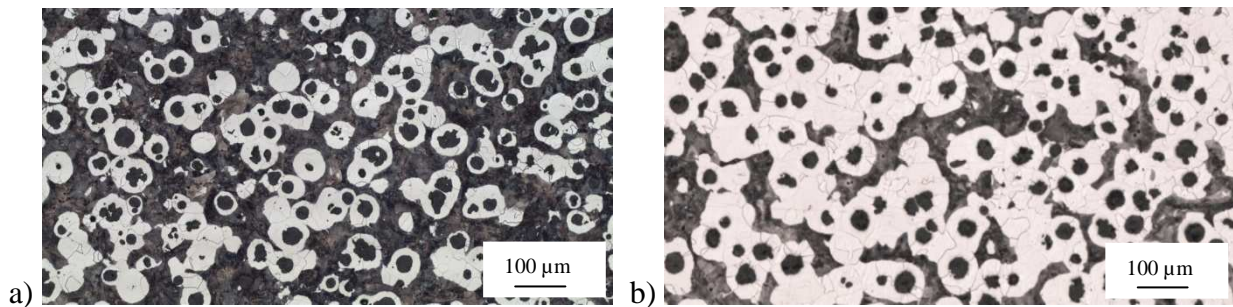


Fig. 1. Typical microstructure of specimens with a) as-cast and sand blast surface, b) fine ground surface, etched with 3 % Nital.

Three sets of fatigue specimens were prepared. One set (Fig. 2a) had one test surface in the as-cast condition and the other ground. Specimens indicated as sand blast (Fig. 2a) had the as-cast surface sand blast after machining. The test surface of the fine ground specimens (Fig. 2a) had a smooth finish achieved by removing the casting surfaces by soft grinding.

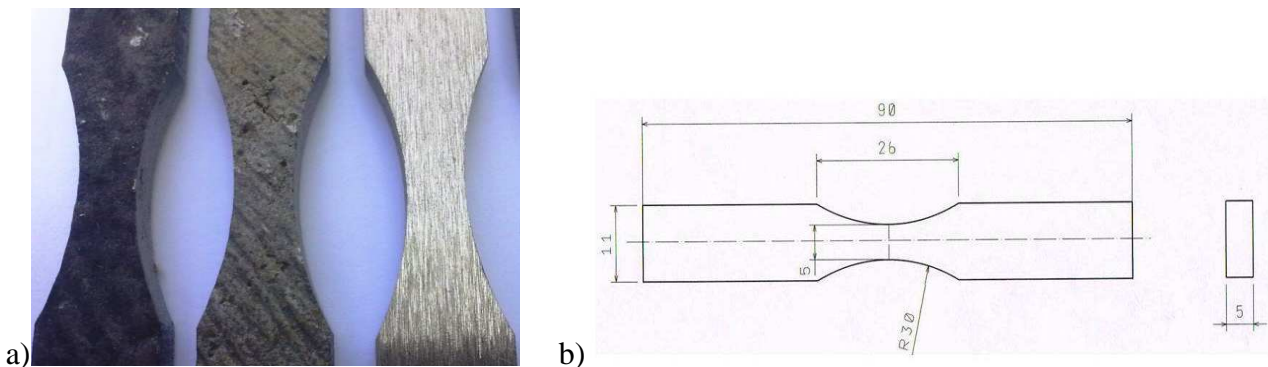


Fig. 2. a) Surface condition of specimens (from left) as-cast, sand blast and fine ground b) dimensions of specimens.

Fatigue tests were performed on specimens, whose geometry is shown in Fig. 2b, using a fatigue test machine for cyclic plane bending with loading ratio $R = 0$ and 25 Hz frequency. Tests were interrupted at $2 \cdot 10^6$ cycles if the specimen did not fail. The ratio $R = 0$ allowed to apply a

cyclic tensile loading to the surface of interest, either *as-cast*, *sand blast* or *fine ground*. The stress amplitude was defined according to $\sigma_a = M/(2S)$, where $S = bh^2/6$ is the section modulus where b and h are width and height of minimal specimen section and $M = P \times L_o$ is the bending moment with P the force monitored by a load cell and L_o the distance between the load cell and an internal support.

3. Results and discussion

Fatigue test results are presented on Fig. 3 where the number of cycles to failure is plotted against the stress amplitude σ_a (i.e. $\sigma_{max}/2$). Trends of the S/N dependence at different surface condition (as-cast, sand blast and fine ground) are identified for the three sets of specimens. They are clearly associated with the surface finishing conditions, which especially control fatigue crack initiation. As expected, specimens with the fine ground surface achieved longer lives for a given stress amplitude compared to the specimens with as-cast and sand blast surface. As-cast and shot blast surfaces give a similar response in fatigue. At 10^6 cycles, the fatigue strength show a decrease going from a fine ground to an as-cast surface in the range of 20 %.

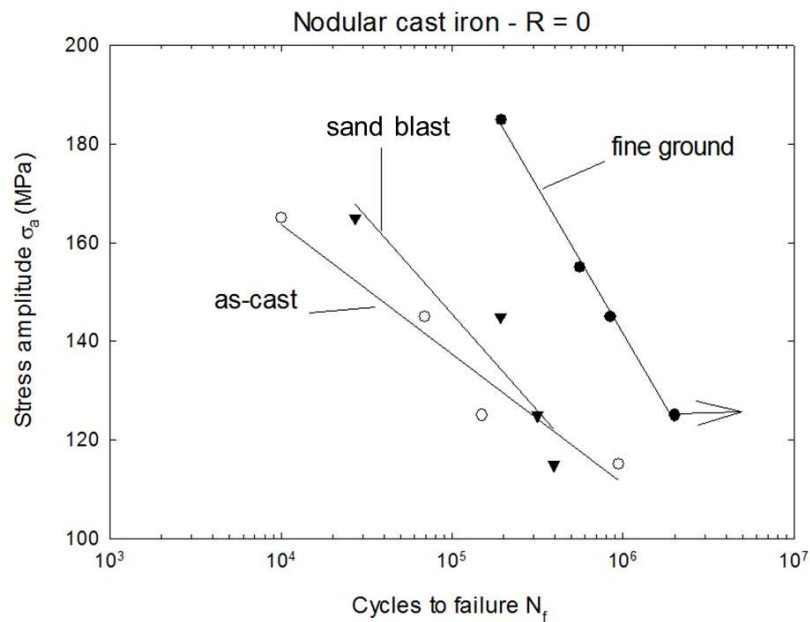


Fig. 3. Fatigue tests results.

Longitudinal sectioning of the specimens allows an evaluation of surface roughness and surface features for the different specimens. The surface roughness coefficient R_v of the three surfaces, see Tab. 2, is coherent with the fatigue ranking of Fig. 3. The as-cast specimen surface is characterized by two different layers above the base NCI structure, Fig. 4a. Top is the surface layer formed by casting, then a transitional pearlitic layer formed by rapid solidification and cooling. Many defects (notch, pinhole and crack) were found in the as-cast surface layer of Fig. 4a. The surface layers thickness is not uniform, (i.e. approximately 100 μm thick). Thicknesses of these layers were measured and are also summarized in Tab. 2.

	as-cast	sand blast	fine ground
vertical roughness coefficient R_v	0.588	0.495	0.066
thickness of casting layer	36 μm	only locally present	removed
thickness of pearlitic layer	80 μm	110 μm	removed

Tab. 2. Characteristics of surface layers of the different specimens.

The sand blasting treatment removes the surface layers and locally deforms the metal but the vertical roughness is still comparable to the as-cast surface. Surface of sand blast specimens is formed by pearlite layer with lamellar graphite, Fig. 4b. Only fine grinding reduces significantly the surface roughness (i.e. by one order of magnitude) by elimination of the cast surface layers entirely.

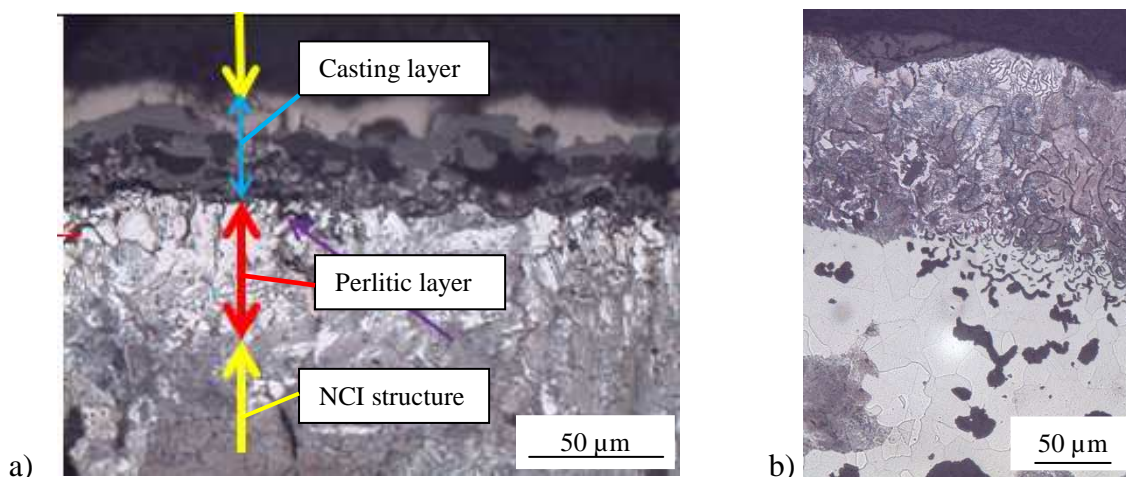


Fig. 4. Magnified view of surface layers of a) as-cast material; b) material after sand blasting.

4. Conclusion

The influence of the specimen surface on the fatigue strength of pearlite/ferrite nodular cast iron was investigated in this study. The following conclusions were reached:

- Fine ground surface achieved the best fatigue performance, with as-cast and sand blast surfaces was associated reducing strength (i.e. approx. 20 % less),
- Fatigue fracture origins of nodular cast iron with as-cast surface can be largely attributed to the roughness and defects existing in the vicinity of the cast surfaces,
- The as-cast surface layers are characterized by significant roughness, defects and a brittle surface microstructure, which is quite different from the base pearlitic/ferritic base metal.

Acknowledgement

This research was supported by project VEGA 1/0242/10.

References

- [1] DAVIS, J.: *Cast irons/Metallurgy and Properties of Ductile Cast Irons*, ASM Speciality Handbook, The Materials Information Society, USA ,1996.
- [2] PETRENEC, M. et al. 2010. *Comparison of low cycle fatigue of ductile cast irons with different matrix alloyed with nickel*. In. *Procedia Engineering* 2, p. 2307-2316.
- [3] VĚCHET, S., KOHOUT, J., BOKŮVKA, O.: *Fatigue properties of nodular cast iron*, EDIS, Žilina, 2001, (in Czech).
- [4] YAMABE, J., KOBAYASHI, M.: *Influence of casting surfaces on fatigue strength of ductile cast iron*. *Fatigue Fract Ingg Mater Struct* 29, pp. 403-415, 2006.
- [5] KONEČNÁ, R., ZÁHOROVÁ, B., MATEJKA, M.: *Influence of SiC additive on fracture of the nodular cast iron*, *Materials engineering*, 4/2000, (in Slovak).
- [6] KOKAVEC, M. - KONEČNÁ, R. - NICOLETTO, G. 2010. *Influence of surface quality on fatigue behavior of nodular cast iron*. In. *Zborník prednášok z konferencie QUO VADIS FOUNDRY III., EKOLOGICKÉ ASPEKTY ZLIEVARENSTVA HUTNÍCTVA I.*, Technická univerzita v Košiciach, Hutnícka fakulta, 2010. p.102-107.



Analysis of Boundary Conditions for the Simulation of Welding in the Repair of Gas Pipelines with Steel Sleeve

*Radoslav Koňár, *Miloš Mičian, *Anton Hopko

*University of Žilina, Faculty of Mechanical Engineering, Department of Technological Engineering, Univerzitná 2, 01026 Žilina, Slovakia, {radoslav.konar, milos.mician, anton.hopko}@fstroj.uniza.sk

Abstract. Theoretical part of the manuscript deals with basic information about repair of gas pipeline with steel repair sleeves and simulation programme SYSWELD. Experimental part includes analysis of boundary conditions in two-pass fillet welding joint. Results of the analysis will be used for simulation in simulation programme SYSWELD.

Keywords: Steel repair sleeves, L360NB, SYSWELD.

1. Introduction

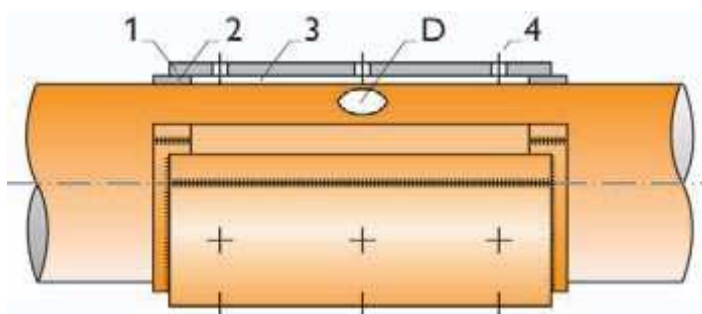
The article deals with the issues of repairing defects in steel gas pipes, in particular of permanent repairs with using steel sleeves.

2. Theoretical Part

2.1. Permanent Repair of Defects in Gas Pipelines with Using Steel Sleeves

The Steel Repair Sleeves can be used for permanent repairing of high pressure gas, pipeline defects without interrupting. With using these repair methods, we can repair defects, such as internal and external corrosion, gouges, dents, grooves, arc burns, cracks, defective girth welds, laminations and leaks [2].

The steel sleeve is composed of segmented steel casing, fitted on two steel distance rings, which defines the space between the sleeve and the repaired pipe. This space is filled with glass beads and epoxy (composite). When epoxide cured, provide a perfect transmission of stresses from pipeline to sleeve, while an equal stress distribution in the pipeline and sleeve. Type of material and thickness sleeve and distance rings, must be same as the thickness of the repaired pipeline. Required mechanical properties of composites obtained after 24 hours of curing. Good space filling composites are checked through the inspection holes [2].



- 1 – steel segmented sleeve
- 2 – distance rings
- 3 – composite
- 4 – inspection holes
- D – pipeline defect
- ++ - weld

Fig. 1. Principle repairs gas pipeline using steel repair sleeve [2].

Depending on the seriousness and type of defect on the pipeline can be sleeves divided to:

- cold sleeve – steel casing fitted on two steel distance rings is welded only longitudinal butt weld,
- hot sleeve - steel casing fitted on two steel distance rings is welded longitudinal butt weld and also is welded with fillet weld to distance rings [2].

2.2. SYSWELD

SYSWELD is a Finite Element software that simulates all usual welding processes such as MMA, MIG, TIG, spot welding, laser welding, heat treatment like bulk hardening, surface hardening, tempering and hardening and tempering, as well as thermo-chemical treatment like case hardening, carbonitriding, nitriding [1].

The software calculates dimensional variations and distortions of parts, hardness, strength and strain at break of the material in use, plus residual stresses, during and at the end of the welding or heat treatment process [1].

Simulation of a welding process requires two successive analyses:

- first a thermo-metallurgical analysis,
- followed by a mechanical analysis.

3. Experimental Part

This experiment includes analysis of boundary conditions for the simulation of welding in the repair of gas pipelines with steel sleeve.

3.1. Experimental Sample

Model used for the experiment was compounded of two 60° pipe sections of materials L360NB (pipe and distance ring). Pipe has a diameter of 323,9 mm, pipe's thickness is 10mm and length 260 mm. Distance ring has diameter of 333,9 mm, ring thickness 10mm and length 90 mm. Welding joint was welded using the MMA process. Experimental sample was welded with two fillet passes of weld. These passes of weld a part of the finished weld.

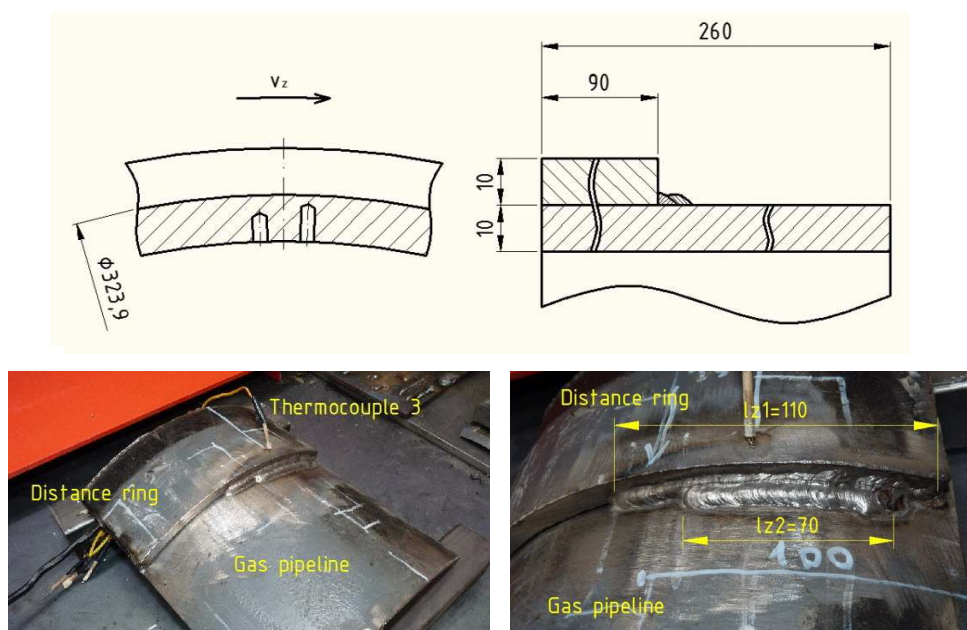


Fig. 2. Experimental sample, scheme (up), real sample (down).

3.2. Experimental Measurements During and After Welding

During welding were measured welding parameters, welding time and thermal cycles in three points. After welding the weld was analysed. Complete analysis of weld for simulation in simulation programme SYSWELD contains:

- parameters of welding (U_w , I_w),
- cross-sectional geometry of the welds (weld metal, heat affected zone),
- welding speed (s_w),
- thermal cycles,

Parameters of welding				
Weld	U_w [V]	I_w [A]	s_w [mm.s ⁻¹]	Q_r [J.cm ⁻¹]
Weld 1	23,6	92	2,2	7895
Weld 2	23,6	92	2,25	7719

U_w - welding voltage
 I_w - welding current
 s_w - welding speed
 Q_r - real heat input ($\eta=0,8$)

Tab. 1. Parameters of welding.

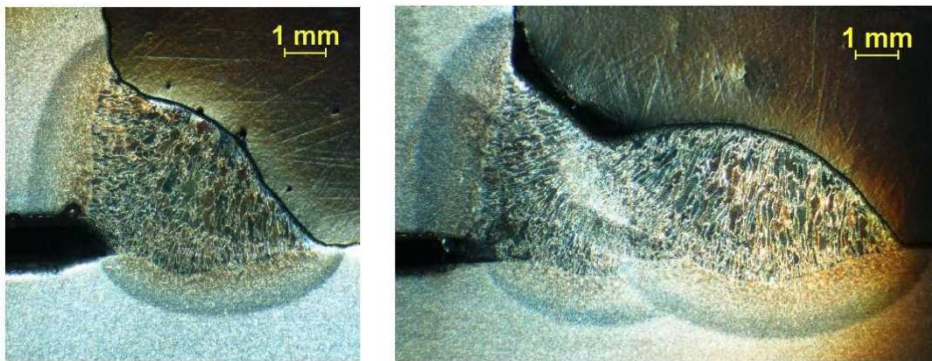


Fig. 3. Macrostructural analysis.

Digitizing of weld macrostructures, we get cross-sectional parameters of welds “Fig. 4.”, which are necessary for the definition of Goldak heat source model.

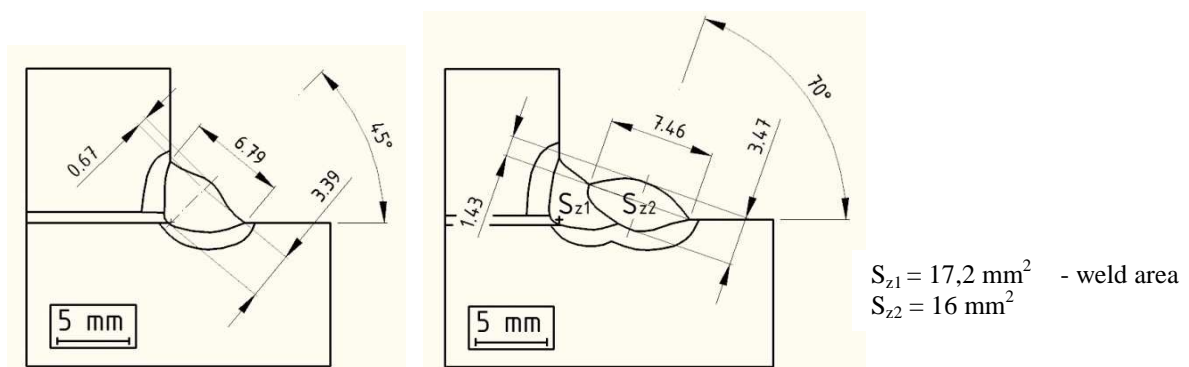


Fig. 4. Cross-sectional parameters of the weld.

Temperature cycles were measured by three thermocouples. Their location is shown in Fig. 5.

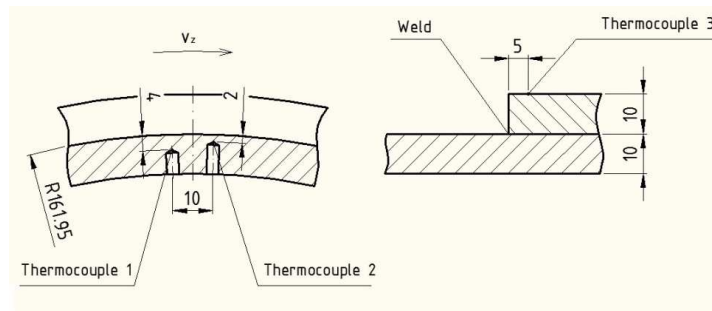


Fig. 5. Location of thermocouples.

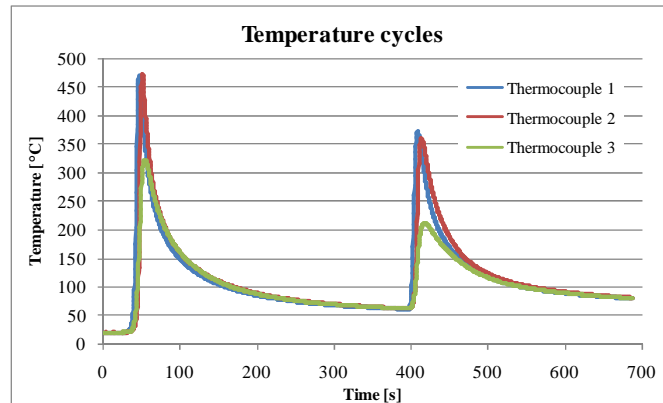


Fig. 6. Temperature cycles in three thermocouples.

Characteristic attributes of temperature cycles			
1. pass of weld			
Thermocouple	T_{max} [°C]	r_{300} [°C.s ⁻¹]	t_{100} [s]
1.	465	9,78	113
2.	480	10,6	117
3.	322	6,5	112
2. pass of weld			
Thermocouple	T_{max} [°C]	r_{300} [°C.s ⁻¹]	t_{100} [s]
1.	373	8,7	136
2.	360	8,5	144
3.	212	-	126

Tab. 2. Characteristic attributes of temperature cycle.

3. Conclusion

Experimental results will serve as a boundary condition for the simulation in simulation programme SYSWELD. The simulation process will provide information about residual stresses arising in the repair of gas pipelines with steel sleeve.

Acknowledgement

This work has been supported by Scientific Grant Agency of Ministry of Education of the Slovak republic, grant VEGA N° V-08-046-00.

References

- [1] MORAVEC, J. *Simulace tavného svařování - simulační program SYSWELD*. In *Zvárač*. ISSN 1336-5045, 2009, vol. VI., issue 2., p. 9-12.
- [2] PAŘÍZEK, P., BRYNYCH, A., STUKBAUER, M. *Trvalé opravy ocelových potrubí bez přerušení provozu aplikací objímek*. In *Plyn*. vol. LXXXVI., online: http://www.ceps-as.cz/download/Opravy-ocelovych-potrubí-bez-preruseni-provozu-aplikaci-objimek_PLYN_2006-11.pdf, 2006.



Ultrasonic Testing of Adhesive Joints With a Low Defectoscopic Susceptibility

*Jakub Kowalczyk, **Marian Josko

* Poznan University of Technology, Faculty of Machines and Transportation, Institute of Machines and Motor Vehicles, Piotrowo 3, 60-965 Poznan, Poland, {jakub.kowalczyk, marian.josko}@put.poznan.pl

Abstract. The article presents the possibility of testing of selected adhesive joints, used in the construction automotive vehicle, with so called low defectoscopic susceptibility. A scope of application of adhesive joints in cars construction was analyzed. In the paper some possibilities of testing of the glue joints in the construction of automotive construction were presented. The paper presents the description of the experiment carried out and its results. As a mine result of the work executed, it was found that there is a possibility of using of non-destructive method for testing the quality of adhesive joints, with low defectoscopic susceptibility.

Keywords: glue joints, ultrasonic testing, non destructive testing

1. Introduction

The glue joints belong to specific adhesive joint group. These joints are used in industry, for example in automotive industry. The adhesive joints are used, particularly, in cars and buses. The adhesive joints are classified as the oldest permanent joints. Despite of the high-tech bonding, in the finished product may occur defect. Majority of existing test methods for glue joints assessment are destructive methods. They are also used non-destructive method to test such connections.

The research was carried out with the aid of non-destructive methods for assessment of adhesive joints quality. Tests can be made using such methods as ultrasonic, infrared, holographic, and resonant sound [1, 2, 3]. The cheapest non-destructive testing method for evaluation of adhesive joints quality is organoleptic method. This method requires a lot of experience from controller of glued joints and also a good knowledge of adhesive technology. With the aid of this method it is possible to verify the uniformity of bead of glue around the edges, joints, which shows the correct amount of adhesive in the weld and the proper pressure to the adhesive in the joint (Fig. 1).

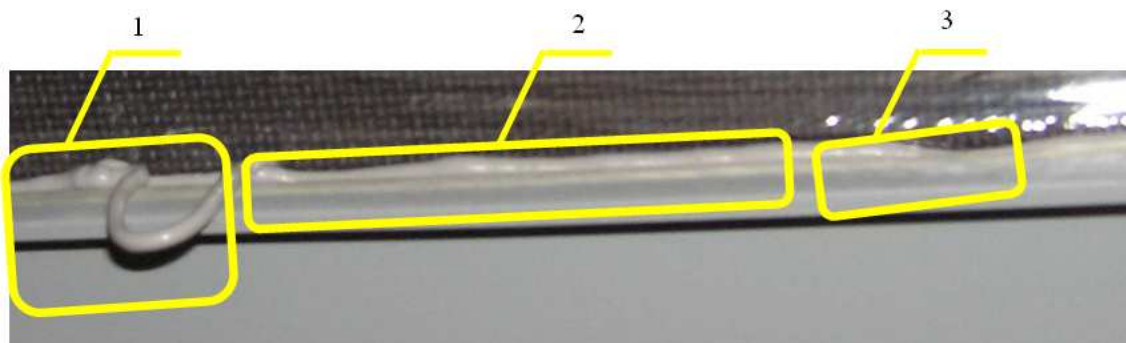


Fig. 1. Verification of the correct bead of glue: 1 - the area where too much adhesive was applied, 2 - the area where a proper amount of adhesive in the joint was applied, 3 - the area where too little adhesive was applied

Other methods in most cases require access to the materials bonded at the application of the adhesive. An example diagram of measurement used by the authors in ultrasonic testing of adhesive joints is shown in Fig. 2.

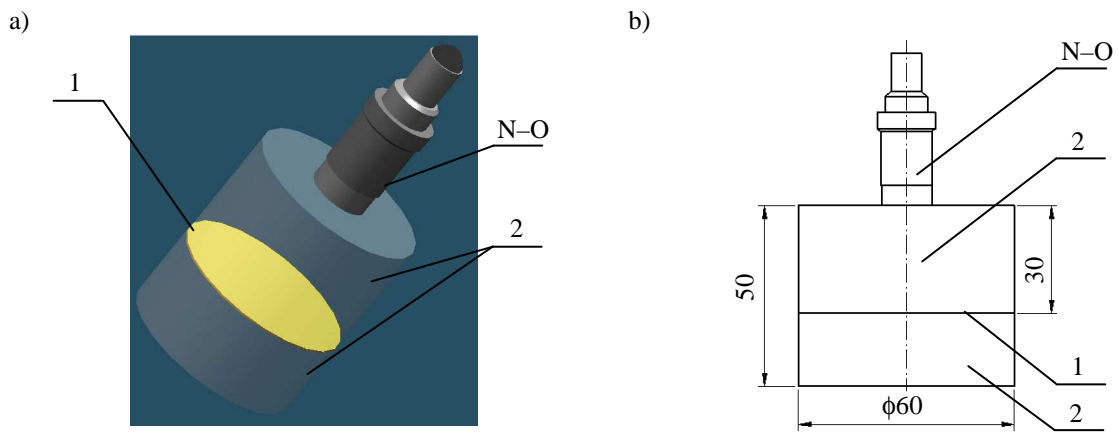


Fig. 2. An experimental setup: a) general view b) scheme; N-O - probe transmitter - receiving, 1 - glue, 2 - 45 steel

Purpose of tests

The main aim of the research is an assessment of the possibility of the use of non-destructive testing for evaluation of adhesive joints with low susceptibility flaw, for example, in the case of an application of the glue for bonding the floor in buses.

2. Description of the experiment

Such tests were glue joints, as used in the construction of buses. The glue connections were investigated with a rectangular profile combined with glue and plywood floor. In this connection there is no possibility of application of us, from the metal directly above the area where the glue was imposed. Strong attenuation of ultrasonic waves in the plywood prevents the measurement from its side. For this reason it was decided to use the Rayleigh wave. This wave penetrates to a depth of approximately one wavelength. It is a special case of transverse waves, since the vibrations of particles are composed of two vectors, and the movement of particles takes place after the slender ellipse. Prior to the tests determined Rayleigh wave velocity profiles in the test, which were about 3200 m / s. The measuring system is shown in Fig. 3

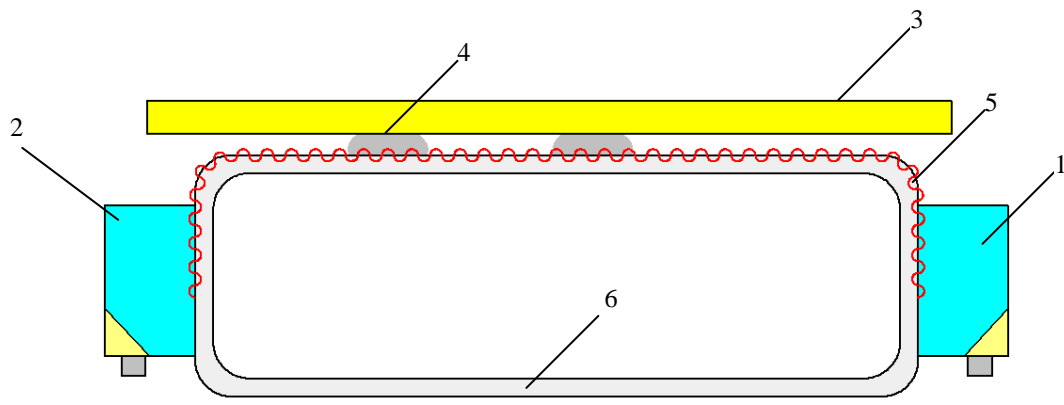


Fig. 3. Measuring system: 1, 2 – ultrasonic probe, 3 – plywood, 4 – adhesive, 5 - Rayleigh wave, 6 - hollow

Some experimental results are shown in Fig. 4 and Fig. 5. Figure 4 shows the image obtained on the screen of ultrasonic flaw detector in the area where the glue was applied properly. in Fig. 5 IS shown the image obtained during the measurements of all point where adhesive is not imposed. As far as the quality of accepted pulse height on the screen ultrasonic flaw detector.

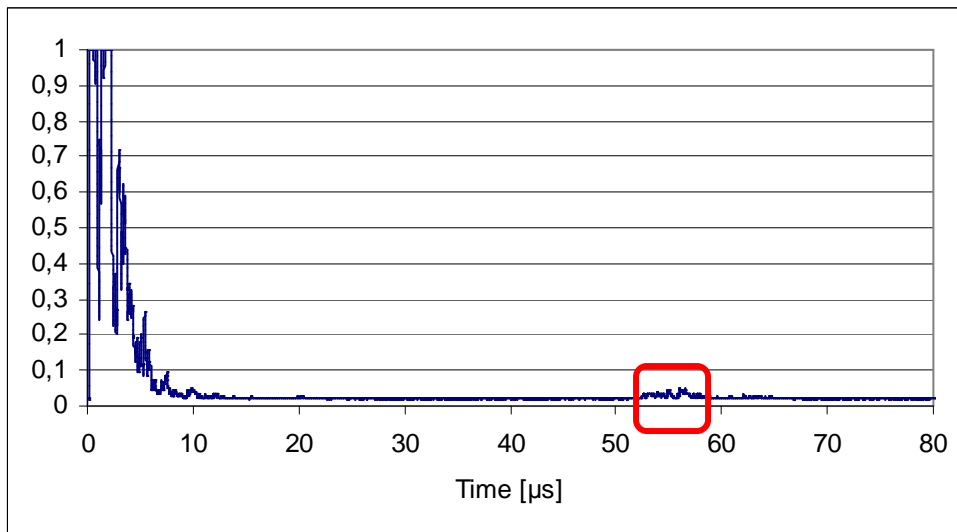


Fig. 4. The image obtained on the screen of ultrasonic flaw detector in the area where the glue was applied

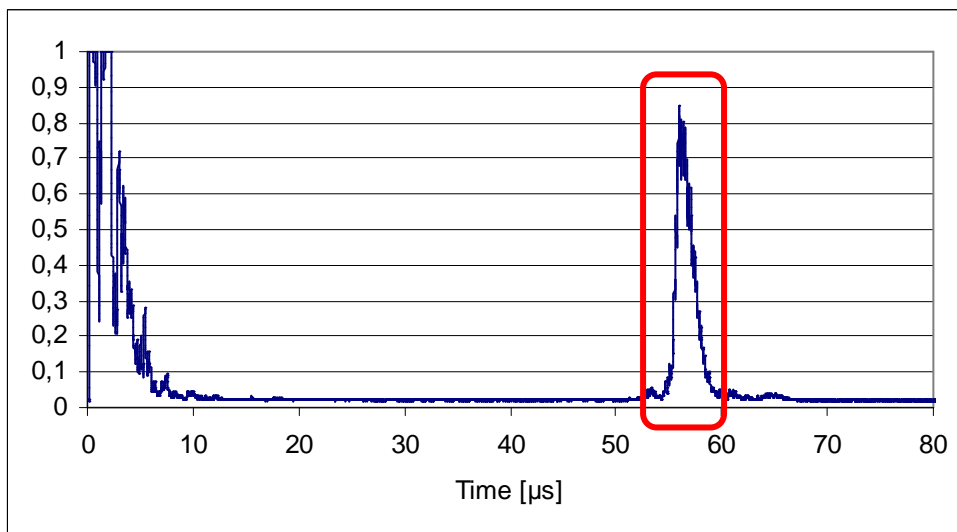


Fig. 5. The image obtained on the screen of ultrasonic flaw detector in the area where the glue was not applied

3. Conclusion

On the basis of the theoretical analysis of the problem studied, and on the grounds of the experiment carried out, we can draw the followings conclusions:

- It was found that the samples can obtain the needed research useful ultrasonic wave pulses.
- During the testing of adhesive joints the surface wave can be used.
- Pulse height obtained on the screen, of ultrasonic flaw detector depends on the quality of the joints.

References

- [1] *Automotive Circle International Conference*, module I: Adhesive bonding and hybrid bonding in body-in-white shop and assembly, 25/26 April, 2006
- [2] JÓSKO M., *Badania właściwości połączenia adhezyjnego typu powłoka–podłoże metodą ultradźwiękową*, *Problemy Eksploatacji*, 2002, 2, s. 105-116
- [3] CAWLEY P., ALLIN J.M., LOWE M. J. S.: *Adhesive disbond detection of automotive components using first mode ultrasonic resonance*. *NDT&E International*, Vol. 36, 7, 2003, pp. 503 – 514.]



The Determination of The Material Composition of The Pressure Vessel By Using EDX Analysis

*Kristína Masláková, **Peter Frankovský

* Technical university in Košice, Faculty of mechanical engineering, Department of applied mechanics and mechatronics, Letná 9, 04001 Košice, Slovakia, kristina.maslakova@tuke.sk

** Technical university in Košice, Faculty of mechanical engineering, Department of applied mechanics and mechatronics, Letná 9, 04001 Košice, Slovakia, peter.frankovsky@tuke.sk

Abstract. This paper presents the material analysis named EDX (Energy Dispersive X- ray Analysis). This method is used in the scientific field for experimental activities. Material analysis is very important for every scientific research. The results indicate the percentage representation of the individual elements and that way about character of the investigated material.

Keywords: EDX analysis (Energy Dispersive X- ray Analysis), sample, pressure vessel, material characteristics

1. Introduction

Nowadays is very necessary make every experiment with knowing properties of investigated material. The one way how can we find out the information about material characteristic is material analysis. The contribution presents EDX analysis (Energy Dispersive X- ray Analysis). After obtaining the accurate information about the appearance of elements in investigated material, is possible to make a required experiment. The analysis of our sample was made for comparison of contractor values and measured values achieved in our laboratories.

2. Energy-Dispersive X-ray Analysis

The EDX analysis exploits the primary electrons impacting to surface of the sample for the excitation of atoms. RTG radiation is detected. The locality of interaction of the prime electrons has a pear shape. On the explored object it is possible to explore the placements of elements on the reserved and suitable surface by microscope adjusted to desired zoom. After the recognition of the elements on the analyzing sample the map of occurrence is appeared hence the displaying of the parts in which these elements are found. The simultaneous combination of the elements is possible and we can observe its overlapping and complementing. The inseparable components are the analyzers that enable to analyze elements on the chosen points of the surface of sample and also to trace the allocation of the elements on the surface of sample. The characteristic RTG radiation of elements is creating when there are the individual electrons of the inner parts of the atoms ejected by the impacts of the prime electrons. These electrons are substituted by the electrons from the higher energetic levels and the differential energy is released in the form of radiation. This energy is characteristic for each individual element. On the records from the analyzers the braking radiation is participating on the continual background image and characteristic radiation of the elements contained in sample creates so called peaks.

2.1. Determination of material characteristics

The investigated pressure vessel with the inner working overpressure of 10 bars and volume 2 l is used as a tank of the brake liquid on the lorry chassis. The pressure tank was made from unalloyed steel class 11 373. The values of the mechanical properties and chemical structure are listed in the table 1.

The data about the material: unalloyed steel of the ordinary qualities suitable for the welding of the steel constructions. Steel suitable for the common use and for the common atmospheric eventually elevated temperatures [1].



Fig. 1. The investigated pressure vessel

Chemical structures [%]				Mechanical properties				
C max.	P max.	S Max.	N max.	Poisson number μ [-]	Tensibility A_{80} [%]	Breaking strength R_m [MPa]	Yield stress $R_{p0,2}$ [MPa]	Modulus of elasticity E [10^5 MPa]
0,17	0,045	0,045	0,007	0,3	24	340 - 470	225	2,06

Tab. 1. Mechanical properties and chemical structures of unalloyed steel class 11 373

For the sake of more exact analysis of the chemical structure of the material of investigated pressure vessel its cap made from the same steel as a vessel was sampled and the sample was cast to dentacryl (Fig.2). The analysis was accomplished on the Technical university in Kosice.



Fig. 2. The sample of investigated material in dentacryl.

The results of the measurement from EDX analysis and contents of individual elements in relation energy/value are depicted on the Fig.3,4,5.

On the Fig.3 is displayed the analysis of the particle containing aluminium and calcium oxids (oxygen is not possible to analyze on the microscopes that was used and therefore it isn't visible in the spectrum) and mangan and ferrum sulphid. Ferrum in the analysis can be either from the surroundings of elements.

On the Fig.4 the analysis was made from the greater part of the fracture surface is pointing out to the average chemical structure of the analyzing spot (there aren't occurs of elements with less atomic number than 11 in the EDX analysis; restriction of the analyzer). Spectrums indicates frequency of the photons in certain energy level and when the impacts of the electrons on the atoms cause the RTG radiation (during the certain satisfied condition) and this radiation has a continual pattern, but it has either characteristic peaks for each element, then we can determine qualitative and quantitative structure of the researched material upon their analyzes.

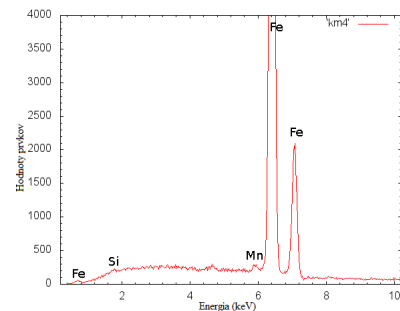
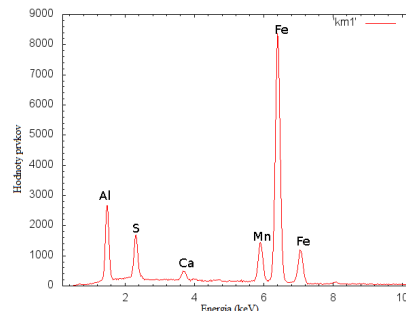


Fig. 3. Analysis of part of sample containing aluminium and Calcium

Fig. 4. Analysis of fracture surface.

Following figures from the electron microscope are recording the fracture surfaces in the analyzing sample. There is depicted ductile fracture on the Fig.5 while the mechanics of infraction is a tube fracture. Breakage was made by hammer in the vice at 20°C. On the Fig.5b is farther indicated the place of which there was made EDX analysis KM3 (Fig.3)

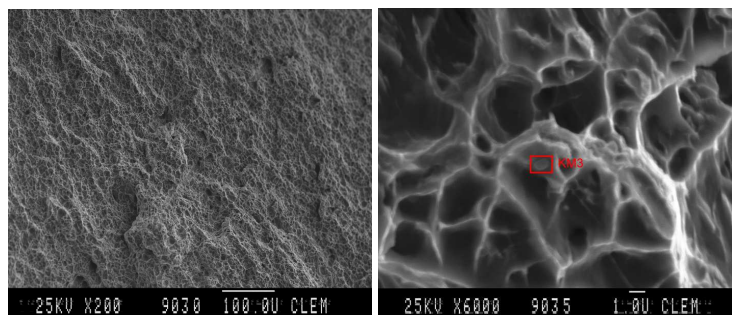


Fig. 5. The ductile fracture with the type of tube fracture.

Fig. 6a, 6b display prevailed polyedric ferritic-perlitic structure shot by the optical microscope.

Fig. 6b displays barely visible segment of perlit (the grains approximetly in the middle) and also it is possible to see, that no whole carbon (cementit) is segregated in the nice polyedric grains of perlit, but on the certain places it suggest something as a degenerated perlit, terciat cementit.

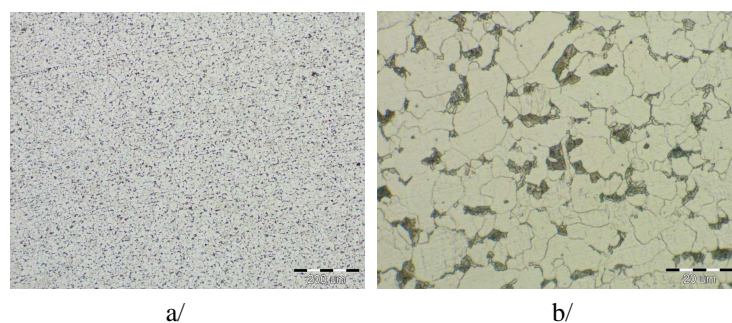


Fig. 6. a/ Polyedric ferritic- perlitic structure, b/ Polyedric ferritic-perlitic structure with the segment of perlit

3. Conclusion

The goal of the experiment was the determination of the material characteristic of the pressure vessel. When we don't dispose material lists of investigated object, material analysis represents inevitable fundament for any experiment in the field of applied mechanics. There was proved upon the reached results, that although the measured values in some elements is different from the values provided by manufacturer about a few hundredths, it is enough for the determination of the

type of material and following activity that will be proceeded on the investigated object. The last point is interpretation of the measured values.

Acknowledgement

This contribution is the result of the project implementation: Center for research of control of technical, environmental and human risks for permanent development of production and products in mechanical engineering (ITMS: 26220120060) supported by the Research & Development Operational Programme funded by the ERDF. The authors expresses their thanks to grant agency VEGA MŠ SR (project No. VEGA 1/0289/11).

References

- [1] FURBACHER, I., MACEK, K.: Lexikon technických materiálů se zahraničními ekvivalenty 3.7., část 3, díl 4, Praha, 2005.
- [2] Fractography 2003 : Fraktografia 2003 : proceedings of the international conference held in the hotel Academia, the High Tatras, Slovakia November 9 -12, 2003 / edited by Ľudovít Parilák. - Košice : Slovak Academy of Sciences, 2003. - 456 s. :. - ISBN 80-968543-2-1.
- [3] HERTZBERG, W. R.: Deformation and Fracture Mechanics of Engineering Materials , 4th ed. - New York : Wiley, 1996. - xxiv, 786 s. - ISBN 0-471-01214-9.
- [4] HRIVŇÁK, I.: Elektronová mikroskopia ocelí, Bratislava : Veda, 1986. - 286 s. - ISBN (viaz.).
- [5] MASLÁKOVÁ, K.: Identifikácia a kvantifikácia vplyvu zvyškových napätí na technický život mechanických prvkov a sústav, Písomná práca k dizertačnej skúške, Košice, 2011.



Analysis of Causes of Blistering in Welded Joints

* Magdalena Mazur, ** Paweł Szataniak, * Robert Ulewicz

* Czestochowa University of Technology, Institute of Production Engineering, Faculty of Management, 42-201 Czestochowa, Armii Krajowej 19B, Poland, ulewicz@zim.pcz.pl, mazur.m@zim.pcz.pl

** WIELTON S.A. Company, 98-300 Wieluń, ul. Baranowskiego 10a, pawel.szataniak@pamapol.com.pl

Abstract. The thesis presents results of analyses for welding incompatibilities formed during the process of welding structures of a semi-trailer frame. The tests results show that welding blisters in blowholes are one of main factors of poor quality welded joints. In order to work out coordinating and preventive actions an analysis of how the blowholes are formed was conducted, taking into account surface blowholes. For the company's needs a list of factors having an impact on joints' porosity was prepared.

Keywords: welding process, welding incompatibilities, blisters and surface blowholes.

1. Introduction

The examination unit presented in the dissertation is WIELTON S.A., a company producing semitrailers, trailers and lorry sidings, as well as agricultural accessories. The company is a leading Polish producer of semitrailers and trailers, with 24% market contribution. One of the main elements of production processes is the process of welding constructions intended for semitrailers.

The use of MIG/MAG methods is of great significance in the contemporary welding production as it is characterised by a constant rising trend. Abbreviation MIG (Metal Inert Gas) concerns welding inert gasses in covers (argon, helium). Abbreviation MAG (Metal Active Gas) concerns only active protective gasses (CO₂, mix CO₂ with inert gasses). Very often it is used to connection this two abbreviations MIG/MAG, because at present the blend of protective gasses, which are using in processes, are multicomponent. That's why the abbreviation GMAW Gas Metal Arc Welding) is more and more universally, which including all kinds of protective gasses in one's description [1]. One of the basic requirements taken into account when selecting appropriate mixture of curtain gases is easiness of their ionization so that to ensure maintaining a stable welding arc.

The ability to compete depends, to a great extent, on being able to provide top quality of products and services [2]. This is why so much emphasis is put on keeping statistics related to failing to provide adequate level of quality.

2. Analysis of Welding Incompatibilities

The entire process comes down to making an inseparable joint of elements which will be performing the previously determined requirements concerning the quality.

In order to make a high quality weld certain parameters in the area of material and immaterial factors must be kept. In the case of immaterial factors one should take into account materials' quality, appropriate technology (welding parameters). Immaterial factors are related to the process functioning (organization, procedures, instructions), as well as to the staff's experience and qualifications.

Every single deviation from an ideal welded joint is called a welding incompatibility. Reasons causing such incompatibilities to occur can be divided into three basic types:

- material and metallurgical (changes of structure, segregation of components, voids, micro cracks),
- construction joints (cracks caused by stress concentration, improper form of the weld),
- technological (being a cause of most incompatibilities) [3].

Analysis of welding incompatibilities includes the welded joint considered as a geometrical fragment of a welded structure, since they can be present in the joint itself or outside the joint, in the Heat Affected Joint, even in native material, e.g. lamellar cracks. Pursuant to PN-EN ISO 6520-1 standard welding incompatibilities are classified into six groups: 1 – cracks – tears in solid state, both in the joint's metal, in the heat impact zone, as well as in the base material, which can be caused by cooling or stresses; 2 – voids – deficiencies in the joint's metal formed by gas that got inside it; 3 – permanent inclusions – foreign bodies trapped in the joint's metal; 4 – incomplete fusion and lack of weld penetration – no or too shallow joints between the joint's metal and the base material; 5 – discrepancies related to shape and dimension – inadequate shape of the joint's external surface or incorrect geometry of the connection; 6 – various welding incompatibilities – all incompatibilities that can be classified as belonging to group 1 - 5 [4]. Fig. 1 presents the types of welding incompatibilities occurring in the research company.

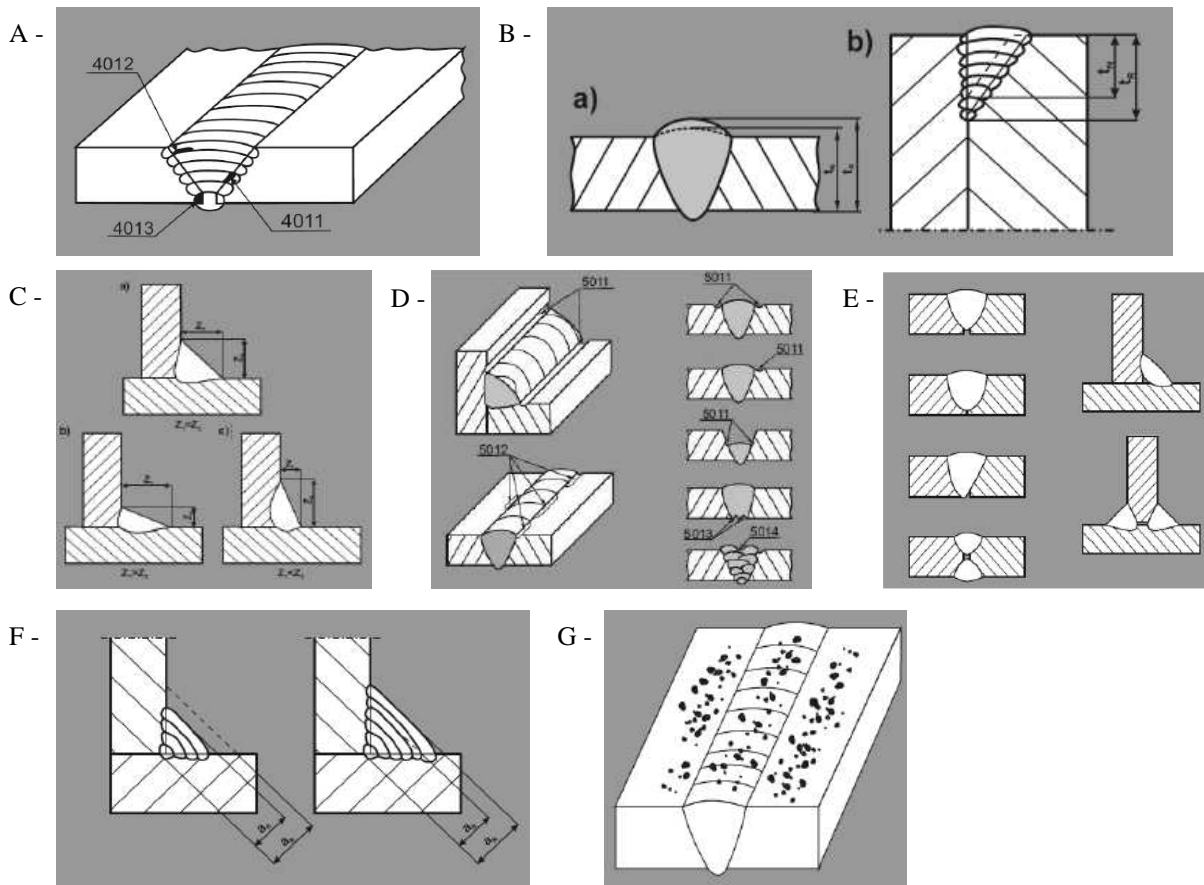


Fig. 1. Scheme of welding incompatibilities in researches company: a – incomplete fusions, b – excessive bulge of the joint, c – wrong geometry of the made weld, d – undercuts, e – lack of joint penetration, f – insufficient thickness of the joint, g – metal spattering.

The most common incompatibility in the examined company are undercuts “Fig. 1d”, i.e. irregular grooves just at the joint's edge. Incompatibility marked as No. 602 in the standard “Fig. 1g” is formed when binder's particles spatter during the welding process and stick to the basic material's surface or the solidified joint. Incompatibilities presented in Fig. 1c and 1f refer to welding in a fillet position and geometry of the made weld. Yet another incompatibility related to the weld's shape is excessive bulge of the joint. In the analyzed company the incompatibility is present both in welds made in butt welds (weld reinforcement) as well as in fillet welds “Fig. 1b”.

Incomplete fusions “Fig. 1a” is a lack of metallic continuity which occurs between the joint and the welded materials (lack of side fusion). The incompatibility occurs in a place where full fusion of one of the welded materials did not occur. Repair of the joint in which incomplete fusions occur means a complete removal (grinding off) of the weld and making it again. The incompatibility related to the lack of joint penetration “Fig. 1e” occurs when a weld of a depth smaller than assumed in the project is made. Occurrence of this incompatibility causes asymmetrical load of the butt joint and extra bending stresses.

3. Formation of Blisters in Welding Joints

Yet another group of incompatibilities occurring in the processes are surface blowholes, a presented in Fig. 2.

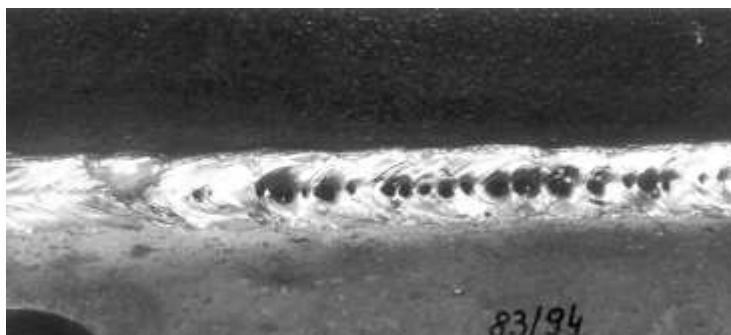


Fig. 2. Samples of a weld with an incompatibility - surface blowholes.

Surface blowholes are formed by gases closed in the weld which, due to the fact they are situated near the weld surface, break its surface forming visible holes, as presented in Fig. 2. In many cases gases solved in a liquid metal intensively react with components present in the liquid thus forming non-metallic inclusions. With time, when the metal temperature decreases, a part of the solved gases comes out from the solution and can be trapped in the metal when it solidifies. Components most conducive to formation of the blowholes are soluble oxides and carbon. In the blowholes formation process, gases trapped in the welds can come from the arc's gas atmosphere (hydrogen, steam, oxygen, carbon oxide and dioxide, nitrogen), from basic or additional materials (atomic hydrogen, oxygen and nitrogen in a form soluble in alloys) and gases formed from metallurgical impurities, such as sulphur, sulphides and metal oxides) [5, 6].

Unfortunately, not all blowholes are situated near the surface and, by breaking the surface, forming surface blowholes. In the standard a group of incompatibilities including "voids" in the welds is distinguished. A part of the blowholes is trapped inside the metal thus forming spherical or canal blowholes. A small number of fine blowholes is not of great impact on resistance properties, while a greater number, of bigger size, or a cluster of blowholes causes a significant decrease in the weld's resistance and flexibility. Apart from resistance properties a significant issue is also leakproofness of the welded joint, especially in the case when canal blowholes are present.

4. Conclusion

The voids (blowholes) which are internal incompatibilities are not as dangerous as those protruding into the surface. Corrective actions for semi-products with incompatibilities such as: open voids (e.g. surface blowholes or cavities in the crater) will only include their total mechanical removal. This means re-welding of these elements after previous grinding off the weld in which such incompatibility is present. A general characteristics of reasons causing formation of blowholes during the welding process, along with ways of preventing this, has been presented in Fig. 3.

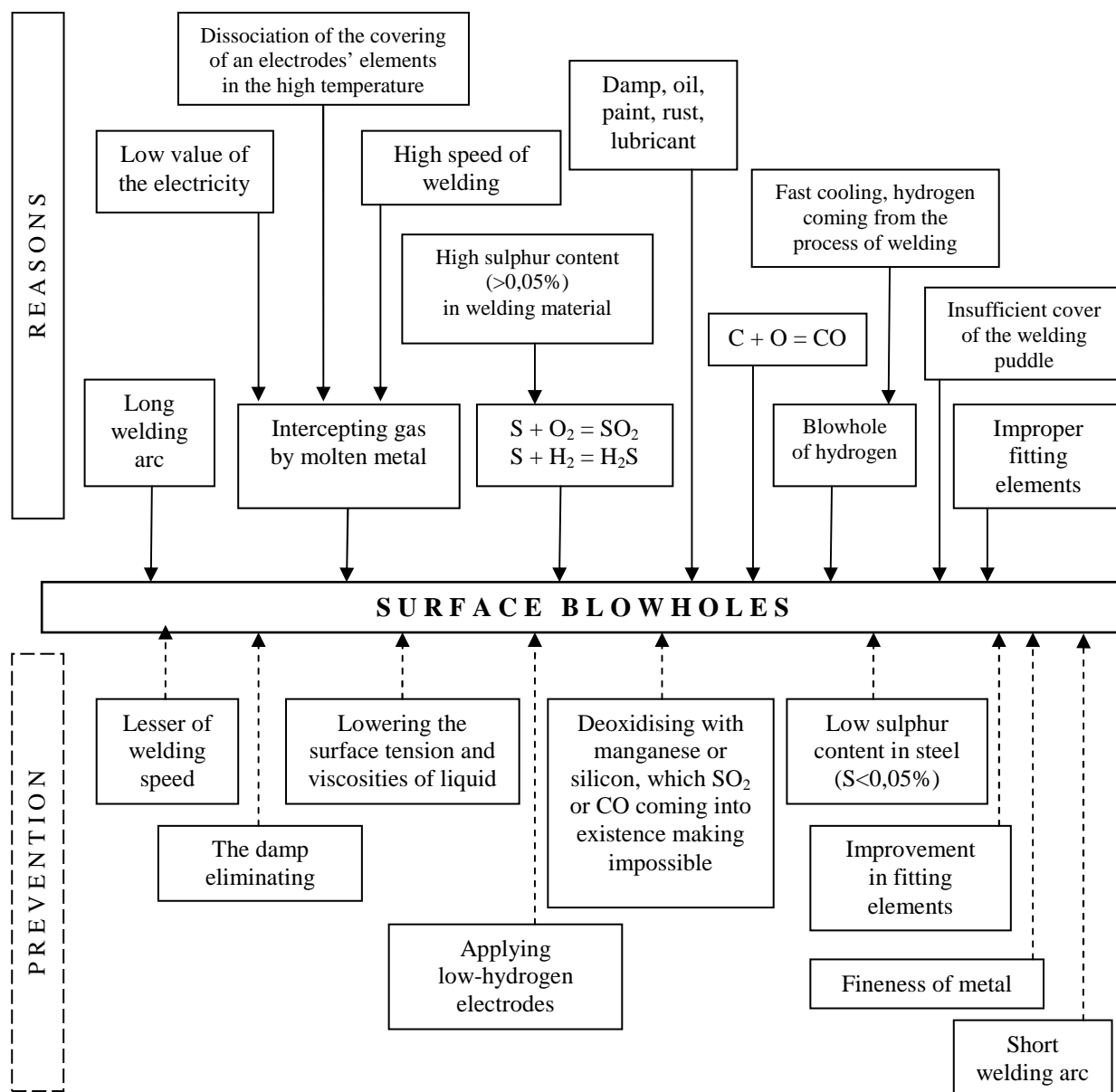


Fig. 3. List of factors having an impact on joints' porosity and the way of preventing them.

References

- [1] PTAK, W., TABOR, A. *Metody oceny jakości wyrobów metalowych: inżynieria produkcji spawalniczej*. Wydawnictwo Politechniki Krakowskiej im. Tadeusza Kościuszki, Kraków 2008.
- [2] KOPCIUSZEWSKA, E., BORKOWSKI, S. *Praktyczne wykorzystanie wybranych narzędzi jakości w celu uzyskania oczekiwanego poziomu jakości wyrobu z tworzywa sztucznego*, [w:] *Narzędzia jakości w doskonaleniu i zarządzaniu jakością*, pod red. Sikory T., Materiały konferencji naukowej, Kraków 2004.
- [3] FERENC, K. *Spawalnictwo*, Wydawnictwo Naukowo-Techniczne, Warszawa 2007.
- [4] PN-EN ISO 6520-1:2009 Spawanie i procesy pokrewne. *Klasyfikacja geometrycznych niezgodności spawalniczych w metalach*. Część 1: Spawanie. Polski Komitet Normalizacyjny, Warszawa 2009.
- [5] FERENC, K. *Technika spawalnicza w praktyce: poradnik inżyniera, konstruktora i technologa*. Wydawnictwo Verlag Dashofer, Warszawa 2007.
- [6] MAZUR, M., ULEWICZ, R., SZATANIAK, P. *Identification of Welding Incompatibilities in the Process of Semitrailers Production*, SEMDOK 2011. 16th International of PhD. Students' Seminar. Zilina - Terchova, Slovakia 2011



Heat Treatment Effect on the Mechanical Properties of Aluminum Alloy AlSi6Cu4 Modified by Antimony

*Dušan Medlen, *Dana Bolibruchová

*University of Žilina, Faculty of Mechanical Engineering, Department of Technological Engineering, Univerzitná 1, 010 26 Žilina, Slovakia, {dusan.medlen, dana.bolibruchova}@fstroj.uniza.sk

Abstract. AlSi6Cu4 alloy was selected for study in the present work due to its wide use in many applications. AlSi6Cu4 alloy is used in automotive and aerospace industries for the complicated castings, which must comply high strength requirements. In order to improve the mechanical properties of these alloys they are often heat treated using a two-step process (i.e. solution treatment and artificial aging). The effect of the heat treatment on the mechanical properties of the AlSi6Cu4 alloy modified by antimony has been investigated.

Keywords: Heat treatment, mechanical properties, AlSi6Cu4, modification, antimony

1. Introduction

The automotive industry has provided the impulse for the development of newer and better methods and manufacturing practices which are required by the more stringent requirements in modern automobiles. Lighter pieces are required to achieve reductions in fuel consumption without impairing the performance of vehicles. One of the more successful cases in weight reduction has been the substitution of grey iron by aluminium alloys in the manufacturing of combustion engines. AlSi6Cu4 alloys are used for castings of complicated shapes with different wall thicknesses. The most commonly are used for castings, which are moderately to highly stressed. (Engine blocks, heads and pistons, clutch housings, exhaust end, die-cast chassis). AlSi6Cu4 alloy is used in the automotive industry for 2.2 l Opel engine also BMW, Fiat, Citroën use this alloy to manufacture engine blocks and cylinder heads. In Slovakia is AlSi6Cu4 alloy used for cylinder heads for 1.6 l engines for Kia Ceed and in the Czech Republic for Skoda Fabia 1.2 TSI. [1, 2]

The structure and mechanical properties of AlSi6Cu4 alloys can be improved not only through modifying, grain refinement but also through applying heat treatment and other technologies. In practice, the most common elements with the modifying effect are strontium, sodium and antimony. Adding these elements leads to a change in the shape of eutectic silicon, resulting in an increase of the mechanical characteristics of alloys and toughness. [3]

2. Experimental Procedure

2.1. Melt Treatment and Casting Procedures

The experiments were carried out in the foundry laboratory of the Department of Technological engineering at the University of Žilina, where as the experimental material was used alloy AlSi6Cu4. Chemical composition of the alloy is listed in Tab. 1. The melting process and the modification were carried out in a graphite-chamotte melting crucible in an resistance oven. The grain refinement process using refining salt AlCuAB6 was carried out while overheating the metal bath to $730\text{ }^{\circ}\text{C} \pm 5\text{ }^{\circ}\text{C}$. The modification process using antimony was carried out under the same technological conditions.

The amount of antimony chosen for each cast is listed in the Tab. 2. This amount was determined based on the most widely used quantities shown in the literature for Al-Si-Cu based alloys.

Elements	Si	Fe	Cu	Mn	Mg	Ni	Zn	Ti	Cr
(wt.%)	6,52	0,43	3,88	0,45	0,29	0,01	0,46	0,15	0,01

Tab. 1. Chemical composition of the AlSi6Cu4 alloy

Number of cast	1	2	3	4	5	6	7	8	9	10	11
Amount of Sb (ppm)	0	100	300	500	800	1000	1500	2000	2500	3000	10000

Tab. 2. Amount of antimony for each cast of AlSi6Cu4 alloy used in the present work

2.2. Heat Treatment

Heat treatment is used to obtain the optimal combination of strength and ductility in a casting. It involves: a) solutionizing to thermally prepare the material; b) quenching to retain the maximum concentration of age-hardening constituent (Mg_2Si , Al_2Cu) in solid solution and c) a combination of artificial and over-ageing to obtain the desired mechanical properties in the casting, solution treatment performs three roles:

- Homogenization of as-cast structure.
- Dissolution of certain intermetallic phases such as Mg_2Si and Al_2Cu .
- Changes the morphology of eutectic Si phase by fragmentation, spheroidization and coarsening, thereby improving mechanical properties, particularly ductility. [4]

Most of the recommended heat treatment of alloys that contain copper restricts the solution temperature below the final solidification point in order to avoid the melting of copper-containing phases. For ageing it is used to precipitate Mg_2Si and Al_2Cu from solid solution to form regions of solute segregations known as GP (Guinier–Preston) zones. GP zones give increases in strength properties but reduction in ductility. [4]

The solution treatment “Fig. 1” was at 510 °C for 6 h, quenched in water at 60 °C, and artificial ageing at 170 °C for 8 h, then they cooled out of the furnace.

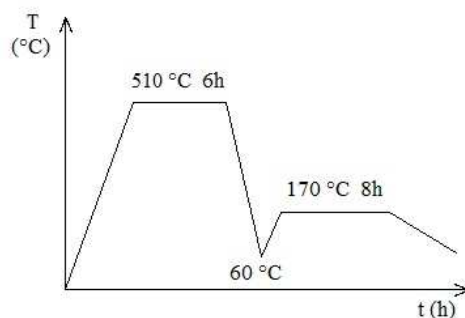


Fig. 1. Used heat treatment of AlSi6Cu4 modified by antimony

2.3. Mechanical Properties

There were 6 samples cast, of which they were made test bars for tensile testing according to EN 10002-1. 3 of them were given a solution heat treatment and other 3 were left in “as cast” condition. The tensile test was performed on a tensile machine ZDM 30 at 21 °C. Values of ultimate tensile strength (UTS) determines the average value of 3 test bars “Fig. 2”. Percent elongation “Fig. 3” was for each sample calculated using mathematical formulas. When measuring the Brinell hardness on the measuring

device CV-3000 LDB, the parameters used were HBS 5/250/15. Hardness values were determined as average values of 5 measurements on one sample of the each cast “Fig. 4”.

Fig. 2a shows increasing amount of the modifying element - Sb, increases ultimate tensile strength. To increase the ultimate tensile strength of not heat-treated (as cast) alloy AlSi6Cu4 about 5 to 10%, is the most appropriate amount of Sb in the range from 1000 to 2500 ppm. Higher amount of modifier has led to a reduction of ultimate tensile strength.

Fig. 2b shows relationship between ultimate tensile strength and amount of antimony for heat treated AlSi6Cu4 alloy. In case of heat treated AlSi6Cu4 alloy UTS for 0 ppm of Sb is 402,7 MPa. Highest value of UTS = 416,77 MPa has been achieved at the amount of Sb is 1000 ppm. Based on experimental works can be claimed at higher amount of Sb than 1000 ppm, there are lower values of UTS.

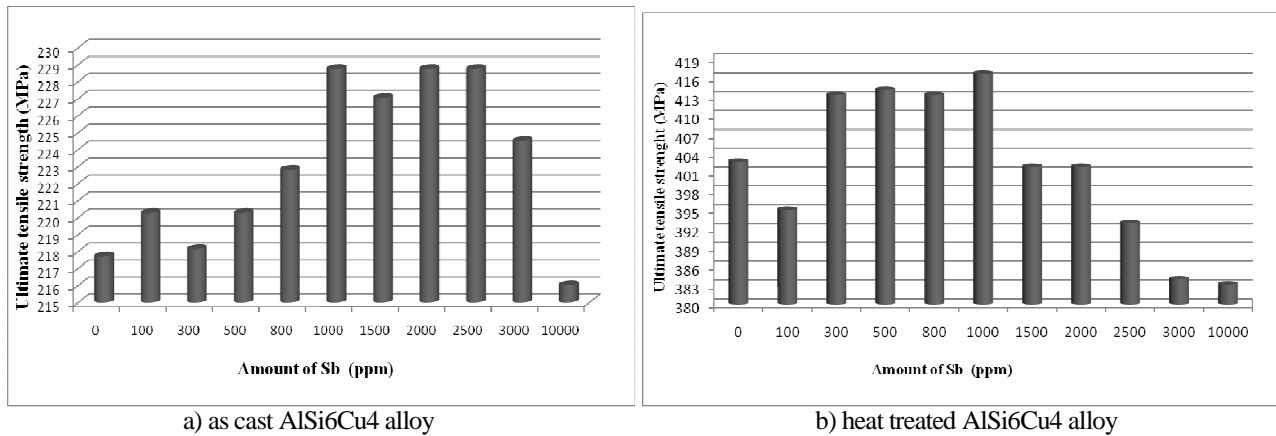


Fig. 2. Relationship between ultimate tensile strength and amount of antimony (ppm)

Fig. 3a demonstrates the as cast AlSi6Cu4 alloy subjected to modification by antimony exhibits very low values of percent elongation, where the highest value of $A_5 = 0.464\%$ was measured in amount of 2000 ppm Sb for as cast AlSi6Cu4 alloy.

Fig. 3b shows effect of heat treatment on AlSi6Cu4 modified by antimony on elongation. Values of elongation increase to 100 % in comparison of AlSi6Cu4 not heat treated alloy with matching amount of Sb.

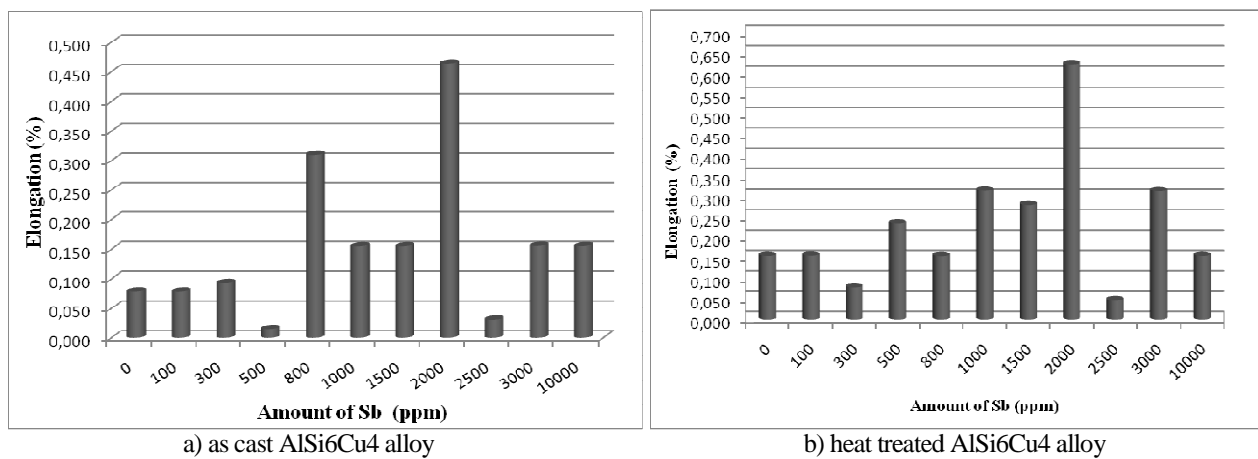


Fig. 3. Relationship between elongation and amount of antimony (ppm)

Fig. 4a shows the relationship between Brinell hardness and amount of antimony. Alloy AlSi6Cu4 reported, in unmodified state, HBS = 109,3. The highest Brinell hardness was measured at 100 ppm Sb HBS = 112,3. The lowest measured value was HBS = 100,3 corresponding to 2500 ppm Sb, which compared with the unmodified state of alloy AlSi6Cu4 was up to 9% reduction in Brinell hardness.

Hardness is one of the most important metallurgical parameters that can control the alloy machinability. In fact, aluminum alloys differ from many other metals in that the machinability of aluminum generally improves as the hardness increases. Most automotive machine shops agree that a minimum hardness of 80 Brinell is desirable. [5]

Fig. 4b shows Brinell hardness of Sb-containing AlSi6Cu4 alloy. The highest Brinell hardness was measured at 2500 ppm Sb HBS = 149,6.

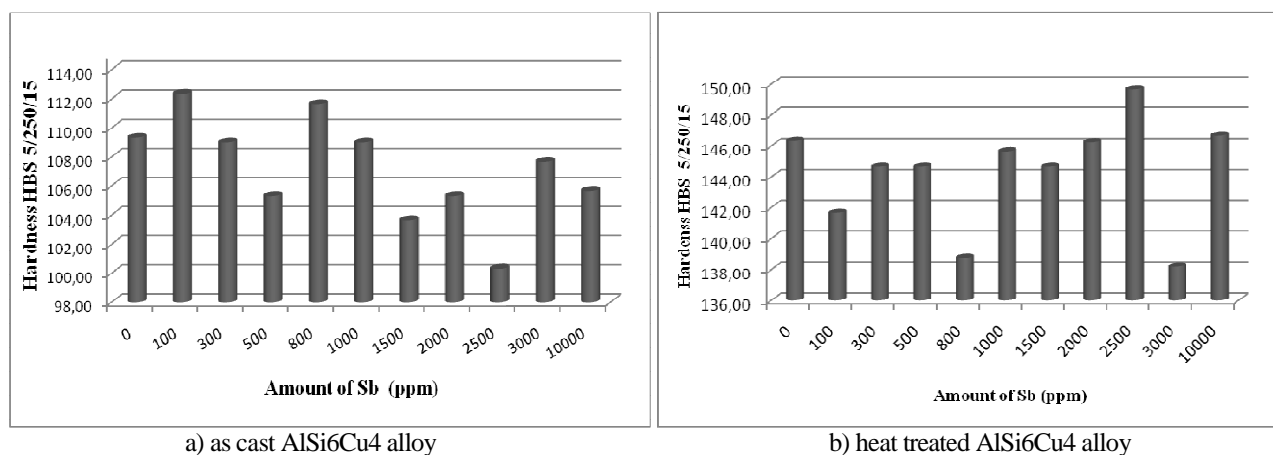


Fig. 4. Relationship between Brinell hardness and amount of antimony (ppm)

3. Conclusion

Based on the experiments can be claimed, that the most appropriate amount of antimony for non heat-treated AlSi6Cu4 alloy is 2 000 ppm Sb. Unmodified AlSi6Cu4 according to experimental works has ultimate tensile strength $R_m = 217,72$ MPa at the highest measured elongation $A_5 = 0,078\%$ and Brinell hardness $HBS = 109,33$. The results of mechanical tests show that for such amount of the modifying element, alloy has an ultimate tensile strength $R_m = 228,76$ MPa at the highest measured elongation $A_5 = 0,464\%$ and Brinell hardness $HBS = 105,33$.

For heat-treated Sb containing alloy AlSi6Cu4 recommended amount of Sb is same as for non heat-treated AlSi6Cu4 alloy, namely 2 000 ppm Sb. Ultimate tensile strength for such treated AlSi6Cu4 is $R_m = 416,77$ MPa which means increase of 4% comparing to heat-treated unmodified AlSi6Cu4. Elongation of AlSi6Cu4 has increased from $A_5 = 0,156\%$ 0 ppm Sb, to $A_5 = 0,625\%$ 2 000 ppm Sb meaning 400 % increase. Brinell hardness $HBS = 146,25$ of AlSi6Cu4 modified by 2 000 ppm of Sb remained on the same value in comparison with unmodified heat-treated AlSi6Cu4.

Acknowledgement

The authors wish to thank European Regional Development Fund for received financial support to create present paper within execution of the project "Equipment for the production of prototype parts by casting on a computer-controlled base" with ITMS code 26220220047.

References

- [1] MEDLEN, D., BOLIBRUCHOVÁ, D. *Theoretical studies of AlSi6Cu4 alloys*, Technológ Vol. 2, 2010 151-156
- [2] GRZINCIC, M. *Manufacturing trends for engine blocks of automobiles*, Slévárenství Vol. 2-3, 2003 74-80
- [3] BOLIBRUCHOVÁ, D., TILLOVÁ, E. *Foundry Alloys Al-Si*, EDIS Žilina, 2005 180
- [4] GARCIA-GARCIA, G., ESPINOZA-CUADRA, J., MANCHA-MOLINAR, H. *Copper content and cooling rate effects over second phase particles behavior in industrial aluminum-silicon alloy 319*, Coahuila, 2005
- [5] TASH, M., SAMUEL, F.H., MUCCIARDI, F. *Effect of metallurgical parameters on the machinability of heat-treated 356 and 319 aluminum alloys*, Materials Science and Engineering A 434, 2006



Analysis of W.Nr. 1.2311 and W.Nr. 1.2311 Toolsteels Used for Less Stressed Components of Cold-Molding Tools.

* Borislav Melo, ** Ján Moravec

* Viena international s.r.o., Kráčiny 2, 036 01 Martin, melo@viena.sk,

** Žilinská univerzita Žilina, Univerzitná 1, 010 26 Žilina, jan.moravec@fstroj.uniza.sk

Abstract. Correct selection of material for components of cold-molding tools is one of basic expectation of its failure-free works. Analysis for use of W.Nr. 1.2311 toolsteel and its comparison with material W.Nr. 1.2312 for less stressed components of cold-molding tools is described in this paper.

1. Introduction

The final quality and utility features of molding tools are predestinated long time before semi-product or tool itself goes to the hardening room for heat processing. Lot of problems, which are connected with possible deformations and possible destruction of molding tools (or their parts) are generated by their design that means at design documentation before the material gets to producer [1]. The next aspect which affects the final usage attributes of the moulding tool, is choice of material itself. The aspect of brand (of chemical composition) has got a primary important role. Inadequate chosen brand can easily cause early end of service life of molding tool. Chemical composition (brand) of steel in majority of cases does not provide requested amount of informations about quality of material. The qualweity of steel is given by its origin, primary and secondary metallurgy, eventually subsequent processing as is annealing or molding. In the case of materials of the same brand, but supplied by two different manufacturets or suppliers differences of hardness after heat treatment can be more than 10%, in wear resistance tenths of percent and these materials can also differ in toughness.

2. Description of material W.Nr. 1.2311

High alloyed and heat treated Cr-Mn-Mo steel with low amount of sulphur, with high level of purity and homogeneity. It has got a perfect machinability, polishability and erodeability. It is suitable for case-hardening, nitriding, inductive hardening and flame hardening.

2.1 Usage

Less stressed components of cold-molding tools, big and medium forms and frames of forms for the processing of plastic materials and mechanical components with higher strength and toughness [2].

2.2. Chemical composition

Chemical composition of material is listed in Tab. 1.

C	Si	Mn	P	S	Cr	Mo	Ni	V	W
0.35 – 0.45	0.2 – 0.4	1.3 – 1.6	Max. 0.035	Max. 0.035	1.8 – 2.1	0.15 – 0.25			

Tab. 1. Chemical composition of material W.Nr. 1.2311

2.3. Material equivalents

- By STN 19520,
- By DIN 40CrMnMo7,
- By Böhler M201,
- By W.Nr. 1.2311.

3. Description of material W.Nr. 1.2312

High alloyed and heat treated Cr-Mn-Mo steel. Amount of sulphur ensures high machinability also in heat treated condition. Polishability is good. Because of high ability of heat treatment into the depth of material the balanced hardness in the whole cross-section is ensured. It is suitable also for nitriding, as well as case-hardening and hard-chrome plating.

3.1. Usage

Less stressed components of cold-molding tools, big and medium forms and frames of forms for the processing of plastic materials and mechanical components with higher strength and toughness [2].

3.2. Chemical structure

Chemical composition of material is listed in Table 2.

C	Si	Mn	P	S	Cr	Mo	Ni	V	W
0.35 – 0.45	0.3 – 0.5	1.4 – 1.6	Max. 0.03	0.05 – 0.1	1.8 – 2.0	0.15 – 0.25			

Tab. 2. Chemical composition of material W.Nr. 1.2312

3.3. Material equivalents

- By STN ~19520,
- By DIN 40CrMnMoS8-6,
- By Böhler M200,
- By W.Nr. 1.2312.

4. Analysis of the damaged part

The clamp plank of active part of molding tool should be made from the W.Nr.1.2311 steel. During the production the confusion of material has happened and the detail was made from the 1.2311 steel. By the load of tool the clamp plank was destroyed.

At the clamp part, in the place of radius, the linear dint in transverse direction of material can be seen (Fig. 1). From this place the disruption which lead to the overall destruction of the detail was initiated.

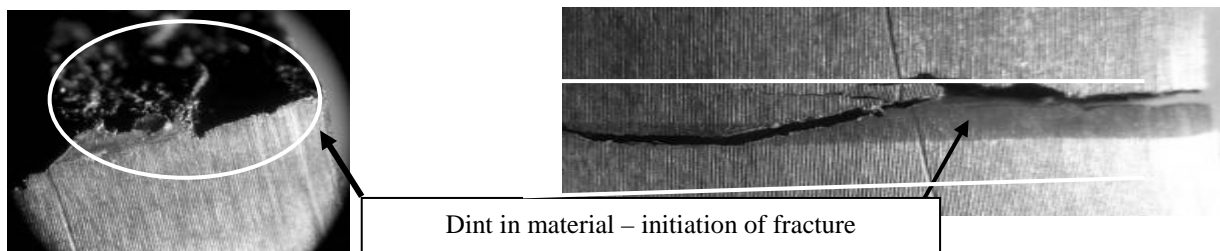


Fig. 1. Initiation of fracture - dint by companion part in transverse direction

4.1. Macrofractographic analysis

In this case it is mixed fracture with quite extensive ratio of fine and glossy facets of brittle fracture. The appearance of fracture is referring to heterogeneity of structure and presence of non-metallic inclusions (Fig. 2).

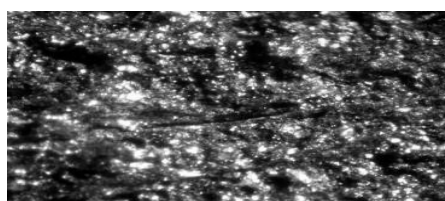


Fig. 2. The surface of breakage of the clamp plank, magnification 10x

4.2. Evaluation of microstructure and hardness of material

Microstructure of analyzed damaged parts was prepared by common metallographic procedure and evaluated at light microscope Neophot 2. Microstructure is quite heterogeneous, and it consists of tempered martensite, bainite and carbides (Fig. 3 and Fig.4). The marked diffusion is reflected by the marked heterogeneity of measured hardness, ranging in interval from 343 HV0.5 to 446 HV0.5.

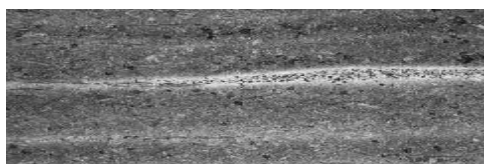


Fig. 3. Microstructure of the basic material, etching 3% Nital

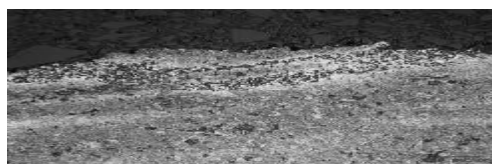


Fig. 4. Boundary line of the surface of fracture and basic material, etching 3% Nital

Measured values of hardness are listed in Tab. 3. The fracture surface expanded mainly along sulphidic inclusions (Fig. 5 and Fig.6), which are characteristic for used material.

1st part	343	395	446	380	357
2nd part	367	386	391	432	408

Tab. 3. Hardness HV 0.5 load 4.9 N (first and second part of clamp plank)

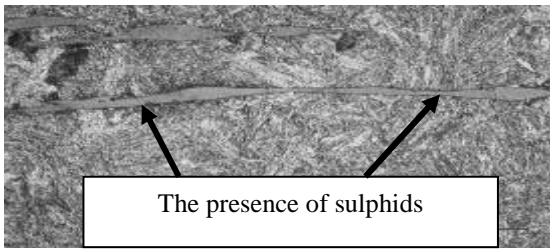


Fig. 5. The presence of sulphidic inclusions in basic material, etching 3% Nital

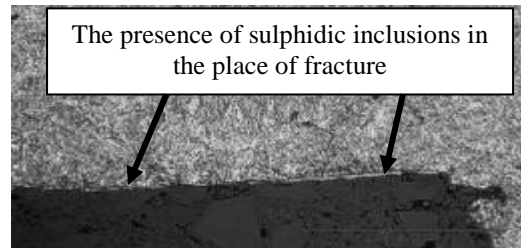


Fig. 6. The presence of sulphidic inclusions in the place of fracture, etching 3% Nital

5. Conclusion

The difference between materials W.Nr.1.2311 and 1.2312 in chemical structure is minimal; the difference is in amount of sulphur. In material 1.2311 the maximum allowed amount of sulphur is 0.035% but in material 1.2312 the maximum amount of sulphur is 0.1%.

Higher amount of sulphur signifies production of inclusions, which are called sulphids. These sulphids form non-homogeneity of material and as can be seen at the previous pictures, the fracture was expanding by the sulphidic lines. In praxis it means that higher amount of sulphur improves machinability but also reduces mechanical attributes as impact value.

Clamp planks of active parts cold-molding tools do not belong among the most stressed components of cold-molding tools, but in spite of that is very important to put emphasis on the right choice of materials for their production. Seemingly the same qualities of materials can have very different mechanical and hardness characteristics, too, which can result in different durability of parts produced from these materials. For the production of clamp planks it is advisable to use materials, which have ensured chemical structure, homogeneous composition and adequate hardness characteristics.

References

- [1] JURČI, P.: *Obecné zásady pro volbu a zpracování nástrojových materiálů*, Medzinárodná konferencia:21.dni tepelného spracovania, Jihlava 2006
- [2] Prospektová literatúra firmy Boehler – Uddeholm Slovakia, 2009



The Surface State of Materials after Thermal Cutting

*Stanislav Môcik, *Anna Mičietová, *Tomáš Berešík

*University of Žilina, Faculty of Mechanical Engineering, Department of Machining and Manufacturing Engineering, Univerzitna 1, 010 26 Žilina, Slovakia, {Mociks, Anna_micietova, Tomas.beresik}@fstroj.uniza.sk

Abstract. The paper deals with the quality of the machined surface after cutting of laser ray and plasma ray. In the experimental part is evaluated roughness and heat affected zone on the selected material.

Keywords: Laser, Plasma, heat-affected zone, roughness of the surface.

1. Introduction

Nowadays it is common to divide not only stock, but also produce finished components by laser ray and plasma. When making a decision to be taken into account a wide range of parameters. The most important criteria, which decides, is the final quality of the surface that can be achieved. It is clear that the technical requirements, directly or indirectly affect the economical and ecological aspects. The term quality cutting surface means the sum of the parameters by which we can assess whether the cutting surface meets the requirements that are required from it. These parameters are mainly cutting surface roughness, heat affected zone size, spacing and width of the cutting gap, which is an important technological factor. The effect on these parameters have: type of laser or plasma source and cutting parameters such as material properties.

2. The Quality of the Surface Formed by Laser Cutting

Surface formed by laser machining is characterized by formation of a striated traces cut. This trace cut arises as a result of the cyclical nature of the energy beam when interacting with the material as a result of oscillation of the melt flow. Laser ray in contact with the material results in their interaction, which are dependent on material properties. After impact of the laser ray, part of the rays are reflected, part are absorbed into the material. Absorbed rays heat the material to be melted by heating. Surface melting area is expanding rapidly and the material further intensive beam will vaporize. In the melting zone by vaporize arise relatively high pressures and melt is extruded and moved from arising hole of pressure vapor. The laser ray by dividing material moves forward, the melt begins to solidify, recrystallized and residual tensions arise [3].

Criteria for evaluation of surface quality after machining by laser ray is a few. Very important parameter by laser machining is ability of workpiece to absorb and reflect laser radiation. Other important parameters that we determine the final quality of the workpiece are by König [2] process parameters, material parameters and cut quality. Process parameters for laser ray cutting include: laser power, cutting speed, width the cutting gap, type of laser / mode, wavelength /, process gas, the focal length and diameter of focused beam. Among the material parameters belongs the physico-chemical properties of the material and geometry of the workpiece. Cutting quality is evaluated using the following parameters: width the cutting gap, rounded edges due to cutting, irregular edges, width heat affected zone (hereinafter HAZ), the formation of cracks, change the structure of the material surface, hardening, residual stress.

Depth HAZ associated mainly with the cutting speed and process gas. He is few tens of micrometers. Given the shape of parts may be the accumulation of heat and thus increase HAZ. If you avoid the creation of micro-cracks, it is possible HAZ removed by suitable annealing cycles.

3. Quality of the Surface Formed by Plasma Cutting

Heat source for plasma cutting is energy plasma ray, generated by ionization of the plasma gas in the electric arc and is concentrated by burner and focusing gas, or water spray. Plasma has a high energy density. Plasma stream exits the nozzle of burner with a great kinetic energy and melts the material. The melt is then blown from the cutting gap. The process is thus based on thermal and dynamical effects of the plasma. Plasma ray in contact with the material results their interaction, which are dependent on the material properties. The final quality of the cutting surface is dependent on cutting parameters and the material properties. Influencing factors by plasma cutting are particularly plasma gas and secondary gas (in gas burners with stabilization), cutting parameters (cutting speed, size, flow and pressure) and the workpiece. That was the best cut quality, must be specified in the workpiece material on cutting assessed the following parameters: surface material, surface treatment, electrical conductivity, thermal conductivity, melting point [1, 4].

4. Experiment

In the experiment was evaluated the surface roughness and heat affected zone. The material used in the experiment was EN ISO S235JR. Samples were cut on laser cutting machine Bystronic Bystar 4025 (Bystronic laser source Bylaser 4400) and the plasma cutting device Vanad Proxima (source Hypertherm HPR130) and in thicknesses 3, 4, 6, 8, 10 and 12 mm. For all samples used were optimal cutting parameters recommended by the manufacturer of laser and plasma devices.

4.1. Evaluation of Surface Roughness

Surface roughness is a summary of inequalities with relatively small distances, which usually contain inequalities that arose mainly used method of production. The surface roughness does not include surface defects, which occur only occasionally (eg accidental damage furrows) or those caused by material (eg cracks, holes). For an objective assessment of surface roughness were introduced various normalized roughness characteristics. In the experimental part of this work were observed R_a and R_z . During measurements, the surface roughness was observed according to the varying thickness of material. To measure the roughness of the surface roughness was used tester Mitutoyo used Surf test 301. The measurement was carried out at five different locations and from these values were calculated the arithmetic mean.

Conditions of experiments:

- Device: MITUTOYO Surf test 301.
- Measured temperature: 20 °C.
- λ_c/L : 2,5 mm.
- Assessment criteria: R_a , R_z .

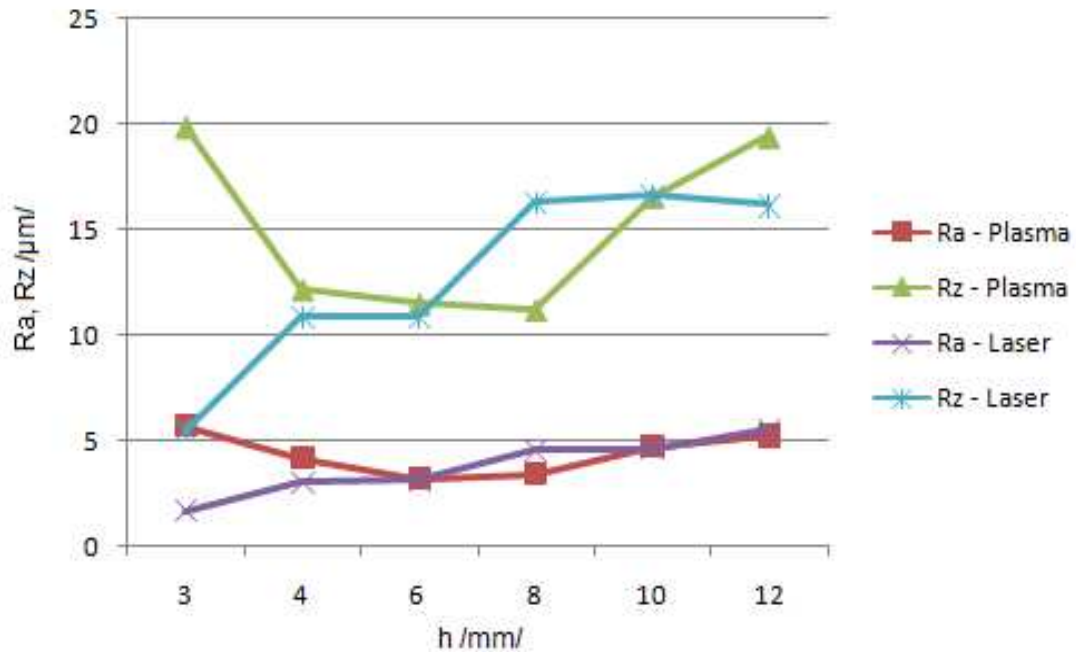


Fig. 1. Depending the surface roughness Ra and Rz of the material thickness after laser cutting and plasma.

4.2. Evaluation of Heat-Affected Zone

Heat affected zone is the area of material, in which was to influence the structure of the basic material due to high temperatures. During measurements, we monitored the size of heat affected zone, in depending on the chosen unconventional method of machining. Samples for metallographic evaluation were prepared as follows. Sample thickness of 6 mm on which was measured roughness, were cut on machine frame saw samples under continuous intensive cooling - is therefore excluded thermal effect on material by splinter division. Subsequently, they were pressed by the apparatus MTH PR30 in bakelite, polished and etched in the Department of Materials Engineering. On observation and subsequent documentation of microstructures was used NEOPHOT 32 microscope with a computer program Lucia 5.0 scale. The thickness of the heat affected zone was measured for the objectivity of the experiment at five different locations, then these values were calculated the arithmetic mean.

Materiál: EN ISO S235JR	Size of heat affected zone / μm /
Unconventional method of cutting	
Laser	120
Plasma	340

Tab. 1. Size of heat affected zone.



Fig. 2. Microstructure of HAZ. Steel EN ISO S235JR. Magnification: 100x. Etched Nital 3%. Laser cut.

5. Conclusion

The issue of state surfaces created by thermal machining process is very complex. There are countless variables that affect the surface condition and must be taken into account. Any change in parameters will affect on the surface after thermic machining. The aim of the experiment was to compare the cutting laser ray and plasma ray in terms of the achieved surface roughness and size of heat affected zone. The roughness measurement results show that only the thickness of the material 3 and 4 mm was achieved roughness Ra less by cutting laser than plasma. The results of the heat affected zone is clear that this area was by cutting laser ray less. The experiment showed a much smaller thermal effect on material in the cutting laser ray.

References

- [1] HÍREŠ, O., PERNIS, R., JURENOVÁ, J. *Charakteristika chýb na povrchoch rezaných plazmou*: Hradec nad Moravicí: Metal 2007
- [2] KONIG, W. *Fertigungsverfahren Band 3*. Düsseldorf: VDI Verlag, 1990. 221 s. ISBN 3-18-401018-X
- [3] MAŇKOVÁ, I. *Progresívne technológie*. Košice: Viena, 2000. 275 s. ISBN 80-7099-430-4
- [4] MIČIETOVÁ, A. *Nekonvenčné metódy obrábania*. Žilina: EDIS. 2001. 376 s. ISBN 80-7100-853-2



Corrosion Resistance of Ti6Al4V Titanium Alloy With Electroerosive Modified Surface

Rastislava Mráziková*, Branislav Hadzima*, Lenka Škublová*

*University of Žilina, Faculty of Mechanical Engineering, Department of Materials Engineering, Univerzitná 1, 01026 Žilina, Slovakia, {rastislava.mrazikova, branislav.hadzima, lenka.skublova}@fstroj.uniza.sk

Abstract. Corrosion behavior of biocompatible Ti6Al4V titanium alloy has been investigated by using electrochemical impedance spectroscopy in Hank's physiological solution for two modified states of titanium surface. Based on the type and shape of Nyquist diagrams obtained from EIS measurements there are assigned probable mechanisms of corrosion in specific corrosion system.

Keywords: corrosion resistance, Ti6Al4V titanium alloy, biocompatibility, EIS

1. Introduction

Titanium and its alloys belong to materials with very high biocompatibility. This material can be widely used because of its low specific density, sufficiently high strength, ductility, corrosion resistance and excellent biocompatibility. Natural oxide layer formed on the surface of pure titanium may consist of different titanium oxide (TiO_2 , TiO and Ti_2O_3), while the Ti6Al4V alloy, which contains alloying elements as aluminum and vanadium forms layer of Al_2O_3 or V_2O_5 on its surface. Vanadium may cause changes in the kinetics of the cell's enzymatic activity which could leads to inflammation [1, 2, 3].

Titanium alloys have good corrosion resistance in almost all saline solutions with pH from 3 to 11 (pH of saline solution is about 7,4). Corrosion rate of titanium alloys in various saline solutions is generally less than 0.03 mm/year. Titanium is mechanically and chemically suitable for orthopedic and dental implants, but there is no biological activity that is necessary to join implant with bone tissue. Many various treatments of surface had been developed to improve biological activity and osteoconductivity of the titanium implants [4, 5].

The main objective of the presented work is the assessment of corrosion resistance of the Ti6Al4V titanium alloy with electroerosive treated surface.

2. Experimental material

Titanium and titanium alloys are non-toxic and well tolerated by the human body. Any of implants must have a secure stability (20 years) in biological fluids, which are composed of salt solutions [6].

As experimental material was used Ti6Al4V titanium alloy, that is widely used in medicine, with standardized chemical composition listed in tab. 1 [6].

Samples were divided into two groups according to the type of surface modification:

- group I – samples with untreated surface (base material of Ti6Al4V alloy),
- group II - samples prepared from Ti6Al4V alloy with electroerosive treated surface (at 29 A discharge).

2.1. Microstructural analysis

Microstructure of Ti6Al4V titanium alloy (Fig. 1a) is biphasic. It consists of elongated polyedric grains of α phase (light grains with average grain size $\sim 6.25 \mu\text{m}$) and of β phase (dark

grains with average size $\sim 5 \mu\text{m}$). Detail of the surface profile after the electroerosive treatment is shown in Fig. 1b. An average high of the modified surface profile is $\sim 190 \mu\text{m}$.

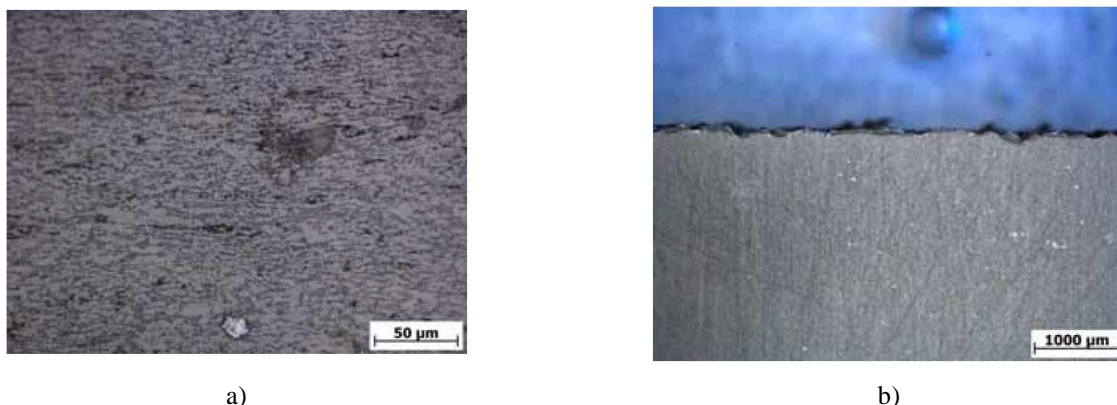


Fig. 1. a) Microstructure of Ti6Al4V titanium alloy, etched in 2 ml HF + 8 ml HNO₃ + 90 ml H₂O [7] , b) surface profile of electroerosive treated surface of Ti6Al4V alloy.

3. Evaluation of corrosion

Electrochemical characteristics were measured by electrochemical impedance spectroscopy (EIS) in Hank's saline ((8 g/l NaCl; 0,4 g/l KCl; 0,14 g/l CaCl₂; 0,1 g/l MgSO₄.7H₂O; 0,06 g/l KH₂PO₄; 0,05 g/l NaH₂PO₄.H₂O a 1 g/l D-glucose [6]) at the temperature of the human body (37°C). EIS method allows to determinate polarization resistance of less conductive corrosion systems, e.g. with sample covered by oxide layer. Polarization resistance R_p is the electrochemical characteristic that characterizes the properties of material's surface in the environment. Higher value of polarization resistance means higher corrosion resistance of the interface metal-electrolyte. To measure the characteristics was used Radiometer Analytical SAS France, Voltalab 10 with a measuring cell PGZ 100 and rotating electrode. Principle of the involvement and measurement is stated in the literature [8,9].

Times of free potential settlement of the samples in electrolyte and frequency ranges are shown in Table 1. AC voltage amplitude was 20 mV. The DC source, which ensures the polarization of the sample during measurement, was set to free potential after settlement of the sample.

Time of settlement	Frequencies
5 min	100 kHz – 5 mHz
1 and 2 h	100 kHz – 10 mHz
4 h	100 kHz – 15 mHz
8 and 16 h	100 kHz – 25 mHz

Tab. 1. Times and frequencies used for EIS investigations.

4. Results

Results of the electrochemical impedance spectroscopy for samples with untreated surface are shown in form of Nyquist diagrams in Fig. 2a. Results for samples with electroerosive treated surface are shown in Fig. 2b.

Process and method of calculating of polarization resistance and other characteristics is described in literature [10,11]. Impedance spectrum of the alloy was evaluated by EC-Lab V9.32 using an equivalent circuit.

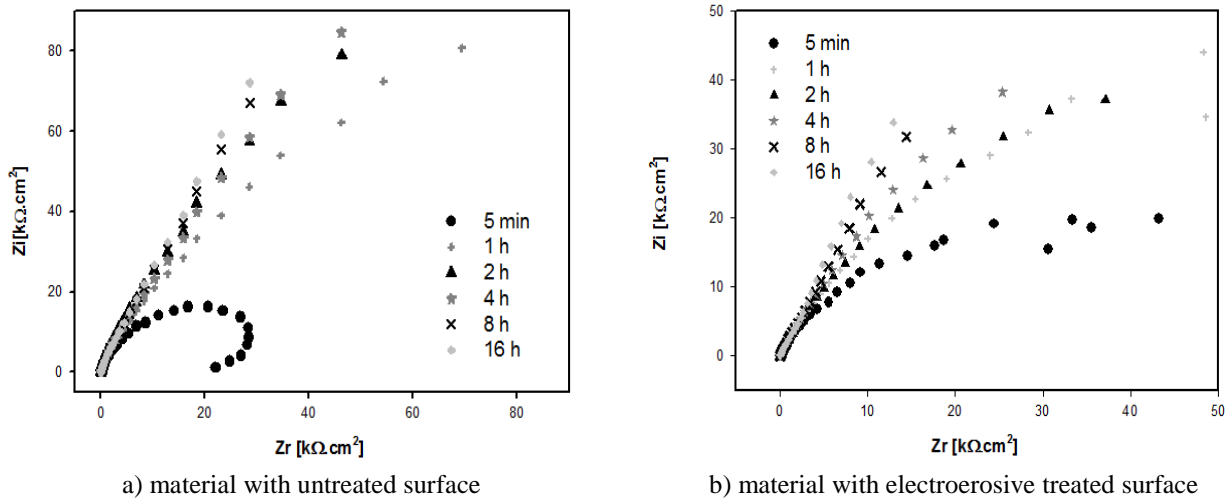


Fig. 2. Nyquist diagrams of Ti6Al4V alloy

Results of the analysis of Nyquist diagrams are listed in the Table 2.

	5 min.	1 h.	2 h.	4 h.	8 h.	16 h.
Untreated material R_p [kΩ.cm ²]	132.1	649.7	768.8	1014	1387	2707
Treated material R_p [kΩ.cm ²]	195.2	392.6	276.6	408.3	633.6	1189

Tab. 2. Values of the electrochemical characteristics of Ti6Al4V alloy with untreated surface in the Hank's solution.

5. Discussion

Results show that with increasing time of exposure, polarization resistance of interface metal – Hank's solution increase as well (tab. 2). Polarization resistance increases for both, sample without treated surface and sample with electroerosive treated surface. Increasing of polarization resistance is associated with increasing of the thickness of passive layer on the surface of the samples that is created immediately after samples are drafted in electrolyte.

The most likely cause is lower stability and higher inhomogeneity of passive layer caused by residual stresses on the surface after electroerosive treating. This can also leads to cracks in the passive layer. During 16 hours of exposure, polarization resistance increases to the value of 1.1 MΩ.cm², that is insufficient compared to basic material. Consequently, corrosion resistance of sample with electroerosive modification of surface is more than half lower than corrosion resistance of basic material.

6. Conclusion

Based on the results of electrochemical impedance spectroscopy the following conclusions were obtained:

- The value of polarization resistance increases during 16 hours of exposure for both samples, basic material and sample with electroerosive modified surface. In case of basic material, value of polarization resistance increases continuously with time of exposure. In case of material with electroerosive modified surface, value of polarization resistance increases between 5 minutes

and 1 hour of exposure. After, between 1 hour and 4 hours of exposure it stagnates and after 8 and 16 hours of exposure increases again.

- The values of polarization resistance show that electroerosive modification of the surface leads to its decrease in comparison with basic material. In this case, residual stresses generated on the surface during and after electroerosive treatment reduce not only its mechanical properties, but also its corrosion resistance. Basic material reached two-times higher values of polarization resistance ($2,7 \text{ M}\Omega\cdot\text{cm}^2$) in comparison with material with electroerosive modification of surface ($1,1 \text{ M}\Omega\cdot\text{cm}^2$).

Acknowledgement

The research is supported by European regional development fund and Slovak state budget by the project ITMS 26220220048 (call OPVaV-2008/2.2/01-SORO).

References

- [1] MIAO, S., WENG, W., LI, Z., CHENG, K., DU, P., SHEN, G., HAN, G.: *Electrolytic deposition of octacalcium phosphate/collagen composite coating on titanium alloy*. In: J Mater Med 20/2009, str. 131-134. ISSN 1573-4838
- [2] THAIR, L., KAMACHI, MUDALI, U., RAJAGOPALAN, S., ASOKAMANI, R.: *Surface characterization of passive film formed on nitrogen ion implanted Ti-6Al-4V and Ti-6Al-7Nb alloys using SIMS*. In: Corrosion Science 45/2003, str. 1951-1967, ISSN 0010-938X
- [3] VASILESCU, E., DROB, P., RADUCANU, D., CINCA, I., MARECI, D. CALDERON MORENO, J.M., POPA, M., VASILESCU, C., MIRZA ROSCA, J.C.: *Effect of thermo-mechanical processing on the corrosion resistance of Ti6Al4V alloys in biofluids*. In: Corrosion Science 51/2009, str. 2885-2896, ISSN 0010-938X
- [4] SHA, W., MALINOV, S.: *Titanium alloys: modelling of microstructure, properties and applications*. Woodhead Publishing, Cambridge, UK, 2009, str. 592, ISBN 1 84569 375 2
- [5] LOPEZ-HEREDIA, M. A., LEGEAY, G., GAILLARD, C., LAYROLLE, P.: *Radio frequency plasma treatments on titanium for enhancement of bioactivity*. In: Acta Biomaterialia 4/2008, str. 1953-1962, ISSN 1742-7061
- [6] ŠKUBLOVÁ, L., HADZIMA, B., BORBÁS, L., VITOSOVÁ, M.: *The influence of temperature on corrosion properties of titanium and stainless steel biomaterials*. In: Materials Engineering 15/2008, No. 4, str. 18-22, ISSN 1335-0803
- [7] PETZOW, G.: *Metallographic Etching*. 2nd Edition, ASM International, Ohio, 2001, str. 240, ISBN 978-0871706331
- [10] HADZIMA, B., LIPTÁKOVÁ, T.: *Základy elektrochemickej korózie kovov*, 1st. ed. EDIS ŽU, Žilina, 2008, str. 116, ISBN 978-80-8070-876-4
- [8] HADZIMA, B., JANEČEK, M., BUKOVINA, M., KRÁL, R.: *Electrochemical properties of fine-grained AZ31 magnesium alloys*. In: Ing. J. Mat. Res 100 (2009) 9, str.1213-1216, ISSN 1862-5282
- [9] ORAZEM, M. E., TRIBOLLET, B.: *Electrochemical impedance spectroscopy*. John Willey and sons, New Jersey, USA, 2008, str. 523, ISBN 978-0-470-04140-6
- [10] HAZLINGER, M., MORAVČÍK, R., ČAPLOVIČ, E.: *Degradačné procesy a predikcia životnosti materiálov*, STU Bratislava, Bratislava 2010, 223 p.
- [11] LIPTÁKOVÁ, T.: *Bodová korózia nehrdzavejúcich ocelí*. EDIS – ŽU v Žiline, Žilina 2009, 69 p.



Comparison of Machinability of Biocompatible Materials Use for Dental Implants

*Michaela Mrázová, *Jozef Pilc, *Dana Stančeková

*University of Zilina, Faculty of Mechanical Engineering, Department of Machining and Manufacturing technology, Univerzita 1, 01026 Žilina, Slovakia, {michaela.mrazova, jozef.pilc, dana.stanckova}@fstroj.uniza.sk

Abstract. Metallic materials, for example, stainless steel, titanium and its alloys, and tantalum are widely used for medical implants in trauma surgery, orthopaedic and oral medicine [1]. Successful incorporation of these materials for design, fabrication and application of medical devices require that they meet several critical criteria. Paramount is their biocompatibility as expressed by their relative reactivity with human tissues [4]. Another is their ability to provide sufficient mechanical strength, especially under cyclic loading conditions to ensure the durability of the medical devices made therefrom. Finally, the material should be machinable and formable, thereby, enabling device fabrication at an affordable cost. Numerous clinical studies of medical devices fabricated from commercial purity (CP) titanium for trauma, orthopaedic and oral medicine have proven its excellent biocompatibility [1].

Keywords: machinability, biocompatible materials, biomedicine.

1. Introduction

The material for dental implants is required to be biocompatible, mustn't be toxic and also shouldn't cause allergic reactions. It must have high ultimate strength R_m and yield point R_p with desirable low density and low modulus of elasticity E [2]. A problem in the course of the development of metallic biomaterials represents not only their actual or potential toxicity but also their allergenic potential [3]. Sensitivity of the population to allergens dramatically increases. An allergy on metals is caused by metallic ions, which are released from metals by body liquids. Commercial pure cpTi "Tab.1" stays the preferred material for dental applications "Fig. 1". It is desirable to increase its other mechanical properties without using even potentially toxic or allergenic elements preserving its low value of modulus of elasticity [2].



Quality	C [%]	Fe [%]	H [%]	N [%]	O [%]	Ti [%]
Grade 2	max. 0,08	max. 0,3	max. 0,015	max. 0,03	max 0,25	to 100
Grade 4	max. 0,08	max. 0,5	max. 0,015	max. 0,05	max 0,4	to 100

Tab. 1. Chemical composition of Ti based on ISO 5832 – 2

Fig. 1. Dental implant [5]

2. Machinability of Titanium Samples

Medical device manufacturers face tough challenges. Their customers are demanding ever smaller, more complex parts produced with extraordinary accuracies from hardmachining materials such as titanium. During the machining of titanium materials is very important the correct choice of cutting material, tool geometry, cutting conditions and cutting environment.

The Department of Machining and Manufacturing Technology, University of Zilina, supported by the grant agency VEGA, on the basis of developments and the progress of new materials and increasingly demanding requirements for accuracy, we started by identifying the basic technological conditions of machining titanium by turning, using a replaceable cutting edges of hard metal “Fig.3, Tab.2”, and intensification of cutting conditions on machining cylindrical samples of commercially pure titanium with a diameter $d = 4$ and 5 mm “Fig.2”.

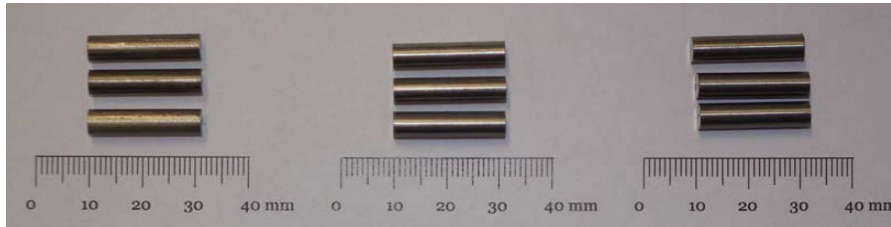
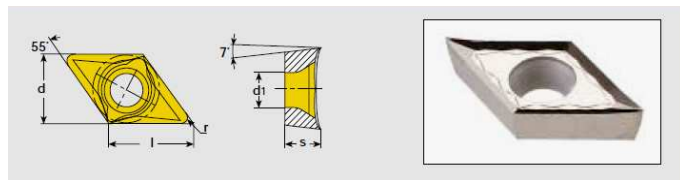


Fig. 2. a) sample of TiGr2 b) sample of TiGr4 c) sample of TiGr

	l	d	s	d_1	r
DCGT 070204	7,75	6,35	2,38	2,8	0,4



Tab. 2. Dimensional parameters of the cutting plate DCGT 070204

Fig. 3. Replaceable cutting edge DCGT 070204

In the experimental measurements were used dry environment as recommended by the manufacturer of cutting tools designed for hard turning, in order to avoid cracking due to thermal shocks. After evaluating the results, kinetic, dynamic and microgeometric machinability and also machinability in terms of shape chip showed that the most appropriate cutting conditions for turning titanium samples at a constant speed $n = 2200 \text{ m}\cdot\text{min}^{-1}$, are $a_p = 0,2$ mm (depth of cut) $f = 0,035$ mm (feed).

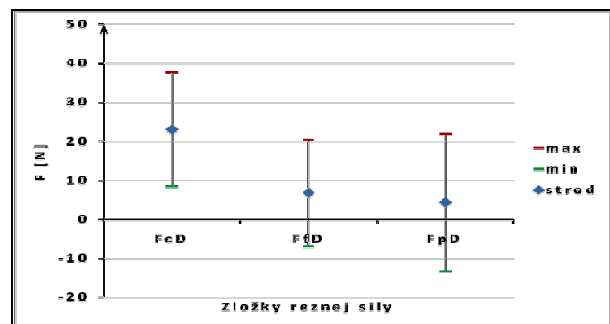
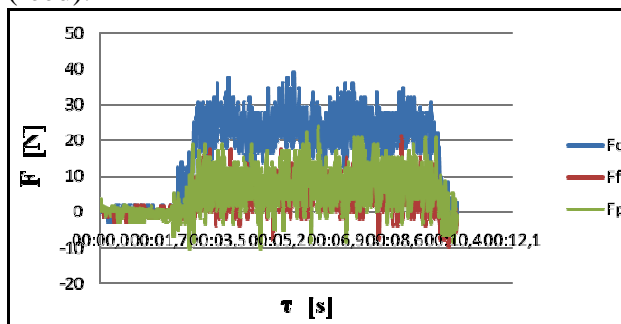


Fig. 4. An example of cutting forces waveform elements, with the cutting conditions: $a_p = 0,2$ mm, $f = 0,035$ mm, the material TiGr4 and also their dynamic elements.

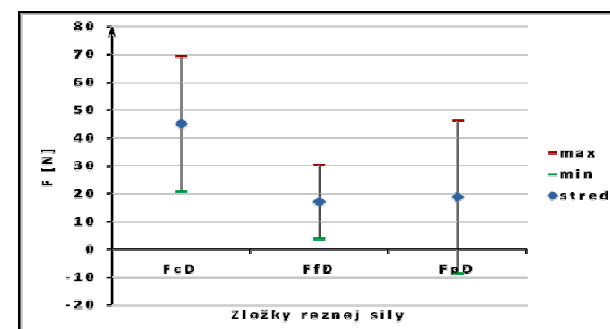
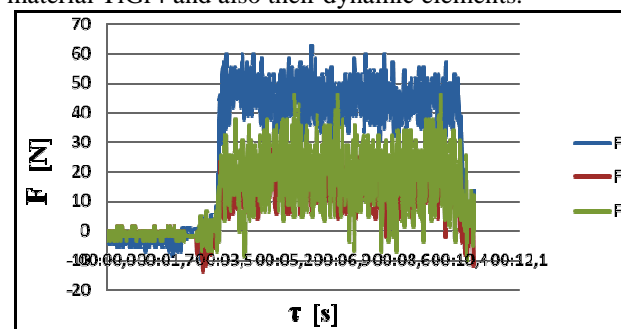


Fig. 5. An example of cutting forces waveform elements, with the cutting conditions: $a_p = 0,6$ mm, $f = 0,035$ mm, the material TiGr2 and also their dynamic elements.

Static values of cutting force elements for both the cutting edges with increasing feed were rising. The biggest impact on the size of elements of cutting forces is the depth of cut a_p . Replacing the edge did not significantly affect the value of static force elements “Fig. 4, 5”.

Dynamic machinability of considered material did not depend on the type of cutting edge. Compared to the reference material (TiGr2) the material TiGr4 shows the class better and TiGr5 equally machined “Fig. 6”.

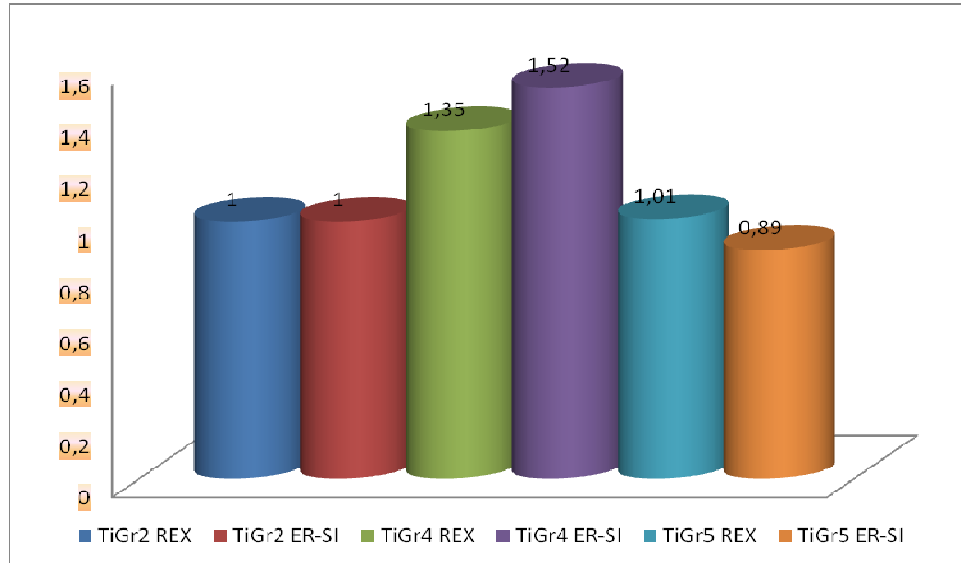

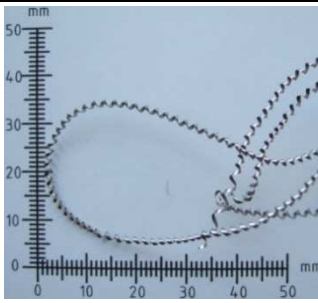

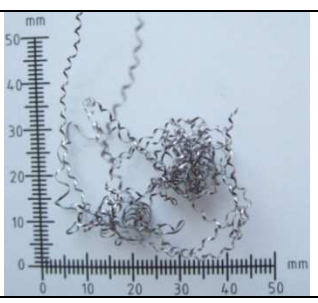

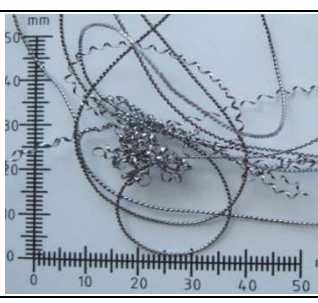








Fig. 6. Graphical representation of the dynamic machinability of compared materials

In point of view of cutting material was designated as suitable cutting plate DCGT 070204 ER-SI (polished), which is much more resistant to thermal shock in the cutting zone and has a greater wear resistance of 70-80% as a cutting plate DCGT 070204 REX (coated).

	TiGr2	TiGr4	TiGr5
a) REX			
	2.3	2.1	2.3
b) REX			
	1.3	1.3	2.1
c) ER-SI			

	5.1	4.1	2.3
ER-SI d)			
	5.3	5.1	5.3

Tab. 3. Example of chip shapes, on which was measurement evaluated.

The cutting edge DCGT 070204 ER-SI, as regards the shape of chip, in all experiments was appropriate than plate DCGT 070204 REX. This is thanks to the polished surface, which causes more resistance material, and the better chip removal “Tab. 3”.

3. Conclusion

On the basis of a grant from the Grant Agency VEGA Department of machining and manufacturing technology attempt to identify the cutting parameters in nanostructured titanium as well as in commercial pure titanium and compare them with each other, and thus continue to research material for dental implants.

References

- [1] BRUNETTE, P., TENGVALL, M., TEXTOR, P., THOMSEN, P. *Titanium in Medicine* (Springer-Verlag Berlin Heidelberg, Germany, 2001).
- [2] PETRUŽELKA, J., DLUHOŠ, L., HRUŠÁK, D., SOCHOVÁ, J. *Nanostructured titanium - application in dental implants*. Sborník vědeckých prací Vysoké školy báňské-Technické univerzity Ostrava, ISBN 80-248-1142-1, 1/2006, roč. 52, s. 177-186.
- [3] NIINOMI, M. *Recent metallic materials for Biomedical Applications*. Metallurgical and materials Transactions A. march 2002. vol 33 A. s. 477-486.
- [4] VALIEV, R. Z., SEMENOVA, I. P., DLUHOŠ, L., A KOL. *Nanostructured Titanium for Biomedical Application*. Advanced Engineering Materials 2008,10, No. 8, Weinheim, IF 1,463.
- [5] HRUŠÁK, D., DLUHOŠ, L., PETRUŽELKA, J. *Nanoimplantát - implantát 3. tisíciletí*. StomaTeam CZ, 2006,2, ISSN 1214-147X, s. 2-3.
- [6] RACK, HENRY, J. *Recent Advances in Titanium Alloys for Biomedical Device Application*, Professor at Clemson University, School of Materials Science and Engineering. (www.timplant.cz)
- [7] CZÁN, A., NESLUŠAN, M. *Trieskové obrábanie ťažkoobrábateľných materiálov*. Žilina: EDIS, 174 s. ISBN 80-969395-2-1.
- [8] BENES, J. *Machining titanium implants*, American Machinist, 17.8.2006
- [9] www.martikan.eu
- [10] www.timplant.cz



Influence of Gigacycle Fatigue on Development of Surface Relief in UFG Copper

*** Lucie Navrátilová, ** Ludvík Kunz, *** František Nový, *** Rastislav Mintách

* Brno University of Technology, Faculty of Mechanical Engineering, Institute of Material Science and Engineering, Technická 2, 61669 Brno, Czech Republic, {navratilova}@ipm.cz

** Academy of Sciences of the Czech Republic, Institute of Physics of Materials, Žitkova 22, 61662 Brno, Czech Republic, {kunz}@ipm.cz

*** University of Žilina, Faculty of Mechanical Engineering, Univerzitná 1, 01026 Žilina, Slovakia, {frantisek.novy}@fstroj.uniza.sk

Abstract. The paper deals with localization of cyclic plasticity in ultrafine-grained copper in gigacycle fatigue regime. The studied copper was prepared by equal channel angular pressing. The cyclic loading was conducted at 20 kHz frequency. It has been found that the cyclic slip bands do not appear well below the fatigue limit, contrary to the conventionally grained copper. Cyclic slip bands develop in “near-by oriented regions”. The length of the cyclic slip bands in these regions exceeds substantially the average grain size. The density of cyclic slip bands in specimens, which failed at 10^{10} cycles, is very low. Observation of surface relief and microstructure of cyclic slip bands by means focused ion beam technique in scanning electron microscope revealed the development of damage below the surface extrusions which finally results in fatigue crack initiation.

Keywords: gigacycle fatigue, UFG Cu, localization of cyclic plasticity, cyclic slips bands

1. Introduction

Fatigue properties of conventional grain (CG) size materials in low- and high-cycle region has been studied very extensively since a long time. The knowledge is described in a great number of textbooks and review publications, e.g. [1, 2]. It holds partially also for ultrafine-grained (UFG) materials, which has been studied intensively since the last two decades [3–5]. By contrast, fatigue properties in gigacycle region (alternatively called ultrahigh-cycle or very high cycle region) has been studied to substantially lesser extent, though fatigue failure of engineering components may appear after a number of cycles of 10^{10} or even higher [6].

Recent studies [7–11] concerning gigacycle fatigue behaviour distinguish two kinds of materials. The first one called Type I includes pure fcc materials like copper. To the second Type II belong high-strength materials containing microstructural heterogeneities. A bearing steel is a typical example. These two types differ by mechanism of fatigue crack initiation. In the case of the first type, fatigue loading in gigacycle region causes surface roughening and subsequent persistent slip band or cyclic slip marking formation, followed by fatigue crack initiation. Materials of the second type most frequently fail by forming of “fish-eye”, which is observed around heterogeneities in material interior, and subsequent propagation of an internal crack. Up to now performed studies of fatigue behavior in gigacycle region were focused on CG materials. Information on UFG materials is practically missing.

The aim of the present work is to extend knowledge on gigacycle fatigue of ultrafine-grained Cu, namely on the localization of the cyclic plastic deformation.

2. Material and experiments

Testing material was copper of commercial purity of 99.9% processed by equal channel angular (ECAP) method. The number of passes was equal to 8 by the B_C route, i.e. after each pass through the die the billet was turned over an angle of 90° along the longitudinal axis. Chemical composition of material is given in Tab. 1.

Cu, no less than	Impurity (%), no more than										
	Bi	Sb	As	Fe	Ni	Pb	Sn	S	O	Zn	Ag
99.9%	0.001	0.002	0.002	0.005	0.002	0.005	0.002	0.004	0.05	0.004	0.003

Tab. 1. Chemical composition of UFG Cu.

Specimens with a diameter of 4 mm in gauge section were manufactured from ECAPed billets. The gauge length of specimens was before fatigue loading fine-grounded, mechanically polished and finally electropolished. Specimens were loaded under constant stress amplitude in symmetrical cycle on an ultrasonic machine with loading frequency of 20 kHz.

Surface relief and microstructure of UFG Cu were investigated by means of scanning electron microscope (SEM) Philips XL30 and focused ion beam (FIB) equipped scanning electron microscope TESCAN LYRA\FEG.

3. Results and Discussion

Fatigue tests in gigacycle regime were conducted in a stepwise manner. The first specimen was loaded with the stress amplitude of 100 MPa for 1×10^{10} cycles. No cyclic slip markings were found by observation of the polished surface by SEM. Similarly the subsequent loading of the same specimen on the stress amplitude of 120 MPa for 8.64×10^9 did not result into formation of slip markings. As lately as the stress amplitude reached 130 MPa cyclic slip markings appeared on the surface and the failure occurred after next 5.18×10^9 cycles. The broken specimen is shown in Fig. 1. A detail of the fatigue crack with cyclic slip markings can be seen in Fig. 1b. The examination of the surface indicates that the density of cyclic slip markings elsewhere than near the crack is very low.

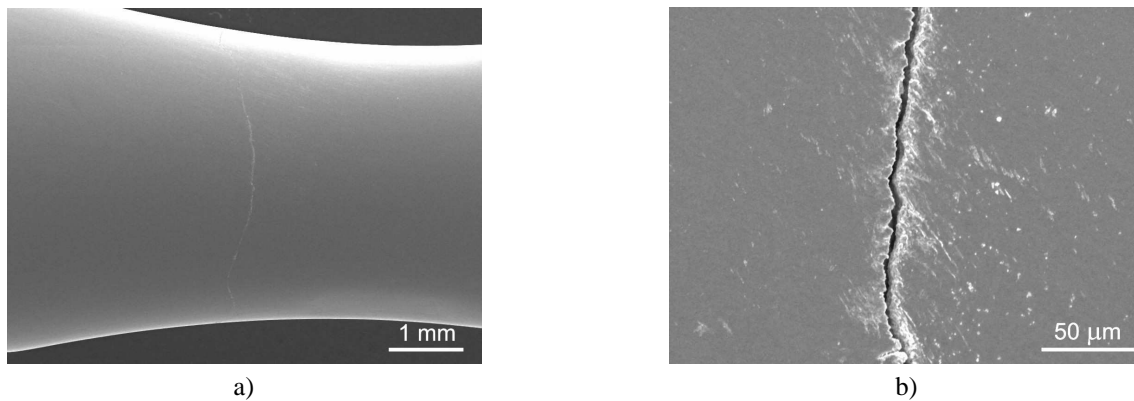


Fig. 1. a) Fatigue crack, b) fatigue crack with cyclic slip markings in its vicinity.

Fatigue slip markings developed after loading with the stress amplitude of 130 MPa as observed in SEM by means of secondary electrons are shown in Fig 2. The same area, but displayed by ion-induced secondary electrons, can be seen in Fig. 2b. It is obvious that the surface slip markings developed in the zone where the grey contrast of neighbouring grains is low. This means that the disorientation between grains is small and the zone can be called “zone of near-by oriented grains”. The length of the cyclic slip markings clearly exceeds the grain size, which is of 300 nm (determined by transmission electron microscopy (TEM) in previous work of one author [5]).

Further, it is evident that microstructure of UFG Cu after fatigue loading remained without substantial changes in grain size and microstructure retained ultrafine-grained character.

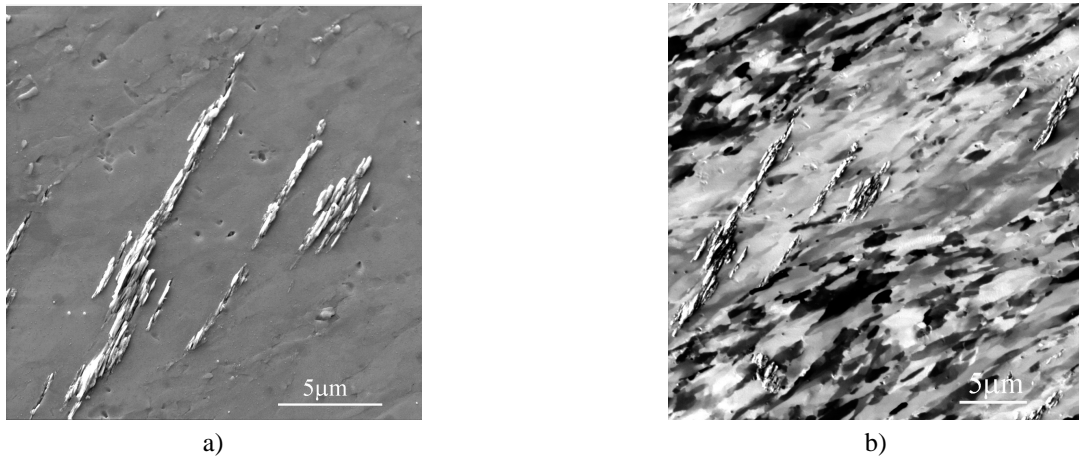


Fig. 2. Slip bands observed by means of a) SEM, b) FIB.

Fig. 3 shows an example of SEM micrograph of a FIB cut performed perpendicular to surface slip markings. By reason of protecting the surface was coated by platinum layer. After that the material was taken away by focused ion beam. The original surface with cyclic slip markings coated by platinum layer is well visible in Fig. 3. Also the grain structure below the surface can be recognized. No grain coarsening near is observed. Further, small approximately parallel cracks, arranged under circa 45° can be seen below the fatigue slip markings. These cracks can be considered the nuclei of fatigue cracks.

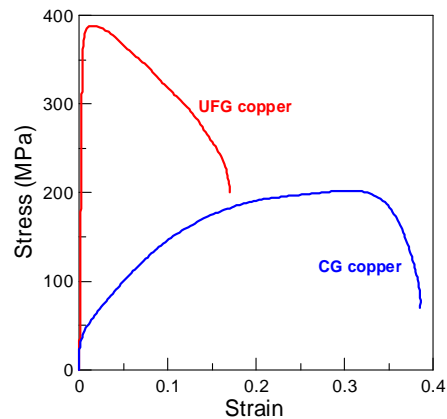
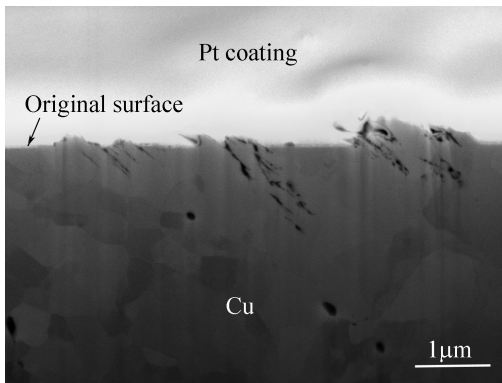


Fig. 3. Microstructure under cyclic slip markings. **Fig. 4.** Comparison of stress-strain diagram of CG and UFG Cu.

In the case of gigacycle fatigue of CG copper it was observed [9] that slip bands are formed not only above, but also below a certain cyclic stress (strain) amplitude value - persistent slip band threshold. Moreover, the slip band density increases with increasing stress (strain) amplitude and the number of cycles. Nevertheless, failure does not occur even if slip bands cover the whole surface; this slip activity is not sufficient to produce fatigue cracks, which are able to grow and result in final fatigue failure. The very high cycle fatigue threshold for formation of persistent slip bands (VHCF-PSB threshold) [10] obtained for CG copper is $\Delta\sigma/2 \approx 45$ MPa after 2.7×10^8 cycles. It is expected that persistent slip bands and small cracks are formed at even lower stress amplitudes. This means that the cyclic slip activity in CG Cu is indispensable at stress amplitudes below the 0.5 of the fatigue limit. The behavior of UFG Cu seems to be different. No slip activity was observed at the stress amplitude of 120 MPa, whereas at 130 MPa cyclic slip bands appeared and finally resulted in fatigue failure of the specimen. The ratio is here about 0.9. The explanation of the

observed behavior can be based on the differences in the shape of the stress-strain curves. Their comparison is shown in Fig. 4. The plastic strain amplitude (measured over the whole gauge length of the specimen) corresponding to the fatigue limit of CG Cu is of the order of 10^{-5} whereas in the case of UFG copper this value is substantially lower. The corresponding part of the stress-strain diagram is practically linear. The cyclic slip localization in UFG Cu takes place in the regions below the cyclic slip markings, Fig. 3. The mechanism consists of dislocation activity in highly localized regions of grains having the near-by orientation, generation of vacancies and finally in formation of cavities, which are sites of fatigue crack initiation. From this point of view the mechanism seems to be similar to that reported by Weidner [11] for CG Cu loaded in gigacycle fatigue region.

4. Conclusions

1. The cyclic slip markings resulting in fatigue crack initiation and fatigue failure appears in the gigacycle region as lately as the stress amplitude reaches 130 MPa. Below this stress amplitude value no surface relief development was observed.

2. Cyclic slip markings, which are sites of fatigue crack initiation, are formed in near-by oriented areas, which are zones of low grain misorientation.

3. Length of the fatigue slip markings on the surface exceeds severalfold the average grain size of UFG Cu.

4. In area underneath the cyclic slip bands form cavities, which cause crack initiation of material.

5. No grain coarsening after gigacycle fatigue loading was observed by means of SEM or FIB.

Acknowledgement

This work was financially supported by the Czech Science Foundation under contract 108/10/2001. This support is gratefully acknowledged.

References

- [1] SURESH, S. *Fatigue of materials*. 2nd ed. Cambridge: Cambridge university press, 1998.
- [2] KLESNIL, M., LUKÁŠ, P. *Fatigue of metallic materials*. 2nd ed. Amsterdam – Oxford – New York – Tokyo: Elsevier, 1992.
- [3] VALIEV, R. Z., LANGDON, T. G. *Principles of equal-channel angular pressing as a processing tool for grain refinement*. Progress in Materials Science 51, 2006, 881-981.
- [4] VINOGRADOV, A., HASHIMOTO, S. *Multiscale phenomena in fatigue of ultra-fine grain materials – an overview*. Materials Transactions, Vol. 42, No. 1, 2001, 1038-1044.
- [5] LUKÁŠ, P., KUNZ, L., SVOBODA, M. *Effect of low temperature on fatigue life and cyclic stress-strain response of ultrafine-grained copper*. Met. Mat. Trans. A 38, 2007, 1910-1915.
- [6] BATHIAS, C., PARIS, P. C. *Gigacycle fatigue in mechanical practice*. New York: Marcel Dekker, 2005.
- [7] MUGHRABI, H. *Fatigue, an everlasting materials problem – still en vogue*. Procedia Engineering 2, 2010, 3-26.
- [8] MUGHRABI, H. *Specific features and mechanisms of fatigue in the ultrahigh-cycle regime*. International Journal of Fatigue 28, 2006, 1501-1508.
- [9] STANZL-TSCHEGG, S. E., MUGHRABI, H., SCHÖNBAUER, B. *Life time and cyclic slip of copper in the VHCF regime*. International Journal of Fatigue 29, 2007, 2050-2059.
- [10] STANZL-TSCHEGG, S. E., SCHÖNBAUER, B. *Mechanisms of strain localization, crack initiation and fracture of polycrystalline copper in the VHCF regime*. International Journal of Fatigue 32, 2010, 886-893.
- [11] WEIDNER, A., AMBERGER, D., PYCZAK, F., SCHÖNBAUER, B., STANZL-TSCHEGG, S. E., MUGHRABI, H. *Fatigue damage in copper polycrystals subjected to ultrahigh-cycle fatigue below the PSB threshold*. International Journal of Fatigue 32, 2010, 872-878.



Solar Energy Storage on the Example of a Paraffin Tank

*Tadeusz Orzechowski, *Katarzyna Stokowiec

*Kielce University of Technology, Faculty of Civil and Environmental Engineering, Heating and Ventilation Division, Aleja Tysiąclecia Państwa Polskiego 7, 25-314 Kielce, Poland,
todek@tu.kielce.pl, katarzyna.stokowiec@gmail.com

Abstract. This paper presents the relationship between several parameters of paraffin tank applied in order to store the excess of solar-energy. The analysis has been conducted for solar collector system equipped with the paraffin tank which supports warm water needs for domestic purposes. The temperature fall in the storage tank has been calculated. Moreover the warm water flux change in time has been analyzed.

Keywords: solar energy, Thermal Energy Storage (TES), Phase Change Materials (PCMs)

1. Introduction

In the last 2000 years the world's population and the worldwide total energy consumption have been continuously increasing, reaching a point in which conventional energy resources are running short. The ongoing growth of the world's population and a growing hunger for energy in underdeveloped and emerging countries imply that the energy consumption would have doubled by 2050 [1]. Due to the fact it is essential to develop, improve and increase the standards and efficiency of renewable energy sources consumption.

The most important of them is the Sun. Solar energy, that is radiation energy, have been converted into heat or power and utilized in solar collectors of different types in order to warm water for use heating, central heating, water in swimming pools heating and in some industrial processes eg. water distillation, desalination or disinfection. Furthermore solar energy can be applied in photovoltaic cells or in solar power plants.

In Poland, during the summer season, the average radiation intensity is about 350W/m^2 [2]. The total quantity of energy, which comes from that source, implies the possibility to cater all demands in the country. However, the most important reason, why solar energy is not commonly utilized, is diurnal and annual diversity of its density. Therefore it is the main barrier to the planned exploitation. Furthermore the heating needs are the biggest in the winter, when the solar radiation is generally slight.

In order to increase the solar energy consumption, its excess should be accumulated and discharged in the intended time with the desired thermal quality. Periodicity of solar radiation demands that the accumulating system is big enough to store the energy when the solar radiation is accessible and works in case of its deficiency or when the Sun operation is low.

There are two main types of Thermal Energy Storage (TES): sensible and latent systems. In case of sensible heat storage system, the energy is stored or extracted by heating or cooling a liquid or a solid, which does not change its phase during the process. Whereas the latent systems' principle is to change the material phase by applying the heat to it and therefore accumulates the energy of fusion or vaporization.

Sensible heat storage systems are easier to produce. On the other hand it is impossible to store and discharge the energy at constant temperature. With its highest specific heat, water is the most commonly used medium. Its most important advantages are inexpensiveness, non-toxicity, wide availability as well as variety and flexibility of water system control [3]. However, there are also disadvantages of applying water, such as freezing, corrosiveness and therefore necessity to add

some chemicals and the limit of temperature, which is obliged to be lower than boiling temperature (below 100°C under ambient pressure) [3].

Other latent heat storage materials are allowed to be applied in systems with higher operating temperature. These are oils or rocks and pebbles packed in insulated vessels.

Latent heat storage systems demand the application of a suitable Phase Change Material (PCM) in a desired temperature range. Applied materials should be chemically stable, non-toxic, inexpensive and non-corrosive. Some of those requirements can be attributed to hydrated salts, paraffin waxes, mineral and synthetic oils, fatty acids and others. The latent heat storage method is more efficient than the sensible one. In order to accumulate 1MJ of solar energy, it is necessary to employ 16 tons of water or 5, 3 tons of organic PCM [4].

The most often used PCMs are paraffin waxes and zeolites. Paraffin is chemically neutral and stable. Its melting temperature range is wide. It is applied in heating systems to store solar energy. The research is conducted in order to use it in housing insulation systems. The zeolites' composition is crystalline and porous. They employ the reversible chemical and physical transformations with the direction connected to the heat flux direction, such as sorption and desorption processes.

Except from heat, cool be also stored (CTES-Cool TES). In this case ice tanks and suspended ice or PCMs with melting temperature below 15°C are used [5], [6]. All the systems are applied in the air-conditioning systems in buildings. The items allow the reduction of overall costs, with only a small increase in total energy consumption if buildings are operated properly.

2. Analysis methodology

A schematic diagram of the system for warm water for use supply by sun's energy stored in a paraffin tank is shown in Fig. 1. The proposed system consists of solar collector, hot water tank and paraffin tank. During daytime, the heat tank circulation loop consists of a solar collector (solar radiation receiver) 13 and an insulated hot water tank 18. When the solar radiation intensity is high, the excess of energy is stored in a paraffin tank 1 and transferred to the cold water.

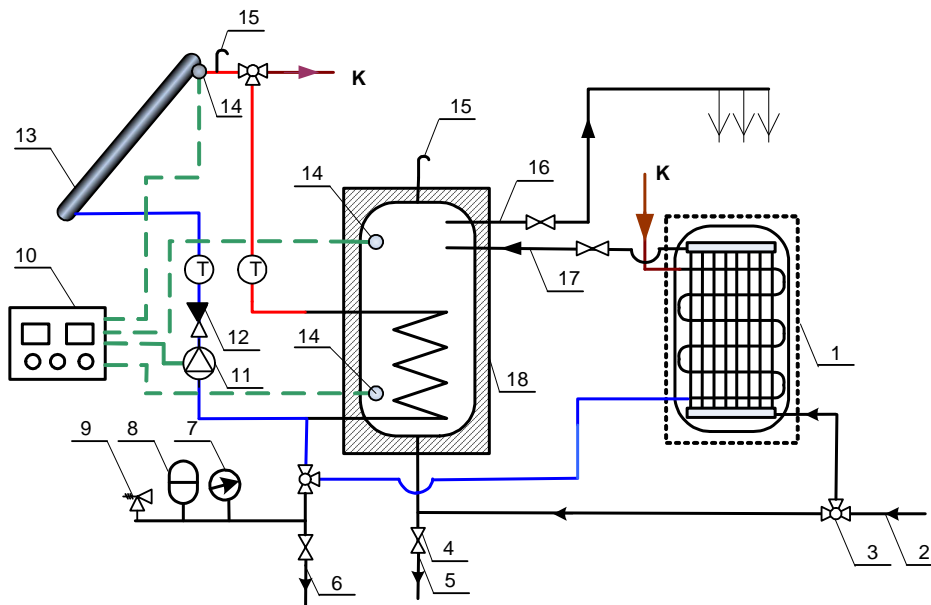


Fig. 1. Schematic diagram of the hot water system with solar collector and paraffin tank

1-paraffin tank, 2-cold water system, 3-three way valve, 4-valve, 5-water drain, 6-collector liquid drain, 7-manometre, 8-expansion tank, 9-safety valve, 10-control unit, 11-solar collector circulating pump, 12-return valve, 13-solar collector, 14-temperature sensor, 15-air-escape valve, 16-residential domestic hot water, 17-hot water supply from the paraffin tank, 18-hot water tank, T- thermometer, K-collector loop

3. Discussion

To calculate the temperature in the paraffin tank as well as the heated water temperature we should use the energy balance. For the considered system, after calculating the heat balance, we can write the following formula:

$$\frac{T_2 - t_z}{T_2 - T_1} = e^{\frac{U \cdot F_w}{\dot{m}_1 \cdot C_{p2}}} \quad (1)$$

where: $T_2 = T_2(t)$ – temperature in the paraffin tank, t_z – cold water temperature, T_1 – temperature of heated water in the paraffin tank, \dot{m}_1 – water mass flux, C_{p1} – water specific heat, m_2 – paraffin mass, C_{p2} – paraffin specific heat, U – overall heat transfer coefficient, F_w – paraffin tank pipe coil area.

The temperature changes versus time in (1) are presented in Fig. 2. The curves show paraffin tank cooling time for different water fluxes – 0,1 l/s to 0,3 l/s. The volume of paraffin tank was accepted as 400 L which allows to heat ca. 350 L of water. Additionally, the Fig. 2 depicts the length of solidification process for each flux as well as the time of both cooling and solidifying processes of paraffin.

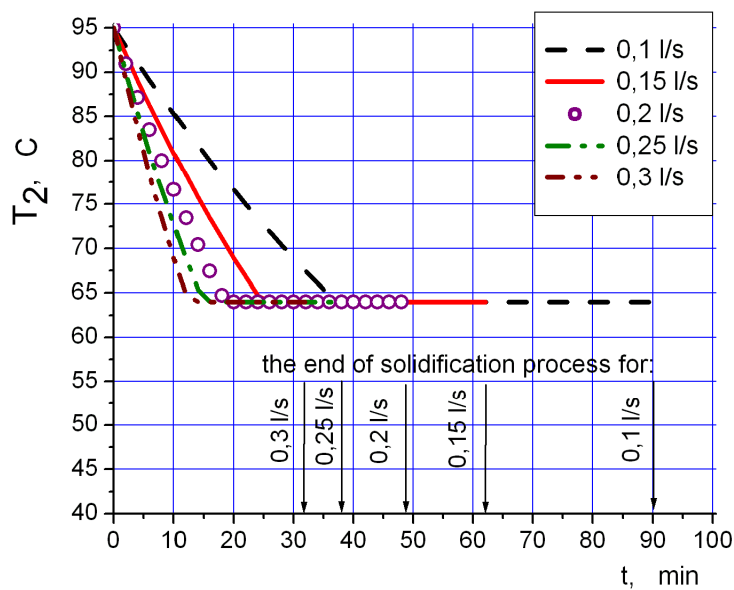


Fig. 2. The diagram of temperature falls in a paraffin tank.

The heat discharging process is the most efficient when maintained the constant hot water temperature outlet, eg. 45°C. Therefore the heat balance for the tank was modified and the dependencies received are presented in Fig. 3. Analogous curves can be applied in order to help to control the heat transfer, when the user demands the constant temperature of hot water delivery.

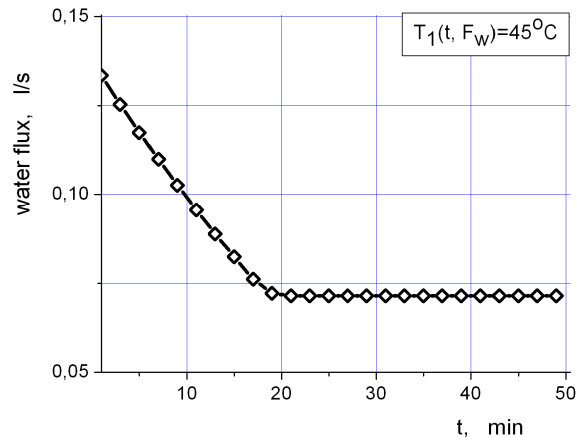


Fig. 3. Diagram of water flux in a paraffin heat exchanger.

4. Conclusions

This paper presents the solar system with paraffin tank that allows obtaining the required temperature even in case of low solar radiation or shortage of the Sun's operation.

The presented Fig. 2 indicates that the paraffin tank discharging process strongly depends on the water flux. For higher water fluxes, the temperature falls faster, what means that water is heated faster.

The Fig. 3 shows water flux for normative conditions when maintained the constant temperature of water 45°C. It presents the water flux fall versus time and its stabilization during paraffin solidification process.

References

- [1] REBHAN, E., *Challenges for future energy usage*. European Physical J. Special Topics 176, 2009, s. 53–80
- [2] SAMOILOV, D.V.: *System for hothouse heating during nighttime by solar radiation energy stored during daytime*. Chemical and Petroleum Engineering, Vol. 44, Nos. 9–10, 2008
- [3] ADEYANJU, A. A., MANOHAR K., *Comparison of Thermal Energy Storage Techniques*. Journal of Engineering and Applied Science 4(3), 2009, s. 221-231
- [4] F. PARADELA, F., QUEIMADA, A. J., MARRUCHO, I. M., C. P. NETO, C. P., COUTINHO, J. A. P., *Modeling the Thermal Conductivity of Pure and Mixed Heavy n-Alkanes Suitable for the Design of Phase Change*. Materials International Journal of Thermophysics Vol. 26, No. 5, 2005
- [5] RIVET, P., *Lód binarny: stan wiedzy*. Chłódnictwo 4, 2007, s. 16-21
- [6] STRITIH, U., RESNIK, D., BUTALA, V., *Energy conservation opportunities of PCM free cooling system*. University of Ljubljana, Faculty of Mechanical Engineering, Ljubljana, Slovenia



Heat Transfer Coefficient Components of the Large Droplets of Water in the Range of Film Boiling

*Tadeusz Orzechowski, *Sylwia Zwierzchowska

*Kielce University of Technology, Faculty of Civil and Environmental Engineering, Heating and Ventilation Division, Aleja Tysiąclecia Państwa Polskiego 7, 25-314 Kielce, Poland,
todek@tu.kielce.pl, sylwia_zwierzchowska@op.pl

Abstract. This paper presents the estimation of the radiation and convection component of overall heat transfer coefficient between the hot surface and the droplet. The experiment has been conducted for the large droplets of the mass $\sim 1\text{g}$ placed on the surface of three different temperatures: 291, 326 and 355°C. The calculated ratio of the radiation component reaches up to 10 % of the total heat transfer coefficient in case of smaller droplets and it is considerably lower for large ones. Additionally, the absorption of thermal radiation by water vapor has been taken into account.

Keywords: droplet evaporation, Leidenfrost point, film boiling regime, radiation and convection heat transfer coefficients, spectral transmittance

1. Introduction

The minimum heat flux, commonly referred to the Leidenfrost point, defines the beginning point of a stable film boiling. A characteristic feature of this phenomenon is a vapor blanket, which separates liquid medium from the heating surface.

Droplet evaporation has been investigated since the middle of the 20th century. The reason was the cooling problems, fuel feedings in rocket engines and so forth. One of the first was Baumeister [1, 2, 3] and Madejski [4]. With the use of energy and mass conservation equations they gave analytical solutions to describe the behavior of a single water droplet under film boiling conditions.

The set of the governing equations includes the radiation component of heat transfer coefficient which makes it nonlinear and impracticable to be solved analytically. It is worth mentioning to mention that the value of that component depends on the size of droplets, due to the geometry of its top and bottom surfaces.

Thin vapor layer cushions a droplet from the heating surface. Spectral transmittance of infrared radiation by water vapor is significantly different than by the air [5]. Therefore, the radiation energy emitted by the surface is partially absorbed by the vapor layer. The result is the less energy is transferred to droplet. The data of the spectral absorbance of water vapor, which shows different levels of infrared radiation transmission, can be found in [5]. For different heating surface temperatures, thermal energy, which reaches to the droplet in the radiation effect, is variable and dependent not only on the surface properties, but also on the properties of the water vapor transmission.

The aim of this paper is to show the correlation between convection and the radiation component of the overall heat transfer coefficient on the example of the water droplets. Experimental apparatus and methodology

Measuring system for testing a rate of drop evaporation from the hot surface has been shown in Fig. 1.

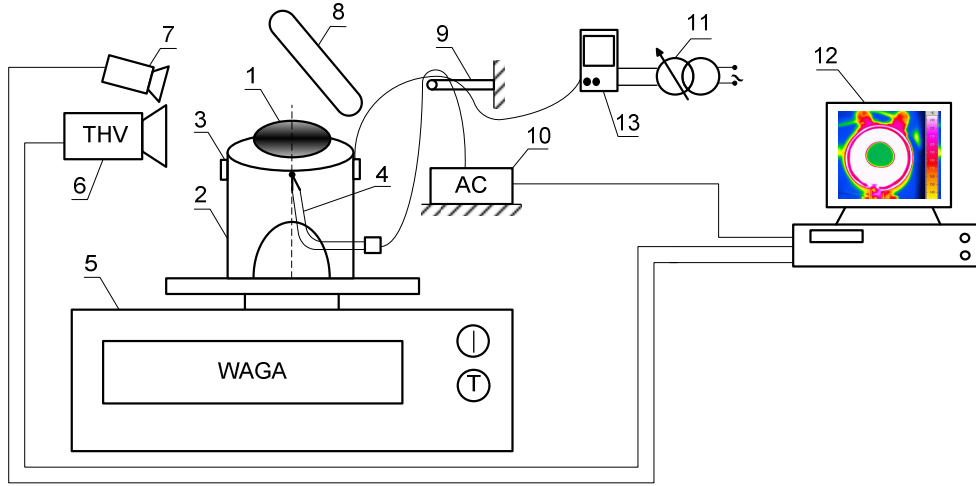


Fig. 1. The experimental set: 1 – droplet of water, 2 – roller heating system, 3 – wrapped heater, 4 – thermocouple, 5 - electronic weight, 6 – infrared camera, 7 – digital camera, 8 – mirror, 9 – tripod, 10 – AC signal processing system/accusation system, 11 – autotransformer, 12 – computer, 13 – voltmeter.

The investigations were conducted during one day, after having the night electronic balance stabilization. More than 30 measurement series for each of the three surface temperatures have been carried out.

In the Fig. 2 the change of the droplet average weight is shown. The results are given for three different heating surface temperatures: 291, 326 and 355°C.

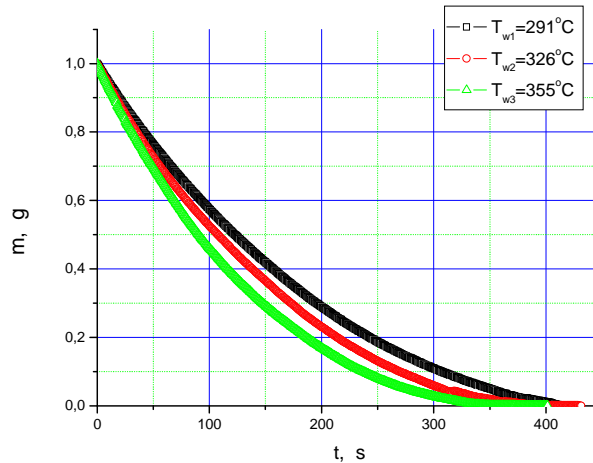


Fig. 2. Average weight of droplet for the different surface temperatures: $T_{w1} = 291^{\circ}\text{C}$, $T_{w2} = 326^{\circ}\text{C}$, $T_{w3} = 355^{\circ}\text{C}$.

The different slope of the curves indicates that the vaporization mass flux considerably changes with the surface temperature of the heating base. During the experiment the temperature of the surface and droplet have been registered on the computer with the data accusation system. Additionally, its mean temperature has been calculated from the thermal images registered by THV camera.

2. Discussion

For the considered system we can write the following energy balance:

$$(\alpha_c + \alpha_r)(T_w - T_d)A = -h_{fg} \frac{dm}{dt} - c_p \frac{dm}{dt} (T_s - T_d) \quad (1)$$

where: α_c , α_r - convection and radiation components of the heat transfer coefficient, T_w - temperature of the heating surface, T_d - droplet average temperature, A - area of the droplet projection on the hot surface, h_{fg} - enthalpy of vaporization, dm/dt - mass flux, c_p - heat capacity, T_s - saturation temperature.

The radiation emitted by the heating surface system is partially absorbed by the vapor layer underneath the droplet. In Fig. 3 the spectral distribution of the heating base is given. The radiation emitted is dumped by the vapor which the spectral absorption coefficient is shown in Fig. 3b. Fig. 3c shows the resultant radiation which reaches the droplet surface after absorption.

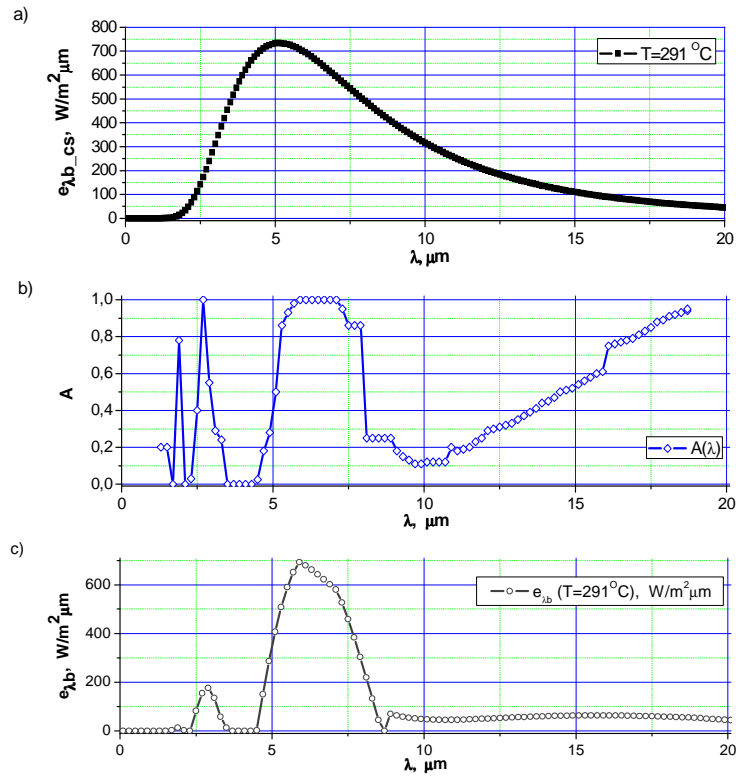


Fig. 3a. Planck distribution for the surface emissive power, **3b.** Spectral absorption coefficient for water vapor, **3c.** The thermal radiation intensity of heating surface after spectral absorption of the water vapor:

The radiation and convection heat transfer coefficients from the heating surface can be calculated after determining all the necessary parameters in equation (1) and the data of the measurements. The calculation results are shown in Fig. 4 and 5.

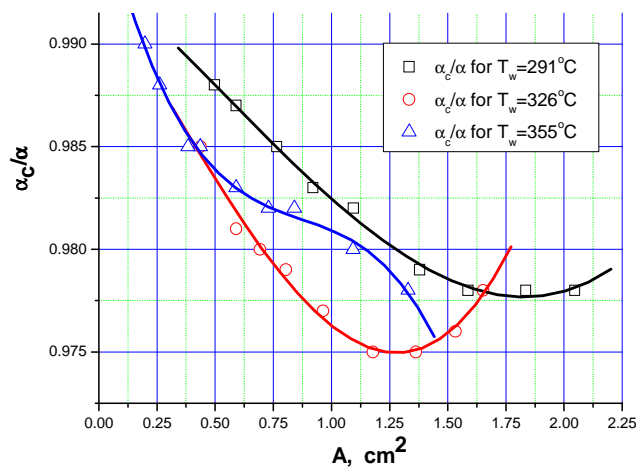


Fig. 4. The ratio of convection component of overall heat transfer coefficient for different heating surface temperatures.

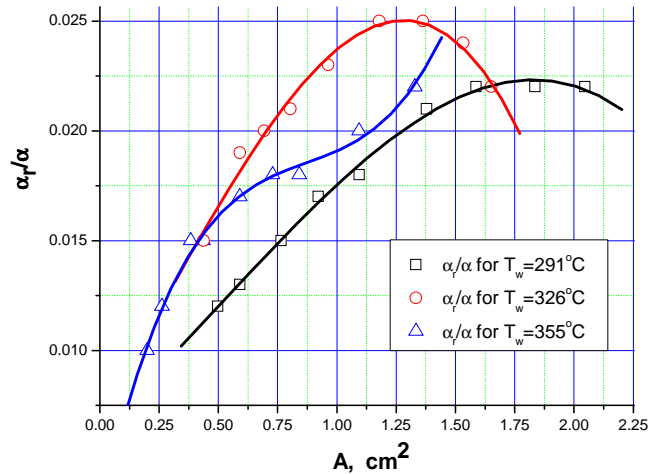


Fig. 5. The ratio of radiation component of the overall heat transfer coefficient for different heating surface temperatures.

3. Conclusions

From the presented Fig. 4 and 5 outcomes that in the initial period, for large droplets, the influence of radiation is negligible. However, for smaller droplets, it increases up to 10%.

Even if you ignore the absorption of thermal radiation by the water vapor, the radiant contribution remains minor due to the vapor cushion. Thus, almost all the heat energy reaches the droplet by convection.

Acknowledgement

I inform that I get a scholarship co-funded by European Union within the framework of the ESF program carried out in the Kielce University of Technology titled “Learning to measure success”.

References

- [1] HENDRICKS, R. C., BAUMEISTER, K. J. *LIQUID or solid on liquid in Leidenfrost film boiling*. Cryogenic Engineering Conference Boulder, Colorado, NASA TM X-52783, June 17-19, 1970.
- [2] BAUMEISTER, K. J., HENDRICKS, R. C., HAMILL, T. D. *METASTABLE Leidenfrost states*. NASA TN D-3226, 1966.
- [3] BAUMEISTER, K. J., HAMILL, T. D., SCHOESSOW, G. J. *A generalized correlation of vaporization times of drops in film boiling on flat plate*. Proceedings of Third International Heat Transfer Conference, Vol.4, 1966, s. 66.
- [4] MADEJSKI, J., STANISZEWSKI, B. *WYMIANA ciepła przy wrzeniu i przepływy dwufazowe*. Ośrodek Informacji o Energii Jądrowej, Warszawa 1971.
- [5] KOSTOWSKI, E. *PROMIENIOWANIE cieplne*. Wydawnictwo Naukowe PWN, Warszawa 1993, s. 92-94.



Chosen Methods and Ways for Barrier Materials Protective Properties Evaluation towards Toxic Compounds Permeation

*Pavel Otřisal, *Stanislav Florus

*University of Defence, NBC Defence Institute, Sídliště Víta Nejedlého, 68201 Vyškov, Czech Republic,
{Pavel.Otrisal, Stanislav.Florus}@unob.cz

Abstract. Finding barrier materials protective properties is possible not only with the help of instrumentally very complicated methods but also with the help of relatively simple devices using QCM detector working of as principle of a piezoelectric event. An advantage of simplicity of usage not only instrumental but also user-oriented both hardware and software equipment is one of the basic distinction of measurement device of PIEZOTEST. This device is employed within NBC Defence Institute of the University of Defence for finding protective properties of barrier materials used in Czech Armed Forces Chemical Corps specialists' individual protection.

Keywords: PIEZOTEST, barrier, lag time, normalization permeation mass, normalized breakthrough detection time.

1. Introduction

An expeditionary character of Czech Armed Forces' (CAF) manpower and equipment employment brings a possibility of operational employment practically wherever in the whole World. This important phenomenon of current time significantly touches CAF Chemical Corps (CC) specialists within fulfillment their tasks in both combat and non-combat operations conducted on the Czech Republic territory and beyond it. Relatively new threats concerning recession from massed usage of Weapons of Mass Destruction generates a real need of ensuring of high quality CAF CC specialists in an environment where a chance of contact with Toxic Industrial Chemicals (TICs) increases. These ones can be either a natural part of territory industrial infrastructure or they can serve as a tool for the assertion of interests by selected groups of inhabitants. To CAF CC specialists could fulfill tasks related to both military forces and civilian population protection it is necessary equip them such devices which are known in advance about their protective properties, which are characterized by periods of a protective effect against the permeation of toxic substances. These properties have to be clearly interpreted within a scientific community.

2. Ways of Finding of Permeation Influence on Barrier Materials

A relatively great number of possibilities and ways how to find up the barrier materials used for isolative protection resistance exist. The Czech Technical Norm [1] of ČSN EN ISO 6529 (83 2732) closely specifies so called analytical techniques defined as a procedure whereby the concentration of a chemical in a collection medium is quantitatively determined. As available analytical techniques the norm considers ultraviolet (UV) and infrared (IR) spectrophotometry, gas and liquid chromatography, conductometry, colorimetry, atmospheric analytical detector tubes and radionuclide tagging/detection counting. In a general conception of analytical techniques it is a probe which runs in a permeation cell divided in two parts. These parts are separated each other by the researched material. In an upper part of the cell the constant concentration of researched TIC is kept. Through the bottom part of the cell goes a flow of a carried gas. This one washes an underside of the researched material which ensures the continual washing out streams of tested TIC in a

bottom part of the cell. A mixture of both carried gas and permeating steams of the chemical is afterwards carried away in a collective medium. An amount of permeation steams caught in the collective medium is subsequently analyzed with the help of above mentioned analytical techniques with the employment of specialized both instrumental and software equipment. The usage of analytical techniques is very inappropriate in conditions of CAF CC operational employment. An inexpedience of their usage in conditions of a field mobile laboratory can be seen mainly from the reason of:

- high costs of acquisition of devises;
- significant demands on service staff, and both because of the necessity of using a complicated laboratory equipment and also in terms of high demands on training;
- necessity of ensuring of a significant number of peripheral devices and therefore the need to ensure that they have to be serviced, calibrated and possible repaired;
- huge demands on the size of working area;
- absence of a real use of the devices necessary for the analysis of permeating TIC. This need exists in the stationary laboratory conditions, where it is often necessary to determine what specific PCHL permeates through the barrier.

The device which significantly eliminates disadvantages of analytical techniques is called as PIEZOTEST. This device uses QCM detectors for detection of penetrating of TIC through the barrier material. QCM detectors are quartz resonators which register a change of a mass with the help of a piezoelectric cut. Quartz Crystal Microbalances are piezoelectric devices which are able to measure very sensitively mass changes with a nano-gram exactness [2]. For these detectors is typical employment of AT-cut of the quartz with the basic frequency of 9 MHz. This one is simply measureable therewith that 1 ng of TIC keeping of the detector surface can be immediately detected as a reduction of a crystal oscillation frequency within 1 Hz [3]. The amount of the gaseous TIC caught on a surface of detection surface of the crystal is thus set. This surface can be made up from appropriate either adsorbent or adsorbent. A sample of a tested isolative protective folio is placed in the permeation cell and hermetically divided it into two parts. The first one is contaminated by the tested TIC and the second one where the QCM detector with a polymeric layer is. The concentration of the TIC which penetrated through the protective folio increases in the close area around the detector. It penetrates by diffuse transmission in the speed of $\text{cm}\cdot\text{min}^{-1}$ in a direction to QCM detector. After that the TIC is caught in the detector polymeric layer which causes its frequency change. A frequency signal is subsequently led through suitable interface into a computer where it is recorded as an exact physical quantity. This one is elaborated into a form of tables (graphs) and it is assessed in accordance with above mentioned norm.

3. Some Ways of Evaluation of Barrier Materials Protective Properties towards of Toxic Compound Permeation

Results gained with the help of either analytical or other methods are necessary to evaluate in accordance with demands set in relevant norms. By this it is possible to achieve their unique interpretation.

The resistance of constructive materials used for isolative protection is possible to consider based on various norms, for instance with the help of ASTM (American Society For Testing And Materials) F739 [4], in the CZ with the help of the Czech Technical Norm of EN ISO 6529 [5]. An example of a particular application for transport coefficient finding up with measurement of a permeation rate can be European Technical Norm of EN 374-3 [6]. These norms define systems (permeation cells) for determination of barrier materials used for isolative protection protective properties and furthermore, specify values (quantities) for evaluation of materials.

3.1. Evaluation of Penetration Characteristics with the Help of set Permeation Rate and Normalized Breakthrough Detection Time

Breakthrough characteristics relative to particular values of the permeation rate provide information about the amount of toxic compound which permeated through researched barrier material on a given exposure surface in a unit of time. From the value of the permeation rate described in norms mentioned above in $\text{ug.cm}^{-2}.\text{min}^{-1}$ is evident its dependency on normed permeated concentration whose achievement will be within each toxic compound constant, the area that is different from the real area of contact and finally, the time needed for reaching of defined concentration. Introduced dependency is, however, valid only for measure systems which are based on a principle of an open-loop, thus such probes during them the new (fresh) medium is fed continually into a permeation cell measure chamber for the purpose of diversion of TIC and afterwards it is analyzed and after it the medium is not deployed in a measure system any more. A schematic expression of penetrating (breakthrough) time for method with sensitivity of $0,05 \text{ ug.cm}^{-2}.\text{min}^{-1}$ respectively for method working with normalization permeation rate equals $0,1 \text{ ug.cm}^{-2}.\text{min}^{-1}$ is illustrated in Fig. 1. Due to defined breakthrough detection time relative to the particular amount of permeated compound in a time unit reached to the principle elimination of the influence of employed both detection and analytical methods for finding real breakthrough time.

For determination of particular value of permeation rate in the close-loop it is defined a term of normalized permeation mass given by the norm of ČSN ISO EN 6529 (83 2732). It is defined as the time at which the permeation rate reaches the normalization permeation rate of $0,25 \text{ ug.cm}^{-2}$ or $2,5 \text{ ug.cm}^{-2}$. From this definition follows that normalized breakthrough detection time is established within one of set normalization permeation mass.

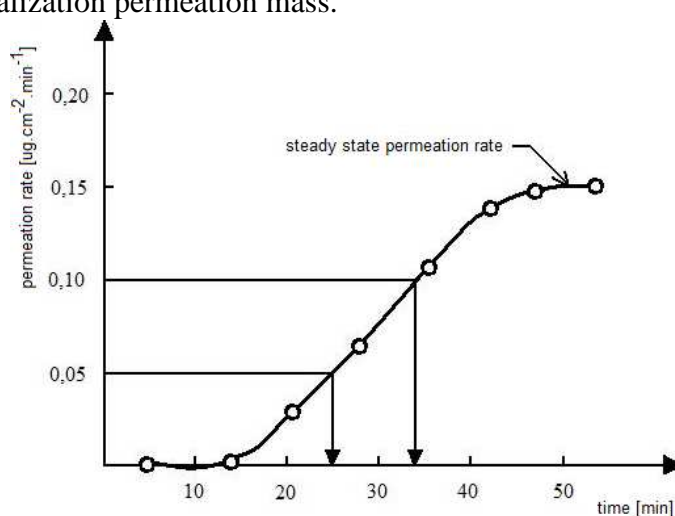


Fig. 1. Breakthrough time for defined permeation rates.

3.2. Assessment of Penetrating Characteristics with the Help of Lag Time

The assessment of barrier material resistance with the help of immediate reading of lag time value seems to be very advantageous for CAF CC specialists. For determination of lag time it is enough to simple construct the dependence of QCM detector working frequency in time by MS Excel editor at the time till steady state permeation rate has been reached. Within this method of protective properties evaluation there is no need to make relatively complicated mathematic calculations whose real value is more commercial then useful for operational commanders. Furthermore, the method of lag time determination gives a piece of immediate information about the speed of barrier material protective properties loss and moreover, simply shows the time which is needed for steady state permeation rate achievement. The steeper is a part of a curve characterized the constant QCM detector increasing the quicker comes to loss of researched barrier material protective properties after the first penetration of TIC on its underside. This dependency is also valid conversely.

4. Discussion

As mentioned above the method of QCM detection is more appropriate for operational usage than analytical techniques. Its advantages can be, from the military-operational point of view, seen in these [7]:

- objectivity of measurement. This one is given by a minimal influence from on the part of the human being;
- automatic measurement of observed values after preparation and launching of measure device;
- explicit evaluation of measurement results thus dependency of QCM working frequency change on time;
- possibility of measurement of breakthrough time for a wide scale of toxic compound;
- good reproducibility of tests;
- experimentally very easy method with no too high demands on managing of employed instrumental, hardware and software equipment;
- minimal demands on other periphery devices including demands on working place equipment and for their operation;
- chance to use various types of permeation cells in the dependency of character of researched material.

From the text introduced above is clear that data concerning breakthrough time enables evaluation in several ways. For operational commanders the simplest and quickest one is a method of making of a tangent line to a linear part of the graph and its cross with an axis x and reading of lag time. More information related to lag time has been provided in chapter 3.2 and it is evident in Fig. 2 and 3. This way appears to be especially appropriate at the time when:

- permeation rate is so low that achievement of QCM detector working frequency on a level of steady state permeation rate is reached in relatively long time and thus a difference between actual breakthrough time and lag time is negligible. It is perceptible from an example in Fig. 2;
- permeation rate is so high that achievement of QCM detector working frequency on the level of steady state permeation rate is reached in a very short period of time. It appears in Fig. 3.

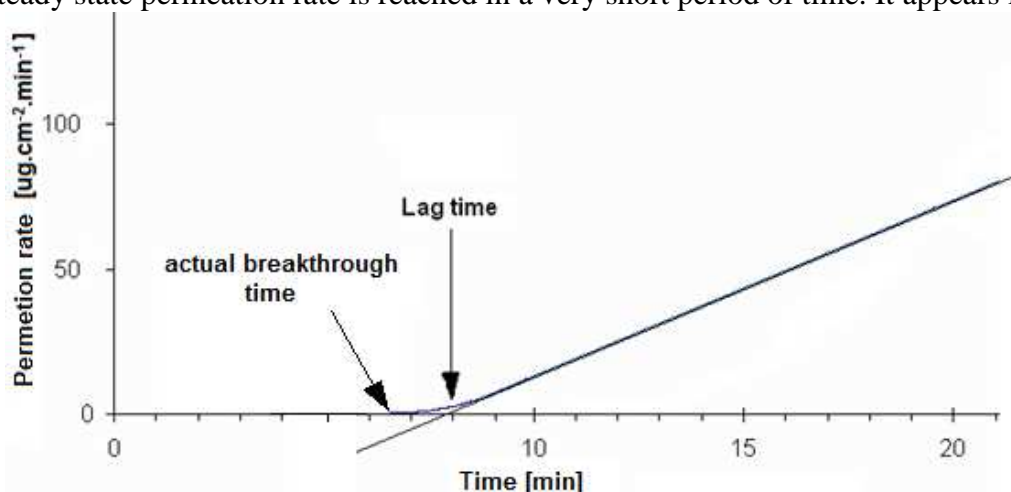


Fig. 2. The example of possibility of actual breakthrough time evaluation and lag time based on their time likeness in case of the low permeation rate.

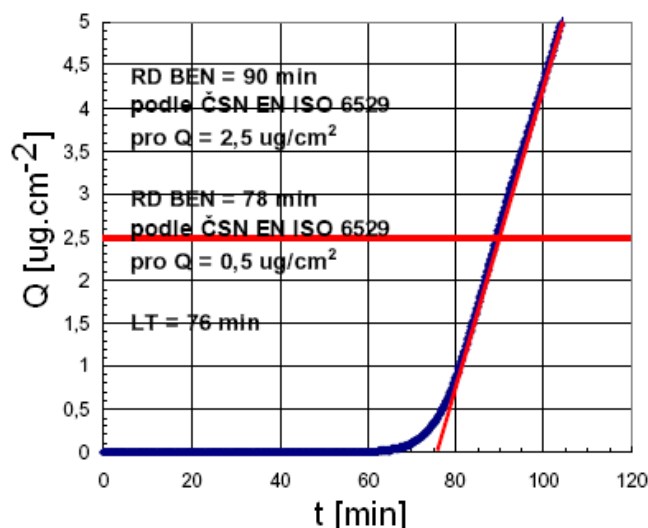


Fig. 3. The example of actual breakthrough time evaluation and lag time based on achievement of normalization permeation mass in the short time [8].

Practical application of the lag time deployment for quick finding of barrier material protective properties seems to be appropriate not only for toxic compounds by which reaching of steady state permeation rate is tied on relatively long time but also for those one whose permeation rate is very high and thus very quickly comes to barrier material protective properties loss due to considerable swelling. In a practice life it means that difference of actual breakthrough time value can be negligible with respect to achievement of steady state permeation rate within both low and high permeating toxic compound (Fig. 2 and 3). From the rate of permeation rate constructed in Microsoft Excel can be clear in advance that to achievement of steady permeation rate comes to either in relatively long time or very quickly. A value of lag time can be tentatively considered as the time corresponding actual breakthrough time without experimentally reached of steady state permeation rate value. In this access it is significantly decreased the necessity of relatively useless and purposeless saturation of QCM detector whose polymeric layer needs relatively long time for recovering of working frequency in a static state thus the time for beginning of another measurement.

5. Conclusion

Testing barrier materials protective properties against permeation of TICs is a relatively new matter and still not fully explored in army conditions. In military practice, it seems expedient to use methods for rapid, easy operation and easy handling and disposing of evaluation without complex mathematical applications. These methods with respecting of valid norms have to provide comprehensible and mainly useful information for the final user who has to know how long their protective devices will provide the protection for particular TIC in both supposed and real conditions. For the practice life it is not basic when an amount of TIC permeates through constructive materials thus when the absolute loss of protective properties appears. Only a technical knowledge of either the time of norm concentration or the amount of TIC does not tell anything about dangerousness of penetrating amount whether this data will not be toughly connected with toxicology information. Immediate both data concerning a beginning of TIC permeation through constructive materials and information concerning time in which the steady state permeation rate is achieved have higher value for the final user then norm values. They can be more designated for commercial purposes. In this way it is necessary to evaluate these values.

References

- [1] ČSN EN ISO 6529 (83 2732): *Ochranné oděvy – Ochrana proti chemikáliím – Stanovení odolnosti materiálů ochranných oděvů proti permeaci kapalin a plynů*. Praha : Český normalizační institut, 2002. 36 s.
- [2] SURI, Raman. Quartz Crystal Microgravimetric Immunobiosensors. *Sensors & Transducers Magazine (S&T e-Digest)*, Vol. 66, Issue 4, April 2006, pp 543-552.
- [3] FLORUS, Stanislav, OTRÍŠAL, Pavel, OBŠEL, Vladimír. Possibilities Of Usage A Piezoelectric Detector To Measure The Breakthrough Time Of Protective Materials. In *Proceeding 7th Symposium on CBRNE threats "Meeting the future challenges"*. Jyväskylä : Defence Forces Technical Research Centre, 8.-11.6.2009, s. 239-243. ISBN 978-951-25-2012-1.
- [4] *ASTM F739: Standard Test Method for Resistance of Protective Clothing Materials to Permeation by Liquids or Gases Under Conditions of Continuous Contact*. Philadelphia : American Society for Testing and Materials, 1999.
- [5] ČSN EN ISO 6529 (83 2732): *Ochranné Oděvy – Ochrana Proti Chemikáliím – Stanovení Odolnosti Materiálů Ochranných Oděvů Proti Permeaci Kapalin A Plynů*. Praha : Český normalizační institut, 2002. 36 s.
- [6] *DIN EN 374-3 Protective Gloves Against Chemicals And Micro-Organisms - Part 3: Determination Of Resistance To Permeation By Chemicals*. Brussels : CEN, 2003.
- [7] OTRÍŠAL, Pavel, FLORUS, Stanislav, OBŠEL, Vladimír. New Methods In Testing Of Selected Barrier Materials Protective Properties. In *Sborník přednášek z konference mladých vědeckých pracovníků „Věda a krizové situace 2009“*. Editoři J. Kamenický a R. Doležal. Liberec : Technická univerzita v Liberci, 22.10.2009, s. 33-38. ISBN 978-80-7372-528-0.
- [8] OBŠEL, Vladimír, DVOŘÁKOVÁ, Jana, ORÁLEK, Jindřich. *Výzkum Možností Aplikací Nanotechnologií A Nanomateriálů V Protichemické Ochráně : Nanostrukturované Materiály A Testování Jejich Odolnosti Vůči Permeaci Toxických Látek*. [Technická zpráva projektu Nanomateriály za rok 2010, etapa 03-07]. Brno : Divize VTÚO Brno. VOP-026. 2010. 122 s.

Experimental Measurement of Thermal Cycles and Drilling Strength at Welding of Fitting

*Peter Pallo, *Miloš Mičian, **Ján Straško

*University of Žilina, Faculty of Mechanical Engineering, Department of Technological Engineering,
Univerzitná 1, 010 26 Žilina, Slovakia, e-mail: peter.pallo@fstroj.uniza.

**SPP- distribúcia, a.s., Mlynské nivy 44/b, 825 11 Bratislava, Slovakia, e-mail: spd@spp-distribucia.sk

Abstract. Article deals with experimental measurement of thermal cycles and drilling strength at welding of gas pipes. Measurements were realized directly in terrene at gas pipes translation. Used technology at gas pipes translation was system TDW Wiliamson.

Keywords: gas pipes, thermal cycles, drilling strength

1. Introduction

Natural gas transport is its distribution by high-pressure transmission gas pipes is the safest and most used transport method natural gas at all. At gas line building is very important its safety. There are situations at working conditions, when the reconstruction of the gas pipe part is often needed to overtake the accident, or there is needed replace of the old used gas pipe parts by new one, or facture the new gas pipe branches.

Experimental measurement of thermal cycles was realized in the real conditions at building. „Highway R1 in part Banská Bystrica, north bypass“. It was natural gas translation VTL DN 300 in km from 3,5 to 3,8. At translation was used Technology T.D. Wiliamson.

Technology T.D. Wiliamson is based on using of fittings and branches. Principle of technology is creation of the parallel gas line with area of needed encroachment, deflection of transported matter in the bypass, encroachment execution on the gas line, return of medium transport through execution area and bypass liquidation. Drilling and closing gas line by Technology T.D. Williamson, is method, which enables repairs, reconstructions, translations, canceling of branches, gas line extension, lock exchanges, or damaged gas line and next specific activities realized in full running gas distribution system, eventually tanks without layoff liquid and gas flow. This remains maximal productivity of gas line during repairs and maintenance, because it is not need to interrupt running gas distribution system. From the economic side this system more lucrative.

longitudinal section of cutting

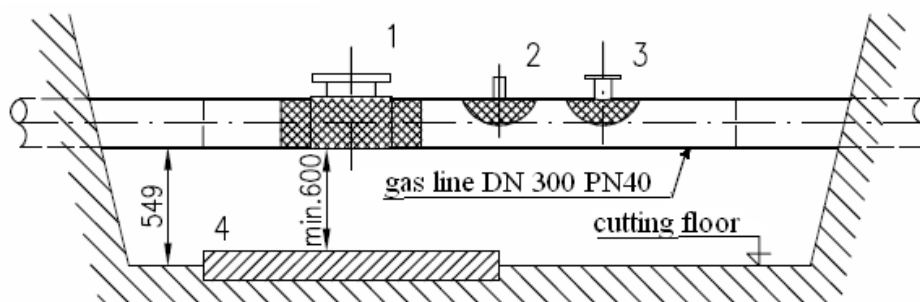


Fig. 1. Longitudinal section of cutting, 1- closing fitting STOPLE ANSI 300 (PN50) – DN 300
2- TOR nipple DN 50, PN 100 for compensating gas line, 3- balloon neck STEELSTOPP DN 80 (3"), PN40

2. Preparation of Experimental Measurement

For weld fittings and branches we used manual metal arc welding by coated electrode, because of open terrain at welding. As welding power source we used weld invertors. Filler metal basic electrode of classified E 42 4 B 42 H5.

Layer on the gas line surface was needed to make without swing out coated electrode, with average $\varnothing 2,5$ mm, in the range of welding power 80-90A. maximal heat input 1,0-1,5kJ/mm. Filling layers were made by electrode of average $\varnothing 3,2$ mm range of welding power 110-120A

At measurement thermal cycles we shoot at circumferential weld of closing fitting STOPLE ANSI 300. At first was needed to make cutting and brake isolation on gas line on the places, where was fitting welded and other additional components. In next step install fitting and make two longitudinal welds according to designed technological procedure. Then were thermocouples installed on fitting and gas line.



Fig. 2. Remote on the place, where fitting was installed on gas pipe in cutting.

2.1. Installation of Thermocouples

For measurement of thermal cycles we used thermocouples type K. Thermocouple type K is compact of two conductors – nickelchrome and nickel. It is possible for use in temperature to 1000 °C. Sensitivity is $42 \mu V/^{\circ}C$. With this joint type (fillet weld) is not possible admission from root, therefore it is not possible to cover by measurement the area of root layer.

We placed thermocouples nearest to the weld on the gas line and fitting sic, that thermocouples will be not a problem for welder at welding. We designed point matrix 2x3 on fitting and one point on gas line. This nest of thermocouples was placed on right also left side of fitting, so for both circumferential welds. “Fig. 3”

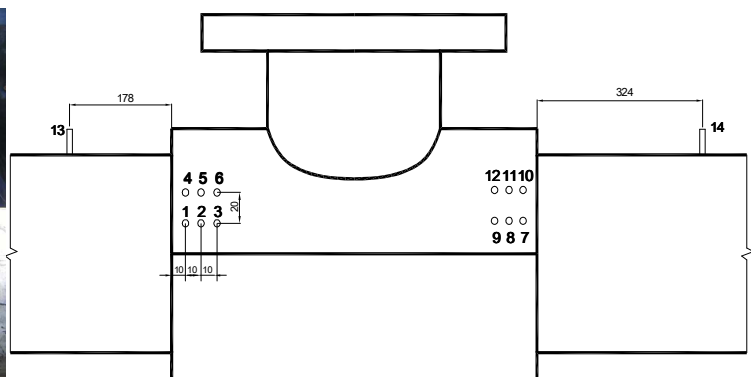


Fig. 3. Thermocouples located on fitting.

For signal processing we used computer software and A/D converters, which were connected from other generator as welding power supply, grinding machines and other electric tools. Thermal cycles were measured at the same time on all 14 thermocouples by sampling frequency 10Hz.

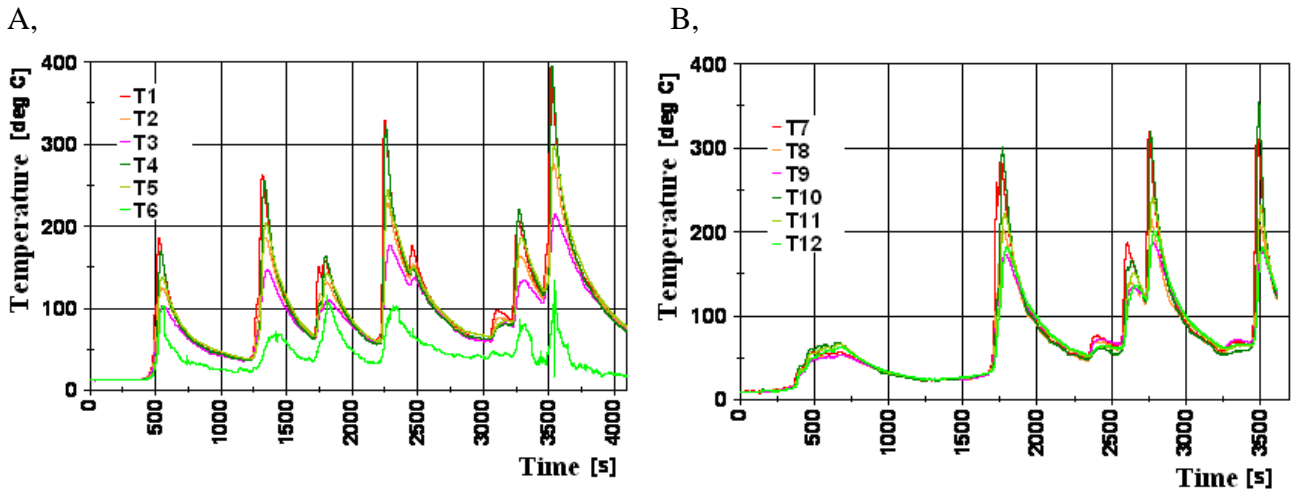


Fig. 4. A, Thermal cycles flow from thermocouples T1 - T6 at welding of first circumferential weld. B Thermal cycles flow from thermocouples T7 – T12 at welding of first circumferential weld. (whole flow)

According to time behavior of temperatures is possible to deduce, that it is composite thermal cycles, at once is possible to identify and number of electric arc transition round place of thermocouple installations, so number of layers. The maximal temperature on thermocouple no. 1 was 394,1°C in 8th layer.

3. Determination of Deformation, Strength and Torque at Drilling

In this section was done measurement of deformations on selected technological component of drilling ring to understand the acting strengths and torques in behavior of drilling hole in existing gas line at generation parallel branch of gas line. On drilling component for these needs were installed tensometers and we measured deformation of drilling component. On flange surface were definite 4 places (0, 1, 2, 3) removed about 90°. in every place were installed 3 tensometers (A,B,C). First in direction of flange centre line, second upright on direction of flange centre line and third inclined about 45° from direction of flange centre line.

We used tensometers of company Vishay, CEA-06-250UW-120, system NI cDAQ with modules NI 9237. In second step we defined strengths and torque actuating on flange.

We can observe from figure 6 non-stationary status of drilling process. At first sight the values are not low, however they show dynamic effects of technology part with weight around 1200 – 1500 kg.



Fig. 5. Location of tensometers on drilling component.

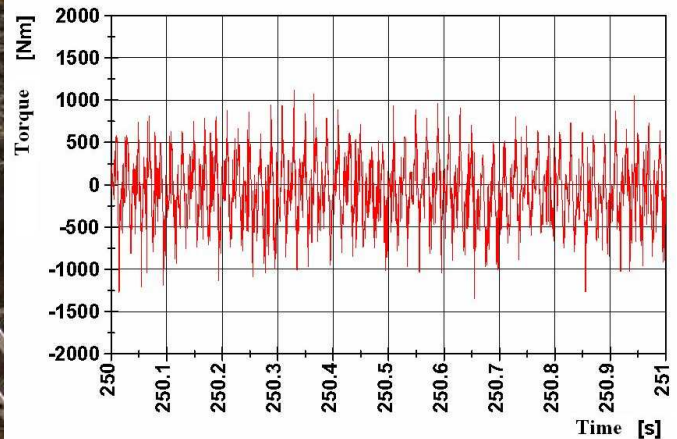


Fig. 6. Course of drilling a hole in gas pipe and behavior of beginning measurement of torque.

4. Conclusion

Because of limited range of article we presented only part of measured results at measuring thermal cycles and part results at measurement torque and bending moments. Thermal input in material at welding first circumferential weld was around 2072 W, what is level of welding procedure specification. From measuring results follow that in spite of cooling effect flowing medium through gas line, the small reheat rises also on longer distance from welding area.

For identification of deformations and stresses at drilling, it would be appropriate to make control calculation of fitting, with reflection of extreme dynamic values and obtained stresses is appropriate to substitute on residual stresses. Values determined by measuring were oncoming about static values.

Acknowledgement

This work has been supported by Scientific Grant Agency of Ministry of Education of Slovak republic, grant VEGA No. 1/0186/09 and KEGA No. 3/3668/08.

References

- [1] LEŽDÍK, V., SOBOTA, M., BEZÁK, J. *Zváranie v plynárenstve*. 1. vyd. Žilina: EDIS, vydavateľstvo ŽU, 2001, 194 s. ISBN 80-7100-902-4.
- [2] PALLO, P. *Analýza teplotného poľa v interakcii zo štruktúrnymi zvarového spoja pri zváraní so zvýšeným dvodom tepla* [Projekt dizertačnej práce]. Žilina. Strojnícka fakulta .2010.72 s.



Construction of Milling Machine for Production Moulds Made by Patternless Process

*Richard Pastirčák, *Dušan Urgela

*University of Žilina, Faculty of Mechanical Engineering, Department of Technological Engineering,
Univerzitná 8215/1, 010 26 Žilina, {richard.pastircak, dusan.urgela}@fstroj.uniza.sk

Abstract. This paper deals with construction of milling machine for production prototype moulds by patternless method. In the paper is in short cut mentioned process of production prototype forms by patternless method. This method significantly reduces the time needed to produce the castings. In the production of a castings by the method Patternless Process don't need pattern equipment, we are eliminated the cost of production and storage facilities pattern equipments. Therefore, the final cost price of one cast by the this method ae significantly lower and less time consuming than production which using traditional methods of production castings. In the paper is also mentioned choice type of construction used in the construction of milling machine, linear systems used in the construction of the machine and also the choice of motors. It is mentioned control program yet.

Keywords: patternless process, moulding mixtures, CNC machining, prototype casting

1. Introduction

Development of information technologies and globalization of capital created a difficult competitive environments. Companies are continually trying to improve produced products. As important factor is the product on the market rather than product from competition. The production of castings is usually necessary a pattern device, whose price is often many times higher than price of finished product. Outside the every introduction into service are produced prototype castings. These prototype castings are used to verify the operation, evaluation form, eliminate errors, or on presentation. Models are mainly produced by hand or machining on CNC machines.

Gradually appeared on the market methods, which didn't require a pattern equipment. One of them is the method Patternless Process. This method significantly reduces the time needed to produce the castings. In the production of a castings by the method Patternless Process don't need pattern equipment, we are eliminated the cost of production and storage facilities pattern equipments. Therefore, the final cost price of one cast by the this method ae significantly lower and less time consuming than production which using traditional methods of production castings.

In production of castings are used several types of CNC machine devices, which differ mainly supporting structure and size of cultivated areas. In our case we chose a portal supporting structure, after which the two sides move stands secure traveling straight lines, which provide movement in the x-axis, is placed on them lead to ensure a linear displacement in the y-axis. On this part of the machine is installer a spindle with router, which provides movement in the z-axis.

2. Patternless Process Method

Principle the method lies in fact that shape of the cast is milled into the block moulding compounds without the use of pattern equipment. First, the 3D CAD program generates a proposal mould, the entire structure including casting inlet system and feeds. Consequently, this proposal transfers data to program CNC machine tools, which forms part of the milled into the shape. On milling operation are used a special 5-axis milling cutters. Throught the milling is an important celection tool speed

and feed rate, which influences the resulting surface roughness mould. We may use one type of instrument, or two types of instrument, one for roughing and second for finishing. For finishing milling operation are used higher speeds than the roughing. Milled moulding mixture is immediately sucks.

In the selection of moulding sand we must regard various factors such as effect of gases and other influences that operated form the mould cavity during filling with liquid metal, as well as the solidification and cooling of the casting form. Also it is necessary regard think a mechanical properties of moulding mixtures. The method of Patternless Process used moulding sands of II. generation, such as moulding sands with contains synthetic resins such as furans moulding sands, phenol formaldehyde moulding sands and etc. The surface of the created mould cavity is coating by the substances, which are hindered the penetration, therefore invasion metal between the grains opening material and which are hindered creation burning-ins. After treatment, the mould cavity protective coatings, we can put together mould and we can poure it.

With using the direct moulding technologies we can produce a large range of castings weights up to 200 tons. A typical applications for this method are the prototypes of all kind, lathe-beds, as well as stands for special machines, beds for drives, pumps and valves and various components for the production of machine devices. Biggest financial savings through production technology Patternless Process can be achieved in the production of large and very large castings. In Fig. 1 is visible cost advantages in using Patternless Process and the classical method.

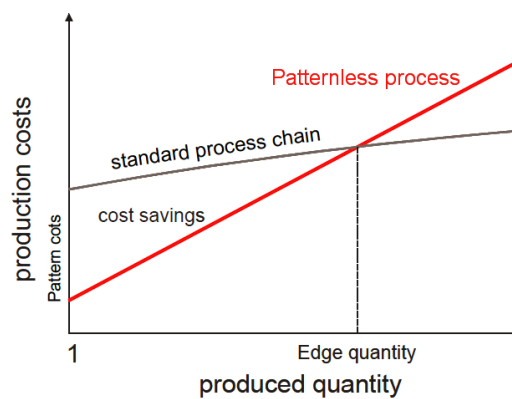


Fig. 1. Cost advantages in using Patternless Process and the classical method.

3. Construction of Milling Machine for Production Moulds Made by Patternless Process

Design the milling machine with mobile portal and stationary working table can be practically unlimited. CNC milling machines can also be constructed of different materials. They may be made from plastic, aluminium or steel. We decided to use aluminium profile, because aluminium has better mechanical properties, better workability and decision utilize slotted system on assembly construction. Aluminium profiles are used in three sizes, 80x80 mm, 80x40 mm and 40x40 mm. Profiles are show in the Fig. 2.

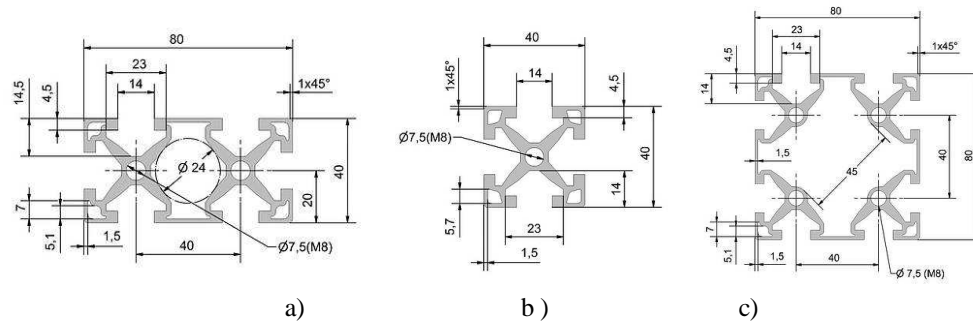


Fig. 2. Aluminium profiles used in the construction of CNC milling device
a) profile 80x40mm, b) profile 80x80mm, c) profile 40x40 mm

3.1 Selection of Construction Type

In the selection of construction, which are usually building, are preferred two types:

- milling machine with mobile portal and stationary working table,
- milling machine with stationary portal and mobile working table.

For our proposed device was chose portalled construction with mobile portal and stationary working table. This construction is used for about 95 % of CNC machining centers. This construction is advantageous because the total size of the produced parts can be virtually unlimited.

Portalled CNC milling machine consist of a structural part, after which on the two sides move stands secure travelling stands secure travelling linear bearings, which provide movement in the x-axis, on the it is installer linear bear which provide movement in the y-axis. On this construction it's installer router which provide movement in the z-axis.

The construction allows use a moulding frame how a part of a construction and thereby increasing the rigidity of the whole system. Moulding frame will be also absorb vibration during machining. Estimated precision machining of the mould cavity is in the range $\pm 0,05$ mm. Size of machining area is 800x800mm and height is 250 mm. Construction of the proposed device shown in Fig. 3.



Fig. 3. Construction of CNC milling machine

3.2 Linear Systems and Motors

A linear motion system is composed of some type of linear bearing and the linear bearing guides. There are a member of types of bearings and guides, each with advantages and disadvantages. A complete linear motion system is a combination of a drive system and linear bearing system, which must keep the forces on the spindle and provide precise linear motion with minimal friction. In our case, the linear motion is provided by ball screws with a diameter of 20 mm and 5 mm pitch.

The size and type of motor can define a CNC router precision, speed, and accuracy. In our CNC milling machine are used stepper motors. The stepper motor is a special kind of multipole synchronous motor. In our case we used two-phase stepper motors from the Klavio Aft Company with torque of 1,7 Nm. The strength of the bolt is 1067 N, which accommodating our requirement of cutting force. Linear systems with motors and with spindle are on Fig. 4.

As the spindle cutters will be used three-phase induction motor made by Teknomotor company, type 3140. Spindle power is 18 000 rpm. Fig. 5 shows a milling spindle installer in a linear bearing in z-axis.

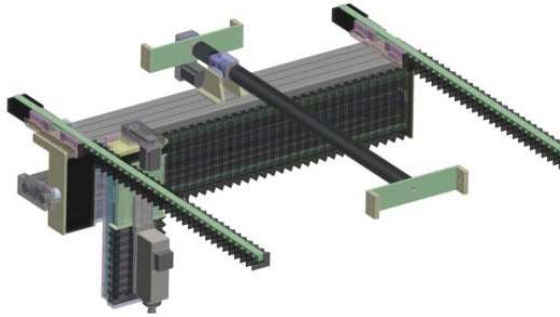


Fig. 4. Drives and linear rails CNC milling machine

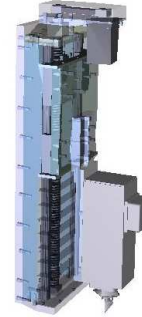


Fig. 5. Spindle installer in a linear bearing in z-axis.

As a tool in our case, we use different kinds of special cutters made especially to work with moulding sands. These cutters are made from spikes from hardly – metal. Slices from hardly-metal on spikes tools are they convertible.

How control program will be used universal program Mach 3 CNC Controller, which can be used for various control electronics. Program allow detailed set of data required to operate. The program uses G-code and M-code, which is normally used in programming CNC machines.

4. Conclusions

This paper deals with construction of milling machine for production prototype moulds by patternless method. The most common are CNC machines assigned for machining technology. The construction of these machines and their management systems allow relative movement between tool and workpiece normally in three axes, with less modification too more. 3D milling is successful method in the production of 3D complex shape parts.

The paper deals with the Patternless Method by milling the mould cavity. Shortly is describes the proposed structure, linear rails, motors and control system. Device is in stage production, so the accuracy of this proposal will be verified after its fabrication.

Acknowledgement

The authors wish to thank European Regional Development Fund for received financial support to create present paper within execution of the project "Equipment for the production of prototype parts by casting on a computer-controlled base" with ITMS code 26220220047.

References

- [1] EDERER, I. *Patternless production of furan bonded sand moulds in rapid prototyping*, Augsburg, Technical forum 2009
- [2] ZHONGDE, S., LI, X., FENG, L., LI, Z. *Rapid Pattern casting technology on CNC manufacturing*, World Foundry Congress, 16-20.10. 2010, Hangzhou, China,
- [3] Router Source. *Building a hobby CNC router*, 2007, [http://www. Cncroutersourc.com/hobby-cnc-router.html](http://www.Cncroutersourc.com/hobby-cnc-router.html)
- [4] GROOVER, P. M. *Fundamentals of Modern Manufacturing*, Second Edition., New York, 2002



Amplitude Dependence of Internal Damping in Extruded Aluminium Alloy AW-2007

*Jakub Porubčan, *Dalibor Blažek, *Peter Palček

*University of Žilina, Faculty of Mechanical Engineering, Department of Material Engineering,
Univerzitná 1, 01026 Žilina, Slovakia, {jakub.porubcan, peter.palcek}@fstroj.uniza.sk, dblazek@gmail.com

Abstract. The aim of this work is to describe and explain internal damping on stress amplitude dependence in an extruded aluminium alloy EN AW – 2007. Dependence was examined after recrystallization annealing at the temperature of 250 °C. In the work the analysis of the internal damping caused by the dislocation breakaways was done. This behavior describe Granato and Lücke model. The method of resonant system quality was used to measure the internal damping. For this method it is necessary to use a specimen, frequency of which is similar to the frequency of the whole resonant system. All experiments were carried out at the frequency around 20.4 kHz at the room temperature.

Keywords: Internal damping, Aluminum alloy, AW-2007, Annealing, Dislocation

1. Introduction

Reduction of mass of mechanical constructions and components has belonged to stable trends in modern progress for many years. Impulse in this direction comes from aviation and automotive industry. Aluminium alloys have been already known few decades and they are widely used in the automotive and aviation industries. The growing interest of these industry departments for Al alloys is due to a goal to reduce fuel consumption of cars and exhaust emissions. The properties that make aluminium alloys the most economical and attractive for a wide variety of uses are appearance, light weight, fabricability, physical and mechanical properties and corrosion resistance [1].

Vibration analysis is an important tool for the systems and material stress distribution own frequencies calculation. By this technique one can determine if the parts or whole components will fill functions, for which they were made. One can also predict results of dynamic loading, such as dynamic strain, fatigue life or noisiness. Optimization of the internal damping of material through changes in the structure is an effective way for controlling and limiting the vibrations amplitude. [2].

Internal damping depends on many factors, such as temperature, purity, grain size, mechanical and heat treatment of the material. Temperature dependence $Q^{-1} = f(T)$ is important for the evaluation of the mechanical relaxation processes. Progress of dependence $Q^{-1} = f(\varepsilon_a)$ is a function of many structural and substructural factors, as a type of chemical composition, mechanical and heat treatment of experimental material, overlapping various partially mechanisms from mechanical dissipation of energy [3, 4].

2. Experimental details

2.1. Microstructure

The aluminium alloy EN AW-2007 was used for internal damping measurement. The basic material was Al-Cu-Mg alloy with Pb addition for machinability improving. Internal damping specimens were machined out of extruded rods without heat treatment. The chemical composition of this material is given in Table 1.

The microstructure of experimental alloy consists of substitute solid solution α phase and intermetallic phases. In as cast state of material it is possible to identify some intermetallic phases, primarily based on: Al-Cu (MgPb), Al_2Cu , Al-Cu (FeSiMn) (Fig. 1a) [5, 6]. The extruded material has been deformed by very high speed. The plastic deformation occur and new deformed structure (fibrous structure) was created (Fig. 1b) [7].

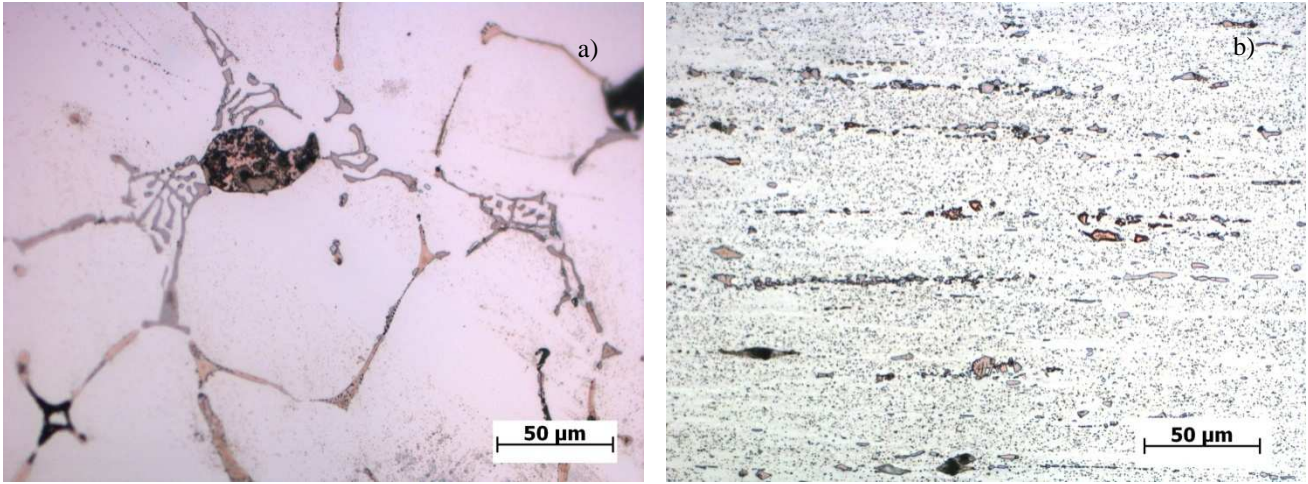


Fig. 1. Microstructure of experimental material EN AW-2007 (a) as cast, non-etched, (b) as extruded, longitudinal direct, etched HF.

	Si	Fe	Cu	Mg	Pb	Mn	Cr	Ni	Zn	Al
AW-2007	0.8	0.8	3.3-4.6	0.4-1.8	0.8-1.2	0.5-1.0	0.1	0.2	0.8	rest

Tab. 1. Chemical compositions of AW-2007 in wt. %.

2.2. Internal Damping Method

The measurement of amplitude dependent internal damping (ADID) was done on equipment used on the Department of Material Engineering. The method of resonant system quality was used for the internal damping measurement. On this equipment it is possible to investigate amplitude, temperature and time dependence of internal damping. For this method it is necessary to use a specimen, frequency of which is similar to the frequency of the whole resonant system, which was about 20.4 kHz. During the measurement, the resonant frequency of specimen little decreased due to the microplastic deformations. The resonant system was actuated by piezoceramic elements. The vibration amplitudes of specimen were forced by loading voltage amplitude and measured by electric current in circuit. The experiment was controlled by computer [8].

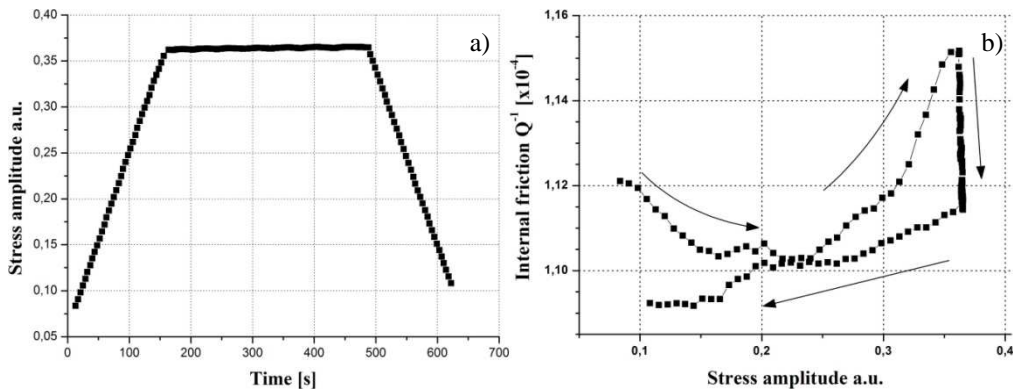


Fig. 2. (a) Time course of experiment and (b) characteristic ADID loop for an experimental material AW – 2007 .

All measured cycles had the same fine determined progress. In Fig. 2 the time course of experiment is presented. First, the stress amplitude is growing from zero up to the maximum load.

At the maximum stress amplitude the specimen is held for about 5 minutes. Last, the stress amplitude decreases. Next measurement run follows after 30 minute break due to the relaxation of dislocation structures into steady state.

3. Results and Discussion

The ADID curves were measured after annealing (at 250 °C for 2 hours). Fig. 3 shows characteristic amplitude dependence loops measured in cycles. The annealing temperature 250 °C was sufficiently high for removing residual stress after mechanical treatment and dislocation forest relaxation.

Annealing at the sufficiently high temperature has significant effect on dislocation structure. All slip systems are activated in material and thermally activated dislocation transport also occurs. At the same time the annihilation of dislocations with opposite direction occurs. The Frank-Read sources are removed due to shortening of the length of dislocations. After quenching at the room temperature the relatively immobile dislocation forest is present in the material that does not contribute to the internal friction and does not generate new dislocations. Preliminary deformation of material is needed to create a balanced structure of mobile dislocations.

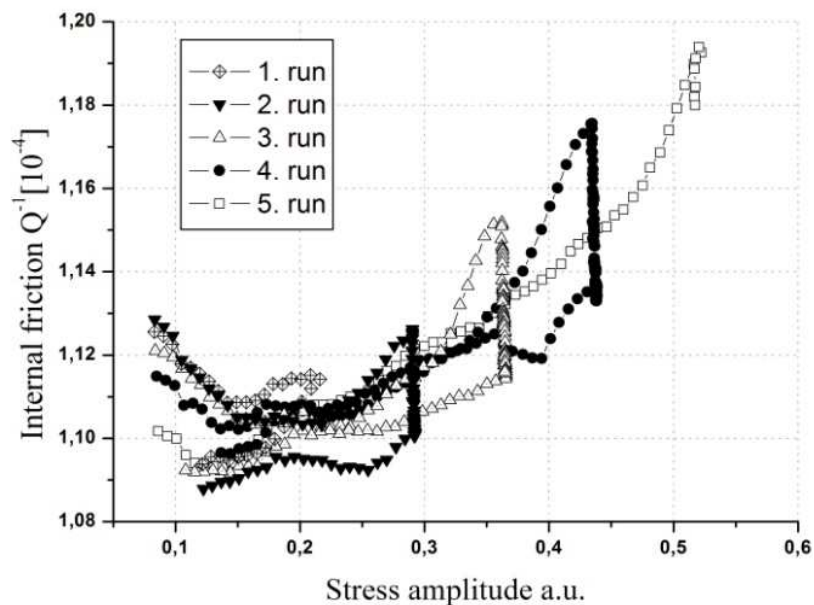


Fig. 3. ADID measurements on sample which was annealed at the 250 °C/2 hours.

Measured ADID curve has characteristic shape. First, the damping is little decreasing, next it is growing until the critical stress amplitude ϵ_{cr2} is achieved at which the microplastic deformation of suitable oriented grains occurs. Next the damping is growing rapidly with deformation amplitude. When the amplitude of vibrations is held constant, the density of dislocations grows up and the dislocation forest saturates itself. The internal damping is falling down and critical stress amplitude ϵ_{cr2} grows up to the actual amplitude of deformations. In the first cycles the increases of damping was relatively small, because microplastic deformation takes place only in some grains. In the next cycles, the number of grains, where amplitude of deformation overcomes the critical value, gradually increases. The maximum of internal damping is higher too.

One can see the displacement of characteristic triangle progress, which appears when microplastic deformation is observed. This displacement into higher deformation amplitudes was linked with changes of dislocation forest structure. The structure of dislocation forest may evolve beyond the critical amplitude ϵ_{cr2} only. Dislocations become temporarily movable and the damping is high. After some time the forest saturate again. Denser dislocation forest is responsible for the lower mobility of dislocations and lower damping.

The damping at the beginning of the following cycle is higher than at the end of previous one due to the higher mobility of dislocation after break during which the dislocation forest is relaxed, dislocations are annihilating and the mobility is growing.

During the measurement specimens passed through fatigue process. One run of measurement takes about 700s which present $1,4 \times 10^7$ cycles, at the maximum stress amplitude about 6×10^6 cycles. In the Fig. 3 the sample reached its fatigue life at the fifth cycle, during the saturation process.

4. Conclusions

This contribution presents amplitude dependence internal damping curves measured on the extruded aluminium alloy AW-2007 after annealing. From these measurements we can make the following conclusions:

- The ADID curve after annealing at temperature of 250 °C was observed and described.
- The annealing temperature has significant influence of dislocations density, structure of dislocation forest and also their mobility. During annealing, the density of dislocation and residual stress decreased.
- During measurement the displacement of characteristic triangle shape was observed. This displacement is linked with the cyclic microplastic deformation of experimental material and increases with the critical amplitude of vibrations ε_{cr2} .
- Cyclic microplasticity does not influence the basic value of internal damping at low deformations amplitudes. After break between measurements break the damping is little higher than at the end of the previous cycle.
- Specimens pass through fatigue process during measurement. They were loaded approximately 1×10^7 cycles at each measured run.

Acknowledgement

The research was supported partially by SK VEGA grant No. 1/0249/09 and project APVV SK-PL-0049-09. Authors gratefully acknowledge this support.

References

- [1] MARTIN J. W.: *Materials for engineering*. Woodhead Publishing: Cambridge, England, Third edition, 2006, ISBN: 1-84569-160-1
- [2] PUŠKÁR, A. 1995. *Vnútročné tlmenie materiálov*. Žilina: EDIS, 1995, 382 s., ISBN 80-7100-260-7
- [3] BLANTER, M.S., et. al.: *Internal Friction in Metallic Materials*. Berlin Heidelberg: ©Springer -Verlag, 2007, ISBN 3-540-68757-2, p. 539.
- [4] LAZAN, B.J.: *Damping of Materials and Members in Structural Mechanics*. Pergamon, Oxford, 1968, 317 p.
- [5] MAŁGORZATA, W.: *Metallographic Techniques for Aluminum and Its Alloys*, Foundry Research Institute, Kraków, Poland. 2004, ISBN: 0-87170-706-3.
- [6] MICHNA, Š., LUKÁČ, I., OČENÁŠEK, V. a kol.: *Encyklopedie hliníku*. Adin, s. r. o. Prešov, 2005
- [7] POLIAK, R., PALČEK, P., CHALUPOVÁ, M.: Al-Mg-Si alloy crack properties after various mechanical processing In: *Materials engineering*, 2008, ISSN 1335-0803, issiu 15, no. 4, p. 33-36.
- [8] BLAŽEK, D., et al.: The internal damping of depinned dislocations in Mg AZ31 alloy In *27th Danubia-Adria symposium on advances in experimental mechanics*. Wrocław University of Technology, 2010, ISBN 978-83-87982-59-1, p. 9-10



Multiparametric Evaluation of Barkhausen Noise Envelopes

*Martin Rosipal, Miroslav Neslušán ** Miroslav Faktor

*University of Žilina, Faculty of Mechanical Engineering, Department of Machining and Manufacturing,
 Univerzitná 1, 01026 Žilina, Slovakia,

** University of Žilina, Faculty of Management Science and Informatics, Department of Informatics
 Univerzitná 1, 01026 Žilina, Slovakia

Abstract. This paper deals with application of Barkhausen noise for analysis of surface integrity in grinding operations. The stress state is analyzed in relation to tool wear. Application of non-destructive testing through the Barkhausen noise is more suitable for grinding operations. Application of Barkhausen noise testing for others operation will require the next research.

Keywords: Barkhausen noise, grinding, residual stress

1. Introduction

Micromagnetic methods based on the Barkhausen noise are suitable for evaluation of surface integrity. This method is based on the continuous rotation of magnetic field that results in to the non continuous magnetization of material. This discontinuity is named as the Barkhausen noise.

Barkhausen noise is damped with increasing depth. The main reason is the damping effect of eddy current influencing electromagnetic fields of the moved Bloch walls. The Bloch walls rotate under the external load to the orientation of magnetic flow. The compressive stresses decreases intensity of Barkhausen noise and the tensile stresses increase this movement [1, 2, 6, 7] “Fig. 2”. Hardness of structure influences intensity of Barkhausen noise too, this influence represents Fig.1.

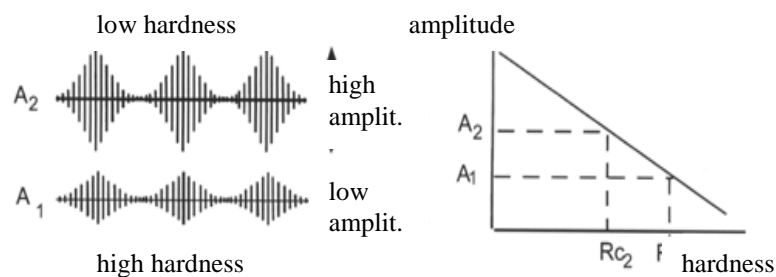


Fig. 1. Influence of hardness on character of Barkhausen noise [2, 3, 4, 5]

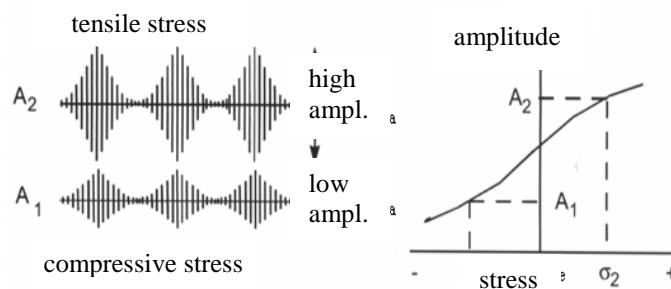


Fig. 2. Influence of stress on character of Barkhausen noise [2, 3, 4, 5, 8]

Barkhausen noise is the suitable tool for investigation of surface integrity, especially for analysis of the thermally induced damage. Surface integrity is very important in the scope of finishing operations on parts. And so, this paper is focused on the application of non – destructive evaluation of surface integrity through Barkhausen noise after grinding.

2. Conditions of Experiments

Experiments were carried out on the roll bearing steel 100Cr6 of hardness 62 HRC. There were made the rings of external diameter 48 mm, internal diameter 40 mm and width 7 mm. These rings were ground under the constant cutting conditions in relations to cutting time, respective the related removed material. Series of the 3 ring were inspected after the certain passes of tool (these passes relate to material removal and cutting time are in Tab. 1.).

time (min)	0	2,5	7	13	20	30	36	44
removed material (mm ³)	2	6,2	19	37	56	87	105	130

Tab. 1. Intervals of measurements of rings and related removed material

Grinding machine: 2BuD, Grinding wheel A 98 80 K9V, Cutting fluid – Emulzín H (2%), cutting depth $a_p = 0,025$ mm (10 passes + 3 spark out passes), feed $v_f = 6,7$ m.min⁻¹, workpiece rotation speed $v_w = 0,44$ m.min⁻¹, cutting speed $v_c = 28$ m.s⁻¹, single crystal diamond dresser. Analysis of stress state was analyzed on 24 rings (3 rings per each 8 series) in 8 points on the periphery of the rings. There was analyzed area of the envelope curve of Barkhausen noise MBN (related to stress state of surface) and the maximum amplitude of the noise MBN max (related to the hardness of the rings). Except this approach the more complex evaluation was carried out.

3. Experimental Results

The cumulative effect of hardness, stress and residual stresses was carried out through the Barkhausen noise. Evaluation of envelope curves was carried out through the special software as illustrates Fig. 3. This way more complex evaluation of Barkhausen noise character could be carried out than the conventional evaluation (based on maximum and area of Barkhausen noise envelope). The parameters evaluated in the special software package are illustrated in Fig. 3 and their detail description is in Tab. 2.

Parameter	Description
AMH	area of envelope curve
Mmax	maximum of envelope
HcM	coercive force on Mmax
PIM	distance between Hc = 0 and offset, Hc - coercivity is the intensity of the applied magnetic field required to reduce the magnetization of that material to zero
HWM	width on effective maximum Mmax
Mmin	minimum of envelope
Mmaxr	maximum of curve after regression
AMHR	area of envelope after regression
EfAMHR	effective width related to the AMHR
SDA	average value of signal variation after regression
SDQ	effective value of signal variation after regression
SDZ	distance between the maximum and minimum of signal variation after regression

Tab. 2. Some parameters derived from Barkhausen noise envelope

Fig. 4 illustrates the influence of grinding wheel tool on residual stress. Residual stresses are significantly increasing with grinding wheel tool “Fig. 4” and the stress state can lead to formation of cracks on the surface.

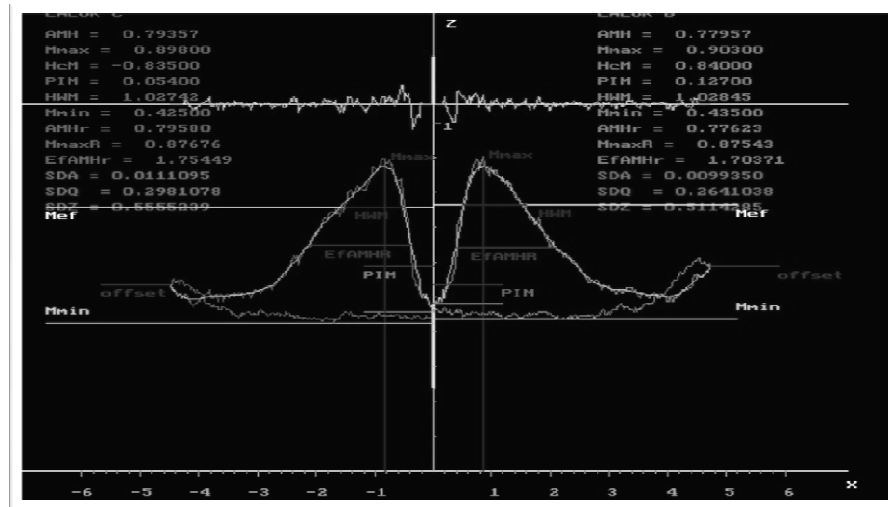


Fig. 3. Screen of the special software for complex evaluation of Barkhausen noise

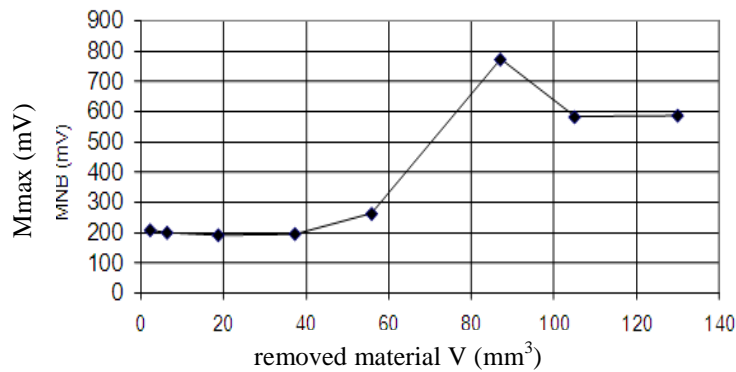


Fig. 4. Influence of grinding wheel wear (represented by removed material) on area of Barkhausen noise after grinding

Process of grinding wheel wear significantly affect thermal load of surface. This thermal load causes shift of surface hardness decreasing and shift of residual stresses to the tensile zone. Fig. 4 show relative stable values of Barkhausen noise area up to the value of $V = 60 \text{ cm}^3$. Above this value, grinding wheel become worn and should be redressed. The next grinding leads to formation of high tensile stresses and so increase of area of Barkhausen noise. It can be easily understood that this way surface damage can be easily identified. “Fig.5, Fig.6”.

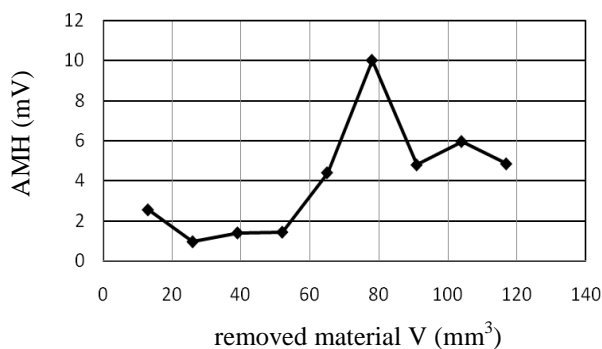


Fig. 5. Influence of grinding wheel wear on area of Barkhausen noise after grinding

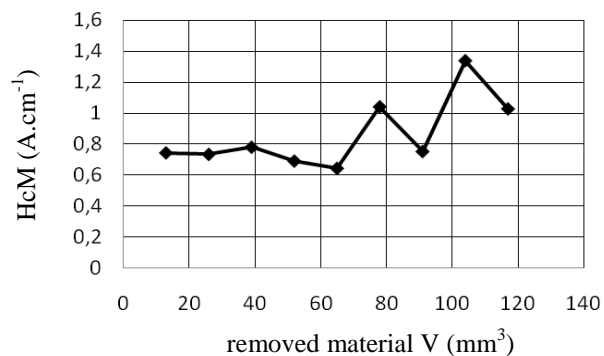


Fig.6. Influence of grinding wheel wear on coercivity of Barkhausen noise after grinding

4. Conclusion

The results of measurement show that application of Barkhausen noise is very suitable for monitoring of thermally affected surfaces after grinding. Multiparametric evaluation enables more detail analysis. Generally, conventional and detail analyses enable to identify of surface thermal damage in grinding operation. However, the conventional approach can fail in other applications such as hard turning. Hard turning process is an alternative operation to the grinding process. On the other hand, character of this process is completely different than grinding operation. And so, formation of surface integrity and its character completely differ from the grinding surface. Surface integrity after hard turning significantly affect first of all tool wear (formation of white layers on the surface). Fig. 7 shows that conventional evaluation of surface through the area of Barkhausen noise can be applied and so the more detail analysis should be carried out. This analysis and related correlation research should determine the suitable parameter for identification of surface damage after hard turning or other similar operations. Except this, it is possible to carry out the next modification of experimental procedures such as evaluation of Barkhausen noise in the low frequency range, frequency analysis, modification of excitation magnetic field, etc. to find suitable process of surface integrity identification.

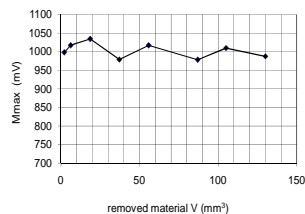


Fig. 7. Influence of tool wear on area of Barkhausen noise after hard turning

References

- [1] KARPUCHEWSKI, B. *Introduction to micro magnetic techniques*, ICBM1 report Hannover 2002
- [2] ABUKU, S., CULLITY, R. D. *A Magnetic Method for the Determination of residual Stress*, Exp. Mech. 11, 1971
- [3] ALTPETER, I., THEINER, W., BECKER, R. *Eigenspannungsmessung an stal deer Güte 22 NiMoCr 37 mit magnetischen und magnetoelastischen Prüfverfahren* 4th Intern. Conf. on NDE in Nuclear Industry, Lindau 1981
- [4] KINOSHITA, M., MURAYAMA, T., HOSHINA, N., KOBAYASHI, A., SHIMIZU, R., IKUTA, T. *The surface damaged layer study of Mn-Zn single crystal ferrites using magnetic domain observation*, CIRP, 1/1976, pp. 449
- [5] NESLUŠAN, M., TUREK, S., BRYCHTA, J., ČEP, R., TABAČEK, M. *Experimentálne metódy v trieskovom obrábaní*, EDIS Žilina, 2007, ISBN 978 – 80 – 8070 – 811 – 8, 349 s
- [6] THEINER, W., HÖLLER, P. *Magnetische vVerfahren zur Spannungsermittlung*, HTM – Beiheft Carl Hanser Verlag 1982
- [7] BRINKSMEIER, E., SCHNEIDER, E. *Nondestructive Testing for Evaluating Surface Integrity*, CIRP, 2/1984, pp.489-496
- [8] THEINER, W. A., WILLEMS, H. H. *Determination of Microstructural Parameters*, Symposium on Nondestructive Methods for Material Property Determination, april 6-8, 1983 Hershey, Pennsylvania



Measurement of Surface Temperature of Polymerization Reaction of Bone Cement with Thermovision Camera

*Róbert Seewald, *Peter Palček, **Martin Brandt, ***Libor Nečas

*University of Žilina, Faculty of Mechanical Engineering, Department of Materials Engineering Univerzitná 1, 01026 Žilina, Slovakia, {robert.seewald, peter.palcek}@fstroj.uniza.sk

**University of Žilina, Faculty of Electrical Engineering, Department of Measurement and Applied Electrical Engineering, Univerzitná 1, 01026 Žilina, Slovakia, brandt@fel.uniza.sk

***Orthopedics and Traumatology Clinics, Teaching Hospital in Martin, Kolárova 2, 03659 Martin, Slovakia, necas@mf.n.sk

Abstract. This article deals with the measurement of surface temperature curves of exothermic polymerization reaction of bone cements by means of thermovision. Measurements were done with thermovision camera FLIR SC640. We were observing the bone cement layer thickness influence to the polymerization temperature and to the duration of polymerization. Then we were dealing with the influence of environment to the polymerization reaction. Bone cement SmartSet® HV was used as experimental material.

Keywords: Bone cement, temperature, polymerization, thermovision.

1. Introduction

Bone cement is used for fixation of total endoprosthesis in human organism. If such surgical intervention is made by experienced surgeon respecting the level of current development that means that people which were condemned to invalidity in the past are now after this intervention and after-treatment able to return to normal life. Since first attempts in sixties of 20th century till present day the bone cements had made great improvements in quality and also in quantity of different modifications. Lot of workplaces are increasing in the world which uses bone cements to fixations of total endoprosthesis every year. Therefore lot of people can use this unique conquest of modern medicine [1].

2. Experimental material

SmartSet HV bone cement was used as an experimental material in order to respect the fact that it is most common bone cement in Slovakia. Composition of bone cement shown in Tab.1 consists of two basic compounds (powder and liquid).

POWDER	w/w %	LIQUID	w/w %
MMA/MA copolymer	84	MMA	97,5
Dibenzoylperoxide	1	N,N-Dimetyl-p-toluidine	≤ 2,5
ZrO ₂	15	Hydroquinone	0,0075

Tab. 1. Quantitative composition (w/w %) of SmartSet® HV bone cement [w = weight]

Bone cements consist of two basic compounds (powder and liquid). These two elements are mixed by the procedure specified by manufacturer. Bone cement hardening is ensured by polymerization reaction, which is highly exothermic. Bone cements are used to fill the space between bone and implant.

The main goal of bone cement is to transfer strains from implant to bone structure. Bone cement layer is supposed to be stable to ensure safe fixation to bone. Maximal stickiness of bone

cement to implants (prosthesis) and to bone should be gained in ideal. Duration of application must be long enough to secure sufficient time for placing of bone cement into the bone and precise location of implant for surgeon. Bone cement has got lower modulus elasticity than metal implant but has sufficient stiffness and excellent biocompatibility [2, 3, 4, 5].

2.1. Influence of Ambient Temperature to Polymerization of Bone Cement

Manufacturers of bone cements provide the mixing duration, waiting duration, working duration and hardening duration in manuals added to bone cements. Basic components of bone cement are mixed during mixing phase and this is the start of polymerization exothermic reaction. Released temperatures were measured during working and hardening phase of bone cement. The explanation of bone cement polymerization depending on the time duration is shown in the Fig. 1. T_{amb} is inception temperature of bone cement polymerization and its value is equal to the ambient temperature. As we can see in the figure the polymerization temperature at the end of working phase starts to increase steeply. Time value is expressed as half of difference between T_{max} and T_{amb} also known as application time of bone cement. The temperature after achieving T_{max} edge also known as polymerization peak temperature just decreases. DT- is time of cement maturing.

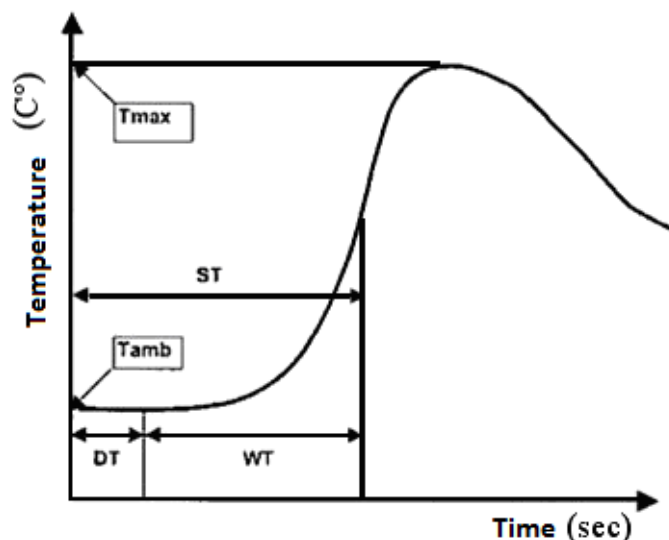


Fig. 1. Curve of polymerization temperature depending on time

Peak temperature values during hardening of bone cement depend mainly on the PMMA/MMA ratio and also on composition of liquid and solid elements of bone cement, also on the polymer powder elements size. Polymer powder small pearls size influences peak temperature of bone cement polymerization in such way that if we reduce the polymerized pearls size the ratio between surface and volume of pearls will increase. Thereby powder will dissolve more in monomer liquid which causes increase of bone cement viscosity. Bone cement viscosity increase leads to Trommsdorff effect which causes heat transfer downgrade that leads to peak polymerization temperature increase and also the bone cement application time will shorten [6,7].

Manufacturer states influence of ambient temperature to the hardening time. Ambient temperature was measured during sample preparation because of this reason. Duration of all phases from mixing to hardening were extending more and more with ambient temperature lowering. Higher the temperature was shorter the processing durations were which was making the manipulation with bone cement more difficult. This effect rules for all used kinds of cements based on polymethylmethacrylates in surgical area. With increase of ambient temperature from 23°C to 25°C the total working time with bone cement will shorten by two minutes. All the manipulation phases with bone cement were shorter at the same time and that is inappropriate for surgical praxis [8].

2.2. Measuring of Temperature During Polymerization by Thermovision Camera

Thermovision camera FLIR SC640 used for temperature measurement is shown in the {Fig. 2.a}. Image created by this thermovision camera is shown in {Fig. 2.b}. Three different thicknesses of bone cement were used (2mm, 3mm a 5mm). Bone cement was after mixing placed in prepared metal form, which secured precise dimensions of measured bone cement. One of the forms is shown in the {Fig. 3a}. Inner diameter of metal forms was 24 mm. Bone cement shown in {Fig. 3b} is after hardening phase and after extracting from metal forms. Dimensions of wall thickness of measured bone cement were chosen because of the possible presence of such dimensions after implantation of implant.

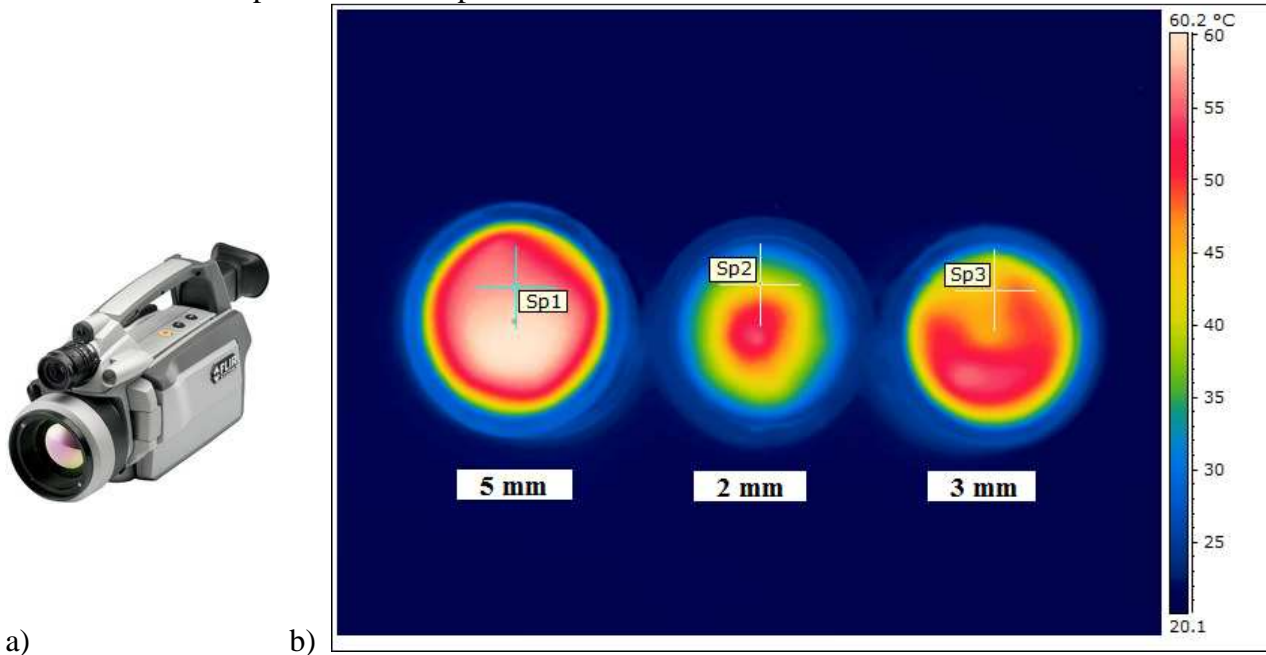


Fig. 2. a) FLIR SC640 Thermovision camera, b) Temperature image from thermovision camera on the meeting of eleventh and twelfth minute of measurement of polymerization temperature.

Measurement of polymerization temperatures of bone cement was done at ambient temperature of 20°C which was constant during whole measuring process.

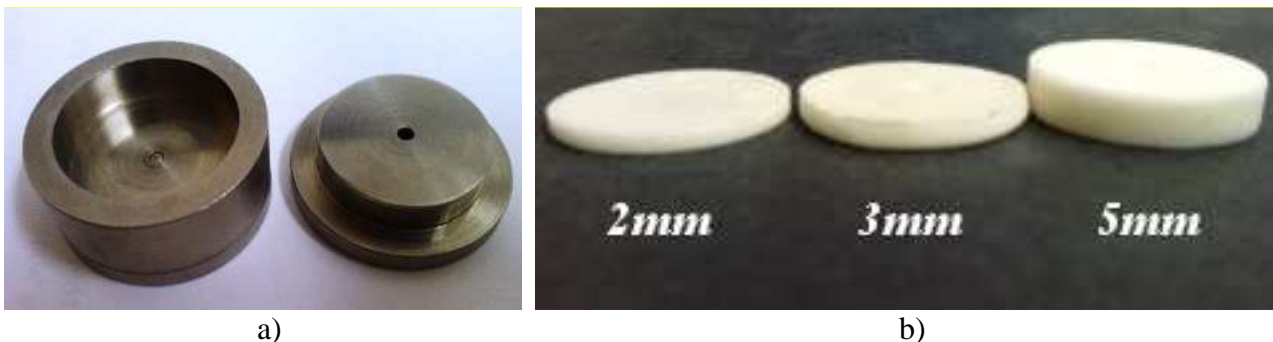


Fig. 3. a) One of the forms used to measurement of polymerization temperature of bone cement, b) Hardened bone cement of extracting from forms.

Measured polymerization temperature courses of individual measured thicknesses of bone cement are shown on Fig. 4. Sample temperature was not very different from ambient temperature within four minutes from the beginning of mixing process of basic components of bone cements (in our case 20°C). Measured values of temperatures are recorded after fourth minute in tables.

We recorded maximal gain of temperatures (peak temperatures) on the border of eleventh and twelfth minute from the beginning of mixing process of components for all measured thicknesses of

bone cement. We are recording then after twelfth minute decrease of measured temperatures, which means that the bone cement achieved full polymerization of molecules strains.

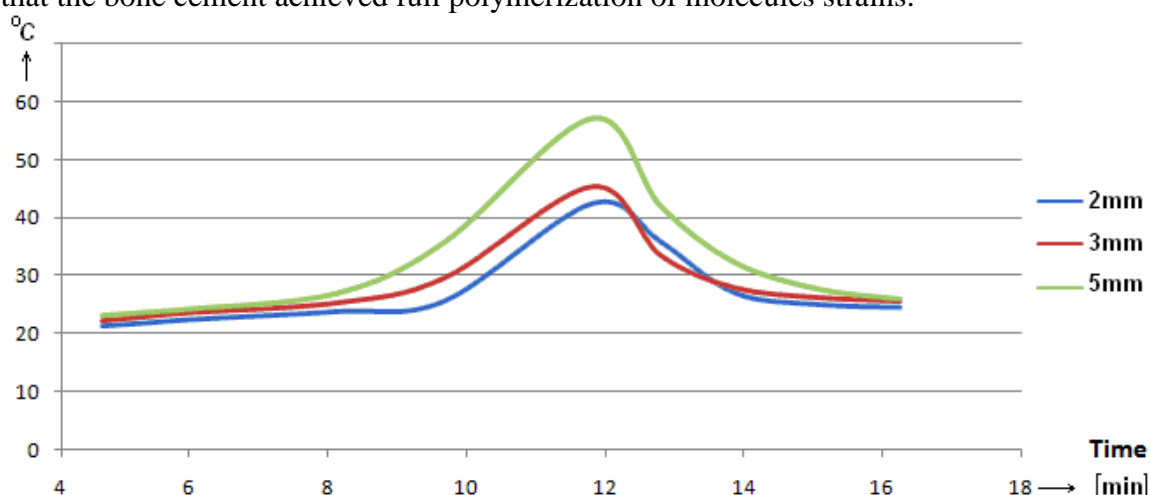


Fig. 4. Measured temperature curves during polymerization of bone cement with various thicknesses.

3. Conclusion

We came to conclusions that thickness of bone cement strongly influences polymerization temperature values during measurement of surface polymerization temperature of bone cement with thermovision camera FLIR SC 640. We recorded peak temperatures in the same exact time of the meeting of eleventh and twelfth minute with all thickness of bone cement which that thickness of bone cement do not influence the polymerization duration of whole matter. It is necessary to know that bone cement mixed at the same time and formed to various shapes by means of polymerization exothermical reaction will harden completely at the same time. Polymerization temperatures of bone cement in human body are significantly lower respecting temperature outlet by inserted implant which is put into human body. They are also lowered by inner circulation of blood, by bone itself and surrounding tissue.

Acknowledgement

This research has been partially supported by VEGA no. 1/0249/09 and SK-PL-0049-09

References

- [1] <http://www.apotheka.sk/print.asp?id=226>, information availability: 10.02.2011
- [2] <http://www.jbjs.org.uk/cgi/reprint/42-B/1/28> - Anchorage of the femoral head prosthesis to the shaft of the femur, information availability: 20.3.2010.
- [3] <http://www.orthopaedie-hamburg.de/pdf/Wiley-Verlag%202004.pdf>–Klinische Anwendungsmöglichkeiten von porösen Biomaterialien im Knochengewebe, information availability: 15.3.2010
- [4] DEB, S., DI SILVO, L., VASQUEZ, B., SAN ROMAN, J. *Water Absorption Characteristics and Cytotoxic and Biological Evaluation of Bone Cements Formulated with a Noval Aktivator*, *Biomaterials*, year (1999), No. 48, p.: 719-725
- [5] CONSTANTZ, BR., ISON IRA, C., FULMER, MT., POSER, RD., SMITH, ST., VAN WAGONER, M., ROSS, J., GOLDSTEIN, St. A., JUPITER, JB., ROSENTHAL, DI. *Skeletal Repair by in Situ Formation of the Mineral Phase of the Bone*. (1995) *Science* p.: 267ff
- [6] BREUSCH, S., MALCHAU, H. *The Well-Cemented Total Hip Arthroplasty: Theory and Practice*, Springer, 2005, ISBN 3540241973.
- [7] YASZEMSKI, M. J., TRANTOLO, D. J., LEWANDROWSKI, K., HASIRCI, V., WISE, D. L., ALTOBELLI, D. E. *Biomaterials in Orthopedics*, Informa Health Care, 2003, ISBN 082474294X
- [8] SEEWALD R.: *Mechanické vlastnosti kostných cementov*. Diploma work, University of Žilina, 2008

Experimental Comparing Evaluation of Tribological Properties of Surface with Geometrical Texture

*Piotr Sęk

* Ing. Piotr Sęk, Chair of Operation Engineering, Faculty of Mechatronics and Machine Building, Kielce University of Technology, 1000-lecia P.P. 19 Road, Kielce, Poland, psek@tu.kielce.pl

Abstract. The paper shows results of experimental investigation on seal rings made of silicon carbide. Experiments were conducted using seal ring without surface modifications and a seal ring with a geometrical surface texture made with Nd:Yag laser, using the T01-M tester.

Keywords: Geometrical Surface Texture, Friction Reduction, Sliding Pair, Laser Surface Texturing

1. Introduction

Current technology has very high requirements for reliability, durability and performance of sliding friction pairs. For that reason new technologies were developed for forming and shaping the micro and macrogeometry of sliding surfaces. That why the manufacturing of surface geometrical texture became so important. Geometrical surface textures are regular, repeatable micro geometrical formations on the surface like micropores, grooves or cavities. The application of surface texturing has influence on:

- reducing the friction resistance both during movement and in rest state,
- widens the range of permissible values of friction node loads,
- assures a lower temperature of friction node in comparison to untextured one,
- restricts the wear and tear of friction pair elements,
- can be beneficial with other wear types like for example with fretting.

2. Object of Experiment

The objects of investigation were two rings made of silicon carbide (Fig. 1). One of them had a micro surface modification made with Nd:Yag laser. The modification was regular situated round shape micropores, each one 15 μ m deep and with a diameter of 87 μ m. The proportion of summary micropore surface to whole test ring surface was 20%. The other test ring for comparison had no surface modifications.

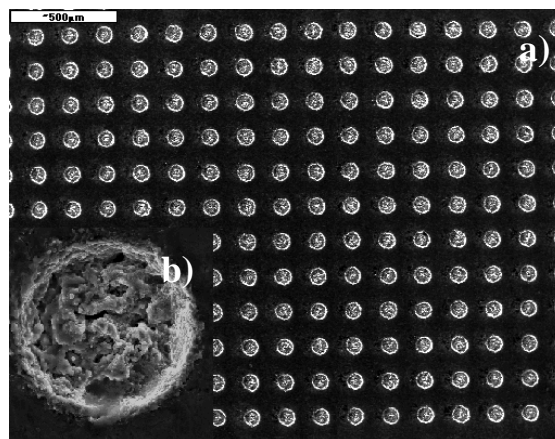


Fig. 1. Surface of a test ring with geometrical texture : a – magnification 50x, b – magnification 1000x.

3. Experiment Methodology

The experiment was conducted in the laboratory of terotechnology in Kielce University of Technology using the T01-M tribological tester machine (Fig. 2). The pressure on the rings was exerted by a steel sliced sphere with diameter of 5mm.

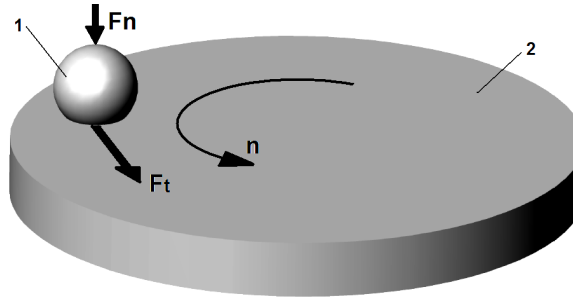


Fig. 2. Scheme of T01-M tester: 1 –sliced steel sphere, F_n – exerted pressure, 2 – test ring, F_t – friction force.

The experiment was conducted for two different exerted pressures: 29,43N and 39,24N and four rotary velocities: $n_1 = 720$ rot/min, $n_2 = 600$ rot/min, $n_3 = 500$ rot/min, $n_4 = 400$ rot/min. The lubricant was stearine oil. The duration of single test was 1200s. Test were conducted 15 times for each parameters set, then the results were averaged.

4. Experiment Results

Average experiment results are shown on Fig. 4, Fig. 3 presents chosen results:

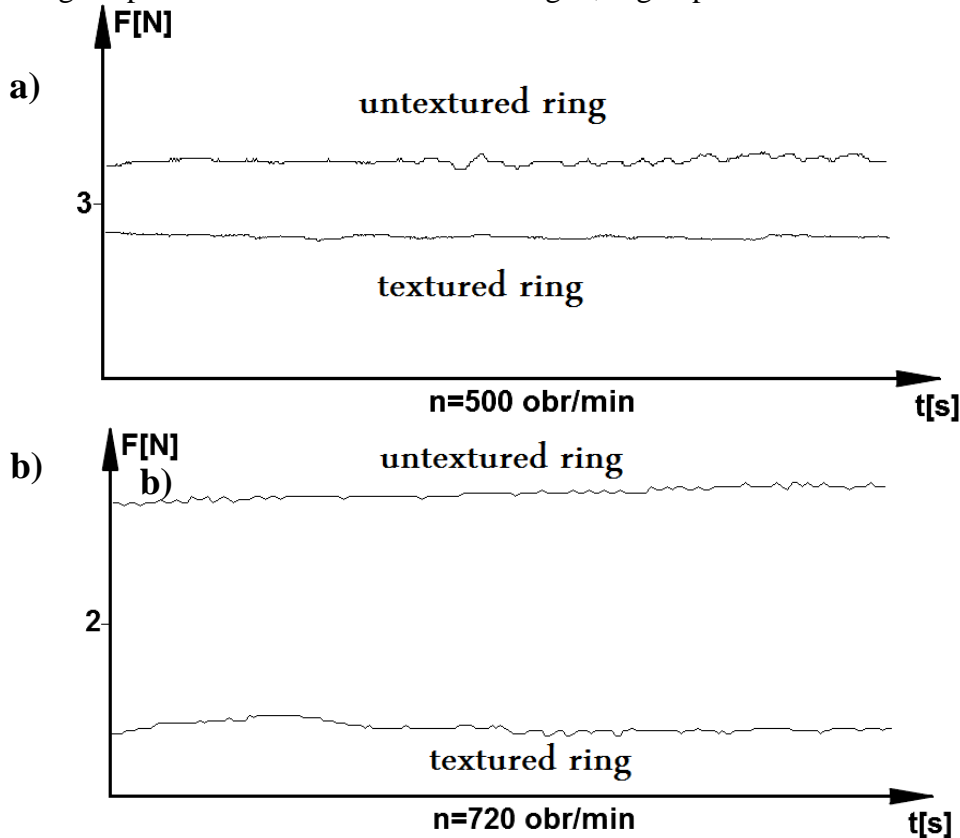


Fig. 3. Chosen results: a - force 29,43N, $n=500$ rot/min; b- force 39,24N, $n=720$ rot/min

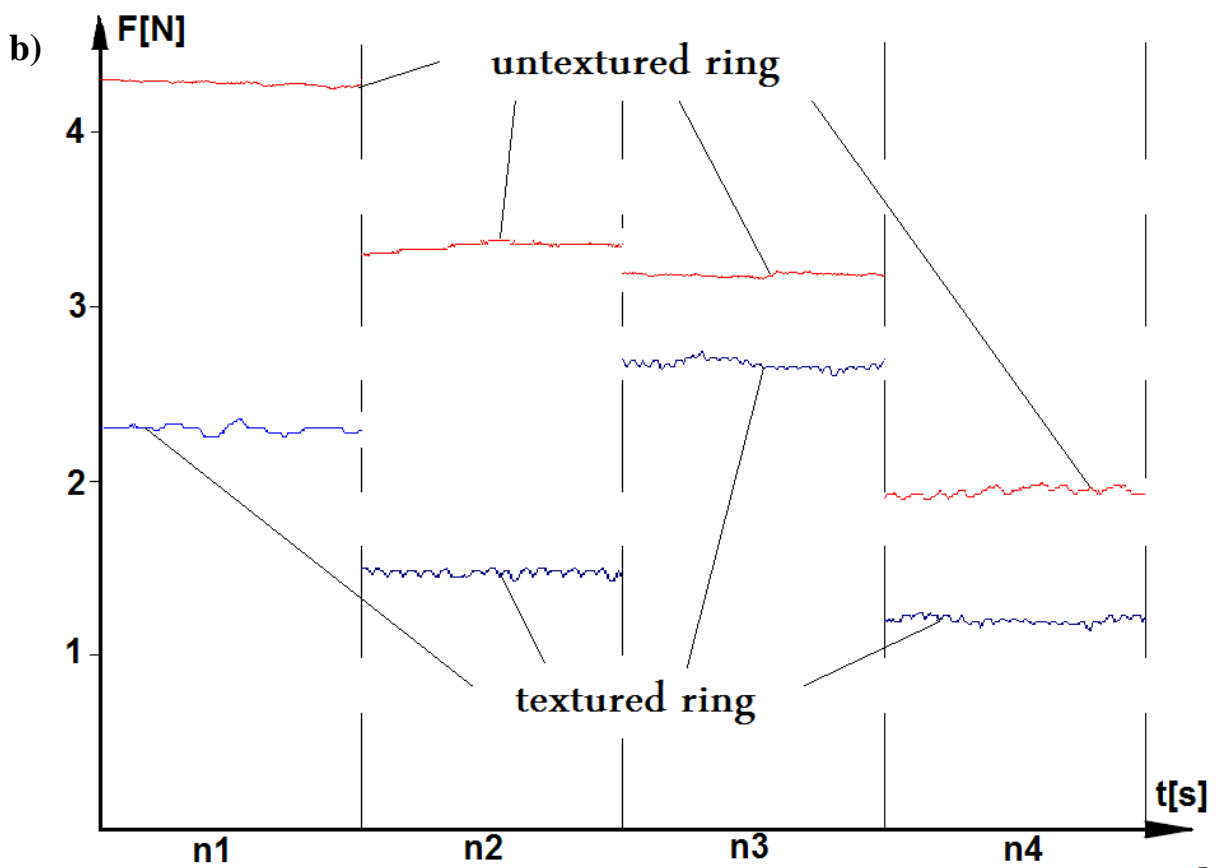
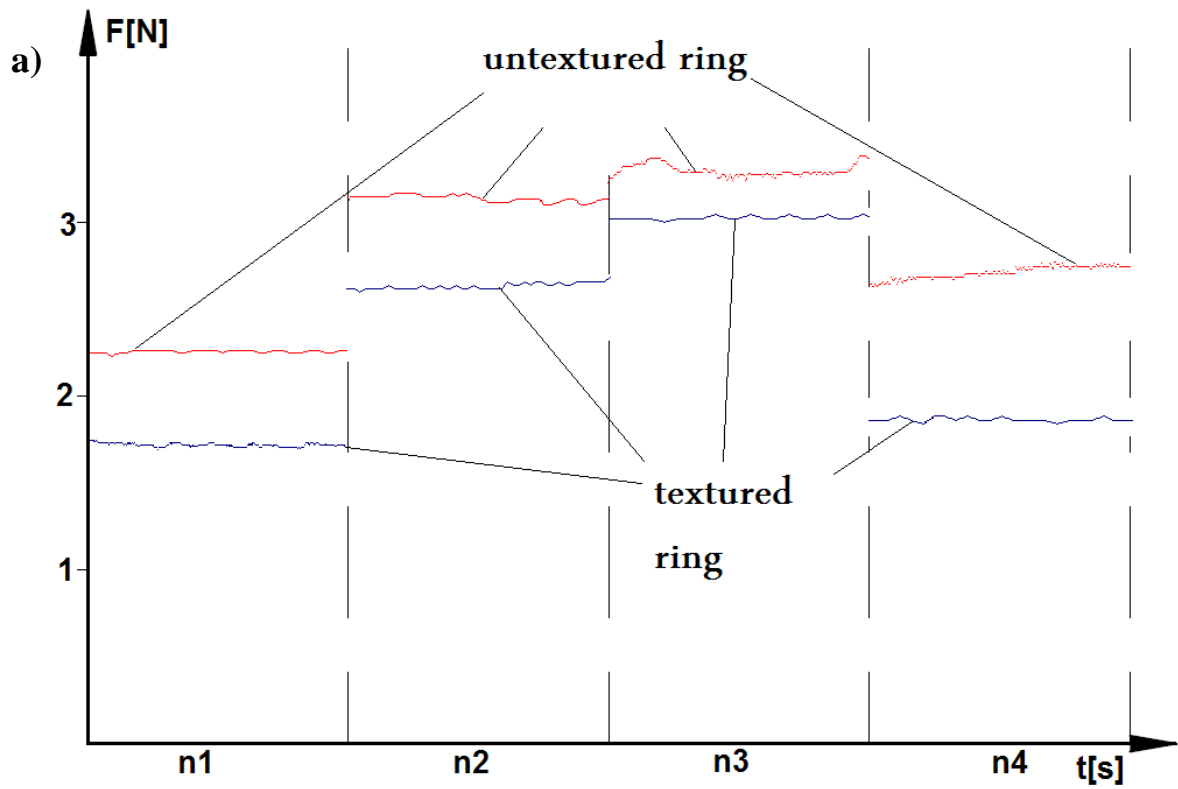


Fig. 4. Experiment results: a - force 29,43N; b- force 39,24N

5. Conclusion

For each parameter set, the application of laser surface texturing had a beneficial influence on reducing friction in presented sliding friction pair. For the applied load of 29,43 N the friction reduction achieved 16% to 34%, for load 39,24N the reduction achieved rate of 22% to 46%. The result show that we can make an unambiguous statement that application of surface geometrical surface has a great and beneficial influence on extending the life cycle and exploitation parameters of sliding friction pairs.

References

- [1] ANTOSZEWSKI, B. *Własności laserowo i plazmowo modyfikowanych ślizgowych węzłów tarcia na przykładzie uszczelnień czołowych*, Wydawnictwo Politechniki Świętokrzyskiej, Kielce 1999
- [2] MANABU, W., YUKIHIKO, Y., SHUZO, K. *Effect of surface texturing on friction reduction between ceramic and steel materiale under lubricated sliping contact*. *Wear* 254 (2003)
- [3] ETSION, I. *State of the Art in Laser Surface Texturing*– Transaction of the ASME January 2005, Vol 127
- [4] ETSION, I. *A Laser Surface Textured Hydrostatic Mechanical Seal Sealing Technology*, March 2003



Efficiency Assessment of Sheet Pile Rolling Technology

*Jacek Selejdak, ** Augustín Sládek

*University of Technology, Faculty of Management, Institute of Production Engineering, Armii Krajowej 19B, 42-200 Częstochowa, Poland, {jacek.s}@zim.pcz.pl

**University of Žilina, Faculty of Mechanical Engineering, Department of Technological Engineering, Univerzitná 1, 01026 Žilina, Slovakia, {augustin.sladek}@fstroj.uniza.sk

Abstract. In the article the subject to analysis was efficiency assessment of technological draw used for sheet piles rolling in period of 12 months. For this purpose there were determined individual times (of labour and downtime) of rolling draw and quality level of produced products. On basis of measured and calculated times there were calculated TPM coefficients. As a result of carried out researches it was found that the longest planned and unplanned standstill occurred in fourth month of research and was adequately 12360 minutes and 13620 minutes. In case of TPM coefficients the most important of them was overall efficiency of rolling draw (OEE) and it reached value above 88%, while quality coefficients (WJ) reached values above 97%. Based on carried out researches it was found that efficiency of sheet piles rolling technology is high.

Keywords: technology, rolling, sheet pile, TPM.

1. Introduction

Technology can be defined as a wide field of specific application of physical sciences and sciences about life and human conduct; it covers the whole range of purely technical problems, and also medical issues, agricultural, managerial and other, together with all its material and immaterial equipment [1]. Efficiency of technology has big influence on company operation [2, 3]. In order that company would operate well it must demonstrate high technology efficiency, which is realized by various types of machinery and equipment. System that provides adequate conditions for exploitation of machinery and equipment, is involved in both the period of their use and operation, and gives us information about efficiency of their use [1, 2, 4] is TPM (*Total Productive Maintenance*) system [5 ÷ 8]. This system means creating the best conditions prevailing in department performing manufacturing process [9, 10], as place where work people and technical objects [5] and improving the overall workplace quality [11].

Currently, World Class system requires very high requirements of the individual TPM coefficients, namely an aim at obtaining the following values of these coefficients:

- overall equipment effectiveness (OEE) at level 85%,
- availability (WD) at level 90%,
- utility (WW) at level 95%,
- quality (WJ) at level 99.9%.

2. Analysis of TPM Coefficients for Rolling Technology

Carried out researches of efficiency of sheet pile rolling technology refer to the period of 12 months. Sheet piles are sections of large dimensions, they find wide use in hydraulic engineering for construction of various dams and land reinforcement, as channel piles, driven piles and sheet piles walls interconnected with locks. Example of connecting sheet piles is presented in Fig. 1.



Fig. 1. Sample sheet piles connection.

All measurements of work times of rolling draw took place in industrial conditions during its operation. Then, based on measured and calculated TPM times there were calculated TPM coefficients. Researches results on times and TPM coefficients are presented in Tab. 1.

Researches period [month]	Shifting available standard hours of work (TZ) [minute]	Planned standstill time (PP) [minute]	Unplanned machines standstill (TA) [minute]	Machine operating time (TZ – TP) [minute]	Availability coefficient (WD) [%]	Number of processed products (P) [ton]	Product processing ideal time per unit (ICJ) [minute/ton]	Product processing real time per unit (RCJ) [minute/ton]	Operation velocity coefficient (WPD) [%]	Useful operation time (UCD) [%]	Utility coefficient (WW) [%]	Quality level (PD) [%]	Quality coefficient (WJ) [%]	Overall efficiency of rolling technology (OEE) [%]
1	44640	6540	1680	36420	95,59	82961	0,438	0,439	99,77	100	99,77	2,32	97,68	93,16
2	40320	5760	960	33600	97,22	73228	0,438	0,440	99,55	95,89	95,46	1,39	98,61	91,52
3	44640	6120	600	37920	98,44	82340	0,438	0,439	99,77	95,33	95,11	1,19	98,81	92,51
4	43200	12360	1260	29580	95,91	63430	0,438	0,438	100	93,92	93,92	1,78	98,22	88,48
5	44640	6420	720	37500	98,12	83620	0,438	0,439	99,77	97,89	97,67	1,43	98,57	94,46
6	43200	5760	840	36600	97,76	80245	0,438	0,440	99,55	96,47	96,03	1,33	98,67	92,63
7	44640	6060	1140	37440	97,05	81121	0,438	0,439	99,77	95,12	94,90	1,51	98,49	90,71
8	44640	5820	1200	37620	96,91	83215	0,438	0,439	99,77	97,11	96,89	1,52	98,48	92,46
9	43200	6060	960	36180	97,42	79620	0,438	0,440	99,55	96,83	96,39	1,86	98,14	92,15
10	44640	6120	900	37620	97,66	83251	0,438	0,439	99,77	97,15	96,93	1,56	98,44	93,19
11	43200	6000	1140	36060	96,94	81682	0,438	0,439	99,77	99,44	99,21	1,31	98,69	94,91
12	44640	6000	1320	37320	96,58	80006	0,438	0,441	99,32	94,54	93,90	1,39	98,61	89,43

Tab. 1. Times and TPM coefficients for rolling technology for period of 12 months.

Based on data presented in Tab. 1, it was found that availability coefficient (WD) reached values within the limits of 95,59% ÷ 98,44 Operation velocity coefficient (WPD) for researched rolling draw reached values within 99.32% to 100%, it reached value of 100% for the four researched month. Next from TPM coefficients - useful operation time (UCD) reached values within 93.32% to 100%, UCD coefficient value of 100% reached only in 1 researched month. Utility coefficient (WW) reached values within the limits of 93.90% to 99.77%. Values of quality coefficient (WJ) in researched period are within the limits of 97.68% to 98.81% (Fig. 2). The most important among TPM coefficients, namely the coefficient of overall efficiency of rolling technology reached values within the limits of 88.48% to 94.91%. The course of coefficient of overall efficiency of sheet piles rolling technology implemented by rolling draw in researched period was shown in Fig. 3.

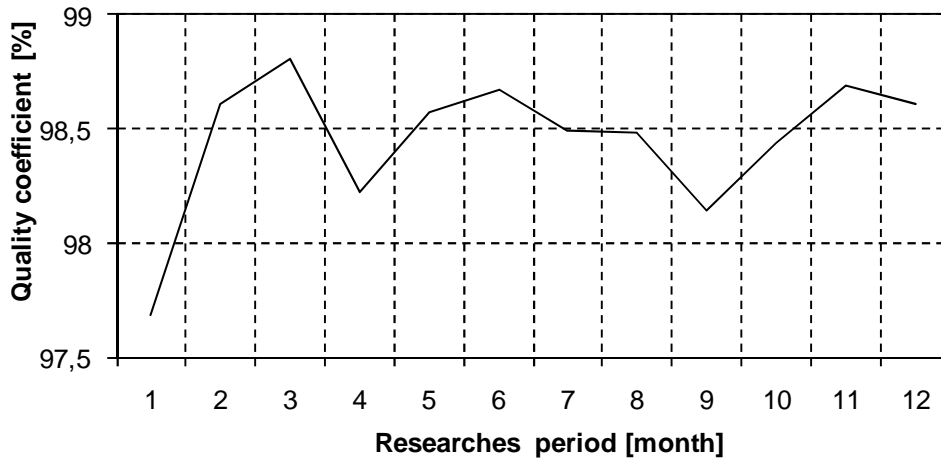


Fig. 2. The course of quality coefficient for sheet pile in researched period.

On basis of Fig. 2 and Tab. 1 it was found that the lowest value (97.68%) was achieved by quality coefficient (WJ) in the first month of research, while in other months, there was no considerable decline in quality coefficient.

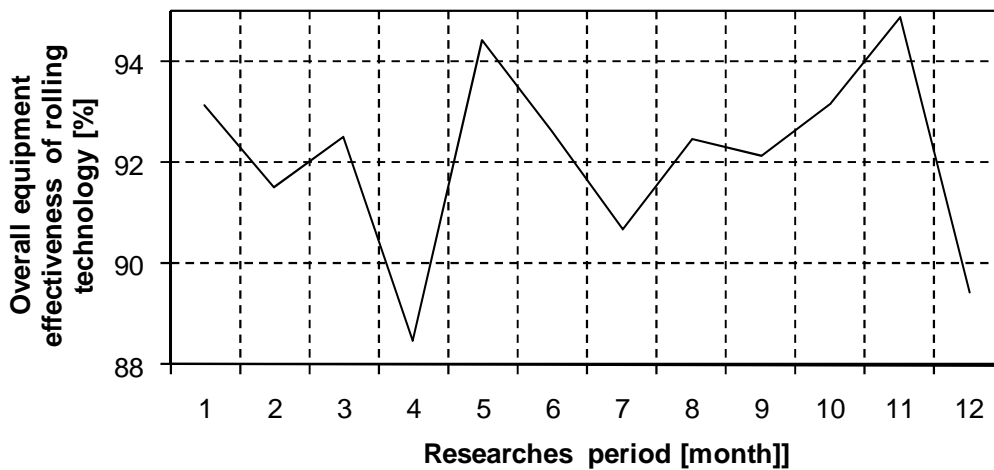


Fig. 3. The course of overall efficiency (OEE) of rolling technology used in manufacture of sheet pile in researched period.

As it results from Fig. 3 clear decline in the value of OEE coefficient for sheet pile rolling technology occurred in 4 and 12 months of research. This was caused by long unplanned standstill (TA) and in 4 month the longest planned standstill time of rolling draw (PP = 12360 min.). In addition, in four month of research useful operating time (UCD) reached the lowest value (93.92%) in researched period, and in 12 research month the lowest value (93.90%) in researched period reached utility coefficient (WW).

3. Summary

As a result of carried out analysis of times and TPM coefficients for rolling technology implemented by rolling draw it was found that individual TPM coefficients reached the following values:

- availability (WD) above 95%,
- utility (WW) above 93%,
- quality (WJ) above 97%,
- overall efficiency (OEE) above 88%.

Thus, the recommendations of the World Class did not meet utility coefficient (WW) in 4 and 12 research months, in which it reached respectively values 93.92% and 93.90%. In these months the

lowest values reached also coefficient of overall efficiency (OEE). OEE coefficient did not reach recommended value. In four month there occurred the longest time of planned standstill (PP = 12360 min.), in which there was carried out repair, maintenance and regulation of rolling draw. The longest time caused by failure (TA = 1680 min.) occurred in first research month, which was caused, inter alia, by damage to the cylinder and its replacement. Next two months in which failure time (TA) was the longest is 12 and 4 months of research (respectively 1320 min. and 1260 min.). In the four research month, unplanned standstills were mainly related to the damage to the rolling mill and extended reconstructions and replacements of rolling stands, however, in 12 research month, unplanned standstills except rebuilding and replacement of rolling stands were primarily associated with damage to several rolling stands in rolling draw and roller tables.

Very high requirements of World Class system, as to quality (99.9%) did not meet also quality coefficient (WJ), which throughout research period did not reach 99.9%. However, the value of quality coefficient is at high level, in the first month above 97%, and in remaining 11 months above 98%.

Thus, recommended values did not reach utility coefficient (WW) in 2 research months and throughout the period quality coefficient. Coefficient of overall efficiency (OEE) of rolling technology reached recommended values in the entire research period.

Based on carried out researches it was found that efficiency of rolling technology used in manufacture of the sheet pile is at high level, which means work of rolling draw without very long breaks and good quality of manufactured sheet piles. In order to achieve even better values of TPM coefficients must first be determined detailed schedule of maintenance and inspections of individual rolling stands and motivate employees to precise verification of rolling technology parameters.

References

- [1] LOWE, P. *Zarządzanie technologią*. Katowice: Wydawnictwo Śląsk, 1999.
- [2] ZAPŁATA, S. *Skuteczność i efektywność systemu zarządzania jakością*. Problemy Jakości 2/2003.
- [3] DRUCKER, P. *Menedżer skuteczny*. Kraków: Akademia Ekonomiczna, 1994.
- [4] SELEJDAK, J. *Rozdział 12. Ocena efektywności eksploatacji maszyn w oparciu o współczynniki PAMCO*. Efektywność eksploatacji maszyn i zdolność jakościowa procesu, oprac. i red. nauk. Hrubeć J., Borkowski S. Warszawa: Wydawnictwo Instytutu Organizacji i Zarządzania w Przemysle "ORGMASZ", 2006.
- [5] BORKOWSKI, S., SELEJDAK, J., SALAMON, S. *Efektywność eksploatacji maszyn i urządzeń*. Częstochowa: Wydawnictwo Wydziału Zarządzania Politechniki Częstochowskiej, 2006.
- [6] MIELCZAREK, K., BORKOWSKI, S. *Chapter 20. Practise of Calculation TPM Coefficients*. Quality Improvement and Machines Exploitation, ed. and scientific elaboration Borkowski, S., Kliber. J. Saint-Petersburg: Publishing and Press Association of Universities Russia, 2008.
- [7] JAGUSIAK, M., BORKOWSKI, S., MIELCZAREK, K. *Chapter 16. Effectiveness Exploitation of Autoclave Basing on the TPM Coefficients*. TPM and PAMCO Coefficient as Basis of Estimation of Machines Exploitation Efficiency, ed. and scientific elaboration Borkowski, S., Kročko V. Saint Petersburg: Publishing and Press Association of Universities Russia, 2008.
- [8] KACZOROWSKI, Ł., ULEWICZ, R. *Rozdział 28. Efektywność eksploatacji maszyny do produkcji wyrobów z drewna*. Efektywność eksploatacji maszyn i zdolność jakościowa procesu, oprac. i red. nauk. Hrubeć J., Borkowski S. Warszawa: Wydawnictwo Instytutu Organizacji i Zarządzania w Przemysle "ORGMASZ", 2006.
- [9] BORKOWSKI, S., ULEWICZ, R. *Zarządzanie produkcją. Systemy produkcyjne*. Sosnowiec: Oficyna Wydawnicza Humanitas, 2009.
- [10] BORKOWSKI, S., ULEWICZ, R. *Instruments of Production Processes Improvement*. Warszawa: Wydawnictwo Menedżerskie PTM, 2009.
- [11] KNOP, K., STASIAK-BETLEJEWSKA, R. *Chapter 5. Quality problems in the process of labeling glass packages*. Evaluation of Production Processes, ed. and scientific elaboration Borkowski, S., Novak, A. Novosibirsk: Novosibirsk State Technical University, 2009.



Analyzing the Shape Deviation Cylindrical Holes Machined by EDM (Electro Discharge Machining) Process

*Sławomir Spadło, *Dominik Dudek, *Piotr Młynarczyk

* Kielce University of Technology, Chair of Metal Science and Material Technologies, Aleja Tysiąclecia
Państwa Polskiego 7, 25-314 Kielce, Poland, E-mail: dominik_dudek@op.pl

Abstract. The paper deals with the investigations of influence parameters of electrodischarge machining (EDM) on the productivity of EDM process and shape deviation of machining parts. BP-93L machine with electronic generator type was used to perform EDM process. Kerosene was used as a dielectric. During EDM process the parameters of current were permanent. The shape of electrode and way of passing dielectric were changed. The following parameters were determined: productivity of EDM process and shape deviation.

1. Introduction

Electric discharge machining (EDM) is a manufacturing process whereby a desired shape is obtained using electrical discharges. Material is removed from the workpiece by a series of rapidly recurring current discharges between two electrodes, separated by a dielectric liquid and subject to an electric voltage. After achievement border electric breakdown follows between electrodes voltage. The accelerated in strong electric field electron crash from atoms of center, causing their ionization. Plasma channels with ions and electrons creates. Temperature of plasma channels achieves 14000 K. The energy of ions striking onto surface of grid electrode heating it. Gas blister about growing diameter round channel creates. Melting of the object's surface in result of local growth of temperature follows local as well as her partial vaporization. Intensive electric discharges influence causes throwing out liquid metal, which solidify as an spherical balls. Discharges crater creates as an final effect. The electrodes is called the tool-electrode, or tool, while the other is called the workpiece.

2. Experimental Investigations of the Technological Characteristics of Electrical Discharge Machine

Experiment was performed by BP-93L (EDM process was done by electronic generator equipped machine). Shape deviation investigations was performed by Laboratory of Computer Measurements Size Geometrical in Kielce University of Technology.

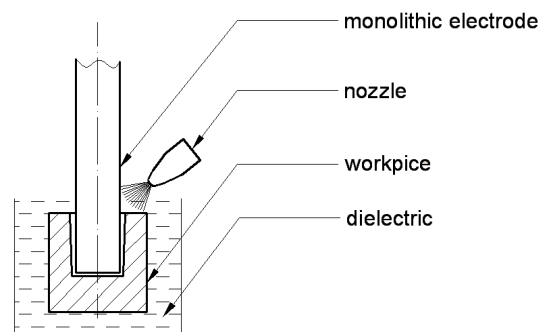


Fig. 1. The diagram of EDM process whit monolithic electrode.

During the tests the following results have been obtained: the influence of electrode shape and way of passing dielectric on productivity of EDM process, and shape deviation the round hole performed by electro discharge machining (EDM).

The diameter of electrode was 12 mm. The specimen's dimensions was: diameter – 25 mm; height – 25 mm. The specimens was made from hardened steel (145Cr6). Electrode was made of electrolytic copper.

The parameters of current were permanent. The intensity of current was 20 ampere, the time of pulse duration was 150 μ s, the time of pause was 7 μ s. The monolithic shape electrode was used in first experiment "Fig 1". Tubular electrodes was used in second and third. The dielectric liquid was injected in the second experiment "Fig. 2", and siphoned off in the third experiment "Fig 3". For tubular tools the dielectric was inside tubular electrode.

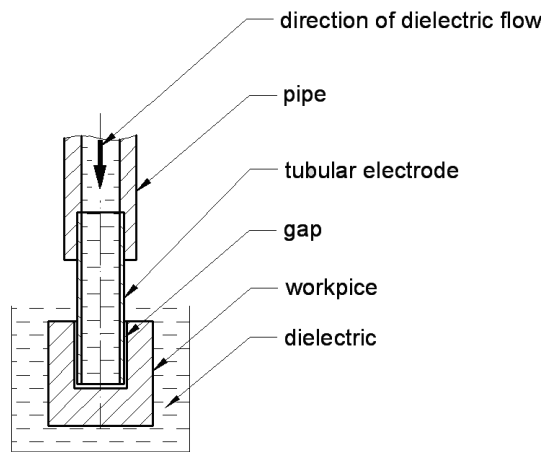


Fig. 2. The diagram of EDM process whit tubular electrode (experiment 2). The dielectric is injected.

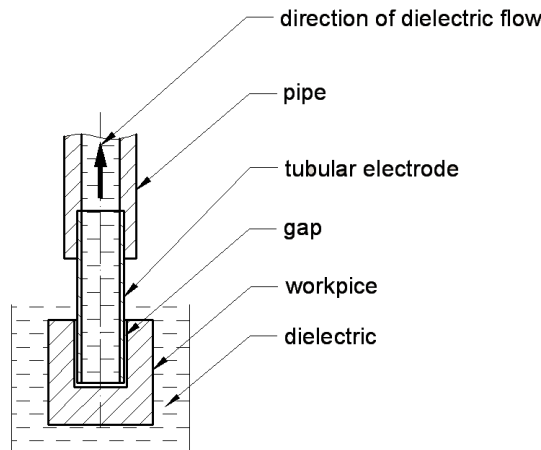


Fig. 3. The diagram of EDM process whit tubular electrode (experiment 3). The dielectric is siphoned off.

Number of experiment	Time EDM process, min	Relative decrease mass of electrode to decrease mass of specimen, %
1	50.00	0.51
2	11.83	3.81
3	22.53	1.84

Tab. 1. The results of experiment.

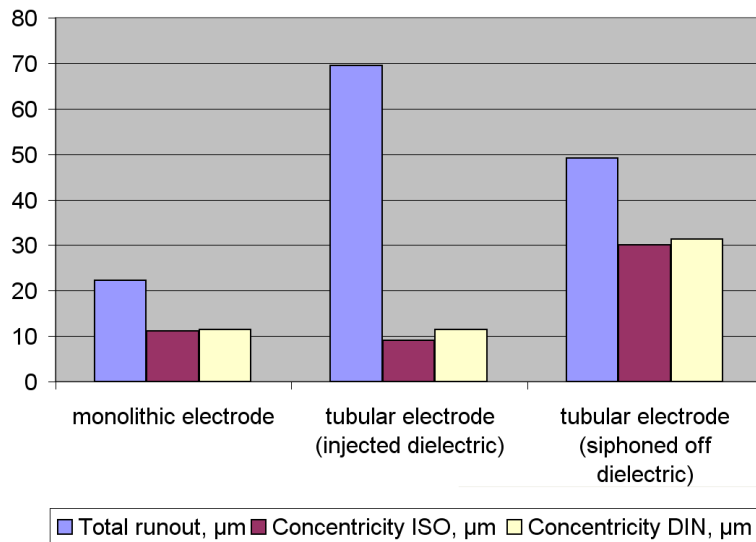


Fig. 4. The graphic composition of results of measurements deviation outlines the cylindricity for individual electrodes after EDM process.

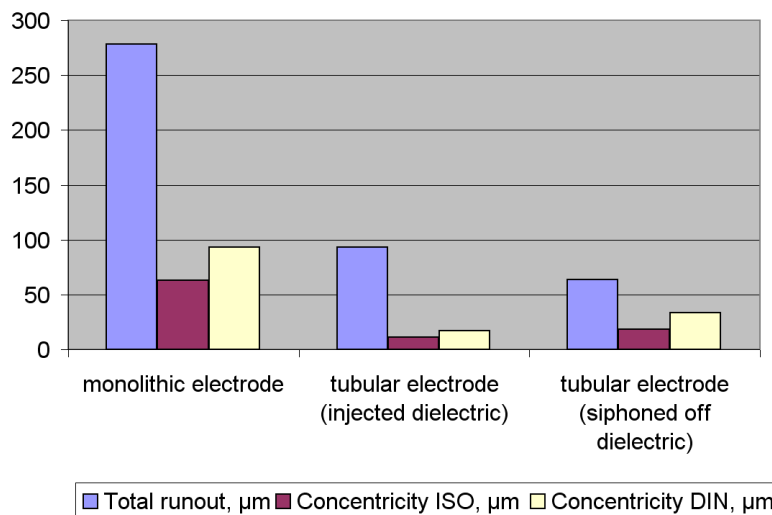


Fig. 5. Measured the deviation of outlines the cylindricity for the hole in dependence from used electrodes and the way of passing the dielectric.

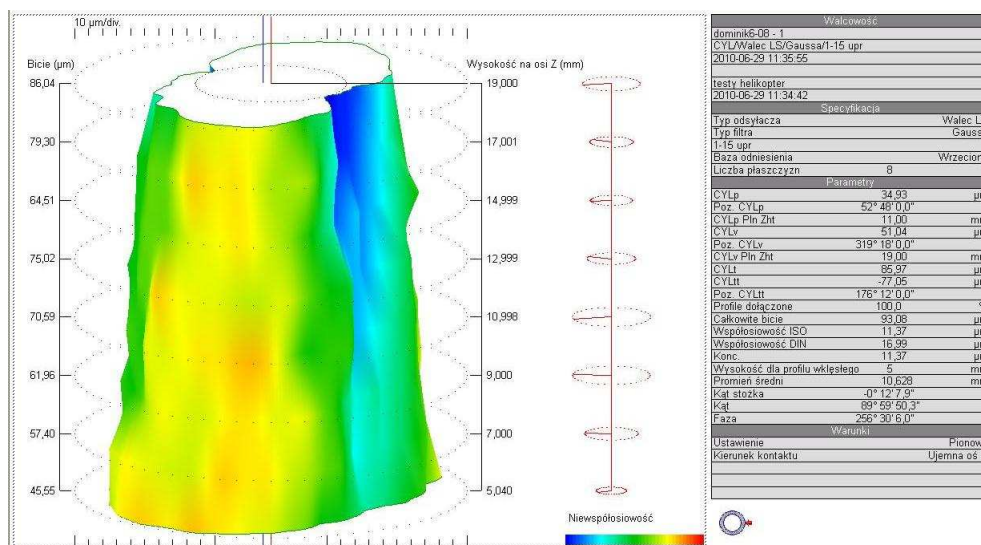


Fig. 6. The example shape of hole for EDM process. The dielectric was injected inside tubular electrode. The current parameters were: intensity of current was 20 A, the time of pulse duration was 150 μs , the time of pause was 7 μs .

3. Conclusion

For the tubular shaped electrode time of EDM process was shorter than for monolithic electrode.

When the dielectric was injected inside the tubular electrode the time of process was the shortest.

Mass decrease of electrode according to mass decrease of specimen was observed in first experiment when the electrode was monolithic.

The biggest mass decrease was observed in the second experiment.

The shape deviation was the smaller for the EDM process when the dielectric liquid was injected inside tubular electrode.

The shape deviation was the biggest when the electrode was monolithic.

Acknowledgement

This paper was created with support of European Union, project name: Program Rozwojowy Potencjału Dydaktycznego Politechniki Świętokrzyskiej: kształcenie w nowoczesnych obszarach techniki, project agreement: UDA-POKL.04.01.01-00-395/09-00

References

- [1] ALBIŃSKI, K. *The Polarity of Electrodes in Electro-Discharge Machining*. Proc. ISEM - XI, Lausanne, 1995, pp. 95-104.
- [2] DAUW, F., VAN COPPENOLLE, B. *On the evolution of EDM research. PART 2: From fundamental research to applied research*. Proc. ISEM-XI, Lausanne 1995, pp. 133-142.
- [3] MIERNIKIEWICZ A. *Doświadczalno-teoretyczne podstawy obróbki elektroerozyjnej (EDM)*, Kraków, 1999
- [4] NOWICKI, B., PIERZYŃSKI, R., SPADŁO, S. *Investigation of electro-discharge mechanical dressing (EDMD) of diamond abrasive wheels with conductive bonds using brush electrodes*. Journal Engineering Manufacture. Proc. IMechE Vol. 220 part B, 2006. pp. 421 – 428.
- [5] SPADŁO, S., DUDEK, D. *Analyzing the technical characteristics of EDM tools*. Proceedings of conference 8-th EUROPEAN CONFERENCE OF YOUNG RESEARCH AND SCIENTIFIC WORKERS -TRANSCOM 2009 Žilina, pp 193-196.
- [6] SPADŁO, S., DUDEK, D. *Badania charakterystyk użytkowych obrabiarki elektroerozyjnej BP-95d*. Zeszyty Naukowe Politechniki Świętokrzyskiej - Terotechnologia 2009, Budowa i Eksploatacja Maszyn nr 13/2009, str. 374-379.
- [7] SPADŁO, S. *Teoretyczno-eksperymentalne aspekty obróbki elektroerozyjno-mechanicznej*. Monografie, Studia, Rozprawy Z 52. Wydawnictwo Politechniki Świętokrzyskiej, 195 s., Kielce 2006
- [8] SPADŁO, S., DUDEK D. *Badania eksperymentalne charakterystyk technologicznych obrabiarek elektroerozyjnych BP-95*. Zeszyty Naukowe Politechniki Świętokrzyskiej Nauki techniczne – Budowa i Eksploatacja Maszyn Z. nr 11/2008 s. 281-288, Kielce 2008.
- [9] SPADŁO, S. *Comparative studies of brush electrodischarge machining with electrodes of alloy steel and tungsten*. Advanced Manufacturing Systems and Technology, International Centre for Mechanical Sciences (CISM), Courses and Lectures - No.437, ISBN 3-211-83689-6, Springer – Veralag Wien New York, 2002, pp. 515-524.
- [10] SPADŁO, S. *Surface quality of the surfaces machining by electroerosion with a flexible electrode*. Proc. of 8 th Int. Sci. Conf. on Production Engineering. Computer Integrated Manufacturing and High Speed Machining - CIM'2002 Brijuni. ISBN 953-97181-3-9. pp. IV-67 – IV-78.
- [11] ZOŁOTYCH, B. N. *Ways of Solving the Problem of Controlling Composition and Properties of Machine Parts Surface Layer Formed under EDM Influence*. 12 - th International Symposium for Electromachining ISEM, 1998



Tool Wear Monitoring by Hard Turning of Hardened Steel 100Cr6

*Michal Šípek, *Miroslav Neslušan

*University of Žilina, Faculty of Mechanical Engineering, Department of Machining and Manufacturing Technology, Univerzitna 8215/1, 01026 Žilina, Slovakia, {michal.sipek, miroslav.neslusan}@fstroj.uniza.sk

Abstract. This paper deals with an application of Acoustic Emission for monitoring of tool wear during hard turning of hardened roll-bearing steel 100Cr6. The results show that the signals of Acoustic Emission and some derived parameters can be applied for monitoring of deformation processes in the cutting zone and process of tool wear. The Acoustic Emission system is capable to detect the specific character of chip formation during hard turning and therefore can be adapted for specific tasks associated with this cutting operation.

Keywords: Hard Turning, Acoustic Emission, Tool Wear

1. Introduction

Hard machining is a competitive finishing process with substantial benefits in many cases [1]. In machining, hard and difficult – to machine materials tend to localize the heat generated due to the strain localization in a narrow band called adiabatic shear band. Adiabatic shear banding [2] is used to describe a localization phenomenon that occurs in the high strain – rate plastic deformation processes such as cutting. [3, 4]. Depending on cutting parameters and workpiece material properties, cutting may either lead to continuous “turning conventional steels - Fig. 1” or discontinuous “turning hardened steels - Fig. 2” chip.

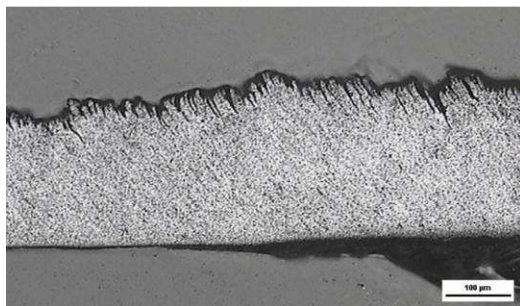


Fig. 1. Chips after turning 100Cr6 (annealed), REM, $v_c = 100 \text{ m}\cdot\text{min}^{-1}$, $f = 0,21 \text{ mm}$

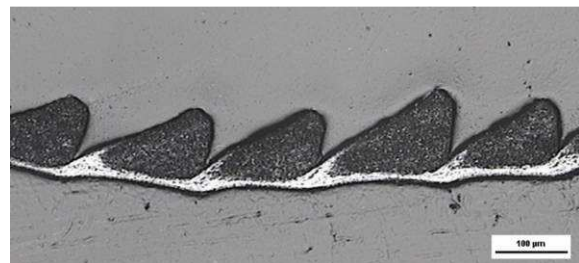


Fig. 2. Chips after turning 100Cr6 (hardened 62 HRC), REM, $v_c = 100 \text{ m}\cdot\text{min}^{-1}$, $f = 0,21 \text{ mm}$

Investigation of a real intensity of deformation processes related to the specific cutting zones is quite difficult and could be realized through Acoustic Emission (AE). The AE non-destructive technique is based on detection and conversion of these high frequency elastic waves to electrical signals. The major AE sources [5, 6, 7] in a metal cutting process are:

- deformation and fracture of work materials in shear zone, tool-chip and tool-workpiece contact,
- deformation and fracture of cutting tool,
- collision, entangling and breakage of chips.

The major advantage of using AE to monitor a machining operation is that the frequency range of the AE signal is much higher than that of the machine vibrations and environmental noises, and does not interfere with the cutting operation [6].

2. Conditions of Experiments

The experimental setup is shown in Fig. 3. Commercial piezoelectric AE sensors (D9241A - frequency range of 20 to 180 kHz, WD – frequency range of 100 kHz to 1000 kHz) by Physical Acoustics Corporation (PSC) were mounted on the top of the tool holder using. To maintain a good propagation of signals from the tool holder to the sensor, a semi-solid high vacuum grease was used. During the experiment, the AE signals were amplified, high passed at 20 kHz, low passed at 1000 kHz, and then sent through a preamplifier at a gain 40 dB to the signal processing software package. All cutting tests were performed on the CNC Lathe. The signals were real-time sampled, amplified, digitized, and then fed to the signal processing unit. The AE signals were post-processed using AWin.

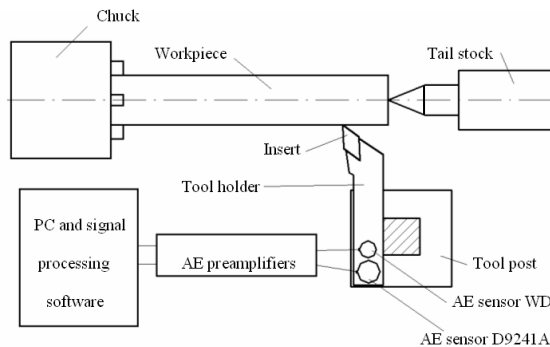


Fig. 3. Schematic of experimental setup

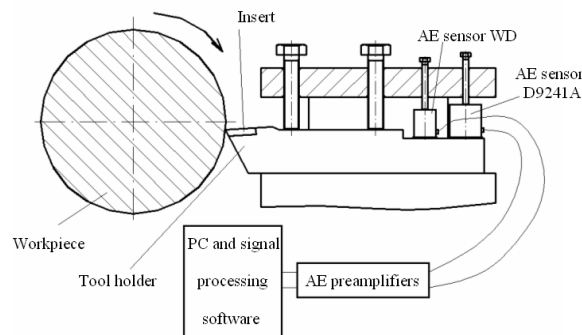


Fig. 4. Detail of sensor placement

Cutting tool:	TiC reinforced Al ₂ O ₃ ceramic inserts DNGA150408 (TiN coating), rake angle $\gamma_n = -7^\circ$
Work material:	100Cr6 (hardened - 62 HRC), external diameter 56 mm, internal diameter 40 mm, 125 mm long
Cutting condition:	$v_c = 170 \text{ m}\cdot\text{min}^{-1}$, $f = 0,09 \text{ mm}$, $a_p = 0,25 \text{ mm}$ (constant), dry cutting
Machine tool:	CNC Lathe Hurco TM8

Tab. 1. Experimental conditions during hard turning

3. Analysis of Results

Characteristic curve of flank tool wear can be seen in Fig. 5. In different stages are different values of VB and in final phase is insert breakage. This transformation can be detected not only by conventional method (cutting forces, etc.) but also through acoustic emission.

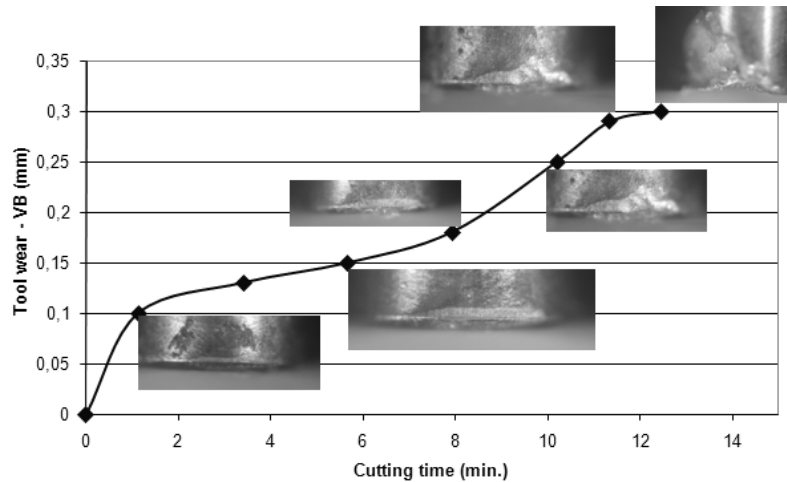
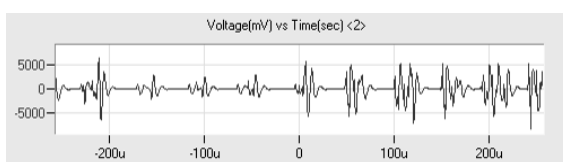
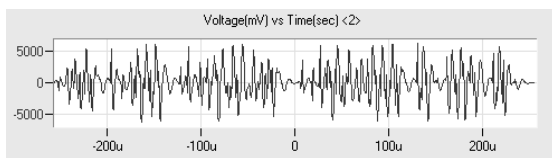


Fig. 5. Characteristic curve of flank tool wear, with pictures of tool wear, $v_c = 170 \text{ m}\cdot\text{min}^{-1}$, $a_p = 0,25 \text{ mm}$

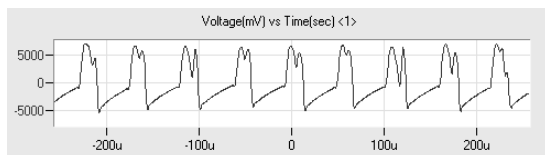
Fig. 6 illustrates the character of AE signal of two sensors in the initial stages of the cutting process “Fig. 6a,c” and in the final stage too “Fig. 6b,d”. First of all, it should be mentioned that each sensor provides a different character of a signal. This difference is attributed to a different frequency range for both sensors. Because of the segmented chip formation the cutting process is very unstable in relation to segments formation. The previous studies investigated that the segmentation frequencies lie in the frequency range of 14 kHz to 90 kHz. Therefore these frequencies can be detected only through the low frequency sensor. It could be viewed that the relaxing character of a signal can be obtained through the frequency sensor. The character of plastic deformation during formation of the segmented chip is connected with relaxation of stress in front of the cutting edge. This relaxation process leads to the formation of a crack in the near surface of a chip. This crack is prolonged towards the cutting edge and transforms to the plastic deformation process in this zone. The cutting zone provides two basic types of signals. The burst type is associated with the crack formation in the shear plane and the continuous one is associated with the friction and deformation processes in the shear zone, tool – chip and tool – workpiece contact “Fig. 7”.



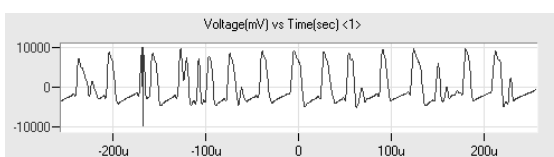
a) High frequency sensor WD
VB = 0 mm



b) High frequency sensor WD
VB = 0,37 mm



c) Low frequency sensor D9241A
VB = 0 mm



d) Low frequency sensor D9241A
VB = 0,37 mm

Fig. 6. Character of AE signal in the initial and final stage of cutting process, $v_c = 170 \text{ m}\cdot\text{min}^{-1}$, $a_p = 0,25 \text{ mm}$

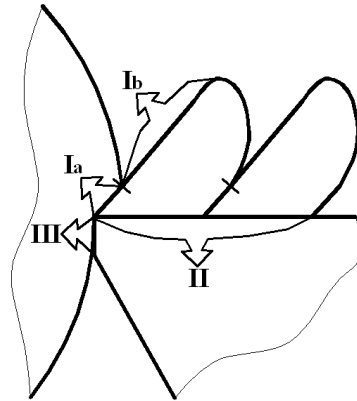
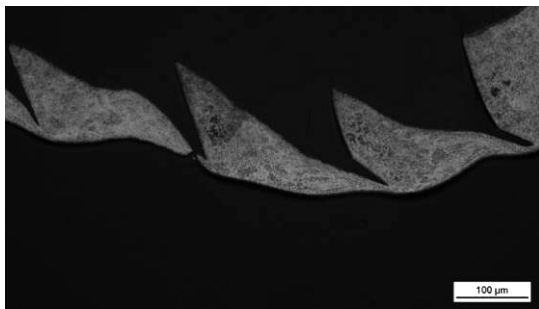
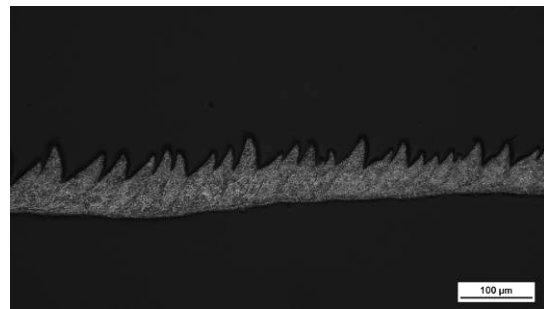


Fig. 7. Cutting zone for hard cutting, Ia) microcracked and plastically deformed shear zone, Ib) cracked region, II) tool – chip contact, III) tool – workpiece contact

Processes in zone II and III “Fig. 7” can be investigated and detected with the application of the WD AE sensor, because the signals related to the chip segmentation (crack propagation) are out of frequency range of this sensor. Segmentation frequencies lie in the range of D9241A sensor. These frequencies are associated with the crack formation and its propagation in the shear zone. Signal associated with a crack formation and its prolongation in the shear zone is very strong (amplitude of AE signals for all feed is on maximum 100dB), generates the massive low frequency and they are not sensitive to friction processes related to plastic deformation in the cutting zone. The initial stage of cutting process provides the relaxing character of AE of the low frequency sensor. The significant changes in the tool geometry significantly change the stress and temperature state in the cutting zone. The chip becomes less segmented “degree of segmentation decreases, see Fig. 8”, length of crack prolongation decreases and deformation processes take a more significant role. The regular character of AE signals (of D9241A sensor) and segmented chips are suppressed.

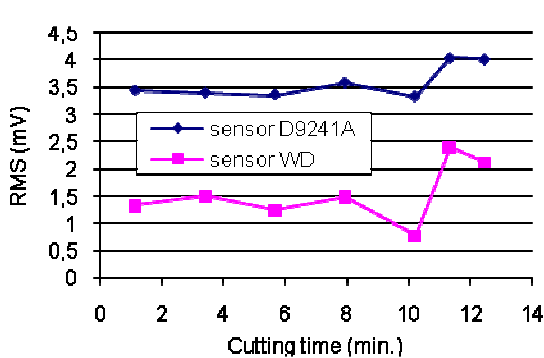


a) VB = 0 mm

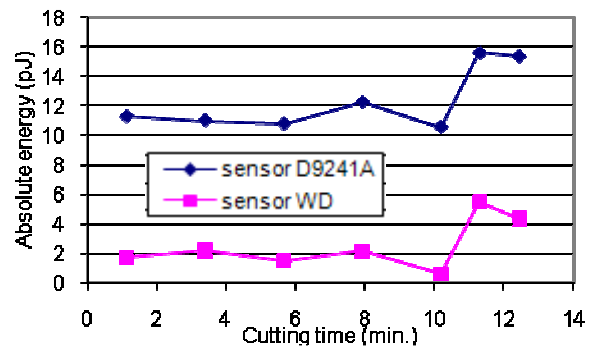


b) VB = 0,37 mm

Fig. 8. Photos of chips in the initial and final stage of cutting process, $v_c = 170 \text{ m}\cdot\text{min}^{-1}$, $a_p = 0,25 \text{ mm}$



a) RMS values



b) absolute energy of AE

Fig. 9. RMS and absolute energy of AE in relation to tool wear, $v_c = 170 \text{ m}\cdot\text{min}^{-1}$, $a_p = 0,25 \text{ mm}$

The significant changes in tool geometry can be investigated through some parameters of AE such as RMS value or absolute energy (for both sensors). The massive breakage (transformation of microchipping to macrochipping) leads to increase in their values “Fig. 9”.

The identification of such parameters as RMS value or absolute energy of AE enables monitoring of cutting process through the AE signal (and derived parameters) under high cutting speeds and cutting depths. In similar experiments with lower speed and cutting depth there was no dependency between this signals and tool wear. That led to new method – ratio of different parameters from low and high frequency sensors.

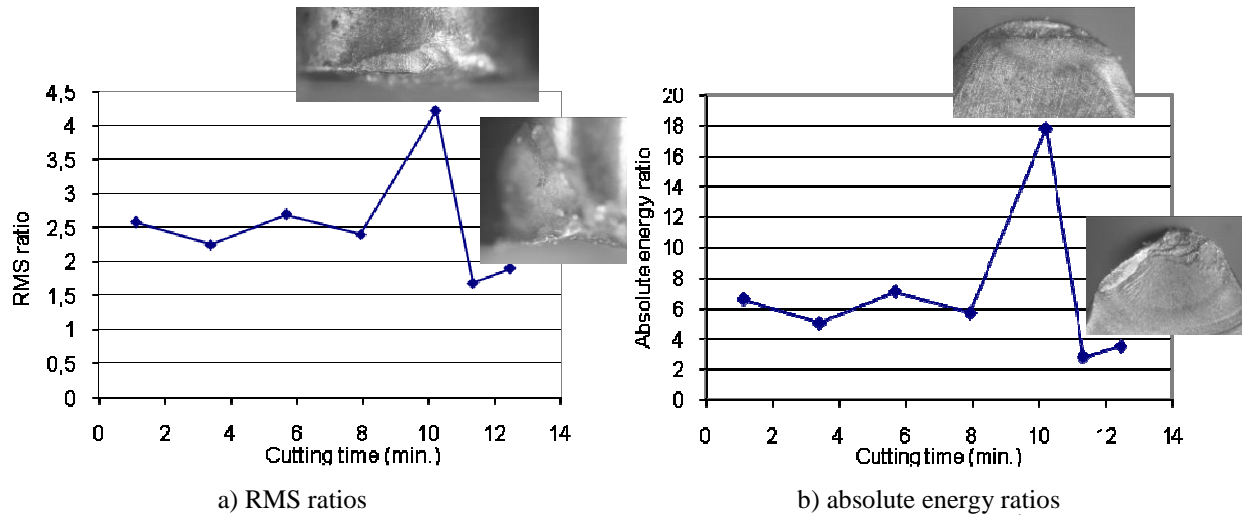


Fig. 10. Ratios of RMS and absolute energy of AE in relation to the tool wear, $v_c = 170 \text{ m}\cdot\text{min}^{-1}$, $a_p = 0,25 \text{ mm}$

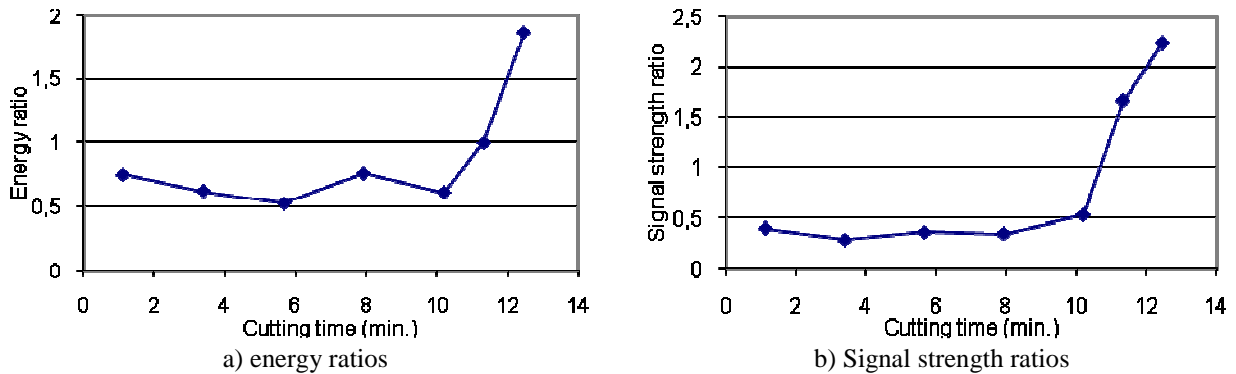


Fig. 11. Ratios of energy and signal strength of AE in relation to the tool wear, $v_c = 170 \text{ m}\cdot\text{min}^{-1}$, $a_p = 0,25 \text{ mm}$

The analysis of RMS and absolute energy ratios is shown at Fig. 10. The maximums of these ratios can be obtained immediately before the macroscopic tool breakage with the following step decrease in the phase of the catastrophic stage of tool wear “Fig. 10, 11”. These parameters are considered to be designed for the real time monitoring of hard cutting through AE as the alerting indicators of oncoming tool massive breakage. On the other hand, steep increase in energy and signal strength ratio is associated with the macroscopic tool breakage and can be applied to indication of this state “Fig. 11”.

4. Discussion and Conclusion

The previous analyses showed that the investigation of ratios of different AE signals (and derived parameters) can provide more sensitive output for monitoring of hard turning. However, some parameters enable process monitoring without the following processing “Fig. 8”. On the other hand, the sensitivity of the following signal processing (calculation of ratios) provide more sensitive tool for process monitoring (except for RMS and absolute energy of the low frequency sensor). This experiments showed that acoustic emission appears as very successful method for online tool wear monitoring.

References

- [1] TONSHOFF, H.K., ET ALL. *Cutting of hardened steel*, CIRP Annals 49/2/200, p. 547 – 564.
- [2] RECHT, R. F. *Catastrophic thermoplastic shear*, Trans ASME, 86 (1964), p. 189 -193.
- [3] ŘEHOŘ, J. *Teoretické a experimentální studium problematiky HSC obrábění ocelí vysoké pevnosti a tvrdosti* : DDP ZČU KTO v Plzni, 2004.
- [4] POULACHON, G., MOISAN, A. *Contribution to the study of the cutting mechanism during high speed machining of hardened steel*, CIRP Annals, 47/1/1998, p. 73-76.
- [5] DORNFELD, D. A. *Acoustic emission in monitoring and analysis in manufacturing* , Proceedings of AE monitoring. Anal. manuf., 14 /1984, p. 124 – 130.
- [6] DORNFELD, D. A. *Manufacturing process monitoring and analysis using acoustic emission*, Journal of acoustic emission, 4/1985, p. 123 - 126.
- [7] INASAKI, I. *Application of acoustic emission sensor for monitoring machining processes*, Ultrasonics, 36/1998, p. 273 – 281.
- [8] GUO, Y. B., AMMULA, S. C. *Real-time acoustic emission monitoring for surface damage in hard machining*, Machine tool and manufacture, 45/2002, p. 1622 – 1627, ISSN 0890-6955.
- [9] NESLUŠAN, M. *Sústruženie kalených ocelí* , vedecká monografia, Edis Žilina 2009, 245 str., ISBN 978-80-554-104-1.
- [10] VARGA, G. *Examination of Stability of Vibration Occurring at Turning* : Proceedings of the 12th International Conference on Tools, University of Miskolc, Hungary, September 06-08, 2007. p. 255-260, ISSN: 1215-0851.
- [11] VARGA, G., DUDAS, I., TANABE, I., IYAMA, T. *Intelligent measurement of cutting tool wear*, Proceedings of the 12th international conference on tools, University of Miskolc, Hungary, September 06-08, 2007, p. 225 - 232, ISSN: 1215-0851.
- [12] MRKVICA, I. *Zkoušky obrobiteľnosti modifikované austenitické oceli 17 240 S*, Vědeckovýzkumná zpráva, Ostrava : VŠB-TU Ostrava, 2005, 16 s. (HČ 346505).



Electrochemical Properties of Heat Influenced Structures Made of Austenitic Stainless Steel

*Viktor Škorík, *Lenka Škublová, *Branislav Hadzima, **Dagmar Faktorová

*University of Žilina, Faculty of Mechanical Engineering, Department of Materials Engineering, Univerzitná 1, 01026 Žilina, Slovakia, {Viktor.Skorik, Branislav.Hadzima, Lenka.Skublova}@fstroj.uniza.sk

**University of Žilina, Faculty of Electrical Engineering, Department of Measurement and Applied Electrical Engineering, Univerzitná 1, 01026 Žilina, Slovakia, {Dagmar.Faktorova}@fel.uniza.sk

Abstract. Article deals with evaluation of corrosion resistance of AISI 316L stainless steel. Temperature dependence of original (after delivering from producer) and after sensitization heat treating specimens were evaluated. Corrosion characteristics were measured using the method of electrochemical impedance spectroscopy. The measurements were realized in 0.1M NaCl solution at temperatures of 20°C, 30°C, 40°C and 50°C. Corrosion characteristic - polarization resistances of specimen surfaces were obtained by circular regression from Nyquist plots.

Keywords: AISI316L stainless steel, electrochemical impedance spectroscopy, physiological solution, polarization resistance.

1. Introduction

Austenitic stainless steel constitutes the largest stainless family in terms of alloy type and usage. This is due to the good resistance of the material to high-temperature creep and corrosion, long-lasting, making thinner and more durable structures possible. It presents architects with many possibilities of shape, color and form, whilst at the same time being tough, hygienic, adaptable and recyclable. Broad applications of austenitic steel for construction of equipment working in various corrosive conditions between cryogenic to elevated temperature range, require methods for evaluating the mechanical properties of welded joints, which frequently determine service life of the structure [1-3].

As it is well known, austenitic stainless steels possess excellent resistance to general corrosion due to the formation of a very thin oxide layer (1–5 nm) called “passive film”. However, stainless steels are not immune to corrosion attack. Localised corrosion (pitting corrosion, intergranular corrosion or stress corrosion cracking) can be developed mainly in chloride-containing environments [4].

Intergranular corrosion of austenitic stainless steel is a conventional and serious problem during welding and high temperature use (450–850 °C). The phenomenon that occurs in this temperature range is the so-called as sensitization, i.e. chromium depletion due to precipitation of chromium carbides (Cr_{23}C_6) at grain boundaries [5,6].

2. Experimental materials

As experimental material was used AISI 316L stainless steel and its normalized chemical composition is in Tab. 1.

Experimental material was heat treated by solution annealing at the temperature of 1050°C with holding time of 20 minutes followed by slow cooling in the furnace on to 800°C during 4 hours. After that the specimen was annealed on 800°C with holding time of 16 hours followed by cooling

in furnace on to 20°C. Main aim of described heat treating is in material damage on microstructure level.

Element	Cr	Ni	Mo	Mn	Si	S	P	C
Content [wt.%]	16.0-18.0	10.0-14.0	2.0-3.0	max 2.0	max 1.0	max 0.015	max 0.045	max 0.03

Tab. 1. The normalized chemical composition of AISI 316L [7].

2.1. Microstructure Analysis

The microstructure of original material (Fig. 1) is created by polyedric grains of austenite with average grain size 21.6 μm. In the grains are evident deformation twins, which arise during the process of production by rolling [8]. It can be seen a lot of line rectified inclusions and carbides.

Microstructure of damaged material (Fig. 2) is created by polyedric grains, which dimension is 3 times higher (67.2 μm) than grain size in original material. Consequence of wrong heat treatment is segregation of carbides on grain boundaries. Segregation of carbides caused decreasing of concentration of major alloying elements (Cr, Ni) in the matrix, which decreased the strength and corrosion resistance of material. Stainless steel with damaged microstructure is sensitive to several types of corrosion. Especially dangerous is intercrystalline corrosion because of its difficult observation [8, 9].

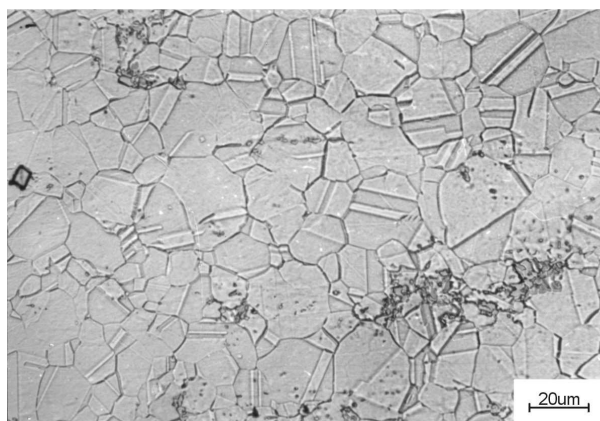


Fig. 1. Microstructure of AISI 316L SS – original

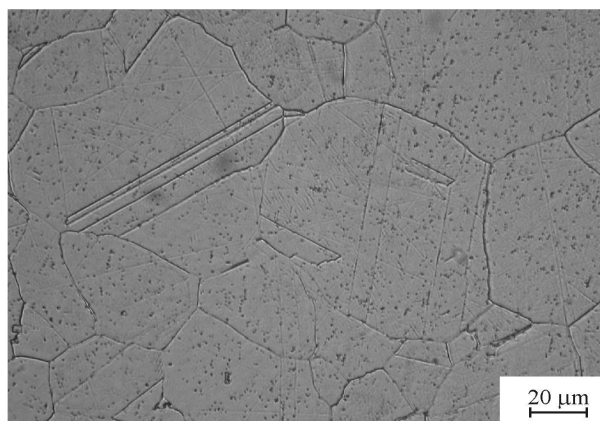


Fig. 2. Microstructure of AISI 316L SS – damaged

3. Results and discussion

Electrochemical tests were realized at temperatures 20°C, 30°C, 40°C and 50°C in the 0.1M solution of NaCl. Connection and measurement principle is described elsewhere [10-12].

Value of polarization resistance R_p was determined by electrochemical impedance spectroscopy (EIS), which is better for the measurement of low conducted layers on the surface of the material. Nyquist diagrams of imaginary and real part of impedance dependence are in Fig. 3 a Fig. 4 for original and damaged specimens respectively.

From Nyquist plots (Fig. 3 and Fig. 4) it can be determined the value of the polarization resistance by circular regressions (the diameter of semicircle is R_p value). Analysis results of Nyquist plots are in Tab. 2 [8].

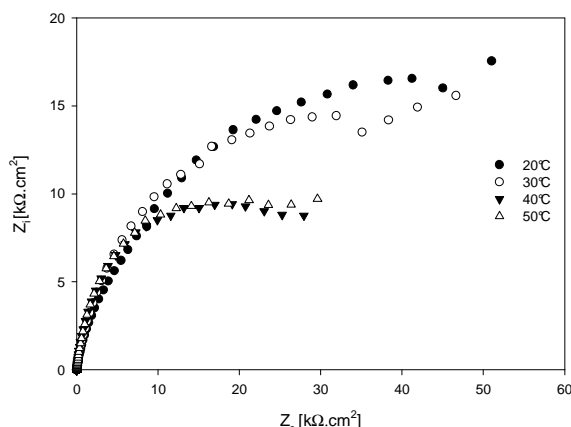


Fig. 3. Nyquist diagram of original material

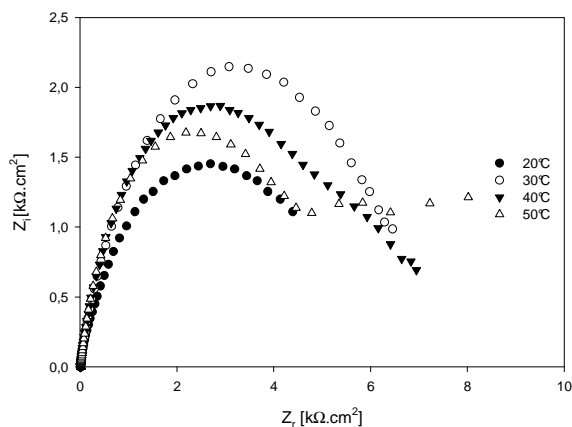


Fig. 4. Nyquist diagram of damaged material

AISI 316L	20°C	30°C	40°C	50°C
original	72.4	49.1	29.3	31.7
damaged	4.7	6.1	6.3	5.8

Tab. 2. Polarization resistances [$k\Omega.cm^2$] of tested materials in 0.1M NaCl at various temperatures

Specimens prepared from original material have higher corrosion resistance at all temperatures of testing solution compared to damaged material.

Polarization resistance of original material is decreasing with increasing of testing temperature between 20 and 40°C. Polarization resistance is approximately equal at testing temperature of 40°C and 50°C. Three times decreasing of polarization resistance is result of increasing of partially reaction activity with increasing of temperature. Diffusion of active components trough passive layer is more quickly at higher temperatures. At the same time the activity of aggressive chloride ions in testing solution is increasing and therefore probability of protective passive layer damage is increasing. The stagnate of polarization resistance between 40 and 50°C can be result of corrosion mechanism change or result of reaching of partial reaction limit speed.

Material with damaged microstructure has different temperature dependence of polarization resistance. Its value is not markedly changed with increasing of testing temperature. Polarization resistance of damaged material at 20°C is about 14 times lower than polarization resistance of original material. Results of the tests at 50°C show 6 times decreasing of polarization resistance between original and damaged material. Ability to passivation of the damaged material surface is very low in aggressive media containing Cl^- ions. It is probably result of $Cr_{23}C_6$ carbides segregation along the boundaries of austenitic grains. It causes the decrease of chrome concentration in solid solution and then lower ability to protective layer creation.

4. Conclusion

On the basic of metallographic analyses and electrochemical impedance spectroscopy measurements of AISI316L stainless steel in 0.1M NaCl at various temperatures we draw conclusions:

- Microstructures of original and damaged materials are created by polyedric grains of austenite. Heat treating that is describing in article results in increasing of grain size (about 3 times). Moreover heat treating results in decreasing of hardness of material and in carbides segregation along austenitic grains.
- Heat treating (1050°C/20 min. + cooling in furnace on to 800°C during 4 hours + 800°C/16 hours + slow cooling in the furnace) resulted in microstructure sensitization and it has very strong influence on corrosion resistance of material. The original specimens have 14 and 6 times

higher polarization resistances at 20°C and 50°C respectively in comparison with polarization resistance of damaged (heat treated) specimens at the same temperatures.

- Temperature of testing solution influenced the polarization resistance of the original material specimens. With increasing of temperature from 20°C to 50°C the polarization resistance decrease from 69,81 kΩ.cm² onto 28,16 kΩ.cm².
- Temperature of testing solution does not influence the polarization resistance of the specimen with damaged microstructure. The values of polarization resistances between 20 and 50°C are not changed.

Acknowledgement

The research is supported by European regional development fund and Slovak state budget by the project ITMS 26220220048 (call OPVaV-2008/2.2/01-SORO).

References

- [1] CUI, Y., Lundin, C.D., Hariharan, V. *Mechanical behavior of austenitic stainless steel weld metals with microfissures*. Journal of Materials Processing Technology 171 (2006) 150–155.
- [2] MOLAK, R.M., PARADOWSKI, K., BRYNK, T., CIUPINSKI, L., PAKIELA, Z., KURZYDŁOWSKI, K.J. *Measurement of mechanical properties in a 316L stainless steel welded joint*. International Journal of Pressure Vessels and Piping 86 (2009) 43–47.
- [3] BADDOO, N.R. *Stainless steel in construction: A review of research, applications, challenges and pportunities*. Journal of Constructional Steel Research 64 (2008) 1199–1206.
- [4] Cristóbal, A.B., ARENAS, M.A., CONDE, A., DE DAMBORENEA, J. *Corrosion of stainless steels covered by exopolymers*. Electrochimica Acta 52 (2006) 546–551.
- [5] YU, X., CHEN, S., LIU, Y., REN, F. A study of intergranular corrosion of austenitic stainless steel by electrochemical potentiodynamic reactivation, electron back-scattering diffraction and cellular automaton. Corrosion Science 52 (2010) 1939–1947.
- [6] RAMÍREZ, L.M., ALMANZA, E., MURR, L.E. Effect of uniaxial deformation to 50% on the sensitization process in 316 stainless steel. Materials Characterization 53 (2004) 79– 82.
- [7] STN 41 7349.
- [8] HADZIMA, B. et al. *Corrosion of biocompatible AISI316 stainless steel in physiological solution*. Materials Engineering, Vol. 15 (2008), No. 4, p.1.
- [9] SKOČOVSKÝ, P. et al: *Konštrukčné materiály*. EDIS ŽU v Žiline, 2000.
- [10] HADZIMA, B., LIPTÁKOVÁ, T. *Základy elektrochemickej korózie kovov*, EDIS – ŽU v Žiline, Žilina 2008.
- [11] HADZIMA, B. et al. *Katódová protikorózna ochrana horčíkovej zliatiny AZ91*. Kovove Mater., 41 (4), 2003, p.257.
- [12] SUCHÝ, P. *Protikorózna ochrana zliatiny Mg-3Al-1Zn konverznými povlakmi* [Dissertation thesis], ŽU v Žiline, Žilina 2008.



Ultra – High Cycle Fatigue of High Grade Carbon Steel

*Libor Trško, *Katarína Miková, * Otakar Bokůvka

*University of Žilina in Žilina, Faculty of Mechanical Engineering, Department of Materials Engineering,
Univerzitná 1, 010 26 Žilina, Slovakia, libor.trsko@ltmetal.net, katarina.mikova@fstroj.uniza.sk,
otakar.bokuvka@fstroj.uniza.sk

Abstract. The authors in this work publish experimental results about ultra-high cycle fatigue of high grade carbon steel obtained at high-frequency loading ($f \approx 20$ kHz, $T = 20 \pm 10$ °C, $R = -1$). The results confirm a continuous downward of fatigue lifetime and surface fatigue crack initiation in the ultra-high cycle region.

Keywords: High grade carbon steel, ultra-high cycle fatigue, high-frequency loading.

1. Introduction

Fatigue of structural materials is the dominant limiting state; more than 90 % of failures are caused by fatigue [1-4]. Fatigue failures can be observable in the low – cycle, high – cycle and also ultra – high cycle region. With the aim to prolong the fatigue lifetime of machine components the ultra – high cycle fatigue is studied very intensively during last ten years at high – frequency loading (with the working frequencies about 20 kHz) [3,5-14]. In this work are stated experimental results from the region of ultra – high cycle fatigue of high grade carbon steel obtained at high – frequency loading.

2. Material and experiments

The high grade carbon steel was used as an experimental material. This structural steel was heat treated by the procedure consisting of austenitization at 820 °C for 50 min, oil quenching and tempering for 90 min at 450 °C (cooled on calm air). Before the fatigue tests, there were carried out other experimental works – quantitative chemical analysis, metallography analysis, tensile test and after fatigue tests fractography with using SEM, Tescan LMU II. The chemical composition and mechanical properties are given in Tab. 1. The microstructure of steel after heat treatment is in Fig. 1 and it consists of tempered martensite.

C	Mn	Si	Cu	Ni	Cr	P	S	R _m (MPa)	A (%)
0.52	0.70	0.34	0.15	0.06	0.16	0.008	0.005	952	15.7

Tab. 1 High grade carbon steel, chemical composition (in weight %) and mechanical properties.

The fatigue tests were realized with using methods by authors [3,5,13] at high – frequency sinusoidal cyclic push – pull loading (testing frequency $f \approx 20$ kHz, temperature $T = 20 \pm 10$ °C, cooled by distilled water with anticorrosive inhibitors, coefficient of cycle asymmetry $R = -1$) and with using high frequency testing equipment KAUP-ŽU Žilina, SK [3,5,13]. Smooth round bar specimens (10 pieces) with 4 mm in diameter ground and polished by metallography procedures in the central working part were used during the fatigue tests. The ultra high cycle fatigue lifetime was investigated in the region from $N \approx 10^6$ cycles to $N \approx 10^9$ cycles of loading.

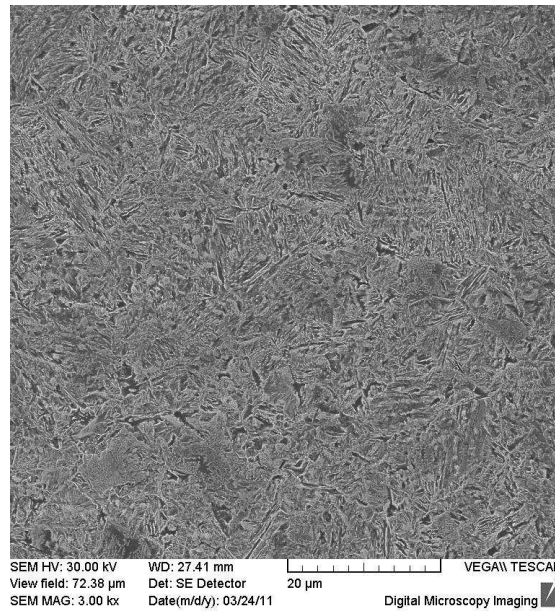


Fig. 1. Microstructure of high – grade carbon steel, SEM, etch. Nital.

3. Results and discussion

Results of high – frequency cyclic loading, the dependence of stress amplitude vs. number of cycles are shown for the high grade carbon steel in Fig. 2. Fatigue lifetime is characteristic by a continuous decrease of fatigue life with increasing number of cycles in the whole region of

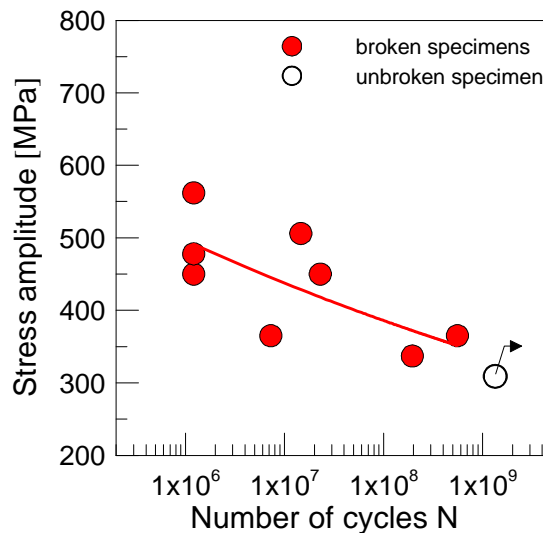


Fig. 2. S – N diagram, high grade carbon steel, high – frequency fatigue loading.

fatigue loading. The difference is $\Delta\sigma_a \approx 150$ MPa ($10^6 < N < 10^9$ cycles of loading) what is comparable with results of authors [8-14] which state values from $\Delta\sigma_a \approx 20$ MPa to $\Delta\sigma_a \approx 200$ MPa (higher values were experimentally obtained at high strength steels or at surface strain hardening steels). The surface fatigue crack initiation, Fig. 3 and Fig. 4 was observed even despite of the fact, that surface has not a decisive role in starting of fatigue degradation mechanisms in the ultra – high cycle region (in the ultra-high cycle region, the subsurface crack initiation is mainly observed, structural heterogeneity plays a very important role, “fish eyes” are created and as an initiation

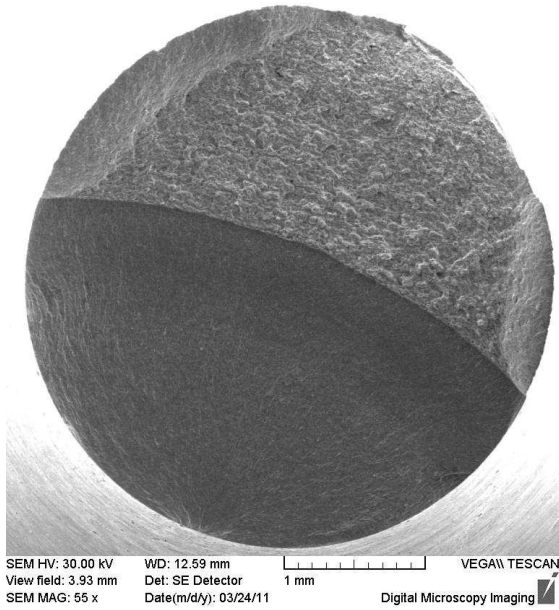


Fig. 3. Surface fatigue crack initiation
 $\sigma_a = 450 \text{ MPa}$, $N = 2.3 \times 10^7$ cycles.

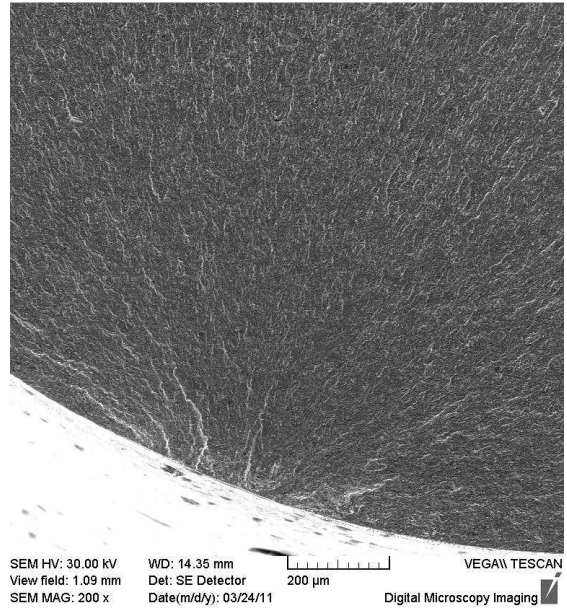


Fig. 4. Detail of fatigue crack initiation detail
 $\sigma_a = 450 \text{ MPa}$, $N = 2.3 \times 10^7$ cycles.

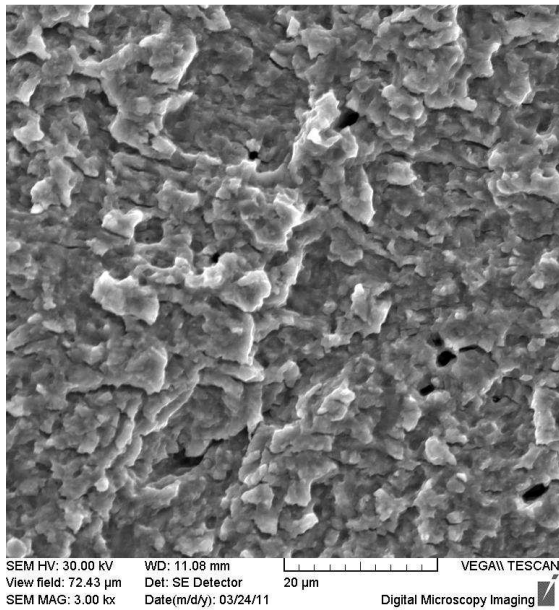


Fig. 5. Detail of stable crack growth,
 $\sigma_a = 450 \text{ MPa}$, $N = 2.3 \times 10^7$ cycles.

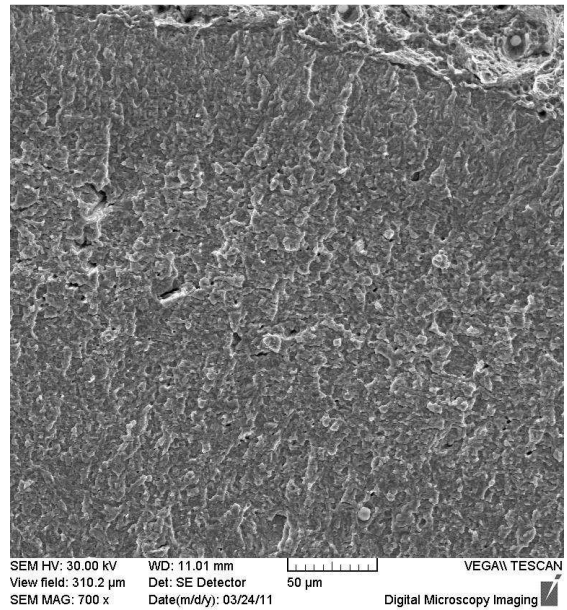


Fig. 6. Boundary between stable and unstable crack
growth, $\sigma_a = 450 \text{ MPa}$, $N = 2.3 \times 10^7$ cycles.

places serve inclusions, microdefects, shrinkages, very small grains, long grain boundaries and so on [15-18]). After surface initiation, the crack grows under stable conditions through a large part of the cross-section, what is shown in Fig. 5. When the cross-section becomes very weak, the crack passes from stable growth to unstable growth as can be observed in Fig. 6. For the rest part of the cross-section is characteristic a ductile fracture with dimple morphology (upper right corner in Fig.6) [17,18].

4. Conclusions

With regards on the obtained data we can pronounce following conclusions:

- the S-N curve has a fluently decreasing character in whole studied region of loading cycles number,
- only surface fatigue crack initiation in the ultra-high cycle region was observable,
- the results about fatigue limit referred to number of cycles from $N = 10^6$ cycles to $N = 10^7$ cycles are overestimated and non-fulfill the demand of reliability and safety,
- the value of "fatigue limit" at $N > 10^7$ cycles (for steels and cast irons) can be determined only as conventional value related to specified number of cycles.

Acknowledgement

The research was supported partially by Scientific Grant Agency of Ministry of Education, Science, Research and Sport of Slovak Republic and Slovak Academy of Science grant No. 1/1093/10.

5. References

- [1] SKOČOVSKÝ, P., BOKŮVKA, O., KONEČNÁ, R., TILLOVÁ, E. *Náuka o materiáli pre odbory strojnícke*. Žilina: EDIS, 2006. 349 s.
- [2] KUNZ, L. *Experimentální stanovení únavových charakteristik materiálů*. Žilina: EDIS, 2003. 81 s.
- [3] BOKŮVKA, O., NICOLETTO, G., KUNZ, L., PALČEK, P., CHALUPOVÁ, M. *Low and High Frequency Fatigue Testing*. Žilina: EDIS, 2002. 100 s.
- [4] PALČEK, P., CHALUPOVÁ, M., NICOLETTO, G., BOKŮVKA, O. *Prediction of Machine Element Durability*. Žilina: EDIS, 2003. 178 s.
- [5] PUŠKÁR, A., BOKŮVKA, O., NICOLETTO, G., PALČEK, P. Equipment and Methods for Ultrasonic Fatigue Evaluation of Metals. *Berichte und Informationen*, 1997, Vol.V, No.1, p. 63-68.
- [6] RŮŽIČKOVÁ, M., BOKŮVKA, O., PALČEK, P., NICOLETTO, G. Rast dlhých únavových trhlín pri vysokofrekvenčnom cyklickom zaťažovaní. *Materiálové inžinierstvo*, 1999, Roč.6, č.15, s. 19-26.
- [7] NICOLETTO, G., BOKŮVKA, O., PALČEK, P., RŮŽIČKOVÁ, M. Rast dlhých únavových trhlín pri vysokofrekvenčnom cyklickom zaťažovaní II. *Materiálové inžinierstvo*, 1999, Roč. 6, č. 18, s. 9-12.
- [8] BURŠÁK, M., BOKŮVKA, O., MAMUZIČ, I., MICHEL, J. Impact Properties of Microalloyed Steel. *Metalurgija, metallurgy*, 2000, Vol. 39, No.4, p. 243-247.
- [9] NICOLETTO, G., BOKŮVKA, O., COLLINI, L., KOPAS, P. Fatigue Resistance in a Very High-cycle Regime. *Transaction of Famena*, 2005, Vol.29, No.1, p. 9-16
- [10] BATHIAS, C., PARIS, P. C. *Gigacycle Fatigue in Mechanical Practice*. M. Dekker, New York, 2005. p. 304
- [11] BOKŮVKA O., NOVÝ, F., ČINČALA, M., KUNZ, L. Gigacyklová únava konštrukčných materiálov. *Acta Mechanica Slovaca*, 2006, Roč.10, č.1, s. 53-58.
- [12] NOVÝ, F., ČINČALA, M., KOPAS, P., BOKŮVKA, O. Mechanisms of High-strength Structural Materials Fatigue Failure in Ultra-wide Life Region. *Materials Science and Engineering*, 2007, Vol. A462, p. 189-192.
- [13] BOKŮVKA, O., NOVÝ, F., CHALUPOVÁ, M., NICOLETTO, G. Gigacycle Fatigue at High-frequency Loading. *Diagnostyka*, 2008, 4/48, p. 53-56.
- [14] KUNZ, L., LUKÁŠ, P., BOKŮVKA, O. Fatigue Behaviour of Ultrafine-grained Copper in Very High-cycle Regime. *Materials Engineering*, 2008, Vol.15, No.4, p. 1-5
- [15] MURAKAMI, Y., NOMOTO, T., UEBA, T. Factors Influencing the Mechanism of Superlong Fatigue Failure in Steels. *Fatigue Frac. Eng. Mater. Struct.*, 1999, Vol.22, p. 581-590.
- [16] PUŠKÁR, A., HAZLINGER, M. *Porušovanie a lomy súčastí*. Žilina: EDIS, 2000. 295 s.
- [17] PALČEK, P., CHALUPOVÁ, M. Fraktografia a mikrofraktografia konštrukčných materiálov. *Materiálové inžinierstvo*, 2002. Roč. 9, č. 2, s. 57-66.
- [18] PALČEK, P., CHALUPOVÁ, M. Fraktografia a zisťovanie príčin porušovania konštrukčných materiálov. In. *Letná škola únavy materiálov*. Žilina: EDIS, 2010, s. 43-56.



Fatigue Properties of S235J2 Steel in the Ultra-High-Cycle Area

*Robert Ulewicz, **František Nový, *Magdalena Mazur

*Czestochowa University of Technology, Institute of Production Engineering, Faculty of Management, 42-201 Czestochowa, Armii Krajowej 19B, Poland, ulewicz@zim.pcz.pl, mazur.m@zim.pcz.pl

**University of Žilina, Department of Material Engineering, Faculty of Mechanical Engineering, Veľký Diel, 010 26 Žilina, Slovakia, frantisek.novy@fstroj.uniza.sk

Abstract. In this work the authors present knowledge about fatigue properties of S235J2 steel in the ultra-high-cycle area of loading ($N = 6 \times 10^6 \div 10^{10}$ cycles) obtained at high-frequency fatigue testing ($f \approx 20$ kHz, $T = 20 \pm 3$ °C, $R = -1$).

Keywords: S235J2 steel, fatigue, ultra-high-cycle.

1. Introduction

Fatigue resistance is one of the most important engineering properties, that plays a significant role in machine design, because of a fatigue is a predominating fracture mode of load-bearing machine parts. Fatigue testing is usually performed to estimate the relationship between the stress amplitude and the cycles to failure (σ - N curve). Majority of published experimental works shows, that the number of cycles of stress that the metal can endure before failure increases with decreasing stress amplitude and for some engineering materials the σ - N curve becomes horizontal at a certain limiting stress known as the fatigue limit or endurance limit. Below the fatigue limit, the material will not fail in an infinite number of cycles [1]. Up to date researches gives some arguments, that this representation of the fatigue resistance cannot be true, because infinite fatigue endurance does not exist. Fatigue strength in the long life region is not a constant value, but it henceforward slowly and in some cases evenly rapidly decreases. Fatigue design based on the usual fatigue limit ($N_f = 1.10^6 - 1.10^7$ cycles) cannot provide the safety design data of mechanical structures [2].

In this work there are published results about fatigue lifetime of S235J2 steel obtained at cyclic loading at gigacycle regimes of loading. Obtained results will be used in the process of selecting material for semi-trailer using generalized objective function. Ideological scheme of the general objective function method presents Figure 1. The method can be found in the paper [3].

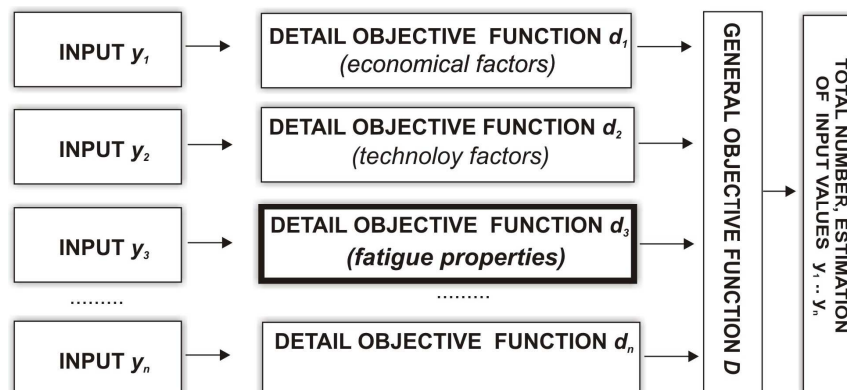


Fig. 1. Scheme of selection function general method.

2. Material and experimental procedures

The S235J2 structural steel of common quality was used as an experimental material. The chemical composition of the steel is introduced in Tab. 1. From the experimental material were prepared specimens for mechanical tests and specimens for fatigue tests.

Chemical compositions [%]								
C	Mn	Si	S	P	Cr	Ni	W	B
0.18	0.52	0.11	0.032	0.014	0.07	0.09	0.012	0.0001
Cu	Mo	V	Ti	Al	Sn	N	Pb	As
0.28	0.01	0.001	0.001	0.003	0.001	0.0065	0.002	0.001
Mechanical properties								
Yield strength Re			Tensile strength Rm			Elongation		Notch impact test
[MPa]			[MPa]			A5 [%]		[J]
255.0			440.0			29		27

Tab. 1. Chemical composition and mechanical properties S235J2 steal.

The results from metallographic analysis are shown in the Fig. 2. For metallographic analysis was used light metallographic microscope NEOPHOT 32. The experimental steel has ferritic-perlitic fine-grained microstructure (Fig. 2), with grain size 10 (classified according to Slovak standard STN 42 0462). Tensile test (according to STN EN 10002-1) was performed using experimental universal mechanical testing machine ZWICK Z 50 (with loading range $F = 0 \div 50$ kN, temperature $T = 20 \pm 2$ °C). For tensile tests were used round standard specimens with diameter $D_0 = 6$ mm.

For fatigue tests was used experimental equipment KAUP-ŽU Žilina. Used testing methods and procedures are described elsewhere [1, 5]. The experiments were carried out on resonant high-frequency fatigue machine in the regime of controlled load using sinusoidal tension-compression loading with the frequency of 20 kHz. The stress ratio of $R = -1$ was used. Fatigue tests were performed at the ambient temperature ($T = 20 \pm 3$ °C). Specimens were cooled by distilled water with anticorrosive inhibitor. Specimen shape and dimension were determine according to the Salama and Lamerand technique [4]. The details, especially about methods and procedures the fatigue high-frequency parameters measuring can be found in the [5].

The fatigue tests, dependence $\sigma_a = f(N)$, were performed in the range from $N = 6 \times 10^6$ cycles to $N = 10^{10}$ cycles. Fatigue tests were aborted in region of $N = 10^{10}$ cycles. The results of fatigue tests are shown in Fig. 3.

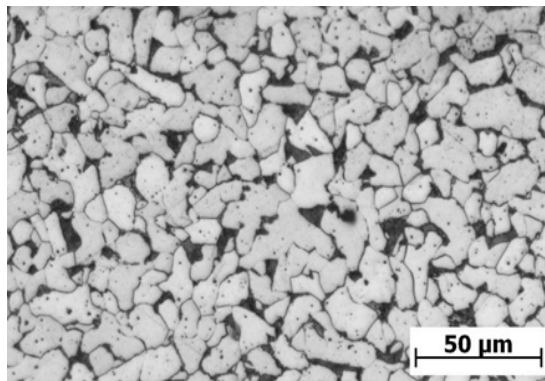


Fig. 2. Microstructure S235J2 steal.

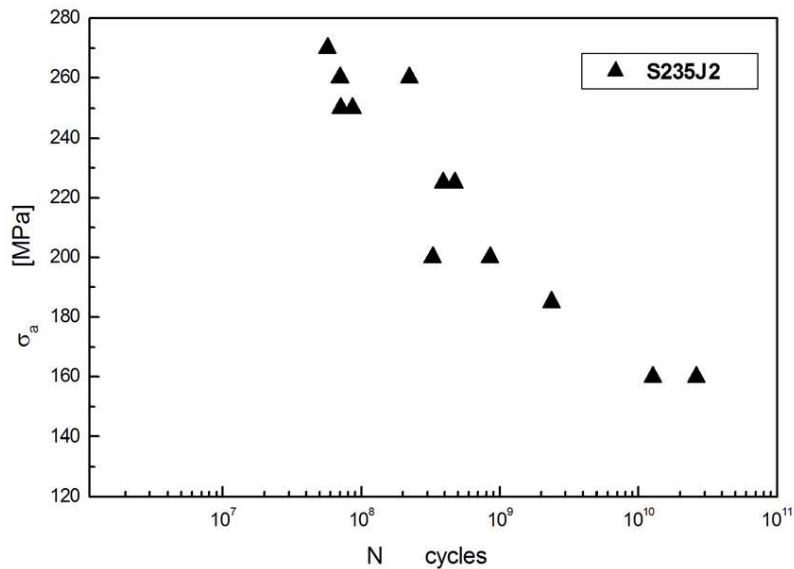


Fig. 3. Fatigue durability, S235JRG2 steel, high-frequency fatigue testing, $f = 20$ kHz, $T = 20^\circ\text{C}$, $R = -1$, $N_c > 10^7$.

Applied amplitude stress σ_a lowered from $\sigma_a = 270$ MPa (for $N_f = 5,7 \cdot 10^7$ cycles) to $\sigma_a = 160$ MPa (for $N_f = 1,3 \cdot 10^{10}$ cycles), which gives the difference in amplitude $\Delta\sigma_a = 110$ MPa. In general we can say that pressure amplitude is still decreasing together with growing number of cycles to increasing failure over conventional cycles limit ($N_C = 1 \cdot 10^6 \div N_C = 1 \cdot 10^7$ cycles - typically used range of cycles in order to determine fatigue limit σ_C) [6, 7]. This fact is very essential due to reliability and safety of machinery and equipment [1].

The fractographic analysis which was carried out by means of TESLA BS 343 (SjF, ŽU). Fatigue scrap material of sample can be classified as trans-crystalline plastic in which there is residual zone (for breaking) (Fig.4) it consists almost exclusively of fields with range lines (Fig. 5). Quite often there occurred large non-metallic inclusions (Fig. 6), but did not affect either initiation or propagation of fatigue cracks.

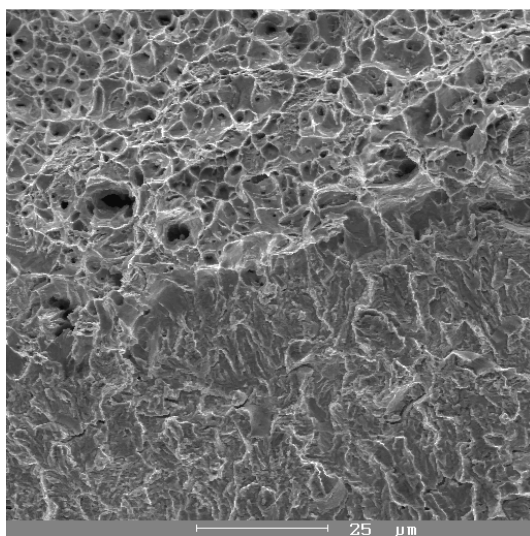


Fig. 4. The transition area between fatigue and ductile fracture, $\sigma_a = 235$ MPa, $N = 7,24 \cdot 10^7$ cycles

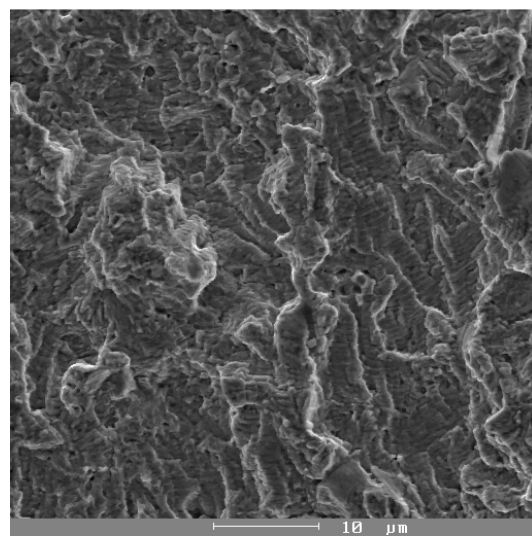


Fig. 5. The characteristic appearance of fields striation, $\sigma_a = 185$ MPa, $N = 4,86 \cdot 10^8$ cycles

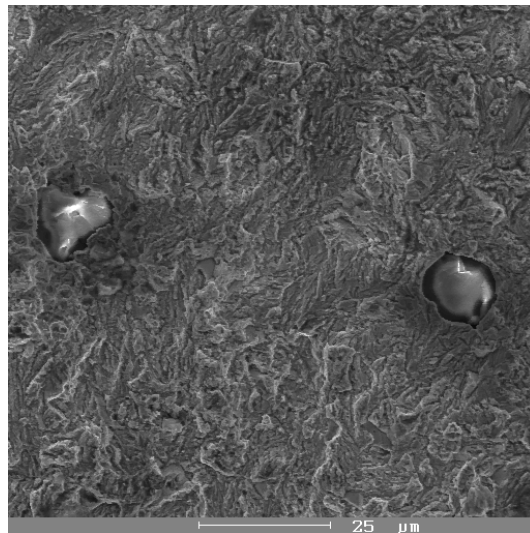


Fig. 6. The local occurrence of nonmetallic inclusions, $\sigma_a = 185$ MPa, $N = 4,86 \cdot 10^8$ cycles

3. Conclusion

As can be seen in Fig.3, the stress amplitude σ_a decreases together with increase of cycles number N beyond conventional fatigue limit $N_c = 10^7$ cycles. In the case of specimens made from S235J2 steel the stress amplitude decreases about $\Delta\sigma_a = 80$ MPa (in the range of $N = 8 \times 10^7 \leftrightarrow N = 10^{10}$ cycles). The analogical knowledge was observed also by other authors [8,9] for chassis materials of lorries. Manufacturers of modern trucks semi-trailers are increasingly being forced to give with high accuracy the period of safe operation [10]. Use of high frequencies of load enables to specify this period, and also use of data to develop generalized objective function of material selection for individual structural elements of trucks semi-trailers.

References

- [1] BOKŮVKA O., NICOLETTO G., KUNZ L., PALCEK P., CHALUPOVA M.: *Low & high frequency fatigue testing*. CETRA and Univerzity of Zilina, Zilina 2002.
- [2] STANZL-TSCHEGG S., MAYER H.: *Fatigue in the very high cycle regime*, Vienna, Austria, 2001.
- [3] ULEWICZ R., NOVY F., BOJANOWICZ P.: *Objective function in selection process of coating on metal products*, Material Engineering, Vol. 13, Issue 3a, 2009.
- [4] SALAMA K., LAMERAND R.K.: *Ultrasonic fatigue*, Conf. Proc., The Met. Soc. of AIME, New York 1982.
- [5] PUŠKÁR A.: *Metodika práce na zariadení KAUP*, Žilina, 1990.
- [6] BOJANOWICZ P., KOPAS P., ULEWICZ R.: NOVÝ F.: *Very high cycle regime fatigue of SGRJ35 steel*, Material Engineering, Vol.12/3,2005.
- [7] BOKŮVKA O., NOVÝ F., KOPAS P., CHALUPOVÁ M., BOJANOWICZ P.: *Very high cycle regime fatigue of selected structural materials*, 22nd International Colloquium. Advanced Manufacturing and Repair Technologies in Vehicle Industry. Częstochowa - Orle Gniazdo, Hucisko 2005.
- [8] KUNZ J., NEDBAL I., SIEGL J.: In: *Proc. Fractography 91*, ÚFM SAV, Košice, 1991.
- [9] KUNZ J., SIEGL J., NEDBAL I.: *Materials Engineering*, Vol. 14, Issue 3, 2007.
- [10] MAZUR M., ULEWICZ R., SZATANIAK P.: *Identification of Welding Incompatibilities in the Process of Semitrailers Production*, SEMDOK 2011. 16th International of PhD. Students' Seminar. Zilina - Terchova, Slovakia 2011.



Analysis of Simulation Technology Faults in Dip and Pulse Transfer of GMAW Welding

*Miloš Varga, *Miloš Mičian,

*University of Žilina, Faculty of Mechanical Engineering, Department of Technology Engineering,
Univerzitná 2, 01026 Žilina, Slovakia, {milos.varga, milos.mician}@fstroj.uniza.sk

Abstract. Arc welding often brings anomalies from normal burnings arc caused by various factors. Subjectively valuation these anomaly is possible realize near manual welding, where lonely welder is judge stability arcing too. Near mechanical behavior is needed these defects analyze, evaluate and accomplish of interference with control system adjustable device, if you like welder robot, eventually of electric parameters welder generator. The paper is dedicated to the compilation of a complete welding department and a monitoring system suitable for the detection of technological defects during online and offline welding. After the proposed technology and simulation defects, approach to assessing samples using standard deviation and the mean welding current and welding voltage in dip and pulse transfer.

Keywords: Monitoring, simulation, technology faults, dip transfer, GMAW welding.

1. Introduction

Present monitoring systems as ADM III (Arc Data Monitor III) or Weld Monitor 4.0 etc. are at high level. Voltage, current and other process signals are measured, displayed and compared with preset nominal values. If the difference firmly set on the actual values exceeds the selected limit, the alarm is started. Selection limits for the parameter is very important in the design of detection algorithms. There are two contradictory requirements that must be deliberate. The first requirement is to choose limits not to make false alarms, the emergence of a situation which occurs in welding and do not affect the welding process itself. In this case, the detector should was not allow stopping the welding process. On the other hand, the "softening" of the detection limits reduces the likelihood of detecting these errors.

2. Monitoring of Welding Process

Monitoring of welding parameters compound welding work on is provided with two measuring systems. The basis of both is contactless current probe PAC 22 and voltage probe HZ 100. Scanned analog signal is further processed and digitalized through a digital oscilloscope ETC M621 or through A / D converter NI6008. Block diagram of the flow of signals from the welding source to the PC is shown in Fig. 1.

Digitalized signals are evaluated in the PC and processed using appropriate software. One of the software for evaluation of monitored parameters is a LabView program, used to monitor the measured parameters in online mode welding. In this program we have put together a similar application of the weld alarm, which is used for on-line error detection technology during the course of welding. Program to be entered limits, beyond which LEDs are lighten up to detect irregularities in the welding process. This irregularity, instability can be caused just by the presence of technological defects at the weld.

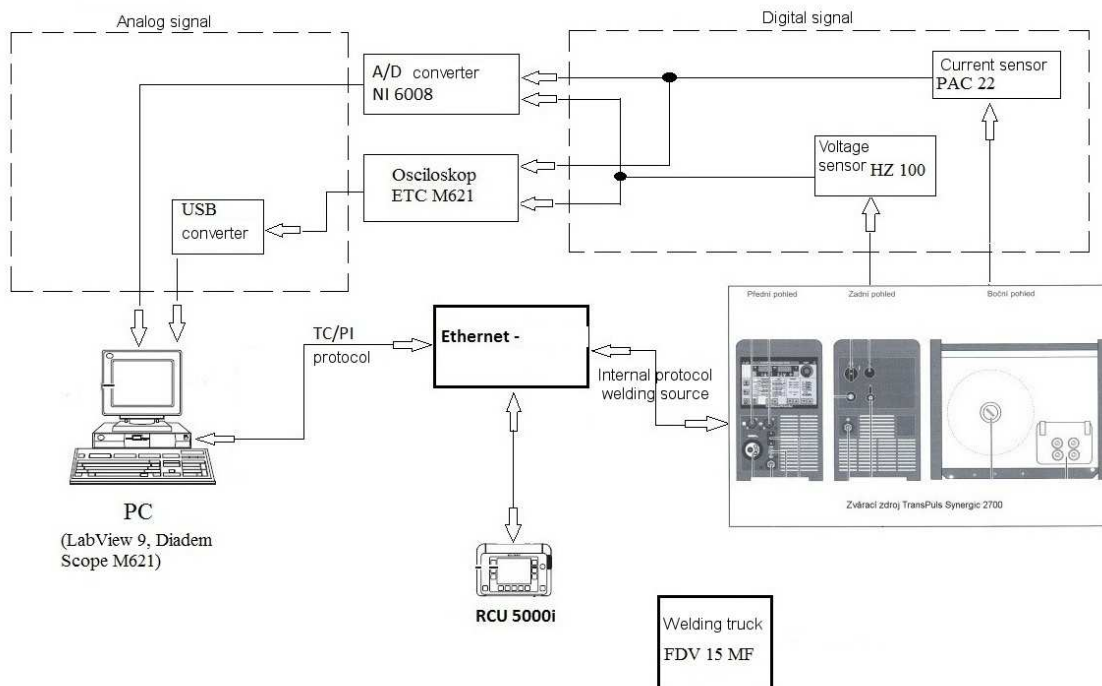


Fig. 1. Block diagram welding department.

3. Simulation Technology of Errors in Dip Transfer and Pulse Transfer Welding

After preparation and involvement of welding department and tried all the functionality of equipment and correct measurements we acceded to alone simulate some of selected technological defects (supply interruption of protective atmosphere, dirty surface of welded parts, resizing of the root gap, “venting” protective atmosphere). On Fig. 2 shows one of the simulated defects after welding. This is a defect marked as a sample 014, where the simulated supply interruption of protective atmosphere.



Fig. 2. Supply interruption of protective atmosphere. P – pulse transfer welding, S – dip transfer welding.

After simulation and preparation of samples, we continue to evaluate individual samples in off-line mode welding. For all the simulated defects, we evaluate the mean welding current and voltage and standard deviation of the welding current and voltage to find out the exact location defects in the weld joint, where the welding alarm we evaluated the defect in the online welding. On Fig. 3 and Fig. 4 is shows the time courses of the standard deviation of welding current for dip transfer and pulse transfer welding.

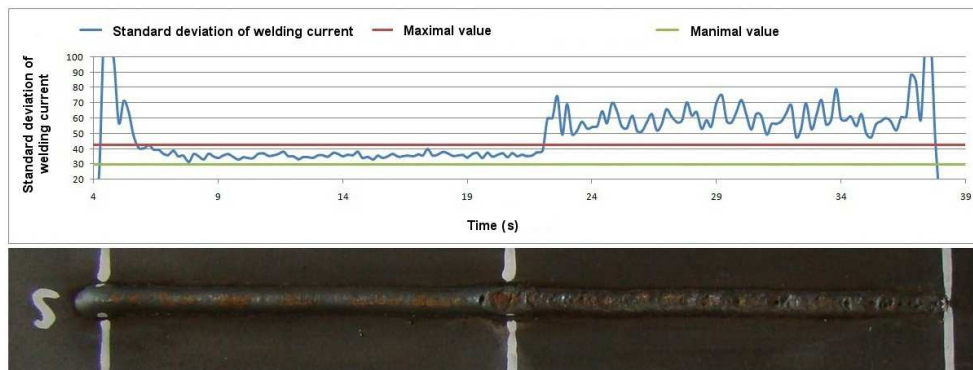


Fig. 3. Sample 014 - time course standard deviation of welding current (dip transfer).

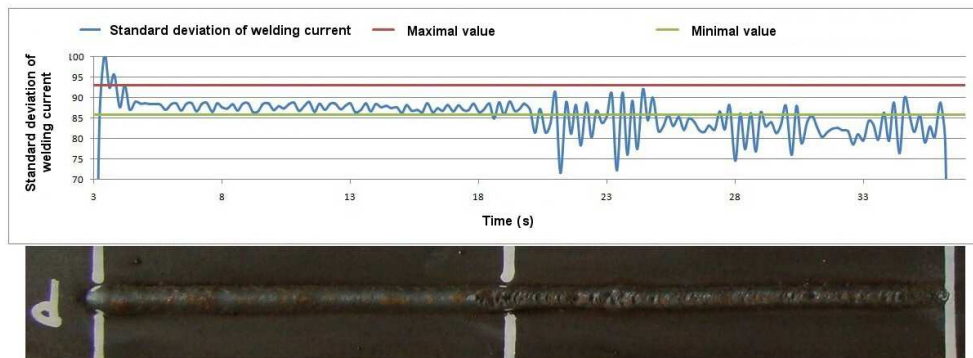


Fig. 4. Sample 014 - time course standard deviation of welding current (pulse transfer).

For sample no. 014 were carried out two, first was dip transfer (on the picture marked with S) and the other was in pulse transfer (on the picture marked with P). Further to this sample in Fig. 3 and 4, which shows the time course of the standard deviation of the welding current, are shown the maximum and minimum allowed values. As the course of the welding current is within those limits, it is a welding of technology without defects. If the course of the welding current is outside of the permitted limits, than we can say it is technological defect. The maximum and minimum allowed values were determined from measurement standards where were simulated optimal welding conditions for dip transfer and pulse transfer. First, we determine the maximum and minimum value, which was located during welding standard. From these values, we expressed the percentage difference and this difference was added to the average value of welding current and voltage for the mean and the standard deviation and we got the maximum allowed value and the deduction for this difference, we get the minimum allowed value for the mean and standard deviation of the welding current and voltage. These percentage differences in the range from $\pm 5\%$ to $\pm 10\%$ for dip transfer and pulse transfer and the standard deviation of the welding current and voltage and also for the average welding current and welding voltage.

On Fig. 5 are shown in the drawing weld deposit sites without defects and defect with simulated technology for dip transfer and pulse transfer.

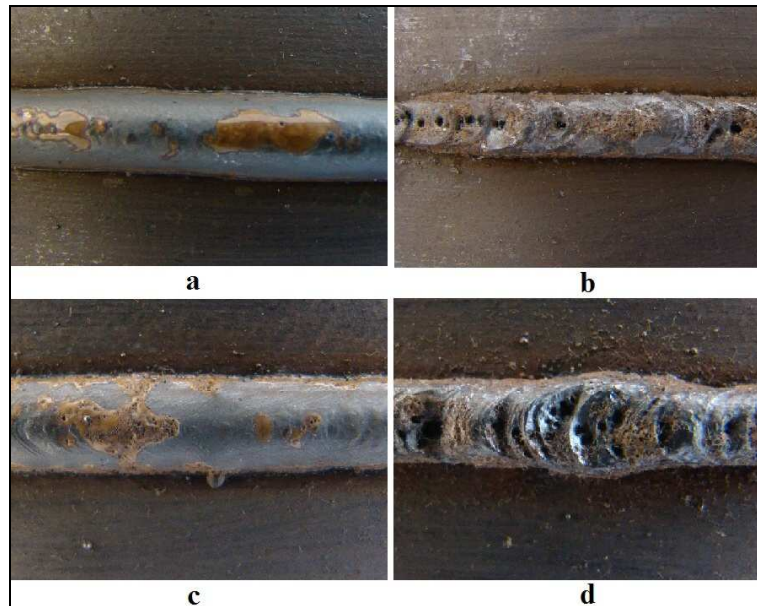


Fig. 5. Sample 014 – drawing bead. a – place without defects (dip transfer), b – place with defect (dip transfer), c – place without defects (pulse transfer), d – place with defect (pulse transfer).

4. Conclusion

In conclusion we can say that the method of detection technology defects using of welding alarm set up in LabView program is suitable for three of the four simulated defects. It is a defects supply interruption of protective atmosphere, “venting” protective atmosphere. The only defect that alarm failed to detect surface with oil contamination is welded parts. In all simulated defects, which can detect the alarm has been seen not only during direct welding, in turn emitting diodes, but also after welding in the evaluation itself. Evaluate the standard deviation and the mean welding current and voltage and dip transfer and pulse transfer welding. When the evaluation was at least one statistical indicator to see the launch of an alarm and a representation of the boundaries and thus the detection of instability. These statistical indicators recommend to compare always together, because the evaluation showed once mean and ever standard deviation uncovers technological defects during welding, whether you are welding current or voltage.

Acknowledgement

This work has been supported by Scientific Grant Agency of Ministry of Education of Slovak republic, grant KEGA No. 3/3668/08 and VEGA project No. 1/0186/09.

References

- [1] BEBIANO, D., ALFARO, S. C. A. *A Weld Defects Detection System Based on a Spectrometer*. Automation and Control Group, University of Brasilia, Faculdade de Tecnologia. ISSN 1424 – 8220, 2009.
- [2] VARGA, M., MIČIAN, M., PALLO, P. *Fault detection technology for gas-shield arc welding*. TechMat 2010, ISBN 978-80-7395-324-9, 2010.
- [3] <http://www.google.sk/patents?hl=sk&lr=&vid=USPAT5521354&id=orkfAAAAEBAJ&oi=fnd&dq=Method+for+arc+welding+fault+detection&printsec=abstract#v=onepage&q&f=false>



ISF Method – Isotropic Superfinishing

*Stanislav Veľas, *Andrej Czán, *Dana Stančeková

*University of Zilina, Faculty of Mechanical Engineering, Department of Machining and Manufacturing technology, Univerzitna 1, 01026 Žilina, Slovakia, {stanislav.velas, andrej.czán, dana.stančekova}@fstroj.uniza.sk

Abstract. Integral part of the production process in the field of machining is finishing machining methods. An important feature of finishing ways of machining is also the possibility of machining hardened materials. This group includes mainly grinding, honing, lapping, superfinishing and fine turning and milling. New finishing method is ISF-superfinishing (super-isotropic). Thanks to the method of isotropic superfinishing we obtain workpieces with very high quality surface, thereby ensuring increased efficiency and extended life which means lower costs for higher performance. In this method are used traditional tumbling devices with ceramic abrasive grinding coils and plastic coils. Chemicals are added to equipment in two phases to accelerate tumbling method. With this method is machined at the same time the entire surface of the workpiece, ruthless on its complexity and shape. It is possible to achieve a mean arithmetic deviation of profile less than $0.02 \mu\text{m}$.

Keywords: Integrity of surface, finish machining, superfinishing.

1. Introduction

When two metal parts are chafed against each other there is always created a heat. These high temperatures cause wearing, reduce an efficiency constantly and finally they lead to the part failure and afterwards also the part exchange. Thanks to the ISF method the machined parts can gain smooth and shiny surface by which we can guarantee an increase of efficiency and lifetime prolongation that means the reduction of costs at higher performance [1].



Parts of gearbox machined by method ISF



Working with high-gloss



Finishing of engine blades

Fig. 1. Examples of using ISF methods [1].

Milling, grinding, honing and lapping results in the more or less rough surfaces. Tops of these rough surfaces are getting smoothed by the ISF method. Thanks to the ISF method the surface is not only smoother, but due to the new structure a friction is reduced and lubrication is improved significantly. Due to the reason that ISF method reduces not only a friction, but also temperature, at the same time it leads also to the prolongation of machined part maintenance interval [1].

ISF method represents an internationally patented kind of chemical speed-up of deburring method. This method uses the conventional deburring equipments and non-abrasive particles for achieving of isotropic surface. It is possible to meet the surface quality of $Ra \leq 0,02 \mu\text{m}$ [1].

This surface is characterized in a possibly highest quality regarding the friction resistance, heat exchange, noise level and machined part wearing also in such industrial areas like bearing

production and drive mechanisms, power train technique, energy production or production of drive mechanisms in the aircrafts [1].

This method used to achieve the isotropic surface the tumbling equipments with ceramic abrasive coils a) and plastic coils b) of different sizes and shapes.

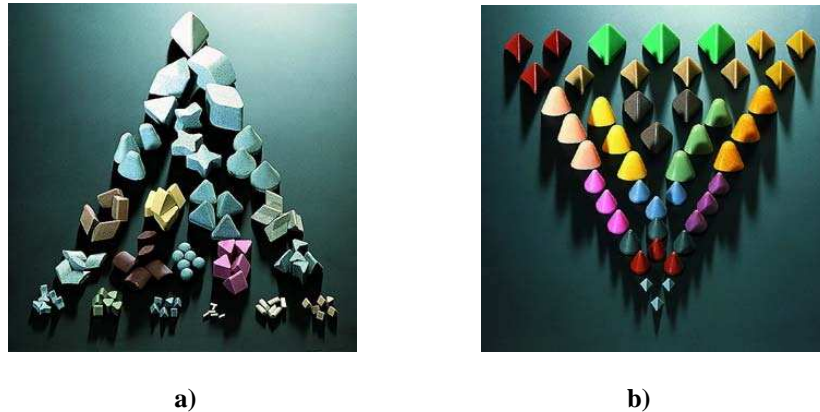


Fig. 2. Tumbling coils [1]

Substances that processed generations of cleaning chemical facilities were usually highly alkaline and strongly enriched completing agents. Nowadays are their major part organic substances, which are almost biodegradable. It is emphasized [1].

2. Process Principle

The ISF process is normally made in two phases:

In the first phase there is supplied and measured a liquid mixture that is fitted in with the part material directly into the polishing and grinding equipment. By influence of the mixture there is created a dark grey oxidation layer on the machined surfaces in normal cases which is taken away together with the highest surface „picks“ of ground part. This oxidation layer is created fluently in a repeated way and is still taken away, but in the meantime the raw material in „sags“ and grooves remains untouched. This material cut off is working purely on principle of wearing and rubbing, but there is not a chemical material cut off. After the required surface quality was achieved there is supplied and measured other liquid mixture as the second phase into the machine in order to remove an oxidation layer and meet the required surface either in shiny or in mat condition. During the second phase there is almost not any material cut off [1].

3. Comparison and Conclusion

After comparison of classical superfinishing and superfinishing by ISF method there is a conclusion that superfinishing ISF has got the following advantages:

- short machining time,
- lower friction,
- low property wearing, physical, by a normal operation,
- low tooling prices,
- low basic investment,
- low costs for energy,
- low noise bundle,

- safe usage,
- high flexibility [1].

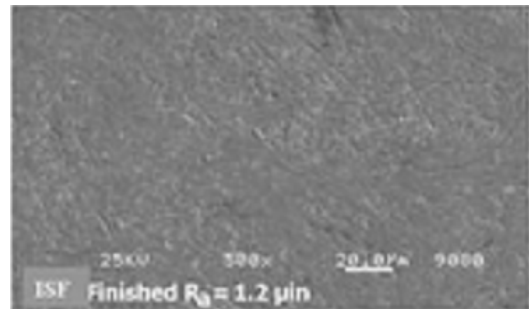
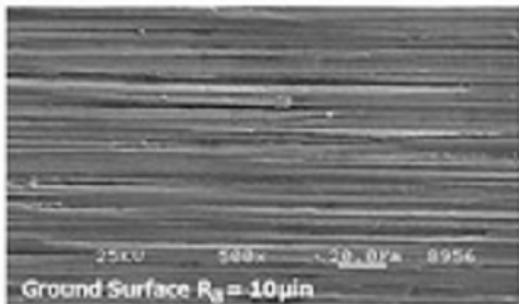


Fig. 3. Compared machined surface before and after using ISF method [1].

The next big advantage is that at using of ISF method the part is machined from each side at the same time and surface roughness is much lower. The measurement was made on oversized bearing rings. The measurement target was to propose finishing operation for given conditions. The prescribed middle arithmetical value of considered profile was $0,15 \mu\text{m}$. The measurements were made on bearing rings of steel 14 are 209.4 (100CrMnSi6-4). Individual machining operations were performed on devices: turning: TOSHULIN SKIQ 12, grinding: Berthiez VGM 180, isotropic superfinishing: Rosler 420 2-E, roughness measurement: HOMEL-TESTER T 1000. For finishing was used these methods: finishing turning, grinding, superfinishing and isotropic superfinishing.

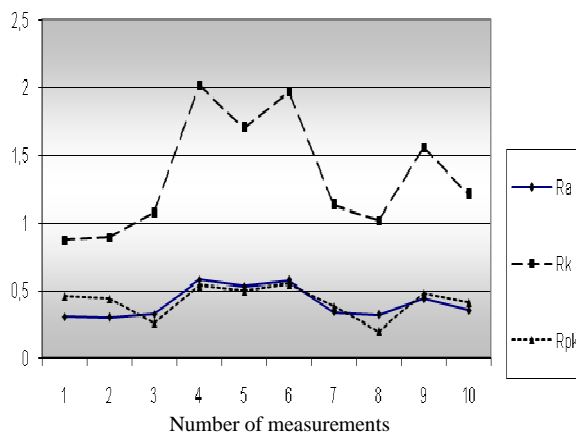


Fig. 4. Finish Turning

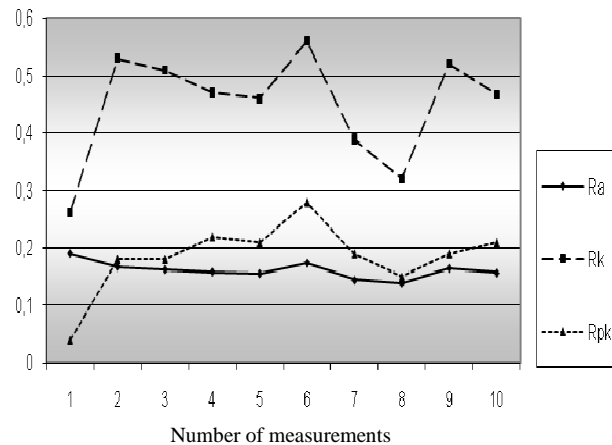


Fig. 5. Grinding

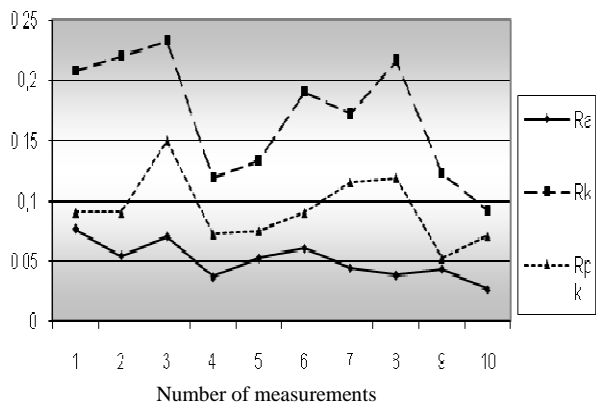


Fig. 6. Superfinishing

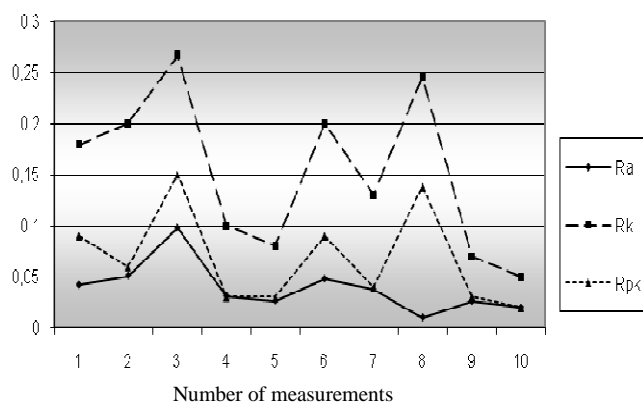


Fig. 7. Isotropic Superfinishing

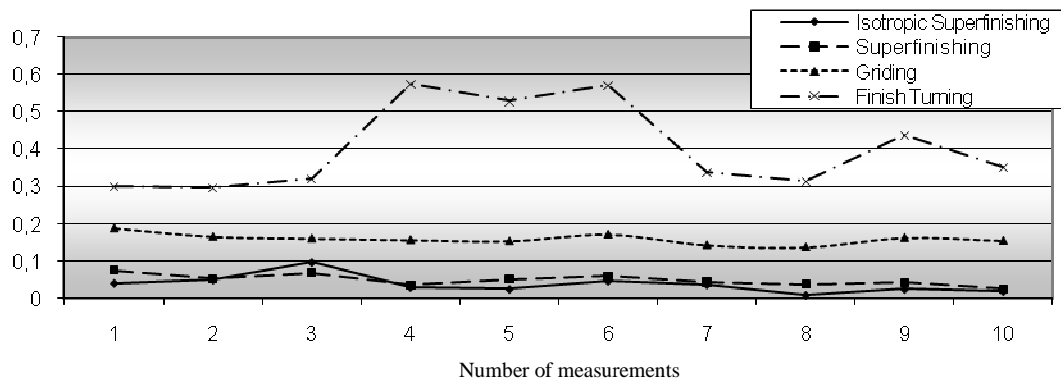


Fig. 8. Final comparison of surface roughness

The measurements were made on the oversized bearing rings on an average of 800 mm. Working condition roughness was less than 0.15 μm . The above graphs shows that among the finishing methods such us Finish Turning, Grinding, Superfinishing and Isotropic Superfinishing had the best surface integrity was in isotropic superfinishing. The measured values were processed into the graphs, which show that the condition failed grinding and finish turning. Conditions were met also in the standard superfinishing. However, consider if oversized bearing rings can worked by classical superfinishing or ISF.

References

- [1] <http://www.rosler.com/> 28.2.2011.
- [2] GAŠPAREK, J. *Dokončovacie spôsoby obrábania*, ALFA Bratislava, 1979.
- [3] STANČEKOVÁ, D., ČILLÍKOVÁ, M., CZÁN, A., MORAVEC, J., ENGLARD, A. *Úvod do inžinierskeho štúdia*.
- [4] ADAMCZAK, S., MICHALSKI, D., STĘPIEŃ, K. *Computer method of geometrical structure of a surface measurements accuracy evaluation*. Konferencja międzynarodowa - International Carpathian Control Conference ICC' 2002. Malenovice (CZ), 27-30 maja 2002. Materiały konferencyjne, str. 27-32 (PR-20 %) – 0,2 pkt..
- [5] ADAMCZAK, S., JANECKI, D., STĘPIEŃ, K. *The function of cross correlation in comparing roundness profiles*. Konferencja międzynarodowa - International Carpathian Control Conference ICC' 2002. Malenovice (CZ), 27-30 maja 2002. Materiały konferencyjne, str. 21-26. (PR-25 %) – 0,25.
- [6] VASILKO, K., BOKUČAVA, G. *Brúsenie kovových materiálov*, ALFA Bratislava, 1988.
- [7] VASILKO, K., HRUBÝ, J., LIPTÁK, J. *Technológia obrábania a montáže*, ALFA Bratislava 1990, ISBN 80-05-00807-4
- [8] VASILKO, K. A KOL. *Valivé ložiská*. Alfa Bratislava, 1988.



Evaluation of Rheological Properties of Thermoplastic Polymers after Degradation

*Michaela Vojsovičová, *Tatiana Liptáková, **Dusan Gaňa

*University of Žilina, Faculty of Mechanical Engineering, Department of Materials Engineering, Univerzitná 1, 01026 Žilina, Slovakia, {michaela.vojsovicova, tatiana.liptakova}@fstroj.uniza.sk

**Mobis Slovakia s.r.o., Gbeľany 405, 013 02 Gbeľany, dusan.gana@mobis.sk

Abstract. The aim of this study is the comparison of selected rheological properties of thermoplastic polymer materials before and after exposure in different environments for exact period: UV radiation, moist soil with higher concentration of chlorides, n-hexane solution with a degradation effect. Rate and depth of degradation induced by the environment were evaluated by Frequency sweep test, which monitors changes in viscoelastic properties of polymers with respect to their molecular structure and their behavior in thermoplastic processes. Degradation process resulted in changes of complex dynamic viscosity, storage and loss modulus, changes in molecular weight and its distribution.

Keywords: polymer degradation, rheology, complex viscosity, loss modulus, storage modulus

1. Introduction

Recently, the development of plastic materials has taken place ahead of traditional, particularly metal materials, because they constantly extend the possibilities of their applications as a replacement of the traditional materials in engineering, construction, electronics, and agriculture and mainly in packing. From all kinds of plastics, especially thermoplastic materials take the significant importance because of their good performance and advanced technologies of their processing [1].

Rheology and its experiments reveal information about the flow behavior of liquids but also the deformation behavior of solids, because it is the typical behavior of polymers. Changes induced by the environment with degradation effect can be evaluated by rheological measurements which monitor changes in viscoelastic properties of the tested polymers. The fundamental of rheological characteristics is viscosity which defines the internal resistance of material against its creep generated by external forces. It is necessary to realize the dual character of majority of polymer materials from viscoelastic point of view. The action of external force on the ideal viscous material results in its deformation i.e. irreversible locomotion (movement) of macromolecules and after removal of the external force material retains its „new“ shape. The action of external force on the ideal elastic material results in its deformation but after the removal of the external force, the material returns to its original shape. Polymers are generally characterized by the viscoelastic nature, which means that external forces cause partly permanent (viscosity element of polymer) and partly reversible (elastic element of polymer) deformation [1, 2, 4].

Viscosity of polymer melt is determined by shear stress and shear rate as well as by other factors like temperature, pressure, molecular weight and its distribution, structure of the polymer, presence of additives in the polymer. Viscosity has a high importance for polymer processing, the change of viscosity is determined by changes of the factors above, which are characteristic for the polymer and may vary according to the effect of degradation processes. The aim of this study is the comparison of selected rheological properties of thermoplastic polymer materials before and after exposure in different environments with a degradation effect.

2. Experimental material

Polyethylene STN EN 1555 (PE 1400) with the trade name Finathene XS 10 YCF S 70111902 provided by the plastics company Nitra (nowadays frequently used to produce pipeline systems); high density, low pressure PE 500 with the trade name PE HMW, and polypropylene PP, both provided by Licharz company were used as an experimental material.

These thermoplastics materials pose very good chemical resistance, relatively low density $0.91 - 0.96 \text{ g/cm}^3$, low absorption, good resistance at high negative temperature, good workability and some other properties like coefficient of friction, abrasion resistance and impact toughness [1,3].

Polymer samples of plate shape with dimension of $10 \times 55 \times 3 \text{ mm}$ were exposed in different environments with degradation effect. Samples of PP and PE 500 were exposed to aliphatic hydrocarbon n-hexane, immersed in a separated container for four months. PE 1400 samples were subjected to long-term (485 days) exposure in moist soil with high chloride concentration simulating conditions of the real working environment. Accelerated aging tests of PE 1400 samples were carried out in UV chamber for a period of 139 days, which represents 700 cycles and intake energy of 5264 kJm^{-2} . One cycle in the UV chamber is represented by 4.8 hours of testing with delivered energy of about 7.52 kJm^{-2} per cycle. Daily cycle runs for 3.8 hour (temperature of $62 \pm 3^\circ\text{C}$; relative humidity of $50 \pm 5\%$; intensity of radiation 0.55 Wm^{-2}) and 1 hour night cycle (temperature of $38 \pm 3^\circ\text{C}$; relative humidity of $50 \pm 5\%$; intensity of radiation 0 Wm^{-2}).

Rheological measurements by Frequency sweep test were carried out after the exposure tests of polymer samples, results and analysis are presented in the experimental section.

3. Experimental part

The evaluation of polymer degradation was performed by measuring of rheological properties by oscillating rheometer Physica Rheometer MCR 301 with CTD 450 conventional thermal device. The chosen method was Frequency Sweep test (FS), which characterize the viscoelastic properties of polymers with respect to their molecular structure and their behavior in thermoplastic processes [4, 5].

The sample was placed between two parallel plates with diameter of 25 mm, in 1 mm distance from each other. Measurements were carried out at the temperature of 160°C and 180°C , according to the nature of the material and following conditions: amplitude of $\gamma = 5\%$, angular frequency of $\omega = 500 - 0.051/\text{s}$.

The principle of material evaluation is based on evaluation of measured parameters which are shown in the diagram (Fig.1). The process of degradation is followed by changes of molecular weight (as networking or macromolecular chains breaking) which should be reflected in the measured parameters.

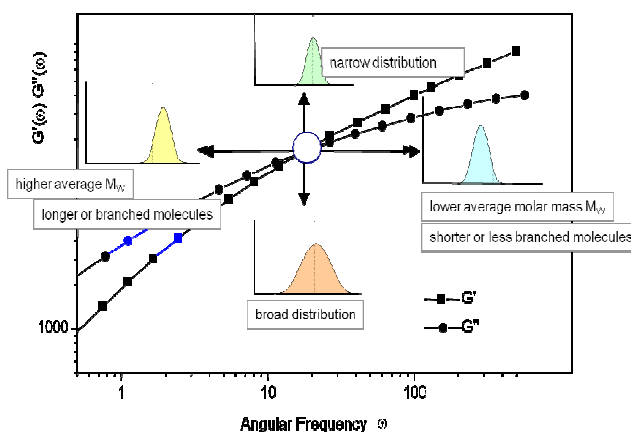


Fig. 1 Determination of selected characteristics of material during FS test and the curve of measurements as result.

As seen in Fig. 1, the values of complex dynamic viscosity η and storage modulus G' and loss modulus G'' can be compared by measuring. Furthermore, we are able to monitor the position of the intersection of the curves characterizing the state of both modulus and indicate the transition from viscous deformation behavior to the more elastic behavior. This intersection is qualitative characteristics of the material [1,4]. The polymer degradation can result in changes of the values of measured characteristics. Shift of the modulus intersection in horizontal direction provides information about the average molecular weight and shift of the modulus intersection in the vertical direction signals the difference in the molecular weight distribution.

Rate and depth of PE 1400 degradation after exposure in UV chamber (after 700 cycles) was evaluated by Frequency Sweep test (FS). The differences in viscosity and modulus defining plastic and elastic properties of PE samples are shown in Fig.2. These measurements were carried out only in exposed surface layers that were replaced from the exposed sample (in depth of 0 to 750 μm and 750 to 1500 μm). There is evident difference in degradation seen from the surface further to the depth and the layer of 750 μm has significantly different viscoelastic properties – material becomes more fragile. Measurement of the sample layer in the depth of 750 - 1500 μm showed that the degradation is much smaller and measured curve is closer to the curve of unaffected sample.

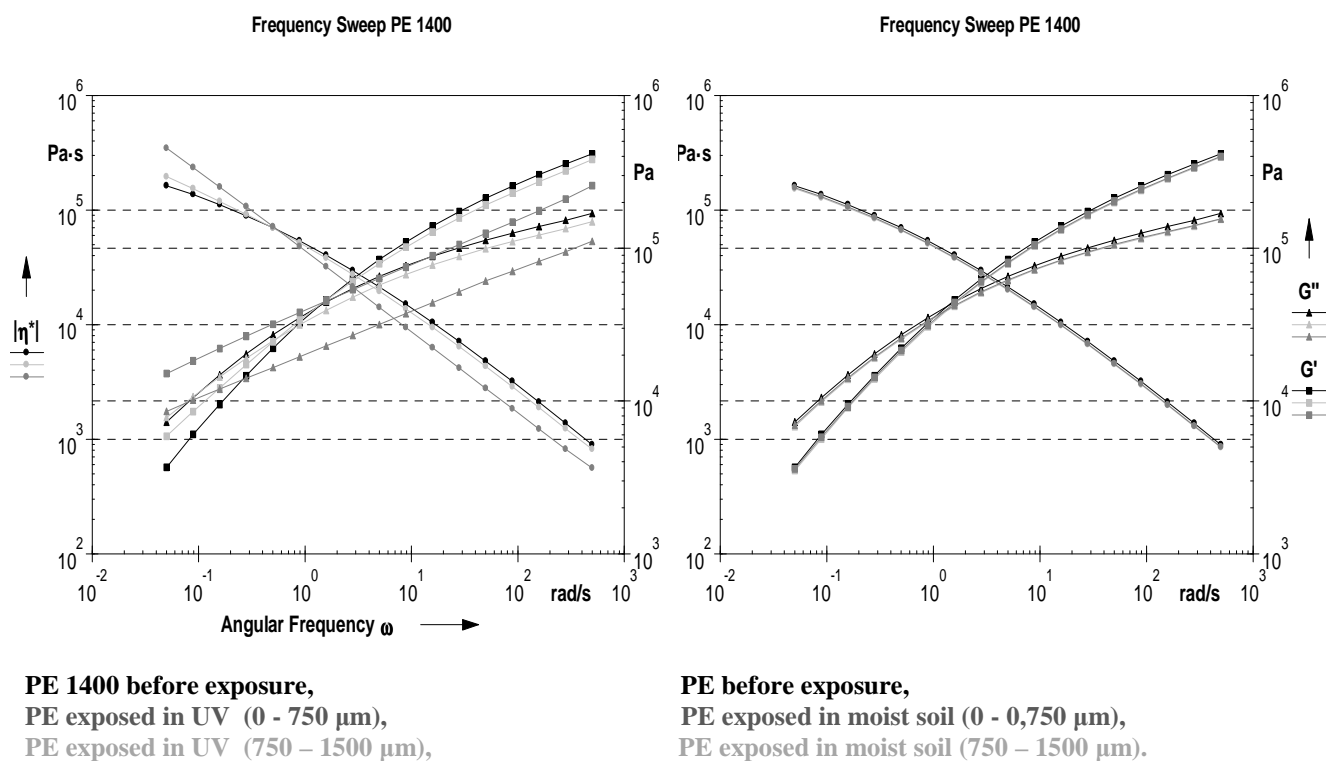
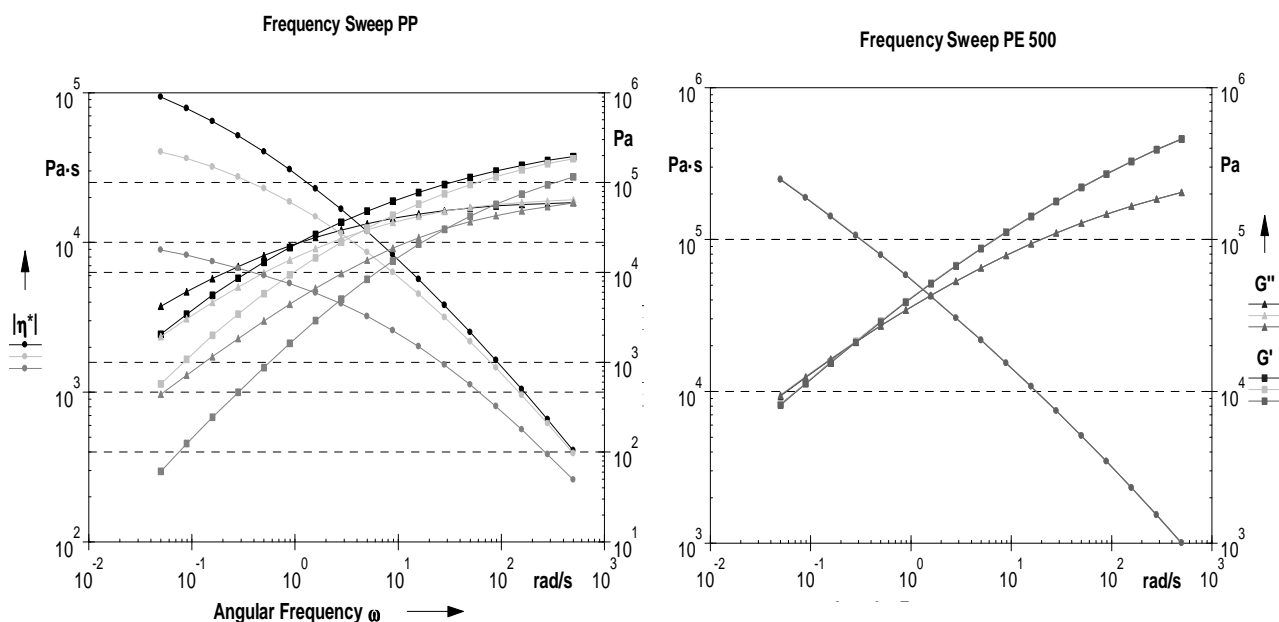


Fig. 2 and 3 Differences in rheological properties of PE 1400 samples exposed 700 cycles in UV testers and after 485 days exposure in moist soil measured in different depth from the surface.

Moist soil with higher concentration of chlorides had no significant degradation influence on PE 1400 even after long-term exposure. Fig. 3 shows that polyethylene material was not damaged in surface layers which was verified by measuring replaced layers in particular depth (0 - 0,750 μm and 750 – 1500 μm) from surface area. According to the results it is clear that neither surface areas nor subsurface areas were influenced by degradation effect because the values of measured variables indicate almost the same course.

Measurements of PP and PE 500 exposed in n-hexane for 3 months period (Fig. 4 and 5) show the changes of viscosity, as well as G' and G'' modulus in both surface layers but only in PP samples. We can monitor that the area in the depth of 300 - 600 μm is affected more than the surface layer of 0 - 300 μm , in which material properties are much more similar to properties of unexposed material. This phenomenon is not very clear to explain yet and is subjected to further study. PE 500 indicates no changes in viscoelastic properties in comparison with the original material.



PE, PP before exposure, PE, PP exposed in n-hexane (0 - 300 μm),
PE, PP exposed in n-hexane (300 - 600 μm).

Fig. 4 and 5 Differences in rheological properties of PP and PE 500 samples exposed in n-hexane for 3 months period measured in different depth from the surface.

5. Conclusion

- Rheological measurements sensitively monitor changes in the structure of studied polymers due to degradation effect in different environments. This was reflected in the measured rheological parameters and variables like viscosity, molecular weight changes and their distribution, modulus characterizing elastic and plastic properties.
- The results show that the exposure of PP and PE 500 in n-hexane only influenced the degradation of polypropylene samples which varied in particular layers. The rheological characteristics of polyethylene material did not change.
- The long-term exposure of PE 1400 in moist soil had no significant effect on viscoelastic characteristics of tested material.

References

- [1] T. Liptáková – P. Alexy - E. Gondár - V. Khunová: Polymérne technické materiály, vysokoškolská učebnica, www.kmi.sk, 2009
- [2] Ch. E. Carraher Jr.: Introduction to Polymer Chemistry, Taylor and Francis Group, ISBN 0-8493-7047-2, USA 2007
- [3] T. G. Mezger: The Reology Handbook, 2nd Edition, ISBN 3-87870-174-8, Hannover 2006
- [4] K. Wollny: Comparison of a propylene reinforced with glass fiber and pure polypropylen over a temperature range from -150 to +180°C, Anton Paar germany GmbH, 2006
- [5] K. Wollny,: Comparison of Polyethylen, melts using Frequency Sweeps, Anton Paar germany GmbH, 2006



Load distribution in Hamburg Wheel Tracking Test

*Josef Žák, *Jiří Vavříčka

*Czech Technical University in Prague, Faculty of Civil Engineering, Department of Road Structures,
Thákurova 7, 16629 Prague, Czech republic, {josef.zak, jiri.vavricka}@fsv.cvut.cz

Abstract. This article deals with load distribution in Hamburg Wheel Tracking Test. Three models of stresses were developed on basis of measurement of the contact surface, depression of the wheel with rubber hoop under load and by application of the Finite Element Method.

Keywords: Hamburg Wheel Tracking Test, load distribution, Finite Element Method

1. Introduction

This article deals with load occurring between the asphalt specimen surface and the wheel of the Hamburg Wheel Tracking device. The wheel reciprocates over the test specimen, with the position varying sinusoidal over time. The wheel passes across the test specimen approximately 50 times per minute. The maximum speed of the wheel is approximately 0.3 m/s and is reached at the midpoint of the slab. While the wheel reciprocates over the test specimen the speed is changing (figure 1). The rut depth is defined as an average value of the profile of the test specimen on 50 mm length in the middle of the test specimen; this profile is measured in more than 25 points approximately evenly distributed. To fit the course of wheel position following equation has been decided as most suitable:

$$x(t) = 0.115 \sin(2.618t) \quad (1)$$

$$v_{\text{speed}}(t) = \frac{d}{dt}(0.115 \sin(2.618t)) \quad (2)$$

Where x is distance in longitudinal direction [m] and $x=0$ represents the middle of tested specimen and v_{speed} is the speed of the wheel [m/s]. The speed change in the middle of the wheel is in the range of ± 25 mm over the middle of test specimen, it means ± 0.00446 m/s. It is a negligible difference and it was calculated with a constant value of speed 0.3 m/s. The speed was used for interchange of the metric domain in direction of travel into time domain.

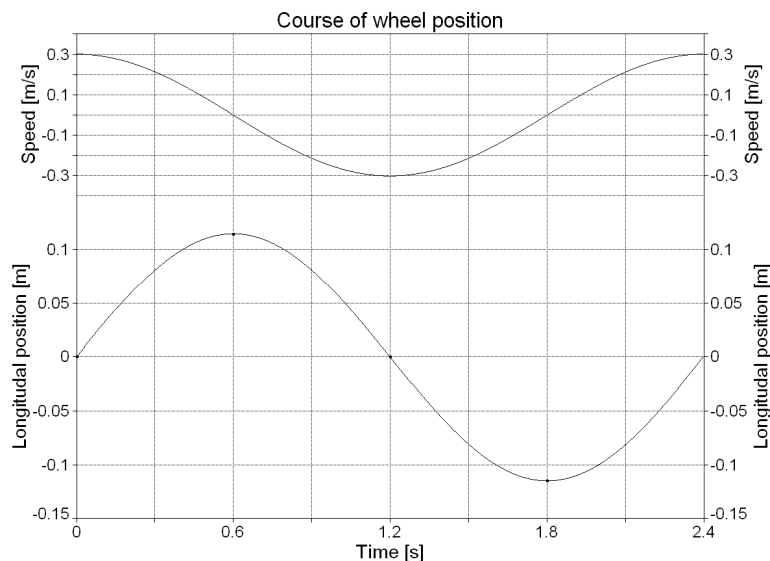


Fig. 1. Course of wheel position

2. Constant Load Approximation (Load #1)

The contact area between the steel plate and the wheel of the Wheel Tracking device was measured. At first, liquid coloring was used, but it was occurred extrusion of liquid coloring in lateral margins and it was difficult to measure the transient area properly. For that reason, we looked for a fine-grained material which would not be extruded. The Plaster of Paris was chosen as the most fine-grained material. The size of the grain was from 14µm to 16µm. The steel plate was sprinkled with the Plaster of Paris and the load wheel was consequently placed onto the steel plate. Further, the rest of Plaster of Paris on the rubber hoop of the wheel was measured with a calliper. The transient area is 0.022 m long and 0.05 mm wide.

The load applied by the wheel is 700 N. The first approximation „Load #1“(Fig. 2) was developed from following equation:

$$\sigma = \frac{\text{Force}}{\text{Area}}$$

$$\sigma = \frac{700}{0.05 * 0.022} \doteq 636\,363\text{ Pa} \quad (3)$$

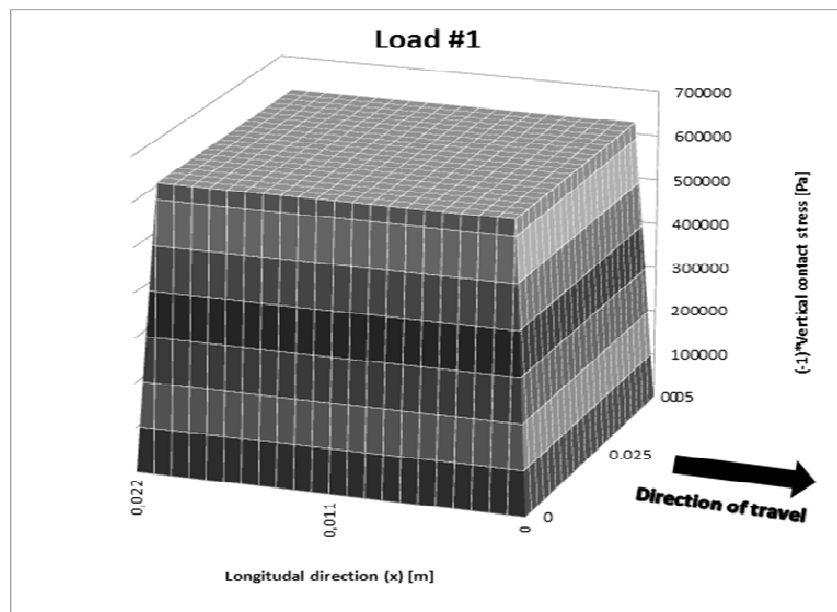


Fig. 2. Load #1

3. Parabolic Load Approximation (Load #2)

Based on previous paragraph, the contact area is 0.022 m long and 0.05 m wide. Diameter of the wheel is 0.2 m and the load applied onto the wheel is 700 N. It is possible to develop the load approximation from this known information and geometric relations with application of the theory of elasticity. The procedure is based on splitting the rubber hoop into infinitely small strips in the longitudinal direction. Each of the strips is under load compressed by itself value of strain. The force response of each strip is in proportion to the deformation and Young's Modulus. Established signification of unknowns and their geometric sense are written in [1].

The equation of Load #2 is (4) and the Load #2 is plotted in Fig. 3:

$$\sigma(x) = E * \frac{R - \sqrt{R^2 + x^2} - \Delta_{max}}{l} \quad (4)$$

With application of the theory of elasticity application, integration over area to express force and consequent substituting values of all measured initial conditions we obtain:

$$700 = 2 * E * \int_0^{0.005} \int_0^{0.011} \frac{0.1 - \sqrt{0.1^2 + x^2} - 6.068412817E - 4}{0.02} dx dy \quad (5)$$

In this lastly specified equation, the value of Young's Modulus is the only unknown which we were not able to measure. The reason allies simply in not being equipped with suitable durometer [3] at our disposal to measure the real IRHD of rubber hoop and other method of measuring Young's Modulus of rubber could not be considered, because the rubber hoop is glued to the steel wheel core. The Young's Modulus of rubber was calculated from equation (5) and is E=31.45 MPa. This value does not correspond with Young's Modulus obtained by prescribed IRHD according to [2], but corresponds with the depth of deformation measured by LVDTs of the Wheel Tracking device after the load were applied and other measured characteristics were gained.

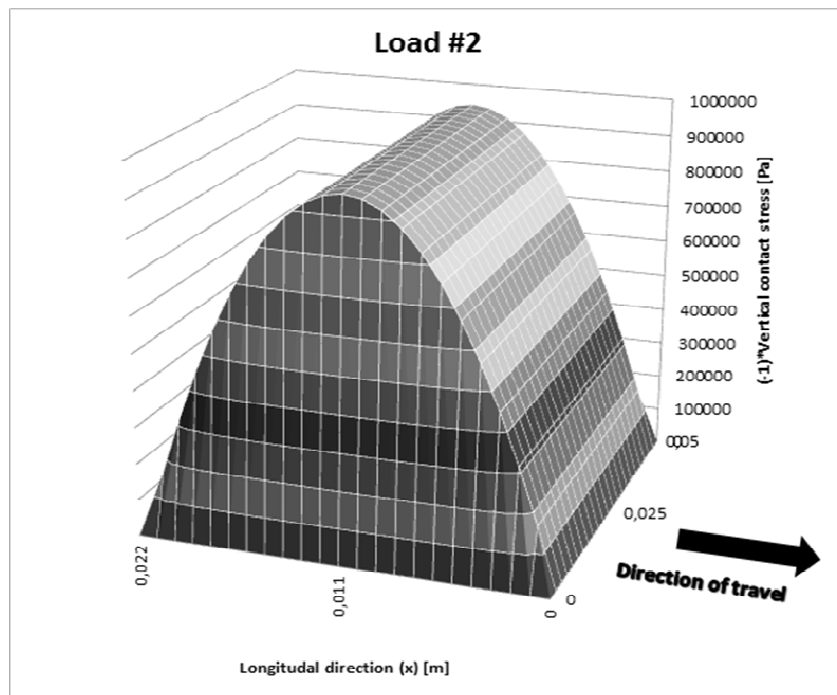


Fig. 3. Load #2

4. Load Approximation Developed by ABAQUS (Load #3)

The wheel with a rubber hoop on a steel plate was modeled by ABAQUS software. The analysis model contains the Steel core, Rubber hoop and Steel underlay desk. The model was split in two steps. Step 1 "Initial" establishes all boundary conditions and step 2 "Apply Force" establishes a load. The load is represented by a gravity force of the Steel core; the density of the Steel core was adjusted to 70978.886 kg/m³ to represent prescribed value of force 700 N. The gravity load prevents the model from concentrated area of loads and represents similar conditions as in reality.

Assembly of the model is following: The Steel core and Rubber hoop are joined together with the normal contact behaviour "Hard contact", not allowing the separation after contact. The contact between the Rubber hoop and Steel underlay desk was characterized by tangential frictional behaviour. Isotropic frictional behaviour with friction coefficient 0.5 was chosen. The right side of the circular surface of the Steel core was fixed against Z- and X-axis displacement and Z-axis rotation. The Steel underlay desk was fixed in all 6 degrees of free.

The static analysis was used for simulating the interaction between the loaded wheel and the steel underlay desk. 0.005 m seeding of the mesh was used for all parts of model. It was not possible to use a smaller seeding because the CVUT University licence of ABAQUS software makes it possible to compute only with 100000 nodes. The deformed model with a view of XY cut plane is plotted in Fig. 4.

Three stresses were obtained from the model. Hereinafter the same denominations for the stresses are used as in [4] and are as follows:

- vertical contact stress: negative in the Y-axis direction, σ_{22} ;
- transverse (or lateral) contact stress: positive in the Z-axis direction, τ_{23} at right angle to the direction of the moving wheel;
- longitudinal contact stress: Positive in X axis direction, τ_{12} , in the direction of the moving wheel;

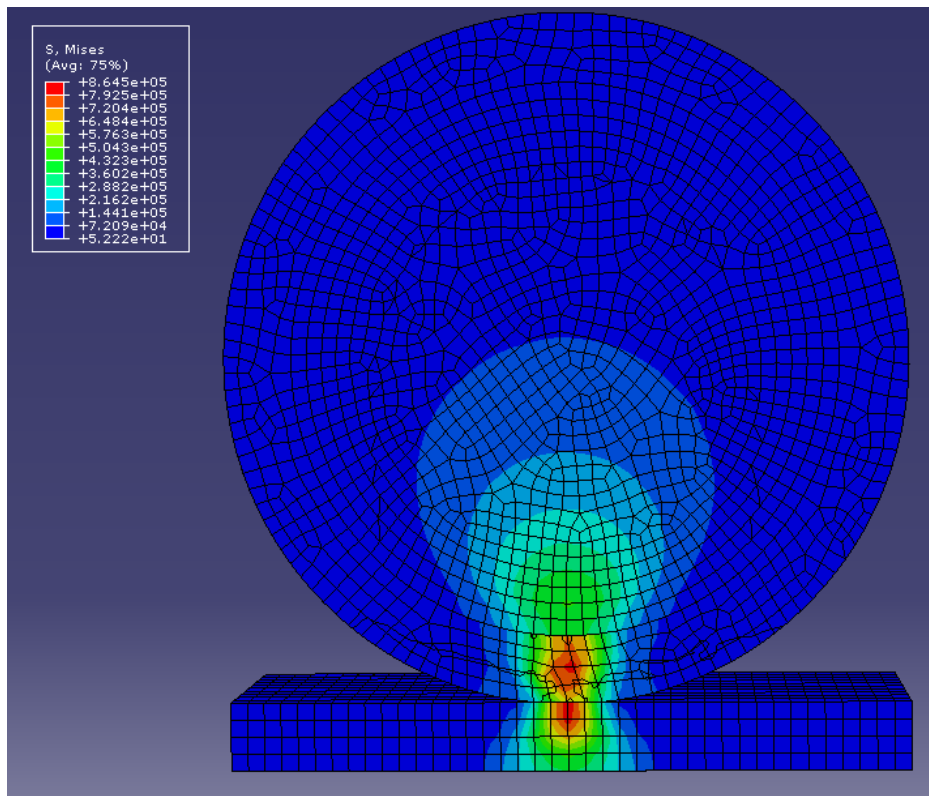


Fig. 4. Model of the Wheel with Rubber Hoop on the steel plate with focus on XY cut plane

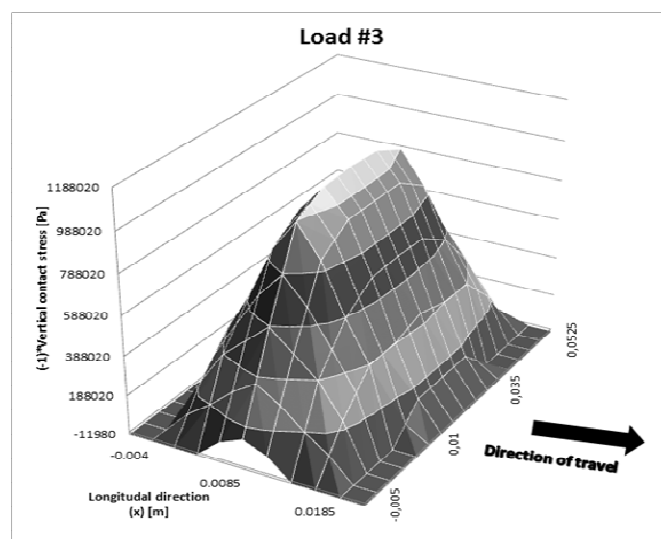


Fig. 5. Vertical contact stress in 3D graph

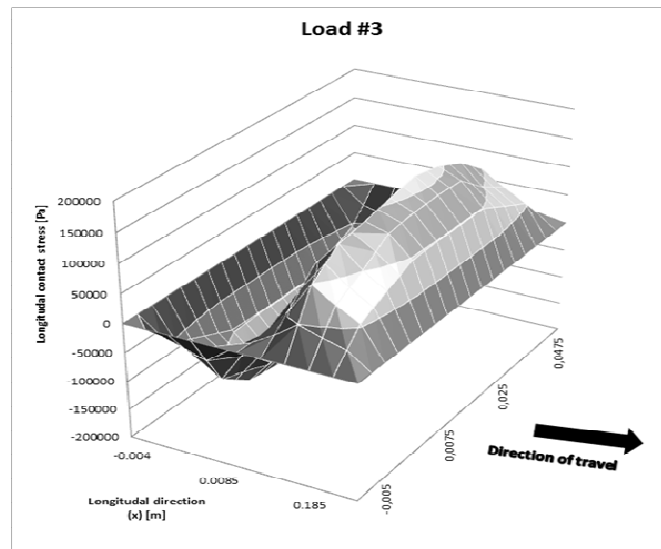


Fig. 6. Longitudinal contact stress in 3D graph

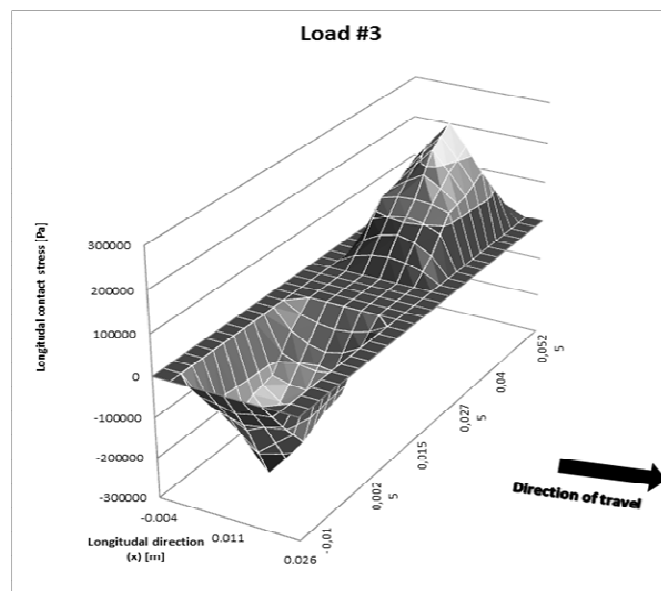


Fig. 7. Lateral transverse stress in 3D graph

5. Conclusion of Loads

The three models of Load were developed for the Wheel Tracking Test. Load model #1 has a constant value of stress and was developed based on measurement of the contact surface between the wheel and the steel desk. Load model #2 has a parabolic shape and was computed from measurement of the contact surface, the depression of the wheel with rubber hoop under loading and Young's modulus of the rubber hoop. With the Finite Element Analysis (FEA) application three dimensional contact stresses (Load #3) were obtained from the Finite Element Method (FEM) simulation of a loaded wheel on a steel plate.

The magnitude of vertical deformation was 5.439×10^{-4} m. The difference between vertical deformation calculated from contact surface and deformation computed from the model is 6.2941×10^{-5} m. We can accept this small difference because of the sensitivity of LVDTs and the accuracy of contact surface measurement.

The vertical contact stress rapidly changes in the X-axis direction. We can see that the maximum Load #2 amplitude of (-953.833 Pa) is lower than Load #3 amplitude (-1.070.000 Pa). Load #3 cannot be characterized as parabolic, might be characterized as polynomial. The vertical

contact stress of Load #3 also changes on the amplitude in Z-axis direction, whereas the Load #1 and Load #2 have constant values on the Z-axis. The slope of the change of Load #3 is significant in lateral sides of the wheel.

In Fig. 8 the comparison of vertical stresses of all concerned Loads is shown in XY plane.

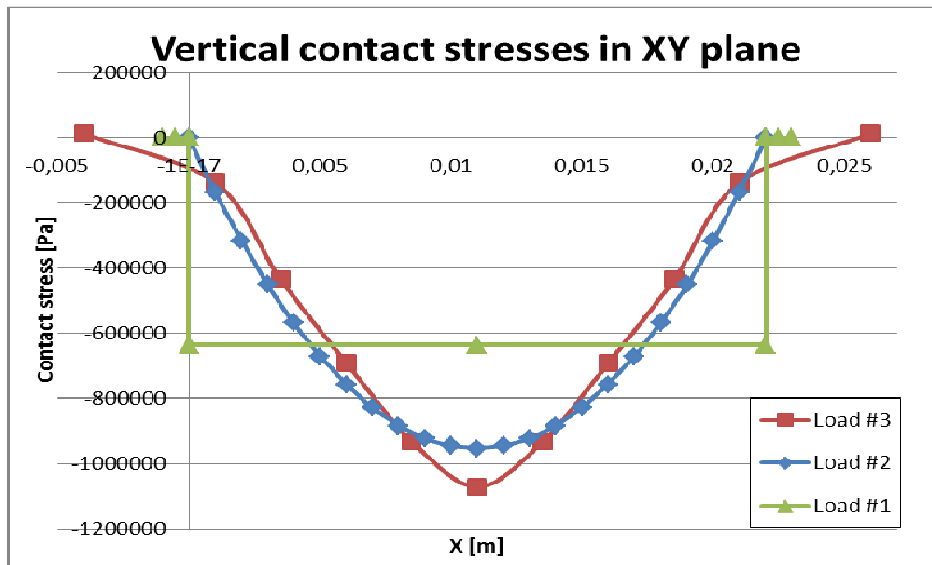


Fig. 8. Vertical contact stresses in XY plane

The lateral transverse stress clearly indicates the inward shear away from the wheel centre direction and this stress is in balance, with zero stress in the wheel centre. The resultant force is zero, but even if the resultant force is zero, the lateral transverse stress contributes to the tension stress close to the wheel edge. This stress tends to pull the HMA from the centre of the wheel. This trend is attributed to the friction between the rubber and the tested material because of the Poisson's effect of material under loading.

The longitudinal contact stresses were indicated in the direction of wheel travel. The magnitude of this stress is lowest from calculated three stresses. The longitudinal contact stress is in balance through the wheel centre as the lateral transverse stress but the symmetry plane of the stress is YZ plane with zero value of stress at the wheel centre. The resultant force is zero. The longitudinal contact stresses are highly dependent on the rolling resistance between the tyre and the road, and on the traction, braking or acceleration [4]. Acceleration or braking does not occur and the speed is approximately constant in the area of interest. Due to this, we can consider this calculated longitudinal contact stress of Load #3 similar to the moving load.

Acknowledgment

This paper has been supported by the research project CG CG712-043-910 of Ministry of Transport.

References

- [1] ŽÁK, JOSEF; *Hamburg Wheel Tracking Test*, Diploma thesis; Czech Technical University in Prague, Faculty of Civil Engineering, K136-Department of Road Structures; January 2011
- [2] ČSN EN 12697-22+A1; *Hot Mix Asphalt-Test methods for Compacted Hot; Mix Asphalt – Part 22: Wheel Tracking Test*
- [3] ISO 48:2010; *Rubber, Vulcanized or thermoplastic - Determination of hardness*
- [4] M. DE BEER, C. FISHER, FRITZ J. JOSTE; *Determination of pneumatic tyre/pavement interface contact stresses under moving loads and some effects on pavements with asphalt surfacing layers*; Division of Roads and Transport Technology, South Africa

Modeling of Non Contact Laser Forming and Microstructure Investigations of Flat Plates

*Zygmunt Mucha, *Piotr Kurp

*Kielce University of Technology, Faculty of Mechatronics and Machinery Design, Centre of Laser Technologies of Metals, Al. Tysiąclecia PP 7, 25-314 Kielce, Polska, kurpp@tlen.pl

Abstract. Thermal forming is a method of changing the shape of an element by heating with a moving source of heat e.g.: laser beam or flame head. In this method expected changes of shape will occur by thermal expansion phenomena. During each of thermal treatment of materials e.g. welding, coating, laser hardening, heat treatment, heat cutting etc. this kind of deformations will occur. Shape changes in this types of treatment are objectionable and should be minimized. For the other hand we are interested in purposeful shape change of material by heat influence. Elaboration of analytical model for heat forming give us opportunity to control and predict the effects of this process.

New analytical model of thermal forming is presented by use laser upsetting mechanism. The experimental results of laser bending are presented as well and compare with calculations for flat plate. Microstructure analysis will answer if any material properties are changed due to temperature influence. Further experiments should give us opportunity to precise this model for construction materials like: angle bars, T-bars, I-bars, C-bars etc.

Keywords: laser forming, laser machining, microstructure after heating.

1. Introduction

Homogeneity upsetting of material along path of heat source beam with minimal bending according to specific shortening is named forming by upsetting mechanism. Field of temperature should have possibly small gradient in perpendicular direction to beam. Zone of higher temperature shouldn't be to much vast simultaneously (because of thermal buckling conditions will appear) and surrounding area must be stiff enough. According to this conditions almost whole material under the beam will be straining during heating phase. Because of both short time of heating and stiffness of element it won't strain but will upset in strain zone. This upset induce its shortening. During cooling down bending torque will appear just after beam incidence point. This torque will make minimal deformation due to small temperature gradient presence.

Fig. 1 presents example of flat bar bending by using triangle (wedge) heat zone. Because of upsetting the material is shortening in perpendicular direction to heating path.

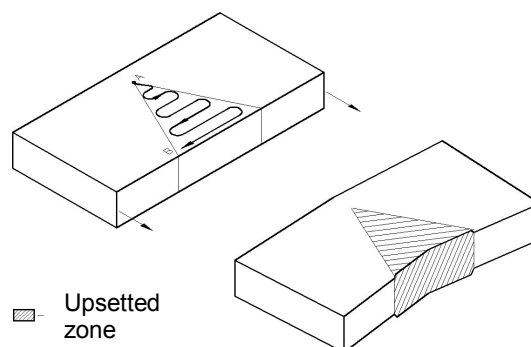


Fig. 1. Flat bar bending by upsetting mechanism

2. Modeling of bend in perpendicular direction to heat source incidence

Analytical models for flat plates laser bending by upsetting mechanism was presented by authors in [3], [1]. That models are very good for flat elements, but cannot describe specific shaped bars bending. In this paper authors will present general analytical model both for plates and bars.

If we considered plate bending in perpendicular direction to heat source incidence (in plate surface), we will assume that plate is heating using triangle straining area (Fig. 2). It is assumed that the temperature of straining is constant in heat zone thru whole thickness of plate as well.

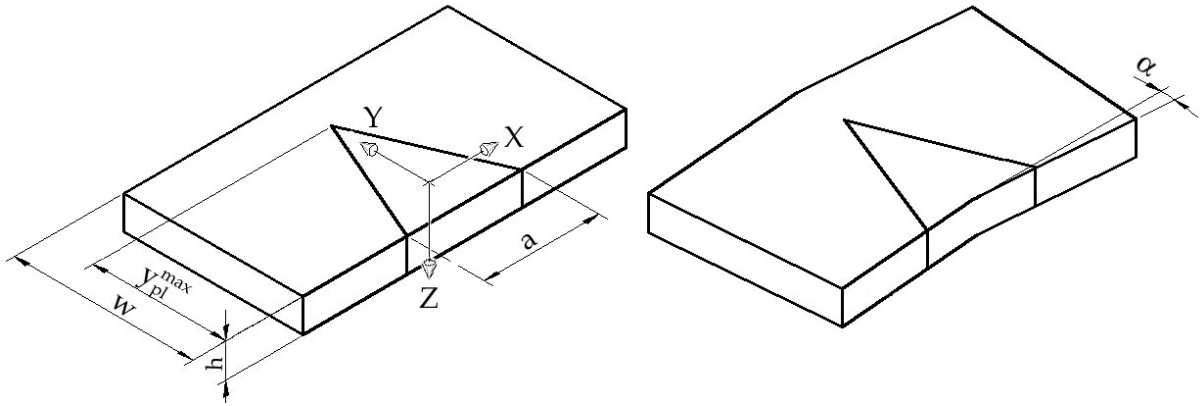


Fig. 2. Model of laser plate bending thru surface by using triangle zone of straining

Model meets conditions of equilibrium thru cross section according to y and z directions. When we take into consideration restrain rigidity coefficient R_r^H and generalize analytical model from reference [2] by addition moment of inertia J , analytical model of bending with triangle (wedge) heat zone will be:

$$\alpha_{\Delta} = 2R_r^H \alpha_{th} \Delta T_{pl} \theta_s \sqrt{\frac{2}{e} F_0 \ln \theta_s} a h y_{pl}^{\max} \frac{3W - 2y_{pl}^{\max}}{12J} \quad (1)$$

where: R_r^H – restrain rigidity coefficient at the heating stage ($R_r^H < 1$) [4], α_{th} – thermal coefficient of expansion; $\Delta T_{pl} = T_{pl} - T_0$; J – moment of inertia according to centre of gravity; surface temperature θ_s described as nondimensional equation:

$$\theta_s = \frac{T_s - T_0}{T_{pl} - T_0} = \frac{2AP}{d\lambda(T_{pl} - T_0)} \sqrt{\frac{\kappa}{\pi v d}} \quad (2)$$

where: A – laser beam absorption coefficient; P – power of the laser beam; d – laser beam diameter; v – velocity of laser beam; $\kappa = \lambda / \rho c$ – thermal diffusivity; ρ – density of material; c – specific heat; λ – thermal conductivity coefficient; F_0 – Fourier number defined as:

$$F_0 = \frac{\kappa b}{v h^2} = \frac{\tau_h}{\tau_d} \quad (3)$$

where: $\tau_h = b/v$ – the interaction time between the heat source and material; $\tau_d = h^2/\kappa$ – time of heat diffusion thru thickness of the material; h – thickness of plate.

3. Experimental flat plate bending in perpendicular direction to beam incidence surface, theoretical calculations and microstructure investigations

3.1. Researches description

The aim of experiment was laser's flat plate bending in perpendicular direction to beam incidence surface and comparing results with theoretical model. The microstructure investigations was made as well. The triangle heat zone model (1) was utilized in this experiment's calculations.

Experiment was performed by CO₂ Trumpf TLF-6000 laser with segmented mirror head. The specimens were made from X5CrNi18-10 stainless steel. To reach triangle heated zone special steel mask was used. The specimen was scanned by 5mm diameter laser beam starting from vortex of triangle as Fig. 3. shown. The change of bended angle was real time measured by non-contact laser range-finder sensor and recorded onto computer. The displacement of measured point helped to calculate real bended angle α as Fig. 2. shown.

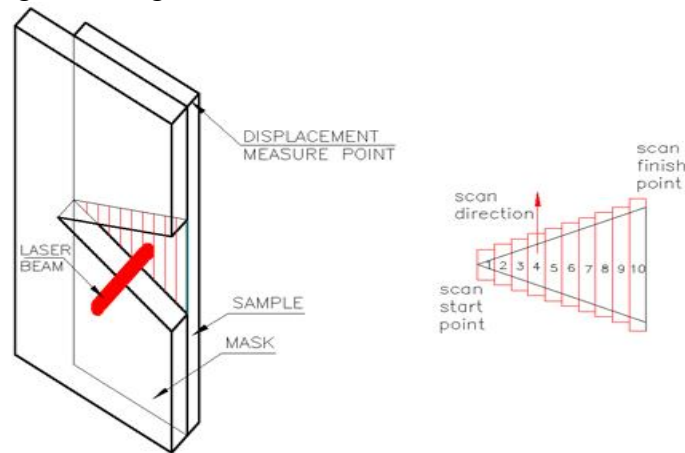


Fig. 3. Schema of experiment and laser beam guide path.

3.2. Experiment results

Three flat plate stainless steel X5CrNi18-10 specimens with dimensions 150×50×3 (length×width×thickness) was covered by mask with triangle cut. Vertex of triangle was on the edge of specimen's width (Fig. 3.). The velocity of laser beam was 0,005 m/s. The laser power was in order: 1st specimen – 400W, 2nd specimen – 700W, 3th specimen – 900W. Absorption of laser power was estimated as 0,7. Effects of laser bendings shows Fig. 4, Fig. 5, Fig. 6.

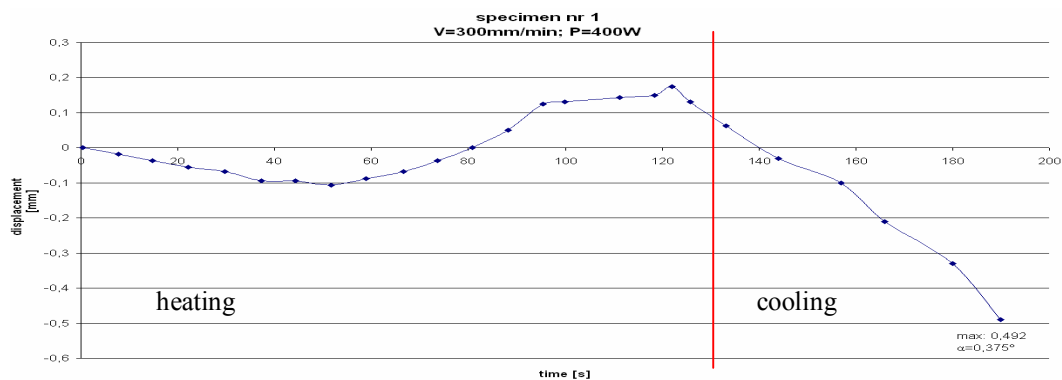


Fig. 4. First specimen bending angle change during heating process and after cool down to 80°.

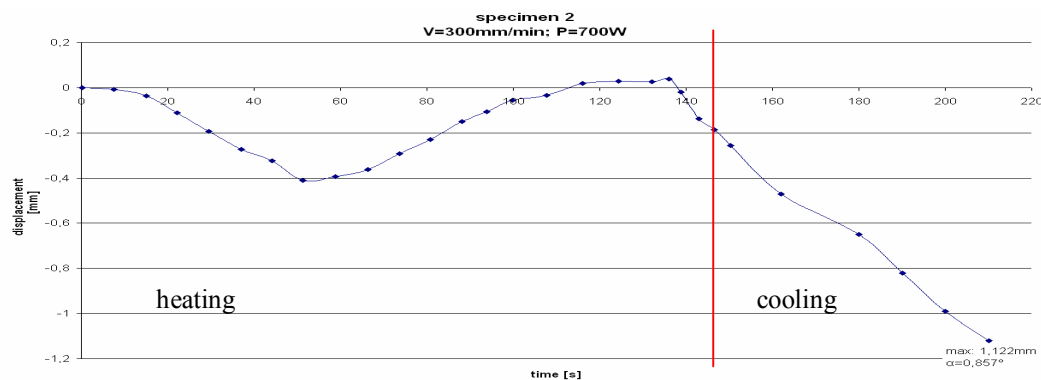


Fig. 5. Second specimen bending angle change during heating process and after cool down to 80°.

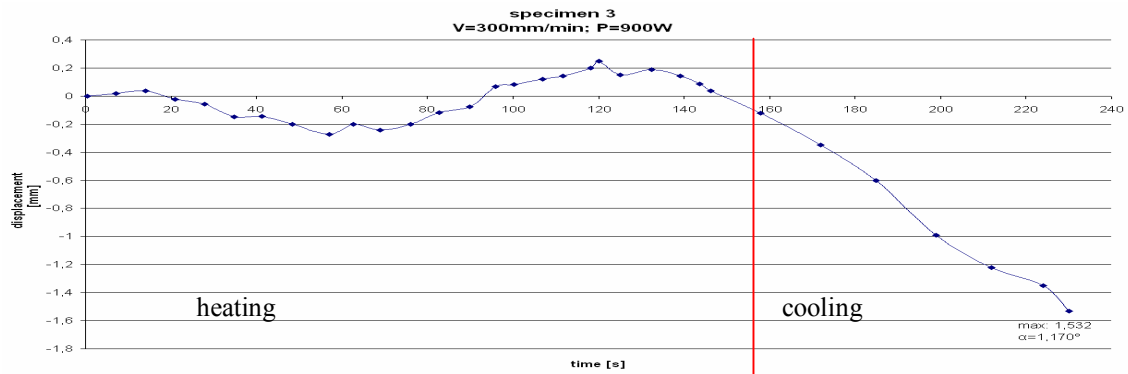


Fig. 6. 1th specimen bending angle change during heating process and after cool down to 80°.

Final angles reach values: 1st specimen – $\alpha=0,375^\circ$, 2nd specimen – $\alpha=0,857^\circ$, 3th specimen – $\alpha=1,170^\circ$.

3.3. Calculation results

Real bended angle was calculated by equation (1) to compare analytical model with experimental results:

The parameters which was used to calculations:

Material's constants (for X5CrNi18-10 stainless steel according to EN 10088-3: 2005):

$\lambda=16$ [W/mK], $\rho=7930$ [kg/m³], $c=500$ [J/kgK], $\alpha_{th}=17,2 \times 10^{-6}$ [m/mK]

Dimensions of specimen (acc. to Fig. 2.):

$a=0,035$ [m], $y_{max}=0,050$ [m], $w=0,050$ [m], $h=0,003$ [m]

Laser's treatment parameters:

$A=0,7$; $v=0,005$ [m/s]; $d=0,005$ [m]

Other parameters and calculations are presented in Tab. 1.

	Parameters		
	Laser's treatment parameters	Results of calculations data	Bending angle calculations
Specimen 1	$P=400$ [W] $\Delta T_{pl}=900$ [K]	$\kappa=0,403 \times 10^{-5}$ [m ² /s] $F_0=0,45$ $\theta_s=1,76$ $J=hw^3/12$	$\alpha=0,278^\circ$
Specimen 2	$P=700$ [W] $\Delta T_{pl}=1100$ [K]	$\kappa=0,403 \times 10^{-5}$ [m ² /s] $F_0=0,45$ $\theta_s=2,52$ $J=hw^3/12$	$\alpha=0,794^\circ$
Specimen 3	$P=900$ [W] $\Delta T_{pl}=1400$ [K]	$\kappa=0,403 \times 10^{-5}$ [m ² /s] $F_0=0,45$ $\theta_s=2,55$ $J=hw^3/12$	$\alpha=1,033^\circ$

Tab 1. Another parameters and calculations

3.4. Microstructure investigation

Microstructure of blank material X5CrNi18-10 was compared with material's sample from heating zone of 3th specimen (temp. of heating ~1400 [K], time of heating ~30 [s]).

The polished sections of two specimens were prepared. After polishing samples were etching with 87 etchant (10ml HNO₃; 20–50ml HCl; 30ml glycerol acc. to ASTM E407). Microstructure was observed with Neophot2 Carl Zeiss microscope with 100 magnification. Austenitic microstructure of both specimens was observed (Fig. 7.)

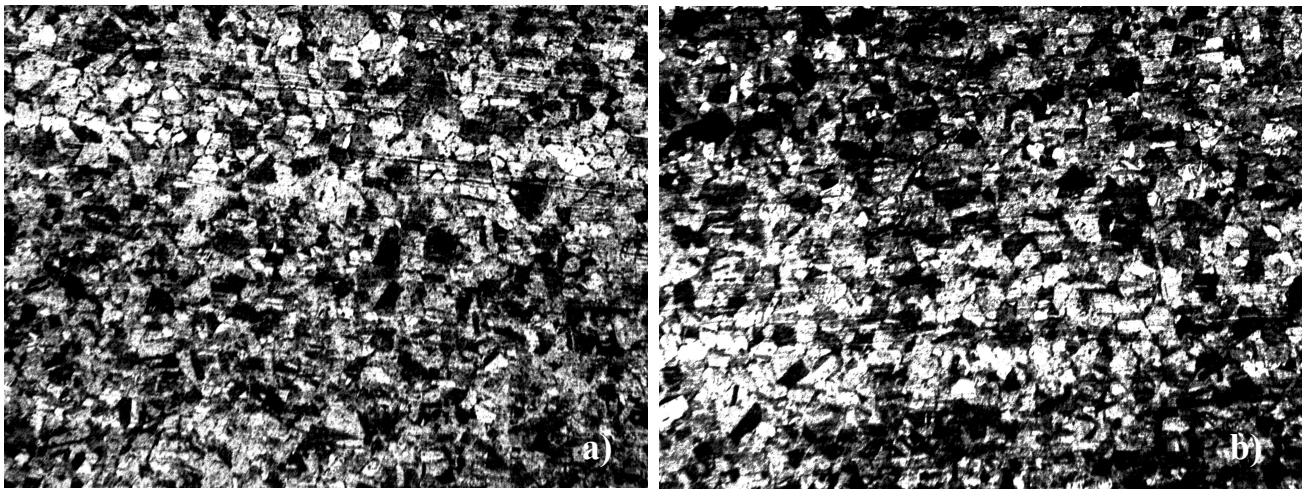


Fig. 7. Microstructure of blank material – a) and heat treated material – b). Magnification X100.

4. Conclusion

1. Possibility of thermal forming in perpendicular direction to beam incidence surface was proved by this experiment. This kind of forming using traditional plastic forming methods will be troublesome and hard to make. Non contact thermal method is easier way to produce bended elements. Experiment was prepared for flat plate, but this method could be apply to bend another industrial bars.
2. Results of experiment are very close to theoretical calculations. Some fluctuations of bending direction during heating stage we can observe. Bend angle direction stabilization appear during cooling stage (Fig. 4, 5, 6).
3. Microstructure investigation shown that austenitic structure both blank and treated material is present. This give us information that microstructure is unchanged after this kind of treatment. Other material properties (e.g. microhardness, tensile test) will be prepared in the future.
4. Experiment was performed using laser beam, but whatever focused heat of source can be apply e.g. plasma flame or acetylene torch.
5. Bend angle analytical equation (1) gives opportunity to choose parameters of machining and to design forming effects for flat plate and industrial bars.

References

- [1] KURP P., *Analytical model of Thermal Bending of Bars*, 8th European Conference of Young Research and Scientific Workers TRANSCOM 2009, Proceedings Section 5 Material Engineering Mechanical Engineering Technologies, pp. 109-114, Slovak Republic, Zilina, June 22-24, 2009.
- [2] MUCHA Z., *Efficiency of Material Laser Forming*, *International Workshop on Thermal Forming and Welding Distortion*, Bremen, Germany, 2008, p. 55-64
- [3] MUCHA Z., *Modelowanie i eksperymentalne badania kształtowania laserowego materiałów konstrukcyjnych*, Kielce, 2004
- [4] TAIRA S., OHTANI R., *Theory of high temperature resistance of materials*, Metallurgija, Moskwa, 1986



9 788055 403748

TRANSCOM 2011

Proceedings, Section 5

Published by University of Žilina

First Editions

Printed by EDIS-Žilina University publisher

ISBN 978-80-554-0374-8